Wrocław University of Technology
Centre of Advanced Materials and Nanotechnology

Materials Science

Poland

IX National Conference on Fast Ion Conductors Wrocław-Borowice, Poland, 9-12 December 2004

Guest Editors:
Anna Gągor, Radosław Czopnik

Vol. 24 • No. 1 • 2006

Oficyna Wydawnicza Politechniki Wrocławskiej

Materials Science is an interdisciplinary journal devoted to experimental and theoretical research into the synthesis, structure, properties and applications of materials.

Among the materials of interest are:

- glasses and ceramics
- sol-gel materials
- photoactive materials (including materials for nonlinear optics)
- laser materials
- photonic crystals
- semiconductor micro- and nanostructures
- piezo-, pyro- and ferroelectric materials
- high-T_c superconductors
- magnetic materials
- molecular materials (including polymers) for use in electronics and photonics
- novel solid phases
- other novel and unconventional materials

The broad spectrum of the areas of interest reflects the interdisciplinary nature of materials research. Papers covering the modelling of materials, their synthesis and characterisation, physicochemical aspects of their fabrication, properties and applications are welcome. In addition to regular papers, the journal features issues containing conference papers, as well as special issues on key topics in materials science.

Materials Science is published under the auspices of the Centre of Advanced Materials and Nanotechnology of the Wrocław University of Technology, in collaboration with the Institute of Low Temperatures and Structural Research of the Polish Academy of Sciences and the Wrocław University of Economics.

All accepted papers are placed on the Web page of the journal and are available at the address:
http://MaterialsScience.pwr.wroc.pl

Materials Science is abstracted/indexed in: Chemical Abstracts; Materials Science Citation Index; Science Citation Index Expanded.

The Journal is supported by the State Committee for Scientific Research

Printed in Poland

Drukarnia Oficyny Wydawniczej Politechniki Wrocławskiej
Zam. nr 274/2006

Contents

Materials Science-Poland, Vol. 24, No. 1, 2006

High-temperature solid-oxide fuel cells New trends in materials research

JANINA MOLENDA*

Faculty of Materials Science and Ceramics,
AGH University of Science and Technology, al. Mickiewicza 30, 30-059 Cracow, Poland

The paper is an overview of basic solid-oxide fuel cells (SOFC) components in terms of their fundamental functional parameters such as chemical stability, transport as well as catalytic and thermomechanical properties under, operational conditions in a fuel cell. An interrelation between the defect structure of these materials related to oxygen nonstoichiometry and their electronic properties and catalytic activity is shown. A single-chamber fuel cell concept is also presented.

Key words: *solid-oxide fuel cell; SOFC; electrode material; electrolyte*

1. Introduction

Recently observed great interest in fuel cell technology is due to the possibility of directly converting energy stored in hydrogen-containing fuels into electrical energy. A relatively simple construction of such a device and a high efficiency of electricity generation, noise-free operation due to the lack of mobile parts, and low level of waste products make this technology the most prospective for future electrical energy sources. The rate of "charging" (fuel refill) and potential reversibility of this process (storage of instantaneous energy excess in the form of chemical energy) are additional benefits. In the large group of fuel cells special attention has been paid to solid -oxide fuel cells (SOFC) [1–4]. Their commercial importance is connected to the construction of stationary generators with powers of at least 1 MW.

A wide application of this technology is hindered by some properties of the electrode materials and of the electrolyte, as well as high-temperature reaction conditions. The presently used yttrium-stabilized zirconia (YSZ), with low ionic conductivity, must operate at about 1000 °C. This implies a short service life of the cell (thermal

*E-mail: molenda@uci.agh.edu.pl

degradation of materials) and requires expensive and toxic materials, like $LaCrO_3$, for interconnectors, which raises problems for miniaturization and safety and increases costs. Lowering the service temperature to 600 °C is considered a strategic goal for the technological development of SOFCs, and calls for application of a suitable solid electrolyte, which at that temperature would have a purely ionic conductivity of 10^{-2} $S \cdot cm^{-1}$ and would be stable within the oxygen pressure range $1–10^{-20}$ atm.

2. Electrical, catalytic and thermomechanical properties of materials used in SOFCs

Figure 1 schematically illustrates the structure and functions of the SOFC components. Different aspects can be considered in the functioning of each component, e.g. transport and catalytic properties or structural and thermomechanical properties.

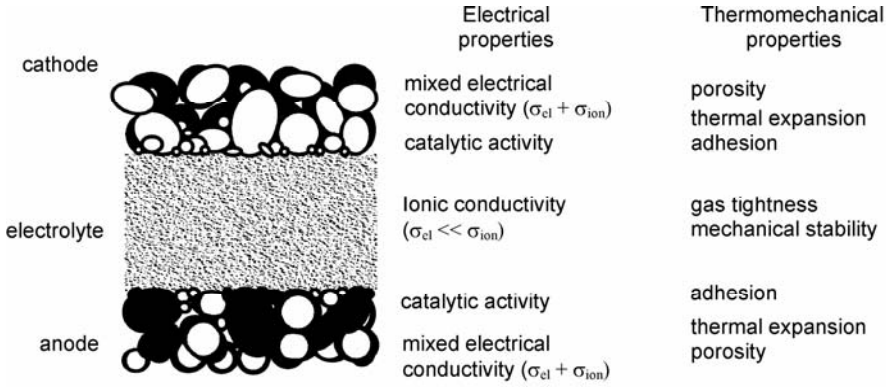

Fig. 1. Schematic cross-section of a SOFC; structure, properties, and functions of SOFC components

2.1. Transport and catalytic properties

The cathode made of $LnMeO_3$-type oxides (Me = Mn, Fe, Co, Ni) with a perovskite structure is a mixed ionic-electronic conductor. The ionic conductivity is related to oxygen nonstoichiometry (oxygen vacancies), while the electronic conductivity to the mixed valency of cations, Me^{3+}/Me^{4+}, depending on the extent of oxygen nonstoichiometry and the amount and type of dopants. The cathode material plays the role of a catalyst for the reduction of oxygen. Since it operates in air or oxygen, the stability of oxides is not a problem.

The solid electrolyte (YSZ, CeO_2 (Gd, Sm)), as a purely ionic conductor with oxygen vacancies as carriers, is stable over a wide range of oxygen pressures ($1–10^{-20}$ atm); near the cathode it operates in highly oxidizing conditions and near the anode (fuel supply) in highly reducing ones. The ionic conductivity at the service

temperature should be about 10^{-2} S·cm^{-1}. So far, no real system has been found to satisfy both mentioned requirements.

The anode (Ni/YSZ or Ni/CeO_2(Gd, Sm) cermet) is an ionic-electronic conductor. Its ionic conductivity is related to oxygen vacancies in YSZ or in CeO_2 (Gd, Sm). The electronic conductivity results from the existence of a conductive percolation path at 30% Ni concentration in the anode material. Nickel catalyses the fuel oxidation. Highly reducing atmosphere is not detrimental for the anode material, furthermore it improves its effectiveness (maintains the catalytic activity of nickel and raises the electrical conductivity of CeO_2).

2.2. Structural and thermomechanical properties

The cathode and anode materials should be porous, in order to allow the penetration of gases. In the layers close to the electrolyte, however, the porosity should be as low as possible to intensify the lattice diffusion of oxygen. The electrolyte is a gas-tight sinter with high strength, preventing a non-productive combustion of the fuel. All the cell components should be chemically and thermally compatible.

3. Electrolytes in intermediate temperature SOFCs (IT-SOFCs)

It seems that some improvements of the properties of solid electrolytes based on ZrO_2 are still technologically feasible. This especially refers to electrical conductivity which might be increased by doping. It has been shown [5] that scandium dopant in zirconia can raise conductivity by two orders of magnitude but its scarce occurrence in the earth crust and high price excludes this element from practical applications. Another possibility for improving the electrical conductivity of zirconia-based electrolytes is to develop the technology of thicker than 1 mm, gas-tight YSZ layers, and to modify the microstructure of zirconia (nanocrystalline layers, a dispersed composite Y_2O_3–ZrO_2–Al_2O_3 electrolyte [6, 7]). Electrolytes based on bismuth oxide, Bi_2O_3, exhibit high ionic conductivity but Bi_2O_3 undergoes reduction to metallic bismuth at low oxygen pressures. Some oxides with the perovskite structure (e.g. $SrCe_{0.95}Yb_{0.05}O_{3-y}$, $CaZr_{0.96}Y_{0.04}O_{3-y}$ [8]), showing proton conductivity, have also been investigated.

From among the many oxide conductors studied, cerium dioxide (CeO_2), stabilized with rare-earth oxides (i.e. with samarium or gadolinium) is most often quoted as a candidate for IT-SOFC. This electrolyte has an electrical conductivity higher than the ZrO_2-based electrolytes and lower activation energy of conductivity. Solid electrolytes $Ce_{0.8}Sm_{0.2}O_2$ (referred to as SDC) and $Ce_{0.9}Gd_{0.1}O_2$ (GDC) have, so far, the highest oxide-ion conductivity, reaching about 10^{-1} S·cm^{-1} at 800 °C [9]. An important benefit of CeO_2-based electrolytes compared to ZrO_2 is their chemical and thermal compatibility with the new generation of cathode materials, $LaMO_3$ (M = Mn, Co, Fe, Ni), with a perovskite structure and the thermal expansion coefficient very close to

that of interconnectors made of high-chromium ferritic steels. The most troublesome deficiency of electrolytes based on CeO_2 in commercial use is that its oxygen non-stoichiometry increases at high temperatures and low oxygen pressures, $pO_2 < 10^{-14}$ atm (reducing conditions near the anode), which gives rise to an undesirable electronic conduction related to the following reaction:

$$O_O^x = V_O^{\bullet\bullet} + 1/2\,O_2 + 2e^- \tag{1}$$

The elimination of electronic conduction and widening of the oxygen pressure range to 10^{-20} atm, where the transport number of oxygen ions equals 1, remains one of the essential problems to be solved. This can be done by doping of the cerium sublattice with selected ions with valencies different from that of cerium. A challenging task for solid-state chemistry is to assess the interrelations between the types of point defects connected with oxygen nonstoichiometry and foreign dopant atoms, their concentrations, crystal structures, and transport properties.

4. Cathode materials in IT-SOFC

Cathode materials in IT-SOFC must satisfy the following requirements: mixed ionic-electronic conductivity, thermal and chemical stability at high temperatures in air and good chemical and thermo-mechanical compatibility with the electrolyte. The cathode material also plays the role of a catalyst in the reduction of oxygen:

$$1/2\,O_2 + V_O^{\bullet\bullet} + 2e^- = O_O^x \tag{2}$$

Mixed ionic-electronic conductivity and a significant open porosity enable oxygen reduction not only on the surface but also in the entire volume of the electrode.

Candidate materials for cathodes in IT-SOFCs are searched for in two groups of compounds with perovskite structures: $Ln_{1-x}Sr_xCo_{1-y}Fe_yO_{3-\delta}$ (where: Ln = La, Sm, Nd, Gd, Dy) – referred to as LSCF – and $Ln_{1-x}A_xM_{1-y}Mn_yO_{3-\delta}$ (where: Ln = La, Nd, Pr; A = Ca, Sr; M = 3d metal other than manganese) [10, 11]. Recently, compounds such as $(La,Sr)Ni_{1-y}Fe_yO_3$ [12] and $LaNi_{1-y}Co_yO_3$ [13] have also been under investigation.

The basic problem concerning $LaMO_3$ (M = Mn, Fe, Co, Ni) cathode materials is their insufficient rate of oxygen-ion transport at 600 °C. Moreover, depending on oxygen partial pressure, the type of dominating defects may change from oxygen excess ($LaMO_{3+y}$) to oxygen deficiency ($LaMO_{3-y}$). For the cathode material, the most advantageous defects are oxygen vacancies. These defects are often formed at oxygen partial pressures $pO_2 < 10^{-3}$–10^{-4} atm, while the cathode operates in air. One of the important research tasks is to shift the stability range of oxygen vacancies to higher oxygen pressures (0.21 atm). It has been reported [4] that strontium-doped (50%) $La_{1-x}Sr_xMnO_3$ changes the conduction mechanism at high temperatures from a small polaron mechanism to metallic conduction, which is a very desirable behaviour in

SOFCs. Metallic conduction can also be obtained in the group of oxides with the formulas $La_{1-x}Sr_xCoO_3$ and $La_{1-x}Sr_xFeO_3$ [14].

Recently, oxides with the perovskite structure have been the subject of extensive studies [15, 16] but most research activities concentrate on their useful properties, i.e. possible applications as cathodes in SOFC. Fundamental studies, which might contribute to better understanding the relations between crystallographic structure, ionic and electronic defects resulting from nonstoichiometry, doping level, electronic structure, and transport properties or the reactivity of perovskite oxides versus oxygen are lacking. These issues are still of great importance. It has been found [4] that the kinetics of the cathode oxygen reduction may restrict the electrochemical effectiveness of SOFC. The catalytic reduction of oxygen on perovskites has not yet been sufficiently clarified. It is known that the rate of oxygen absorption by the cathode material depends on the concentrations of both oxygen vacancies and quasi-free electrons in the cathode material. Oxygen vacancies are donor centres providing quasi-free electrons on ionisation. Therefore, oxygen nonstoichiometry and foreign dopants affect the location of the Fermi level in the cathode material [17] which – according to Volkenstein's theory – controls the catalytic activity of the cathode material. The extent of oxygen nonstoichiometry (dependent on the synthesis conditions, i.e. temperature and oxygen pressure) as well as the type and concentration of dopants (which also affect oxygen nonstoichiometry) [18, 19] can control the Fermi level position and catalytic activity of the cathode material.

5. Anode materials in IT-SOFC

Anode material in high-temperature SOFCs is Ni/YSZ cermet, whereas in IT-SOFCs it is Ni/CeO_2 (Sm, Gd) [20]. The anode material, similarly as the cathode material, should be an ionic-electronic conductor. Its ionic conductivity is associated with oxygen ion transport via oxygen vacancies in YSZ or in CeO_2 (Sm, Gd). Electronic conductivity originates from the presence of metallic nickel in the anode material. For a nickel concentration of 30%, a percolation path is formed manifesting itself in macroscopic metallic properties of the anode material. Metallic nickel additionally plays the role of a catalyst in the oxidation of fuel.

Investigations of the Ni/YSZ system under operating conditions of the cell [21] indicate that the optimisation of its microstructure is necessary. Current flow brings about nickel agglomeration in the anode/electrode system, which lowers the electrochemical efficiency of the anode to a significant extent.

6. Single-chamber cell concept

The concept of a single-chamber cell, a new and very promising one, put forward by Hibino [22–24], overcomes many difficult problems unresolved so far. In this cell,

the cathode and anode, both with selective electrocatalytic properties for oxygen and hydrogen, respectively, are mounted in a common space filled with a mixture of fuel and oxidant. The electrocatalytic properties of the anode in this system must be sufficient to eliminate the need for preliminary conversion of the natural fuel. The ionic current in the cell depends on the difference between the catalytic activities of the electrodes. It becomes pointless to separate the gases around the anode and cathode (simple battery design). The electrolyte can be porous and permeable to gases, which eliminates the technological difficulties connected with manufacturing thin plates of ceramic electrolytes with high strengths. As the oxygen pressure in the reaction chamber of this cell is relatively high (fuel/air mixture) compared to the oxygen pressure in the anode space of the classical cell, the instability of some oxide electrolytes, which have competitively high electrical conductivities (e.g. bismuth oxide), is no more a problem. The optimum operating temperature of a single-chamber cell is 600 ºC, for higher temperatures both electrodes catalyse the non-productive combustion of the fuel. It should be stressed that the materials selected earlier for characterization and application in classical IT–SOFCs, electrolytes (based on CeO_2) and electrode materials (cathodes based on the perovskite-type oxides $LnMO_3$ (M = Mn, Fe, Co, Ni) and anodes of $Ni/CeO_2(Gd)$ cermet), are also suitable for single-chamber cells. In the development of materials for single-chamber cells, special attention should be paid to the catalytic selectivity and activity of both electrodes.

Acknowledgment

The work was supported by the Polish Committee for Scientific Research under the grant PBZ-KBN 100/T08/2003.

References

[1] DOKIYA M., Solid State Ionics, 152–153 (2002), 383.
[2] YAMAMOTO O., Electrochim. Acta, 45 (2000), 2423.
[3] BADWAL S.P.D., FOGER K., Ceramics International, 22 (1996), 257.
[4] MINH N.Q., J. Am. Ceram. Soc., 76 (1993), 563.
[5] YAMAMOTO O., Electrochim. Acta, 45 (2000), 2423.
[6] AGRAWAL R.C., GUPTA R.K., J. Mater. Sci., 34 (1999), 1131.
[7] SORA I., SCHMIDT C., J. Eur. Ceramic Soc., 22 (2002), 1645.
[8] GLERUP M., POULSEN F.W., BERG R.W., Solid State Ionics, 148 (2002), 1645.
[9] DUDEK M., MOLENDA J., Defect Diff. Forum (in press).
[10] LI S., JIN W., XU N., SHI J., Solid State Ionics, 124 (1999), 277.
[11] WALLER D., LANE J.A., KILNER J.A., STEELE B.C.H., Solid State Ionics, 86–88 (1996), 767.
[12] PHILIPS M.B., SAMMES N.M., YAMAMOTO O., Solid State Ionics, 123 (1999), 131.
[13] HROVAT M., KATSARAKIS N., REICHMANN K., BERNIK S., KUSCER D., HOLC J., Solid State Ionics, 83 (1996), 99.
[14] LAURET H., CAIGNOL E., HAMMOU A., Proc. II Internat. Symp. on Solid Oxide Fuel Cells, F. Gross, P. Zegers, S. C. Singhal, O. Yamamoto (Eds.), Luxemburg, 1991, p. 479.
[15] FLEIG J., Ann. Rev. Mat. Res., 33 (2003), 361.
[16] SHAO Z., HAILE S.M., Nature, 431 (2004), 170.

[17] MOLENDA J., KUBIK A., Solid State Ionics, 117 (1999), 57.
[18] MOLENDA J., High Temperature Mater. Processes, 10 (1992), 223.
[19] MOLENDA J., NOWAK I., JEDYNAK L., MARZEC J., STOKŁOSA A., Solid State Ionics, 135 (2000), 235.
[20] ATKINSON A., BARNETT S., GORTE R.J., IRVINE J.T.S., MCEVOY A.J., MOGENSEN M., SINGHAL S.C., VOHS J., Nature Materials, 3 (2004), 17.
[21] IVERS-TIFFEE E., WEBER A., HERBSTRITT D., J. Europ. Ceramic Soc., 21 (2001), 1805.
[22] HIBINO T., IWAHARA H., Chem. Lett., 7 (1993), 1131.
[23] HIBINO T., WANG S., KAKIMOTO S., SANO M., Electrochem. Sol. State Lett., 27 (1999), 317.
[24] HIBINO T., HASHIMOTO A., INOUE T., TOKUNA J.-L., YOSHIDA S.-I., SANO M., Science, 288 (2000), 2031.

Received 10 December 2004
Revised 17 February 2005

Materials Science-Poland, Vol. 24, No. 1, 2006

Oxide-ion conductors for fuel cells

F. KROK[1*], I. ABRAHAMS[2**], W. WROBEL[1], A. KOZANECKA-SZMIGIEL[1], J. R. DYGAS[1]

[1]Faculty of Physics, Warsaw University of Technology, ul. Koszykowa 75, 00-662, Warsaw, Poland.

[2]Centre for Materials Research, Department of Chemistry,
Queen Mary, University of London, Mile End Road, London E1 4NS, United Kingdom

The principal materials used in the construction of solid oxide fuel cells (SOFCs) are discussed. Some of the problems encountered with high temperature fuel cells (HT-SOFCs) might be overcome by lowering the operating temperature to 500–700 °C, through the development of suitable materials for intermediate temperature fuel cells IT-SOFCs. Candidate electrolyte materials are discussed, including cerium gallium oxide, lanthanum strontium gallium magnesium oxide, and electrolytes based on doped bismuth oxide. While high ionic conductivities can readily be achieved in these materials at intermediate temperatures, stability in reducing atmosphere is still a problem. This might be overcome by careful chemical design of electrolytes containing stabilising dopants. Two zirconia-doped bismuthate systems are discussed in this respect. In both cases, the obtained materials exhibit different structures – one is $Bi_3Nb_{1-x}Zr_xO_{7-x/2}$ of the δ-Bi_2O_3 type, and the other, $Bi_4V_{2-2x}Zr_xO_{11-x}$, has a layered structure of the Aurivillius type.

Key words: *fuel cell; solid electrolyte; bismuth oxide*

1. Introduction

Fuel cells are the most efficient power-generating devices; they convert the chemical energy of fuel directly to electrical energy, without the need for intermediate conversion to thermal energy. Therefore, the efficiency of a fuel cell is not subject to the Carnot limitation. The principal components of a fuel cell are an ion conducting electrolyte and two electrodes: an anode and a cathode. For practical applications, single cells are typically connected in series. The connectors between cells (called interconnectors or bipolar separators) are therefore also important parts of the device. Electrolytes allow the fast conduction of ions between the two electrodes but the conductivity of electrons should be negligible. Electronic conduction occurs in the external circuit and can be used for

*Corresponding author, e-mail: fkrok@mech.pw.edu.pl
**Corresponding author, e-mail: I.Abrahams@qmul.ac.uk

external load applications. The critical component of any fuel cell is the electrolyte, the choice of which dictates the choice of the other components.

There are various types of fuel cells, depending on the type of electrolyte used. The most intensively studied fuel cells are polymer electrolyte-membrane fuel cells (PEMFCs), also called proton exchange-membrane fuel cells as they are based on proton conducting electrolytes and solid oxide fuel cells (SOFCs) based on solid oxide electrolytes. There are several of comprehensive reviews on recent developments in fuel cells (see eg. [1–3]).

Pure hydrogen represents the ideal fuel for fuel cells. There are many problems, however, associated with the production, storage, and distribution of pure hydrogen [1], and if the widespread use of fuel cells is to be achieved then other fuels need to be considered at least in the short term. Suitable alternatives include methanol and hydrocarbons such as methane. For these fuels, optimal cell operating conditions generally occur at high temperatures, i.e. within the normal operating range of SOFCs. This is one of the main reasons for the growing interest in SOFCs as alternatives to PEMFCs, which have lower operating temperatures.

Well-established high temperature (ca. 1000 °C) SOFC technology (HT-SOFCs) is based on the oxide-conducting yttria-stabilised zirconia (YSZ) electrolyte. In recent years, however, the need for smaller low-power SOFCs (up to a few tens of Watts), which could be operated at intermediate temperatures (ca. 500–700 °C, IT-SOFCs), has been expressed. The operation of SOFCs at intermediate temperatures would for example enable their application in electric vehicles. In this paper, the principal materials relevant for IT-SOFCs are discussed. In this respect, oxide ion conductors studied in our own work are examined in terms of their potential application in IT-SOFCs.

2. General requirements for fuel cells

Target power densities of fuel cells are typically of the order of 1 $kW \cdot kg^{-1}$. To meet this goal, the area specific resistivity (ASR) of the combined system (electrolyte plus both electrodes) should not exceed 0.5 $ohm \cdot cm^2$ [2]. Assuming approximately equal contributions from each component to the ASR, the requirement for the electrolyte alone is about 0.15 $ohm \cdot cm^2$.

The general requirements for the principal components of fuel cells are as follows:

Electrolyte: high ion conductivity with negligible electronic conductivity; dense non-porous microstructure (to avoid the permeation of neutral gas fuel molecules).

Electrodes: high mixed ionic-electronic conductivity (ionic – to ensure good electrical contact with the electrolyte, electronic – to ensure good electrical contact with the interconnector); porous microstructure (to allow gas transport to and from the electrolyte).

Interconnector: high electronic conductivity with negligible ionic conductivity; dense non-porous microstructure (to prevent gas mixing).

Moreover, a high stability (both temperature stability and phase stability in contact with reducing and/or oxidising atmospheres and other cell components) of each component and similar thermal expansion coefficients for components to avoid cracking during operation are required.

3. SOFCs based on YSZ

The most commonly used electrolyte material in HT-SOFCs is YSZ. Suitable electrodes for this cell are nickel/YSZ cermet for the anode and doped lanthanum manganite perovskite for the cathode. The component materials are discussed below.

Electrolyte: YSZ is a solid solution formed between ZrO_2 and Y_2O_3 with a general formula of $Zr_{1-x}Y_xO_{2-x/2}$, with the highest conductivity around $x = 0.1$ [4]. The structure is based on that of fluorite (CaF_2), with a cubic close-packed Zr/Y and O located at the tetrahedral sites, resulting in eight-coordination for the cations. The introduction of subvalent Y^{3+} for Zr^{4+} is compensated for by vacancies created on the oxide ion sublattice. High vacancy concentration combined with high mobility results in a very high oxide-ion conductivity in this material at temperatures above 800 °C.

Anode: To provide the desired properties of the anode, usually a composite (cermet) of the electrolyte material (in this case YSZ) and powdered metal is used [5]. Nickel metal is commonly used due to its low cost. The role of the YSZ electrolyte in the cermet anode is to support the nickel-metal particles and prevent their agglomeration and coarsening. The content of nickel in the cermet anode has to be higher than the percolation threshold of this system to assure the high conductivity of the material. The percolation threshold for conductivity in this system is about 30% vol. of nickel content [5].

Cathode: Many oxides have been examined as potential cathodes in SOFCs. The crucial parameters which have to be taken into account in the assessment of suitability are electrical conductivity, phase stability, and the coefficient of thermal expansion. On this basis, strontium-doped lanthanum manganite, $La_{1-x}Sr_xMnO_3$ (LSM), was found to be particularly suitable [6]. Partial substitution of La^{3+} by Sr^{2+} in $LaMnO_3$ is charge compensated by the oxidation of Mn^{3+} to Mn^{4+} and results in an increase in electronic conductivity.

If the cell design is to be based on self-supporting YSZ, the minimum electrolyte thickness needs to be about 150 μm [2]. Thinner membranes can be produced, but only as thin layers supported on substrates. For self supporting YSZ, a target ASR of 0.15 ohm·cm^2 is obtained only at temperatures higher than about 950 °C, and there are many problems associated with cell construction at these temperatures. For example, under these operating conditions there is a limited choice for the interconnector material. Co-doped $LaCrO_3$ is commonly used [7]. There is concern, however, over the use of chromium poisoning the cathode performance.

Lowering the fuel cell operating temperature through the design of novel SOFCs operating at intermediate temperatures (IT-SOFC) could solve many problems associated with HT-SOFCs.

In order to keep YSZ as the electrolyte material and to maintain the assumed target ASR of 0.15 ohm·cm^2 at lower temperatures, much thinner electrolyte membranes are required. The minimum useful thickness for the YSZ membrane is about 15 μm, since thinner membranes exhibit significant levels of gas permeation [1]. For the YSZ membrane of 15 μm, the ASR of 0.15 ohm·cm^2 can be obtained at 700 °C [2]. For IT-SOFCs based on YSZ, the same electrodes as for HT-SOFCs can be used. In this case, however, there is no need to use a Cr-containing perovskite material for the interconnector, since at 700 °C simple stainless steel will suffice.

4. New materials for IT-SOFCs

There are other materials that exhibit electrical conductivities higher than that of YSZ at temperatures lower than 700 °C, and these materials can be considered as potential electrolytes in IT-SOFCs. The Arrhenius plots of conductivities of some candidate materials are presented in Figure 1. The most intensively studied materials in terms of the above-mentioned application are gadolinium-doped ceria (CGO) [8] and lanthanum-strontium-gallium-magnesium perovskites (LSGM) [9]. The best oxide ion conductors at low temperatures are based on Bi_2O_3 [10], and these also have to be considered in this respect.

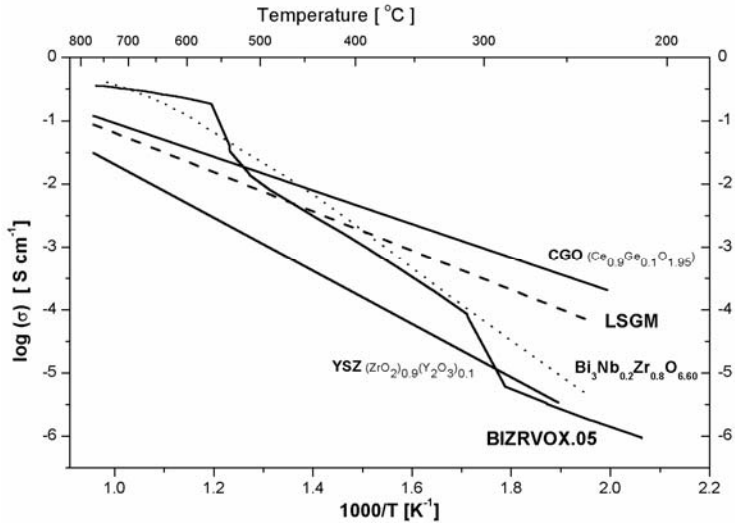

Fig. 1. Arrhenius plots of conductivities of selected oxide-ion conducting electrolytes

Like YSZ, ceria (CeO_2) exhibits a fluorite-type structure which is well suited for high oxide-ion conductivity [11]. Doped CeO_2 can exhibit even higher conductivity than stabilised zirconia [8]. This material shows a significant electronic conductivity at high temperatures, however, which results in cell short-circuiting. Electronic con-

ductivity arises from the reduction of Ce^{4+} to Ce^{3+} in the reducing atmosphere of the cell. At sufficiently low temperatures (about 500 °C), the electronic contribution can be neglected for some compositions, e.g. $Ce_{0.8}Gd_{0.2}O_{1.9}$ [12].

Another potential electrolyte for IT-SOFCs is doped lanthanum gallate $LaGaO_3$ [9]. The introduction of the divalent ions Sr^{2+} and Mg^{2+} into trivalent La^{3+} and Ga^{3+} sites, respectively, results in the creation of oxide ion vacancies and consequently in an increase of ionic conductivity in the obtained system (LSGM). The best electrical properties have been found for the composition $La_{0.9}Sr_{0.1}Ga_{0.8}Mg_{0.2}O_{3-\delta}$ [9]. It is very important that this compound is a purely ionic conductor over a very wide oxygen partial pressure range (large ionic domain). The main problem with LSGM is the difficulty in obtaining a single-phase material.

For IT-SOFCs based on both CGO and LSGM electrolytes, alternative electrodes are required.

5. Bi_2O_3-based electrolytes

There is a natural temptation to use the materials based on the best oxide ion conductor, δ-Bi_2O_3 [10], as electrolytes in IT-SOFCs. Bi_2O_3 shows a significant polymorphism with two stable phases, α and δ [13]. High conductivity appears only in the high-temperature δ-phase of a fluorite-type structure. Numerous studies have been carried out on stabilising the δ-phase to room temperature through the substitution of Bi by various metals [10]. Besides the δ-phase, these studies have revealed a number of new phases. The main drawback of Bi_2O_3 and related compounds is the lack of stability in contact with reducing atmospheres. However, there is a possibility of applying highly conductive Bi_2O_3-based conductors as solid electrolytes in single-gas chamber SOFCs, where reducing conditions for electrolytes are not that strict since they operate in a gas mixture of fuel and oxygen [14]. Moreover, there are several of possible ways to overcome the problem of the instability of Bi_2O_3-based materials, for example by covering them with a thin passivating layer resistant to reduction, e.g. of ZrO_2 [15]. Another possibility is a suitable doping of the Bi-based oxide which can lead to a material with a wider ionic domain. For example, $Bi_{1.6}Er_{0.4}O_3$ doped with zirconium is reported to have enhanced the stability to reduction [15]. Below, we present examples of the results of such studies carried out in our laboratories.

5.1. δ-Bi_2O_3-type materials

The substitution of 25% of Bi in Bi_2O_3 by Nb results in a room temperature–stable δ-Bi_2O_3-related phase with a formula of Bi_3NbO_7 [16]. In this compound, there is a lower, but still significant, number of oxide ion vacancies. Using Bi_3NbO_7 as the base composition, it is possible to vary the vacancy concentration by suitable substitution of Nb. For example, substitution of pentavalent Nb by subvalent cations, such as

tetravalent Zr, results in an increase in vacancy concentration and consequently in an increase in ionic conductivity [17]. An X-ray diffraction study of the system $Bi_3Nb_{1-x}Zr_xO_{7-x/2}$ has revealed that in the composition range $0 \le x \le 0.4$ a single cubic δ-Bi_2O_3 -type phase is observed. At higher compositions, a second fluorite-related phase (δ′) appears. The δ′ phase has a larger cubic cell parameter ($a \approx 5.51$ Å) than the original δ-phase ($a \approx 5.47$ Å). At compositions with $x \ge 0.6$, the system shows the presence of additional phases, viz. unreacted α-Bi_2O_3, ZrO_2, and β_{III}-$Bi_{2-x}Zr_xO_{3+x/2}$.

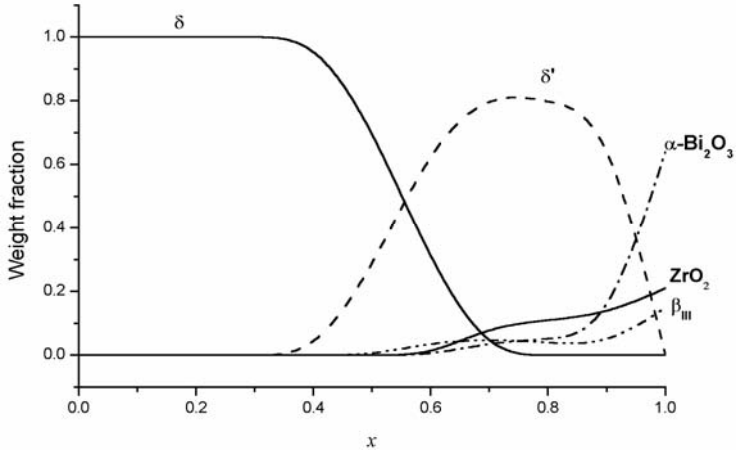

Fig. 2. Variation of the weight fractions of principal components with composition in the system $Bi_3Nb_{1-x}Zr_xO_{7-x/2}$

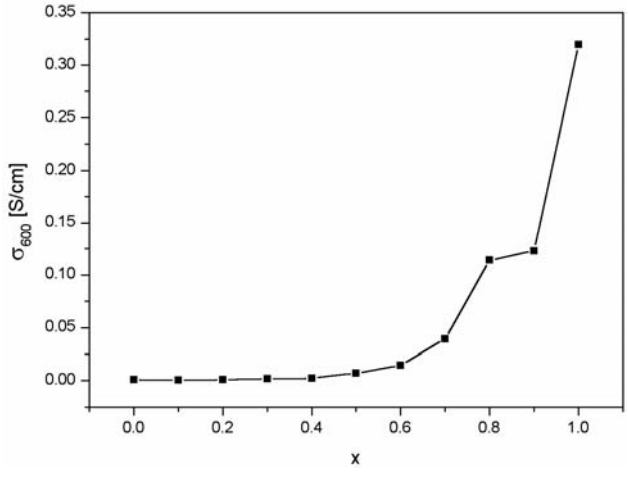

Fig. 3. Variation of total conductivity at 600 °C with composition in the system $Bi_3Nb_{1-x}Zr_xO_{7-x/2}$

The variation in the weight fraction of these phases in the studied system, presented in Figure 2, shows a gradual increase in their concentration with increasing Zr

content. The variation in electrical conductivity at 600 °C as a function of chemical composition is shown in Figure 3. The steep increase in electrical conductivity in the region corresponding to the appearance of the δ′ phase cannot be explained only by the calculated increase in vacancy concentration with increasing *x*. It must also be associated with a change in structure between the δ and δ′ phases. The higher conductivity of the δ′ phase suggests a greater ionic mobility within this less dense structure.

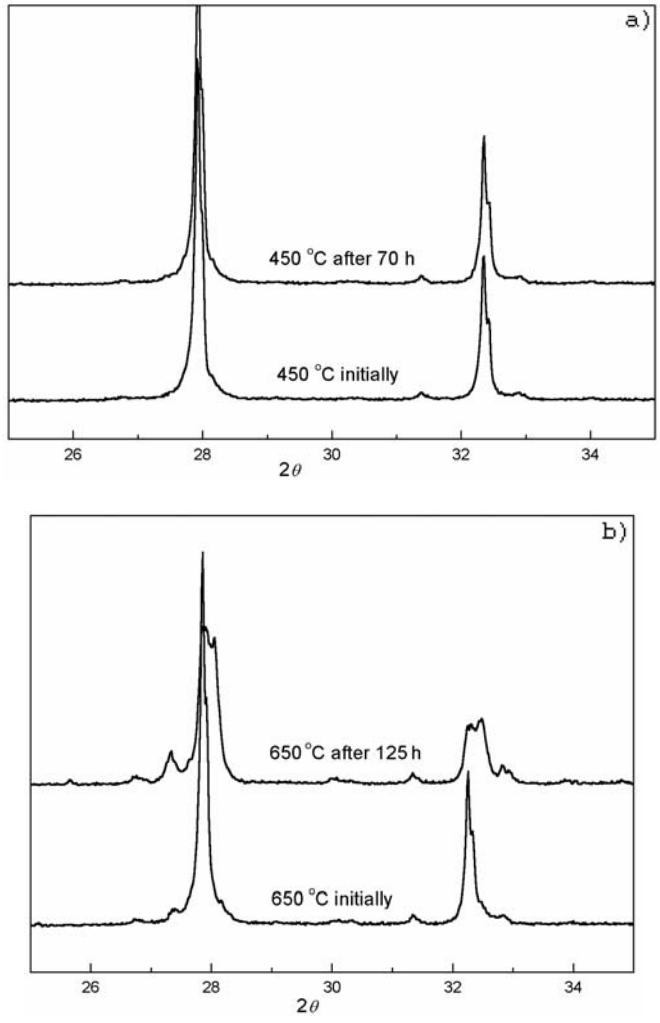

Fig. 4. X-ray powder diffraction patterns at 450 °C (a) and 650 °C (b) for a sample with the composition of $Bi_3Nb_{1-x}Zr_xO_{7-x/2}$ ($x = 0.7$)

The obtained high conductivity in the δ′ phase is a positive feature of this system but it is not sufficient to warrant its application as an electrolyte in IT-SOFCs. The other requirements to be fulfilled are stability at high temperatures and the proper

ionic domain in conductivity (stability in contact with a reducing atmosphere). The first requirement has been examined – a material with the composition lying within the range of dominance of the δ′ phase ($x = 0.7$) was subject to prolonged annealing at elevated temperatures [18]. The obtained results indicate that the δ′ structure is maintained upon annealing at 450 °C. A significant degree of material degradation is evident, however, upon annealing at 650 °C (Fig. 4). The nature of this degradation, i.e. phase transition or phase separation, is now under study. The stability of the material under a reducing atmosphere is also being investigated.

5.2. Layered Aurivillius-type structures

Interesting results have been obtained in the system Bi_2O_3–V_2O_5, where the layered compound, $Bi_4V_2O_{11-\delta}$ (δ is associated with V reduction), is obtained [19]. This

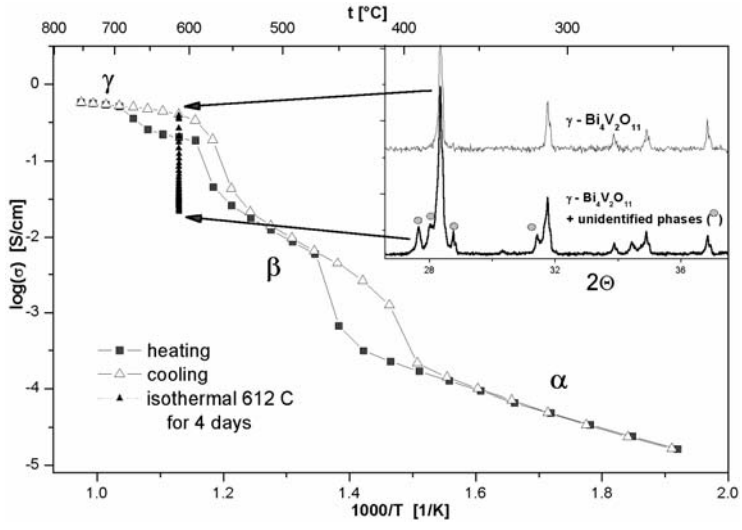

Fig. 5. Arrhenius plot of total conductivity for $Bi_4V_2O_{11-\delta}$, showing conductivity decay upon prolonged annealing at 612 °C. The insert shows initial and final (after annealing) X-ray powder diffraction patterns

compound shows significant polymorphism, with three principal phases – α, β and γ – observed over particular temperature ranges. High electrical conductivity is characteristic only of the high temperature tetragonal γ-phase. A great deal of work has been carried out in the stabilisation of this phase at room temperature through the substitution of vanadium by aliovalent cations [20]. The resulting family of solid electrolytes have been termed the BIMEVOXes. In many cases, the BIMEVOXes show a significant enhancement of electrical conductivity at low temperatures in comparison to the parent $Bi_4V_2O_{11-\delta}$. We have examined the possible use of BIMEVOXes as electrolytes in IT-SOFCs. The zirconium member of the BIMEVOX family (BIZRVOX) [21–23] was investigated. As in the bismuth niobates, the reason for the choice of BIZRVOX

was the reported enhanced stability to the reduction of Bi_2O_3-based compounds when doped with Zr [15]. The thermal stability of $Bi_4Zr_{0.1}V_{1.9}O_{10.95}$ in air at elevated temperatures was investigated by ac impedance spectroscopy upon prolonged annealing and compared to the behaviour of the parent material, $Bi_4V_2O_{11-\delta}$, under similar conditions.

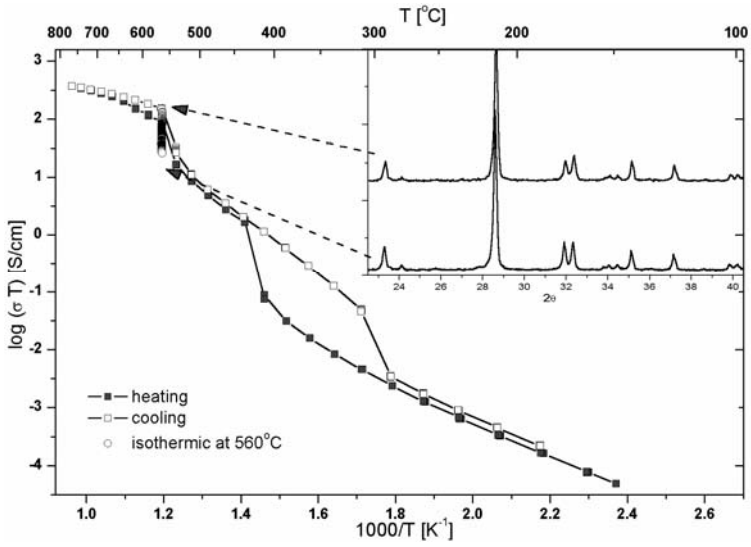

Fig. 6. Arrhenius plot of conductivity for $Bi_2Zr_{0.05}V_{0.95}O_{4.75-\delta}$, showing conductivity decay upon prolonged annealing at 560 °C. The insert shows initial and final (after annealing) X-ray powder diffraction patterns

The results summarised in Figures 5 and 6 indicate that conductivity decay occurs in both materials upon prolonged annealing. The degree of conductivity degradation, however, is much smaller in BIZRVOX, where the partial substitution of V by Zr takes place. Parallel X-ray studies confirm the phase separation of these compounds upon prolonged annealing [24], but the degree of phase separation in BIZRVOX is significantly reduced.

6. Conclusions

New families of potential electrolytes for IT-SOFC applications continue to be developed. While high conductivities can be readily achieved at intermediate temperatures, much work still needs to be carried out on enhancing the stability of these electrolytes. Careful chemical design, including studies of doped systems, may offer a way forward in the development of novel IT-SOFCs. Two zirconia-doped bismuthate systems, $Bi_3Nb_{1-x}Zr_xO_{7-x/2}$ of a δ-Bi_2O_3-type structure and $Bi_4V_{2-2x}Zr_{2x}O_{11-x}$ of a layered Aurivillius-type structure, are discussed in this respect. In the latter system, a signifi-

cant increase in thermal stability in the doped material in comparison to the parent compound was observed.

Acknowledgements

We gratefully acknowledge support under the EC framework 5 Centre of Excellence CEPHOMA (Contract No. ENK5-CT-2002-80666).

References

[1] *Handbook of Fuel Cells*, W. Vielstich, A. Lamm, H.A. Gastiger (Eds.), Fundamentals, Technology and Applications, Wiley, New York, 2003.
[2] STEELE B.C., HEINZEL A., Nature, 414 (2001), 345.
[3] MINH N.Q., J. Am. Ceram. Soc., 76 (1993), 563.
[4] PORTER D.L., HEUER A.H., J. Am. Ceram. Soc., 62 (1979), 298.
[5] DOES D.W., CLAAR T.D., EASLER T.E., FREE D.C., MRAZEK F.C., J. Electrochem. Soc., 134 (1987), 2141.
[6] KUO J.H., ANDERSON H.U., SPARLIN D.E., J. Solid State Chem., 83 (1989), 52.
[7] BATAWI E., PLAS A., STRAUB W., HONNEGGER K., DIETHELEM R., Solid Oxide Fuel Cells (SOFC6) Singhal S.C. and Dokija M. (Eds.) The Electrochemical Society Proceedings, Pennigton, NJ, PV99-19, 767 (1999).
[8] GODICKEMEIER M., SASAKI K., GAUKLER L.J., J. Electrochem. Soc., 144 (1997), 1635.
[9] FENG M., GOODENOUGH J.B., J. Solid State Inorg. Chem., 31 (1994), 663.
[10] See for example a) SAMMES N.M., TOMPSETT G.A., NAFE H., ALDINGER F., J. Eur. Ceram. Soc., 19 (1999), 1801, b) SHUK P., WIEMHOFER H.-D., GUTH U., GOPEL W., GREENBLATT M., Solid State Ionics, 89 (1996), 179, c) MAIRESSE G., [in:] *Fast Ion Transport in Solids*, B. Scrosati, A. Magistris, C.M. Mari, G. Marioto (Eds.), Kluver Academic Publ., Dordecht, 1993, p.271, d) BOVIN J.C., MAIRESSE G., Chem. Mater., 10 (1998), 2870.
[11] KUDO T., OBAYASHI Y., J. Electrochem. Soc., 123 (1976), 415.
[12] DOSHI R., RICHARDS V.L., CARTER J.D., WANG X., KRUMPELT M., J. Electrochem. Soc., 146 (1999), 1273.
[13] TAKAHASHI T., IWAHARA H., NAGAJ Y., J. Appl. Electrochem., 2 (1972), 97.
[14] HIBINO T., IWAHARA H., Chem. Lett., 69 (1993), 1131.
[15] FUNG K.Z, BAEK H.D., VIRKAR, A.V. Solid State Ionics, 52 (1992), 199.
[16] CASTRO A., AGUADO E., ROJO J.M., HERRERO P., GALY J., Mater. Res. Bull., 33 (1988), 31.
[17] KROK F., ABRAHAMS I., WROBEL W., CHAN S.C.M., KOZANECKA A., OSSOWSKI T., Solid State Ionics, 175 (2004), 335.
[18] KOZANECKA-SZMIGIEL A., ABRAHAMS I., KROK F., WROBEL W., to be published.
[19] ABRAHAM F., DEBREVILLE-GRESSE M.F., MAIRESSE G., NOVOGROCKI G., Solid State Ionics, 28–30 (1988), 529.
[20] ABRAHAMS I., KROK F., J. Mat. Chem., 12 (2002), 3351.
[21] KROK F., ABRAHAMS I., MALYS M., WROBEL W., KOZANECKA A., Mol. Phys. Rep., 35 (2002), 94.
[22] KROK F., ABRAHAMS I., WROBEL W., CHAN S.C.M., MALYS M., BOGUSZ W., DYGAS J.R., Solid State Ionics, 154 (2002), 511.
[23] WROBEL W., ABRAHAMS I., KROK F., KOZANECKA A., MALYS M., BOGUSZ W., DYGAS J.R., Solid State Ionics, 175 (2004), 425.
[24] WROBEL W., ABRAHAMS I., KROK F., KOZANECKA-SZMIGIEL A., to be published

Received 10 December 2004
Revised 20 January 2005

Materials Science-Poland, Vol. 24, No. 1, 2006

$Bi_8V_2O_{17}$ – a stable phase in the Bi_2O_3–V_2O_5 system

W. WROBEL[1*], F. KROK[1], I. ABRAHAMS[2],
A. KOZANECKA-SZMIGIEL[1], M. MALYS[1], S. C. M. CHAN[2], J. R. DYGAS[1]

[1]Faculty of Physics, Warsaw University of Technology, ul. Koszykowa 75, 00-662, Warsaw, Poland

[2]Centre for Materials Research, Department of Chemistry, Queen Mary,
University of London, Mile End Road, London E1 4NS, United Kingdom

$Bi_8V_2O_{17}$ is commonly observed as an intermediate phase in the synthesis of compounds in ternary systems of the type Bi_2O_3–V_2O_5–Me_xO_y. It is also seen as an end product at particular compositions in these systems. A rhombohedral substructure model for this phase is presented along with electrical parameters. Evidence from the Arrhenius plot suggests a phase transition at around 550 °C. The existence of a limited solid solution of $Bi_8V_2O_{17}$ with ZrO_2 is also discussed.

Key words: *bismuth vanadate; oxide ion conductor; electrical conductivity; crystal structure*

1. Introduction

The Bi_2O_3–V_2O_5 system has attracted much attention in recent years. A number of phases have been identified in this binary system, including $BiVO_4$ [1, 2], $Bi_4V_2O_{11}$ [3], $Bi_{3.5}V_{1.2}O_{8.25}$ [4], $Bi_{23}V_2O_{44.5}$ [5] and $Bi_8V_2O_{17}$ [6]. While much research has gone into the orthovanadate phase $BiVO_4$, particularly regarding its catalytic properties (see e.g. [7]) and $Bi_4V_2O_{11}$ which is the parent compound of the BIMEVOX family of solid electrolytes [8], little attention has been paid to the other phases in this binary system.

$Bi_8V_2O_{17}$ is commonly observed as an intermediate phase in the synthesis of compositions in ternary systems of the type Bi_2O_3–V_2O_5–Me_xO_y [9]. This compound also appears as a final product of reaction in these systems for particular compositions (eg., $Bi_2Zr_xV_{1-x}O_{5.5-(x/2)}$ and $Bi_2Mg_xV_{1-x}O_{5.5-(3x/2)}$, x = 0.50) [10–12]. Here we present a study of the structure and electrical conductivity of $Bi_8V_2O_{17}$.

*Corresponding author, e-mail: wrobel@if.pw.edu.pl

2. Experimental

Preparations. Polycrystalline $Bi_8V_2O_{17}$ and samples of general formulae $Bi_2Zr_xV_{1-x}O_{5.5-(x/2)}$ ($0.20 \le x \le 0.50$) and $Bi_2Mg_xV_{1-x}O_{5.5-(3x/2)}$, $x = 0.50$, were prepared by standard solid-state methods. Appropriate amounts of Bi_2O_3 (Aldrich, 99.9%), V_2O_5 (ABCR, 99.5%), ZrO_2 (Aldrich, 99.5%) and MgO (POCh, 99,5%) were ground together as a toluene paste using a planetary ball mill. The dried powder was heated in a platinum crucible at 650 °C for 12 h. After cooling, the ground powder was pelletised and subjected to isostatic pressing at the pressure of 400 MPa. Pellets were sintered at 840 °C for 10 h and subsequently slow cooled in air to room temperature over 12 h.

Single crystals of $Bi_8V_2O_{17}$ were prepared by slow cooling a melt of appropriate starting materials. Bi_2O_3 and V_2O_5 were ground together in ethanol using an agate mortar and pestle. The dried mixture was heated at 650 °C for 10 h followed by subsequent heating at 800 °C for 20 h. Melting was carried out at 900 °C and the sample was kept at this temperature for 40 h before slow cooling in air to room temperature over 24 h. A single crystal of dimensions $0.15 \times 0.15 \times 0.12$ mm^3 was extracted from the cooled melt for diffraction studies.

Electrical measurements. Electrical parameters were determined by ac impedance spectroscopy up to ca. 800 °C using a fully automated Solartron 1255/1286 system in the frequency range from 1 Hz to 5×10^5 Hz. Samples for impedance measurements were prepared as rectangular blocks (ca. $6 \times 3 \times 3$ mm^3) cut from slowly cooled sintered pellets using a diamond saw. Platinum electrodes were sputtered by cathodic discharge. Impedance spectra were recorded automatically over two cycles of heating and cooling at programmed temperatures after 15 min of temperature stabilisation. Impedance at every frequency was measured repeatedly until consistency was achieved or a maximum number of 25 repeats had been reached. In addition, impedance at selected frequencies was measured before and after each spectral collection in order to determine the extent of drift. Where the summed differences exceeded a preset tolerance of 2%, the process was repeated.

Crystallography. Single-crystal X-ray intensity data were collected on an Enraf-Nonius CAD-4 diffractometer using MoK_α radiation (λ = 0.71073 Å) with ω–2θ scans at 20(2) °C. Data for 176 reflections were collected with 38 independent reflections in rhombohedral symmetry with $I > 2\sigma(I)$. The data were corrected for the Lorentz and polarization factors and corrected for absorption by empirical methods (Ψ-scan) [13]. The structure was solved by direct methods using SHELXS-97 [14] and refined on F^2 by full matrix least squares using SHELXL-97 [14]. Anisotropic thermal parameters were refined for all atoms. WINGX [15] was used to prepare material for publication. Crystal and refinement parameters for $Bi_8V_2O_{17}$ are summarised in Table 1.

A high resolution X-ray powder diffraction pattern was collected for pure $Bi_8V_2O_{17}$ at room temperature using an INEL CPS-120 fixed position sensitive detector system on an Enraf-Nonius FR590 X-ray generator. The curved position sensitive

detector allows simultaneous data collection in 4096 bins over 0° to 120° in 2θ. The sample was mounted on a Si-711 cut crystal and data collected in the 2θ range 0–120°, using Ge 111 monochromated CuKα_1 radiation (λ = 1.54056 Å), in fixed flat-plate geometry with the incident beam striking the sample holder at the angle of between 2° to 5°. Data were collected for a total scan time of 80 min. High temperature X-ray powder diffraction data were collected on $Bi_8V_2O_{17}$ at 700 °C on a Philips X'Pert X-ray diffractometer using graphite monochromated CuK$_\alpha$ radiation (λ_1 = 1.54056 Å and λ_2 = 1.54439 Å) with an Anton-Paar HTK 1200 high-temperature camera. Data were collected in flat plate $\theta/2\theta$ geometry on a Pt sample holder. Calibration was carried out with an external Si standard. Measurements suitable for Rietveld analysis were performed in the 2θ range 10–110°, in steps of 0.02°, with a scan time of 10 s per step. Unit cell dimensions and structural parameters were refined by Rietveld whole profile fitting using the program GSAS [16]. The single crystal derived parameters for $Bi_8V_2O_{17}$ were used as a starting model.

Table 1. Crystal and refinement parameters for $Bi_8V_2O_{17}$ substructure

Empirical formula	$Bi_{0.80}V_{0.20}O_{1.70}$
Formula weight	204.57
Temperature	293(2) K
Wavelength	0.71073 Å
Crystal system	trigonal
Space group	$R\bar{3}m$
Unit cell dimensions	a = 3.815(4) Å, α = 90° b = 3.815(4) Å, β = 90° c = 9.990(8) Å, γ = 120°
Volume	125.9(2) Å^3
Z	3
Density (calculated)	8.093 mg/m^3
Absorption coefficient	84.663 mm^{-1}
F(000)	254
Crystal size	0.15 × 015 × 0.12 mm^3
Θ range for data collection	6.13–24.56°
Reflections collected	176
Independent reflections	38 (R(int) = 0.2537)
Final R indices (I > 2sigma(I)]	R1 = 0.0479, wR2 = 0.1071
R indices (all data)	R1 = 0.0479, wR2 = 0.1071
Extinction coefficient	0.002(8)
Largest diff. max. and min.	2.652 and –1.460 e.Å^{-3}

X-ray powder diffraction data were collected on $Bi_2Zr_xV_{1-x}O_{5.5-(x/2)}$ and $Bi_2Mg_xV_{1-x}O_{5.5-(3x/2)}$ samples at room temperature on an automated Philips PW1050/30 X-ray diffractometer, using Ni filtered CuKα radiation (λ = 1.5418 Å). Data were collected in flat plate $\theta/2\theta$ geometry in the 2θ range 5–120°, in steps of 0.02, with scan times of 10s per step. Calibration was carried out with an external Si standard. Unit cell pa-

rameters were refined using a multiple phase refinement with the program GSAS [16]. The structures of γ-BICOVOX [17], ZrO_2 [18] and the single crystal derived parameters for $Bi_8V_2O_{17}$ were used as initial models in structure refinement.

Thermal Analysis. Differential thermal analysis was carried out using a Perkin Elmer DTA 7 apparatus at the heating/cooling rate of 10 °C·min^{-1} over an approximate temperature range 25–800 °C.

3. Results and discussion

The refined atomic parameters for the rhombohedral model for $Bi_8V_2O_{17}$ derived from the single crystal analysis are given in Table 2, along with significant contact distances. In this model, Bi and V share the 3*a* position (0, 0, 0) with oxide ions partially occupying the 6*c* position (–1/3, 1/3, 0.92). The fitted X-ray diffraction pattern

Table 2. Refined atom positions parameters and significant contact distances in the $Bi_8V_2O_{17}$ substructure. Estimated standard deviations are given in parentheses

Atom positions coordinates						
Atom	Site	x	y	z	Occ.	U_{eqv} (Å^2)
Bi/V	3a	0.0(–)	0.0(–)	0.0(–)	0.8/0.2(–)	0.0040(2)
O	6c	–0.3333(–)	0.3333(–)	0.092(13)	0.85(–)	0.031(19)

Anisotropic thermal parameters (Å^2)						
Atom	U_{11}	U_{22}	U_{33}	U_{23}	U_{13}	U_{12}
Bi/V	0.0043(3)	0.0043(3)	0.0034(2)	0.0(–)	0.0(–)	0.0022(1)
O	0.04(3)	0.04(3)	0.010(6)	0.0(–)	0.0(–)	0.021(15)

Contact distances (Å)	
Bi/V–O	2.39(5) Å × 6
Bi/V–O[a]	2.41(13) Å × 2

[a]Symmetry equivalent: $-x - 1/3, -y + 1/3, -z + 1/3$

at room temperature for pure $Bi_8V_2O_{17}$ is presented in Figure 1. The structure has been modelled on the single crystal parameters and clearly shows a number of reflections not accounted for by the rhombohedral model. These peaks cannot be attributed to any other phases in this system and are due to superlattice ordering. It can therefore be concluded that the refined rhombohedral structure represents the disordered substructure and that the true cell is significantly larger. The substructure model is similar to that of $BiLa_2O_5$ [19] and is fluorite related, however, full structural analysis requires optimisation of the oxygen positions within the superlattice, which is currently underway using high resolution neutron diffraction data. Nevertheless, the disordered substructure model does allow for reasonable analysis of X-ray powder diffraction data where scattering is dominated by the heavy cations.

Polycrystalline $Bi_8V_2O_{17}$ exhibits a relatively low conductivity, with values of 9.0×10^{-4} S·cm^{-1} at 600 ºC (σ_{600}) and 8.7×10^{-7} S·cm^{-1} at 300 ºC (σ_{300}). The Arrehnius plot of conductivity for $Bi_8V_2O_{17}$ is presented in Fig. 2. The data can be fitted to two linear regions above and below ca. 550 ºC, with activation energies of ΔE_{ht} = 1.09 eV and ΔE_{lt} = 1.02 eV, respectively, indicative of a phase transition. X-ray data collected at high temperature (700 ºC) reveal no obvious changes in superstructure from the pattern at ambient temperature. This may suggest that, if present, the phase transition is subtle.

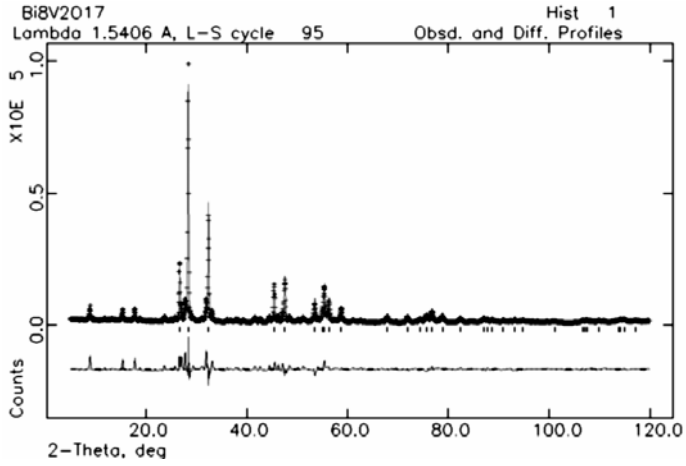

Fig. 1. Fitted X-ray diffraction pattern of polycrystalline $Bi_8V_2O_{17}$ at room temperature using rhombohedral substructure model. Observed (points) fitted (line) and difference (lower) profiles are shown. Calculated reflection positions are indicated by markers

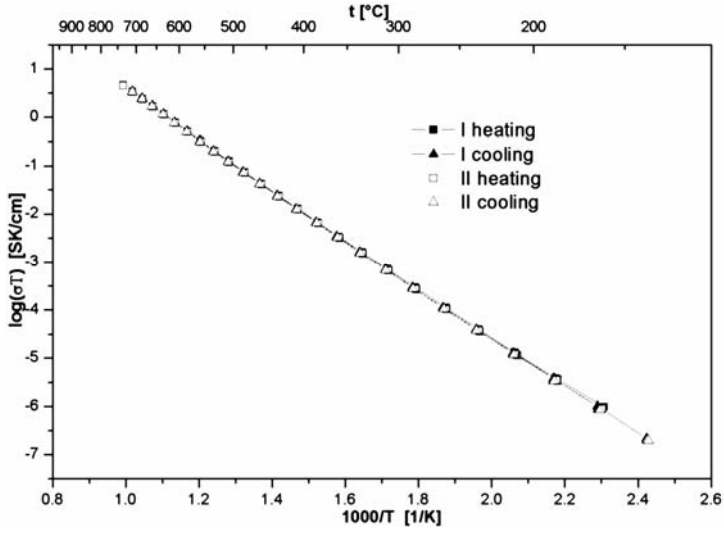

Fig. 2. Arrhenius plots of total electrical conductivity for polycrystalline $Bi_8V_2O_{17}$ over two cycles of heating and cooling

$Bi_8V_2O_{17}$ is observed as a product in the pseudo-binary system Bi_2ZrO_5–$Bi_2VO_{5.5}$ ($Bi_2Zr_xV_{1-x}O_{5.5-x/2}$) for compositions above the BIMEVOX solid solution limit [12] at around x = 0.20. At higher values of x, tetragonal γ-BIZRVOX appears along with peaks corresponding to $Bi_8V_2O_{17}$ and ZrO_2. These three phases persist up to x = 0.40, with $Bi_8V_2O_{17}$ becoming more dominant, until at x = 0.50 γ-BIZRVOX is undetectable. The variation in unit cell parameters for the $Bi_8V_2O_{17}$ type phase with composition in these samples is shown in Figure 3. The variation, particularly in the c-parameter, suggests limited solid solution formation. The electrical properties also show compositionally dependent variation. As x increases, ΔE_{ht} of the sample increases and conductivity decreases up to x = 0.50. At this composition, an Arrhenius plot of conductivity similar to that of pure $Bi_8V_2O_{17}$ is observed (Fig. 4), but with lower total conductivity (σ_{600} = 2.8 ×10^{-4} S·cm^{-1} and σ_{300} = 3.3 × 10^{-7} S·cm^{-1}). The value for the low-temperature activation energy (ΔE_{lt} = 1.01 eV) is close to that of pure $Bi_8V_2O_{17}$, however, the high temperature activation energy (ΔE_{ht} = 1.23 eV) is significantly larger than that of the pure compound.

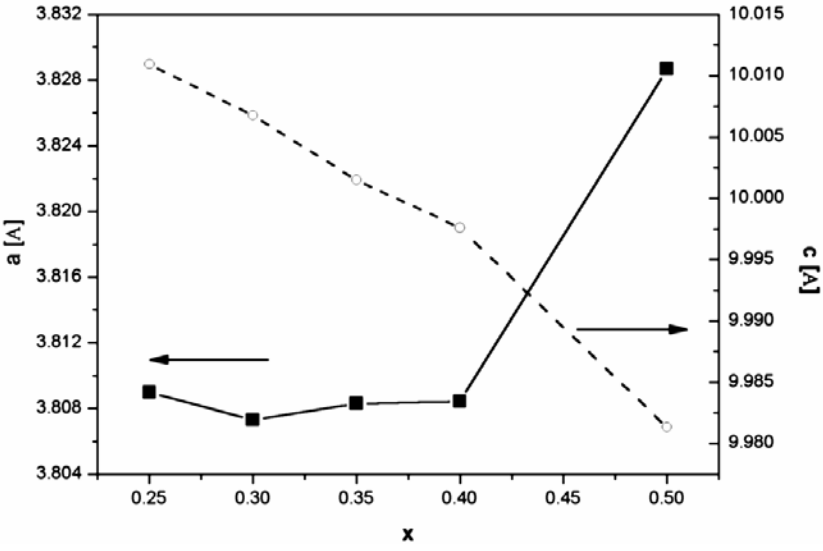

Fig. 3. Variation in $Bi_8V_2O_{17}$ unit cell parameters with composition for the polyphase system $Bi_2Zr_xV_{1-x}O_{5.5-x/2}$

A similar behaviour is also observed in the $Bi_2Mg_xV_{1-x}O_{5.5-(3x/2)}$ system at compositions above the BIMEVOX phase stabilization limit (x = 0.33 in this system) [11]. For compositions above x = 0.33, a polyphase system is observed with BIMGVOX and $Bi_8V_2O_{17}$ phases present, until at x = 0.50 the BIMEVOX phase is undetectable. MgO is not observed due to a relatively low scattering factor of this component in X-rays. In this system, the Arrhenius plot for the x = 0.50 composition (Fig. 4) is identical with that of $Bi_8V_2O_{17}$. In addition, refined unit cell parameters for the $Bi_8V_2O_{17}$ type phase at this composition (a = 3.818, c = 9.933 Å) are close to those of the pure compound.

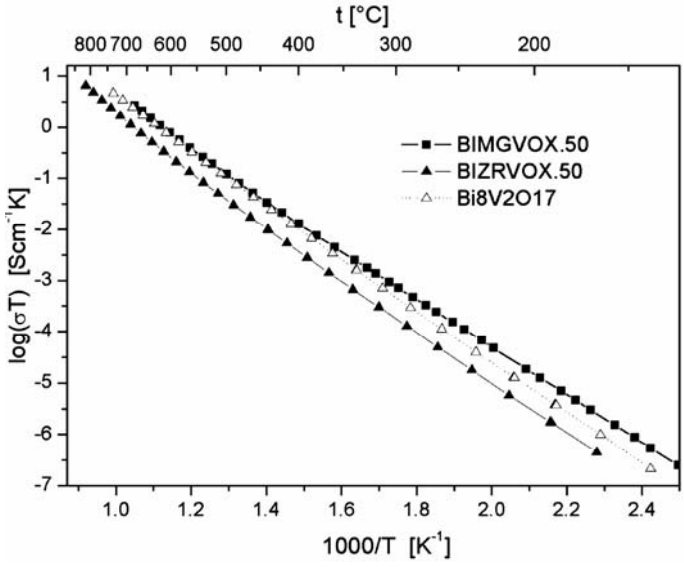

Fig. 4. Arrhenius plots of total electrical conductivity for polycrystalline $Bi_2Zr_{0.5}V_{0.5}O_{5.25}$ and $Bi_2Mg_{0.5}V_{0.5}O_{4.75}$. The plot for $Bi_8V_2O_{17}$ is included for comparison. The data correspond to the first cooling runs

4. Conclusions

$Bi_8V_2O_{17}$ appears to be a discrete stable phase in the Bi_2O_3–V_2O_5 binary system. It has a fluorite-related substructure closely resembling that of rhombohedral $BiLa_2O_5$. Electrical data appear to be consistent with a phase transition at around 550 °C.

$Bi_8V_2O_{17}$ is observed above the BIMEVOX solid solution limits in the systems $Bi_2Zr_xV_{1-x}O_{5.5-x/2}$ and $Bi_2Mg_xV_{1-x}O_{5.5-(3x/2)}$ and is the dominant phase at compositions containing a 4:1 ratio of Bi_2O_3:V_2O_5. Variation in total conductivity and unit cell parameters suggest that a limited solid solution may be formed with ZrO_2.

Acknowledgements

We gratefully acknowledge support under the EC framework 5 Centre of Excellence CEPHOMA (Contract No. ENK5-CT-2002-80666). The authors wish to thank Dr. R.M. Wilson at Queen Mary for high resolution X-ray powder diffraction data collection and M. Motevalli at Queen Mary for his assistance in single crystal data collection.

References

[1] QURASHI M.M., BARNES W.H, Amer. Mineralogist, 38 (1953), 489.
[2] COX D.E., MOODENBAUGH A.R., SLEIGHT A.W., CHEN H.Y., NBS Special Publication, 567 (1980), 189.
[3] ABRAHAM F., DEBREUILLE-GRESSE M.F., MAIRESSE G., NOWOGROCKI G., Solid State Ionics, 28–30 (1988), 529.

[4] WATANABE A., J. Solid State Chem., 161 (2001), 410.
[5] WATANABE A., KITARNI Y., Solid State Ionics, 113–115 (1998), 601.
[6] ICDD Powder Diffraction File, PDF-2, ICDD, Pennsylvania, USA, 1998, Card 44–171.
[7] LEE M.D., CHEN W.S., CHIANG H.P., Appl. Catal. A., 101 (1993), 269.
[8] ABRAHAM F., BOIVIN J.C., MAIRESSE G., NOWOGROCKI G., Solid State Ionics, 40/41 (1990), 934.
[9] VERNOCHET C., VANNIER R-N., HUVE M., PIROVANO C., NOWORGROCKI G., MAIRESSE G., VAN TENDELOO G., J. Mater. Chem., 10 (2000), 2811.
[10] LAZURE S., VANNIER R-N., NOWOGROCKI G., MARIESSE G., MULLER CH., ANNE M., STROBEL P., J. Mater. Chem., 5 (1995), 1395.
[11] ABRAHAMS I., KROK F., MALYS M., WROBEL W., CHAN S.C.M, BOGUSZ W., DYGAS J.R., Solid State Ionics, 157 (2003), 155.
[12] WROBEL W., KROK F., ABRAHAMS I., KOZANECKA A., MALYS M., BOGUSZ W., DYGAS J.R., Solid State Ionics, 175 (2004), 425
[13] NORTH A.C.T., PHILLIPS D.C., MATTHEWS F.S., Acta Crystallogr., Sect. A, 24 (1968), 351.
[14] Programs for Crystal Structure Analysis (Release (97-2), SHELDRICK G.M., Insitüt für Anorganische Chemie der Universität, Tammanstrasse 4, D-3400 Göttingen, Germany, 1998; SHELDRICK G.M., Acta Crystallogr., Sect. A, 46 (1990), 467; SHELDRICK G.M., SHELXL-93, University of Göttingen, 1993.
[15] FARRUGIA L.J., J. Appl. Cryst., 32 (1999), 837.
[16] LARSON A.C., VON DREEL R.B., Los Alamos National Laboratory, Report N^{o}. LA-UR-86-748, (1987).
[17] ABRAHAMS I., KROK F., NELSTROP J.A.G., Solid State Ionics, 90 (1996), 57.
[18] SMITH D.K., NEWKIRK H.W., Acta Crystallogr., 18 (1965), 983.
[19] WOLCYRZ M., KEPINSKI L., HORYN R., J. Solid State Chem., 116 (1995), 72.

Received 10 December 2004
Revised 12 September 2005

Materials Science-Poland, Vol. 24, No. 1, 2006

Structure and electrical properties of oxide-ion conductors in the Bi_3NbO_7–Bi_3YO_6 system

A. KOZANECKA-SZMIGIEL[1], F. KROK[1*], I. ABRAHAMS[2**]
W. WROBEL[1], S. C. M. CHAN[2], J. R. DYGAS[1]

[1]Faculty of Physics, Warsaw University of Technology, ul. Koszykowa 75, 00-662, Warsaw, Poland.

[2]Centre for Materials Research, Department of Chemistry, Queen Mary, University of London, Mile End Road, London E1 4NS, United Kingdom

A study of the structure and electrical conductivity of $Bi_3Nb_{1-x}Y_xO_{7-x}$ is presented. X-ray diffraction confirms full solid solution formation ($0.0 \le x \le 1.0$) in this system, with the adoption of a fluorite-type structure. Superlattice ordering of the anion sublattice is evident in neutron diffraction data, the nature of which varies with composition. At low values of x, long-range ordering is present, whereas above $x = 0.4$ only local ordering is observed. Arrhenius plots of the total electrical conductivity of all samples containing yttrium show two linear regions with different activation energies, with evidence for a phase transition between 450 and 680 °C.

Key words: *bismuth oxide; bismuth-niobium-yttrium oxide; oxide-ion conductor; solid electrolyte*

1. Introduction

Solid electrolytes based on δ-Bi_2O_3 show extremely high oxide-ion conductivity and are of interest for electrochemical devices. The high conductivity of δ-Bi_2O_3 originates in its defect cubic fluorite-type crystal structure. The structure is very open and has a high intrinsic vacancy concentration (25%) on the anion sublattice, which along with a high polarizability of Bi $6s^2$ lone pairs results in remarkable oxide ion conductivity. The δ-Bi_2O_3 phase is only stable over a narrow temperature range, namely 730–825 °C [1], which is one of the reasons excluding it from practical application in devices. It was shown that this fluorite-type phase can be stabilized down to room temperature through the formation of a solid solution with other metal oxides

[*]Corresponding author, e-mail: fkrok@mech.pw.edu.pl
[**] Corresponding author, e-mail: I.Abrahams@gmul.ac.uk

[2–7]. This usually leads to a decrease in conductivity at high temperatures, but also to a significant increase in low temperature conductivity (below ca. 600 ^{o}C). For many of the stabilized compounds, the dependence of conductivity on temperature shows an Arrhenius-type behaviour over two distinct temperature regions. These two regions have different activation energies and have been connected to the existence of an ordered phase at low temperatures and a disordered phase at high temperatures.

Several fluorite-related phases have been isolated in the Bi_2O_3–Nb_2O_5 binary system [8–10]. At a 3:1 mole ratio, room temperature stabilization of a fluorite-type structure with a formula of Bi_3NbO_7 is observed [11]. The electrical conductivity of this compound is not particularly high, mainly because of a significantly lower vacancy concentration compared to its parent δ-Bi_2O_3. Using Bi_3NbO_7 as a base composition, however, it is possible to increase the vacancy concentration and therefore conductivity through subvalent substitution of Nb by suitable cations [12]. Substitution by Y^{3+} represents a system, in which a full solid solution might be possible, since Bi_3YO_6, which corresponds to the fully substituted compound, is known to adopt a cubic fluorite-type structure [13]. Here we present an investigation of the structural and electrical effects of yttrium substitution into Bi_3NbO_7, using X-ray and neutron diffraction and AC impedance spectroscopy.

2. Experimental

Preparations. Samples of $Bi_3Nb_{1-x}Y_xO_{7-x}$ ($0.0 \le x \le 1.0$) were prepared using appropriate amounts of Bi_2O_3 (Aldrich, 99.9%), Y_2O_3 (Aldrich, 99.99%), and Nb_2O_5 (Aldrich, 99.9%). Starting mixtures were ground in ethanol using a planetary ball mill. The dried mixtures were heated initially at 740 °C for 24 h, then cooled, reground and pelletised. Pellets were pressed isostatically at the pressure of 400 MPa, then sintered at 800 °C for 10 h. Sintered samples were slowly cooled in air for over 12 h.

Electrical measurements. Electrical parameters were determined by ac impedance spectroscopy up to ca. 800 °C using a fully automated Solartron 1255/1286 system in the frequency range fro 1 Hz to 5×10^5 Hz. Samples for impedance measurements were prepared as rectangular blocks (ca. $6 \times 3 \times 3$ mm^3), cut from slowly cooled sintered pellets using a diamond saw. Platinum electrodes were sputtered by cathodic discharge. Impedance spectra were recorded over two cycles of heating and cooling and collected at programmed temperatures after 15 min of temperature stabilisation. The impedance at each frequency was measured repeatedly until consistency (2% tolerance in drift) was achieved or the maximum number of 25 repeats had been reached.

Crystallography. X-ray powder diffraction data were collected at room temperature on an automated Philips X'Pert X-ray diffractometer using graphite monochromated Cu-K_α radiation (λ_1 = 1.54056 Å and λ_2 = 1.54439 Å). Data were collected in

the flat plate $\theta/2\theta$ geometry in the range of 2θ 10–100°, in steps of 0.02°, with a scan time of 5 s per step.

Powder neutron diffraction data were collected on a Polaris diffractometer at the ISIS facility, Rutherford Appleton Laboratory. Data were collected on back-scattering and low-angle detectors over the respective time of flight ranges of 1.0–20 and 0.5–20 ms. The samples were contained in cylindrical 12 mm vanadium cans located in front of the back-scattering detectors.

3. Results and discussion

X-ray powder diffraction patterns for all studied compositions in the $Bi_3Nb_{1-x}Y_xO_{7-x}$ ($0.0 \le x \le 1.0$) system are presented in Figure 1. It can be seen that basic fluorite structure is maintained throughout the composition range. There is no evidence in the X-ray diffraction patterns for satellite reflections associated with superlattice ordering. Neutron diffraction patterns for the same samples, however, do exhibit additional

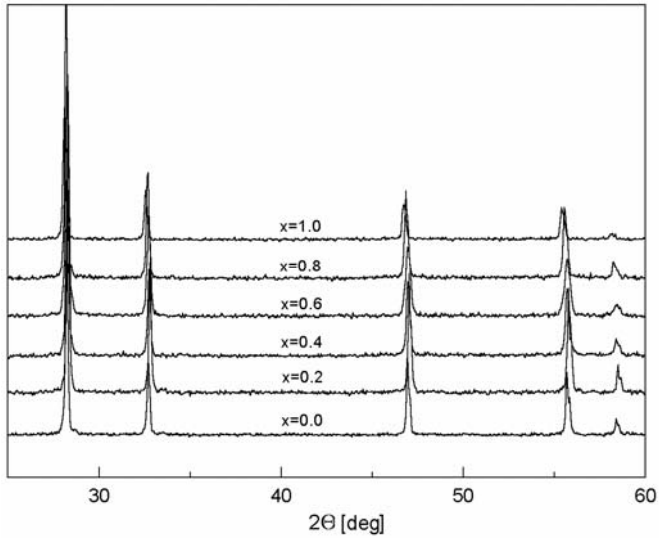

Fig. 1. Room-temperature X-ray diffraction patterns for $Bi_3Nb_{1-x}Y_xO_{7-x}$

peaks (Fig. 2). The presence of these satellite peaks in the neutron diffraction patterns and their absence in the X-ray diffraction patterns suggest that they are due to ordering in the oxide sublattice, which would show weak scattering in X-rays compared to that of heavy cations. The nature of ordering of superlattice changes with composition. At x = 0.0, a large number of weak peaks which could not be indexed on the basic cubic fluorite structure are observed. Ling and Johnson have recently modelled the structure of Bi_3NbO_7 on a tetragonal super cell of dimensions a = 11.52156 Å and

c = 38.5603 Å. [11]. On the substitution of a small amount of Nb by Y this pattern simplifies, but all peaks observed at x = 0.2 are also present in the pattern of the parent compound. At x = 0.4, however, a simpler superlattice structure is detected, with peaks that do not coincide with those observed at lower compositions. At compositions x = 0.6 and x = 0.8 no superlattice peaks are visible, instead a broad hump in the background profile is observed in the range 12–16 ms at the x = 0.6 composition and also to a lesser extent at x = 0.8. The appearance of a broad background feature in the place of superlattice reflections is indicative of a change from long-range vacancy ordering at low substitution levels to local vacancy ordering at higher substitution levels. This local ordering may be interpreted as a random distribution of locally ordered microdomains.

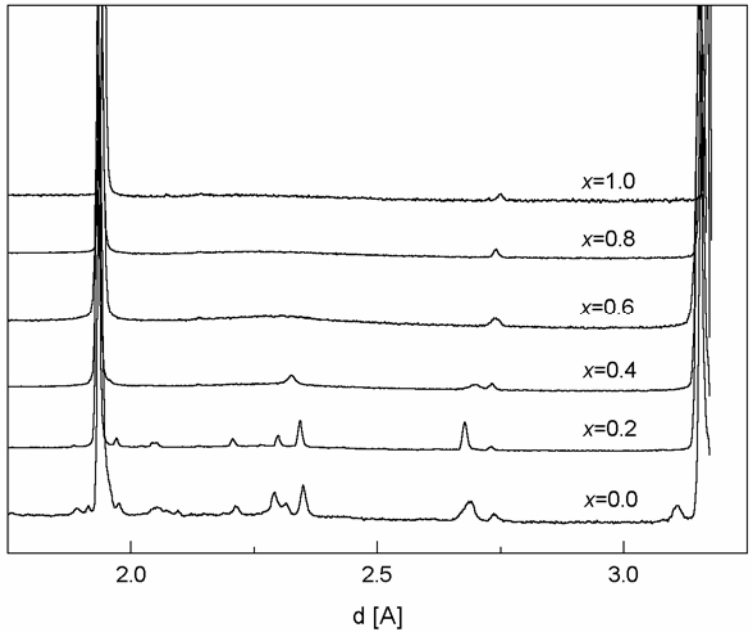

Fig. 2. Room-temperature neutron diffraction patterns for $Bi_3Nb_{1-x}Y_xO_{7-x}$

All samples showed fully reversible conductivity behaviour in heating and cooling runs. The Arrhenius plots of total conductivity during cooling are presented in Figure 3. For x = 0.0, a linear Arrhenius plot is evident over the entire measured temperature range. For all the studied compositions above x = 0.0, two linear regions, one at low and the other at high temperatures, can be distinguished. The appearance of a second linear region at high temperatures probably corresponds to a change in the conduction mechanism, which may be associated with a corresponding phase transition.

Electrical conductivity for compositions with $x \geq 0.4$ shows non-Arrhenius behaviour, with a curvature over a wide range of intermediate temperatures, from 450 to

680 °C. The gradual change in activation energy over a wide temperature range, rather than a sharp transition, is observed in many other systems and may be associated with a kinetically slow change in the favoured conduction mechanism, which may be related to small differences in oxide ion distributions at different temperatures.

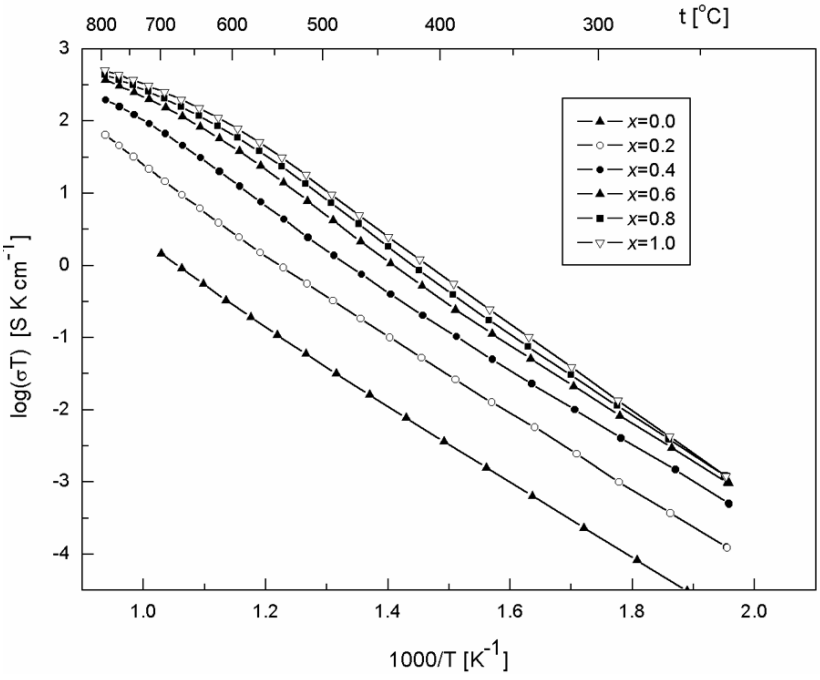

Fig. 3. Arrhenius plots of the total conductivity for various $Bi_3Nb_{1-x}Y_xO_{7-x}$ compositions during first cooling run

The compositional variation of isothermal conductivity at 300 °C (σ_{300}) and the low-temperature conductivity activation energy (ΔE_{lt}) are presented in Figures 4 and 5, respectively. Electrical conductivity exhibits a general increase with increasing yttrium content, which reflects the gradual increase in oxide ion vacancy concentration. Interestingly, the activation energy also shows a general increase with increasing x, from ca. 1.0 eV at x = 0.0 to ca. 1.2 eV at x = 1.0. These phenomena may be explained by considering changes in the defect structure with changing composition. It is clear from the neutron data that there is a change from long-range to short-range ordering in the anion sublattice. Even in the short-range ordered compositions, however, there will still be a significant energy term associated with defect trapping. One must therefore take into account other changes in structure. Indeed, Boyapati et al. [14, 15] have observed a similar behaviour in rare earth-doped bismuth oxide, where both activation energy and conductivity were observed to decrease on ageing, which was attributed to changes in the relative occupancies of normal lattice and interstitial oxide sites. Similar reasoning

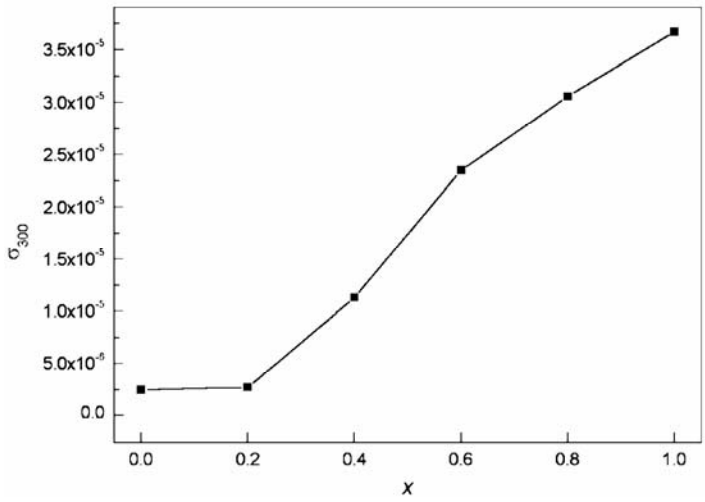

Fig. 4. Compositional variation in total conductivity σ_{300} at 300 ºC for $Bi_3Nb_{1-x}Y_xO_{7-x}$

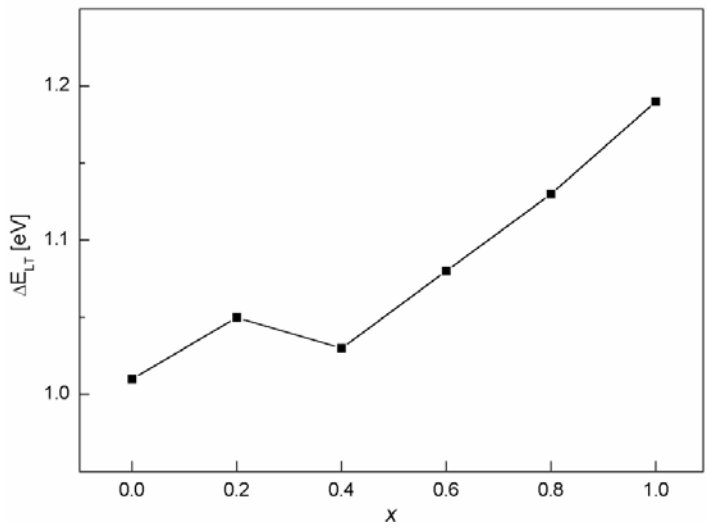

Fig. 5. Compositional variation in low-temperature activation energy ΔE_{lt} for $Bi_3Nb_{1-x}Y_xO_{7-x}$

could be used to explain the observations in the present work, and a detailed analysis of the neutron diffraction data is currently underway.

4. Conclusions

Niobium can be fully substituted by yttrium in Bi_3NbO_7. The obtained solid solution, $Bi_3Nb_{1-x}Y_xO_7$, maintains the basic fluorite-type δ-Bi_2O_3 structure. Long-range superlattice ordering of the anion sublattice was detected in neutron diffraction data at

low levels of substitution, and is replaced by short-range ordering at higher levels of substitution. While changes in the total conductivity reflect an increase in vacancy concentration with increasing yttrium content, the corresponding changes in activation energy are consistent with changes in the distribution of anions within the anion sublattice.

References

[1] TAKAHASHI T., IWAHARA H., NAGAJ Y., J. Appl. Electrochem., 2 (1972), 97.
[2] MAIRESSE G., [in:] *Fast Ion Transport in Solids*, B. Scrosati, A. Magistris, C.M. Mari, G. Mariotto (Eds.), Kluwer, Dordrecht, 1993, p. 271.
[3] BOVIN J.C., MAIRESSE G., Chem. Mater., 10 (1998), 2870.
[4] SHUK P., WIEMHÖFER H.D., GUTH U., GÖPEL W., GREENBLATT M., Solid State Ionics, 89 (1996), 179.
[5] SAMMES N.M., TOMPSETT G.A., NÄFE H., ALDINGER F., J. Eur. Ceram. Soc., 19 (1999), 1801.
[6] AZAD A.M., LAROSE S., AKBAR S.A., J. Mater. Sci., 29 (1994), 4135.
[7] GOODENOUGH J.B., MANTHIRAM A., PARANTHAMAN M., ZHEN Y.S., Mater. Sci. Eng., B12 (1992), 357.
[8] ZHOU W., JEFFERSON D.A., THOMAS J.M., Proc. R. Soc. Lond., A 406 (1986), 173.
[9] LING C.D.,WITHERS R.L., SCHMID S., THOMPSON J.G., J. Solid State Chem., 137 (1988), 42.
[10] CASTRO A., AGUADO E., ROJO J.M., HERRERO P., ENJALBERT R., GALY J., Mater. Res. Bull., 33 (1988), 31.
[11] LING C.D., JOHNSON M., J. Solid State Chem., 177 (2004), 1838.
[12] KROK F., ABRAHAMS I., WROBEL W., CHAN S.C.M., KOZANECKA A., OSSOWSKI T., Solid State Ionics, in press.
[13] BATTLE P.D., CATLOW C.R.A., DRENNAN J., MURRAY A.D., J. Phys C, 16 (1983), 561.
[14] BOYAPATI S., WACHMAN E.D., JIANG N., Solid State Ionics, 140 (2001), 149.
[15] BOYAPATI S., WACHMAN E.D., CHAKOUMAKOS B.C., Solid State Ionics, 138 (2001), 293.

Received 10 December 2004
Revised 10 January 2005

Materials Science-Poland, Vol. 24, No. 1, 2006

Some structural aspects of ionic conductivity in zirconia stabilised by yttria and calcia

M. M. BUĆKO*

AGH University of Science and Technology,
Faculty of Materials Science and Ceramics, al. Mickiewicza 30, 30-519 Cracow, Poland

Nanopowders with nominal constant oxygen vacancy concentrations of 8, 10, and 12 mol % were prepared in the ternary ZrO_2–CaO–Y_2O_3 system. The constant oxygen vacancy concentrations were obtained by incorporating calcia and yttria into zirconia solid solutions at different ratios. The Rietveld refinement method was used to characterise the structural changes in the zirconia solid solution. X-ray diffraction analysis was also used to characterise the phase composition of the samples and lattice parameters of the cubic phase. The four-probe method was applied for determining electrical properties of the samples. The conduction properties of the samples were characterised with respect to their structural features.

Key words: *zirconia; ionic conductivity*

1. Introduction

Fully stabilized cubic zirconia has been actively investigated as an oxide ion conductor in solid oxide fuel cells (SOFC), oxygen sensors, or electrochemical oxygen pumps [1, 2]. Consequently, several approaches have been taken to improve the electrical properties of zirconia materials. Structural modification of cubic zirconia is one of promising ways to ameliorate the ionic conductivity of zirconia-based electrolytes. The ionic conductivity of zirconia solid solutions (s.s.) is strictly related to the ionic radius and valency of cations incorporated into the zirconia structure [3, 4]. It is well known that for fluorite-structure oxides the conductivity is optimised by matching the size of the dopant and structural ions [5]. A special form of ion site instability occurs, however, when a compound is on the verge of a transition between two phases, one of which is a slight distortion of the other. In such a case, an unstable structure should have its maximum ionic conductivity at the minimum stabilizing dopant concentration

*Corresponding author, e-mail: bucko@uci.agh.edu.pl

[6]. Structural stress and the formation of complex defects (e.g., a host or dopant cation with an oxygen vacancy) should also be taken into consideration when explaining the connection between structure and ionic conductivity.

It is worth noting that the phase transition, and therefore the ionic conductivity, of zirconia could be controlled by the presence of two stabilizing cations in its structure. A few papers have concerned yttria-stabilised zirconia materials, additionally containing rare earth elements [7, 8]. In these materials, depending on the chemical and phase composition, an improvement (mostly) or in some cases a decrease in ionic conductivity was observed. Strickler et al. [9] found that a relatively big addition of calcia to cubic zirconia stabilised with yttria decreased its ionic conductivity. Several works on the electrical properties of $CaO–Y_2O_3–ZrO_2$ materials were reported by Gong et al. [10–12]. Generally, single-phase samples were characterised by better electrical properties as compared to "pure" yttria-stabilised material, and the ionic conductivity showed a local maximum for the equimolar doping composition.

The aim of the present work was to prepare solid-state electrolytes with constant vacancy concentrations in the ternary $CaO–Y_2O_3–ZrO_2$ system and to investigate their structural and electrical properties.

2. Experimental

Three series of zirconia powders, containing nominally 8, 10, or 12 mol % of oxygen vacancies were prepared by introducing yttria and calcia to zirconia in appropriate proportions. The samples throughout the work are marked as 8C*n*Y*m* (8% series), 10C*n*Y*m* (10% series), and 12C*n*Y*m* (12% series), where *n* and *m* indicate the fractions of the oxygen vacancies introduced to the zirconia structure by CaO and Y_2O_3, respectively. The values of *n* and *m* ranged from 0 to 100%, with a step of 10%.

Zirconyl, yttrium, and calcium chloride aqueous solutions were used as starting materials to prepare the zirconia solid solution nanopowders. Each solution was dropwise introduced into a vigorously stirred, concentrated NaOH solution, and then the slurry was hydrothermally treated for 4 h at 240 °C. The powders were washed with water solutions of ammonia and then additionally washed with propanol. After drying at room temperature, the granulated powders were isostatically cold-pressed under the pressure of 200 MPa. The green bodies of the 8, 10, and 12 series were pressurelessly sintered for 2 h at 1300, 1400, and 1500 °C, respectively.

The Rietveld refinement method, based on precise X-ray diffraction measurements, was used to characterise the structural changes in the zirconia cubic phase. The phase composition of the sintered bodies and lattice parameters of the respective phases were also determined.

The four-probe method was applied to recognise the electrical properties of the samples. Measurements were performed at temperatures from 300 to 1000 °C with an external current source. Partially reversible platinum electrodes deposited from paste were applied.

3. Results and discussion

The phase compositions of the sintered bodies are shown in Figure 1. In the samples containing 8 mol % of oxygen vacancies, the cubic phase was observed only in samples stabilised mainly by yttria (up to 8C50Y50). Increasing the calcia content in the stabilising mixture caused tetragonal phase formation. The samples of 10 series with a calcia-to-yttria ratio smaller than 70:30 were fully cubic, and the others were composed of both cubic and monoclinic phases. X-ray diffraction analysis showed that the sintered bodies of the 12 series were composed of cubic zirconia alone.

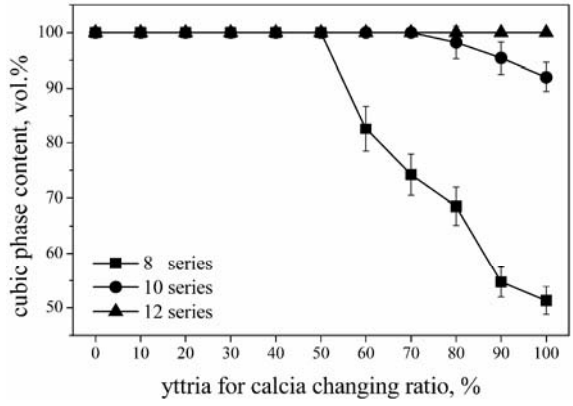

Fig. 1. The compositional dependence of cubic zirconia phase content

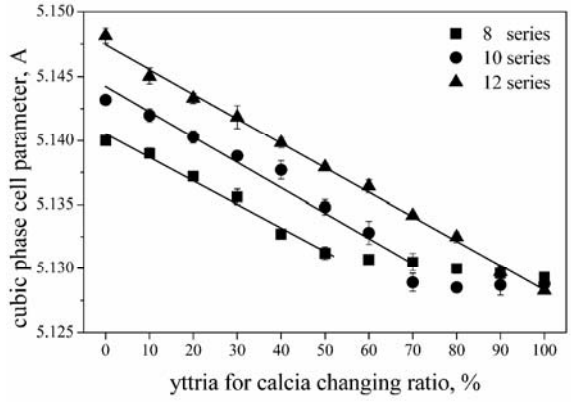

Fig. 2. The compositional dependence of cubic zirconia cell parameters

Figure 2 presents the lattice parameters of the cubic phase as a function of the chemical composition for each experimental series. Variations of the cubic phase lattice parameters in the single-phase regions are linear and can be related to the molar ratios of the stabilizing cations. In the bi-phase regions, the cubic phase lattice parameters change to a smaller degree (series 8) or are almost constant (series 10).

This is probably connected with differences in the chemical compositions of both zirconia phases, the total concentration of the stabilisers as well as the calcia-to-yttria molar ratio in both phases being significant.

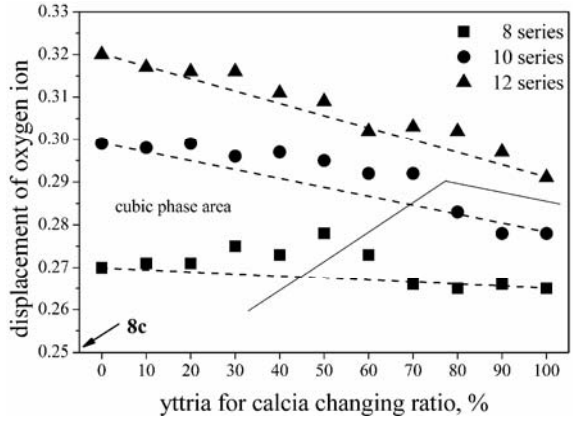

Fig. 3. Displacement of oxygen ions from site 8(c) to the site 48(g)

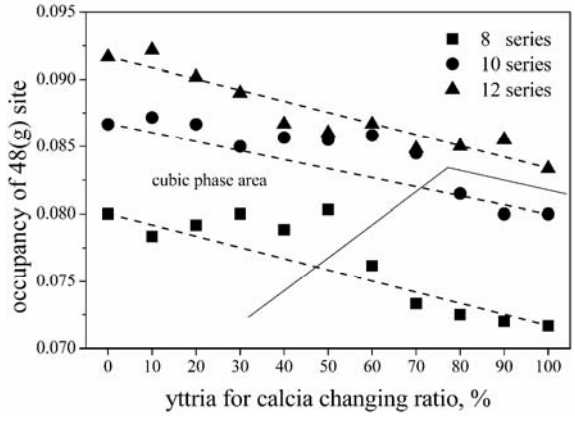

Fig. 4. The occupancy of the 48(g) site by oxygen ions

An initial model for Rietveld refinement was based on the real cubic zirconia structure determined by EXAFS as well as X-ray diffraction methods. Ishizawa et al. [13] stated that in yttria-stabilized zirconia Y ions occupy the 4(a) sites, whereas Zr ions occupy the 32(f) sites. Almost half of the O ions occupy 8(c) sites and the rest are shifted along <001> and occupy 48(g) sites [13]. A similar distortion of the elementary cell was found in cubic zirconia stabilized with calcia [14]. Figure 3 presents oxygen ion displacements, as a fraction of the cell parameter, from position 8(c) to position 48(g). The extreme points on the chart, corresponding to samples containing only one stabilizer, were connected by the dashed line, representing graphically a “mixture rule”. It is shown that oxygen ion displacement for some samples of the

8 and 10 series differ from the mixture rule and that these differences are larger in the case of the 8 series. Changes in the occupancy factor of oxygen ions at 48(g) sites exhibit a similar character (Fig. 4). In samples of the 8 and 10 series, distinct differences between the mixture rule and determined values are visible. Contrary to the changes in the anion sublattice, the changes in zirconium ion displacement from the 4(a) position to the 32(f) position are almost linearly related to the chemical compositions of the samples. A comparison of the results from Figures 2–4 implies that in the samples brought closer to the stabilization threshold, the oxygen sublattice becomes more distorted and the amount of moveable oxygen ions increases. This effect decreases with the total content of stabilizing oxides. The mentioned facts are in good agreement with the mechanism of the cubic-to-tetragonal phase transition, in which oxygen ion movements are much more extensive than the movements of the cations [15].

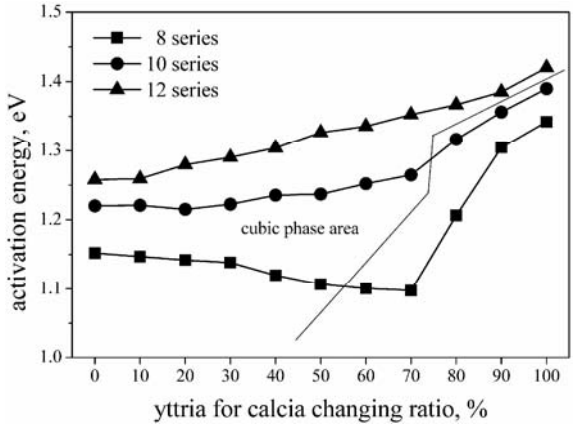

Fig. 5. The compositional dependence of the activation energy of ionic conductivity

Four-probe measurements revealed that the temperature dependences of ionic conductivities drawn in the Arrhenius coordinates have a linear character for all samples investigated. Basing on these relationships, the activation energies of ionic conductivity were calculated. Figure 5 shows the influence of sample chemical composition on the activation energy. In all series, samples containing the same oxygen vacancy concentrations and stabilized only by calcia have higher activation energies than those stabilized with yttria. Changes in activation energy with chemical composition are linear in the case of samples with 12 mol % of oxygen vacancies. For the 10 series, a deviation from linearity towards lower activation energies arises. This effect is much stronger in the 8 series, where a distinct minimum of the activation energy is observed. In this case, the lower activation energies are attributed to samples closer to the transformation verge.

Taking into account the relations between chemical compositions, phase content, and structural changes, it can be stated that an increase in oxygen sublattice distortion at the verge of the phase transition is responsible for the decrease in the activation

energy of ionic conductivity. This effect, in the studied materials, is caused by an exchange of the weaker stabiliser (calcia) by the stronger one (yttria) and generally diminishes with increasing total stabilizer content. The decrease in the lattice parameter of the cubic phase with calcia content could be considered an additional factor; distances between equivalent ion positions during diffusion are shorter.

Acknowledgements

This work was carried out under contract No. 7 T08A 030 20, financed by the State Committee for Scientific Research.

References

[1] HAILE S.M., Acta Mater., 51 (2003), 5981.
[2] SKINER S.J., KILNER J.A, Materials Today, 6 (2003), 30.
[3] STAFFORD R.J., ROTHMAN S.J., ROUTBORT J.L., Solid State Ionics, 37 (1989), 67.
[4] BAUMARD J.F., ABELARD P., *Defect Structure and Transport Properties of ZrO_2-based Solid Electrolytes*, [in:] N. Clausen, A.H. Heuer (Eds.), *Advances in Ceramics*, Vol.12, Science and Technology of Zirconia II, American Ceramic Society Inc., New York, 1984, p. 555.
[5] KILNER J.A., BROOK R.J., Solid State Ionics, 6 (1982), 237.
[6] SHLICHTA P.J., Solid State Ionics, 28–30 (1988), 480.
[7] CORMAN G.S., STUBICAN V.S., J. Amer. Ceram. Soc., 68 (1985), 174.
[8] KANEKO H., JIN F., TAIMATSU H., USAKABE H., J. Amer. Ceram. Soc., 76 (1993), 793.
[9] STRICKLER D.W., CARLSON W.G., J. Amer. Ceram. Soc., 48 (1965), 286.
[10] LI Y., TANG Z., ZHANG Z., GONG J., J. Mat. Sci. Lett., 18 (1999), 443.
[11] GONG J., LI Y., TANG Z., ZHANG Z., J. Mat. Sci., 35 (2000), 3547.
[12] GONG J., LI Y., TANG Z., ZHANG Z., Mat. Lett., 46 (2000), 115.
[13] ISHIZAWA N., MATSUSHIMA Y., HAYASHI M., UEKI M., Acta Cryst., B55 (1999), 726.
[14] MORINAGA M., COHEN J.B., Acta Cryst., A36 (1980), 520.
[15] KISI E.H., HOWARD C.J., *Crystal Structures of Zirconia Phases and Their Inter-Relations*, [in:] *Key Engineering Materials*. Vols. 153–154, Trans Tech Publications, Switzerland, 1998, p. 1.

Received 23 December 2004
Revised 12 January 2005

Materials Science-Poland, Vol. 24, No. 1, 2006

Ceria-yttria-based solid electrolytes for intermediate temperature solid oxide fuel cell

M. DUDEK*, J. MOLENDA

AGH University of Science and Technology, Faculty of Materials Science and Ceramics
al. Mickiewicza 30, 30-059, Cracow, Poland

Pure ceria and ceria-yttria solid solution powders with formula $Ce_{1-x}Y_xO_2$, where $0 < x < 0.30$ were prepared by the coprecipitation-calcination method. The samples were sintered at 1250–1600 °C for 2 hours. The XRD method was used to determine cell parameters of the samples. Their electrical properties were investigated by ac impedance spectroscopy in the temperature range of 100–700 °C in air. It was found that the electrical conductivity, fracture toughness, and flexural strength of the samples increase with yttria concentration and reach a maximum for $Ce_{0.85}Y_{0.15}O_2$. The obtained material seems to be a promising solid electrolyte for IT-SOFC.

Key words: *ceria; solid electrolyte; electrical properties; mechanical properties; zirconia*

1. Introduction

Solid oxide fuel cells (SOFC) are very attractive due to their high efficiency and very low pollutant emission. Until now, solid oxide fuel cell systems have been based mainly on yttria-stabilized zirconia (YSZ) ceramics, because of their nearly pure oxygen conductivity in oxidizing and reducing atmospheres as well as good mechanical properties [1]. ZrO_2-based electrolytes, however, require high operating temperatures – over 900 °C – in order to maintain high oxygen ionic conductivity. Such high operating temperatures result in large fabrication costs and accelerate the degradation of the fuel cell systems [2, 3]. Recently, intensive research has been conducted aiming at reducing the operating temperature of SOFC to 700–650 °C. Ceria-based solid solutions have been regarded as being the most promising electrolytes for intermediate temperature SOFC (IT-SOFC), since their ionic conductivities are higher than that of YSZ in the intermediate temperature range [4]. The ionic conductivity of ceria-based solid electrolytes doped with various cations (e.g., Ca^{2+}, Sr^{2+}, Y^{3+}, La^{3+}, Gd^{3+} and

*Corresponding author, e-mail: potoczek@uci.agh.edu.pl

Sm^{3+}) at various dopant concentrations has been extensively investigated [5, 6]. Literature data on the electrical and mechanical properties of ceria-based electrolytes versus dopant types and concentrations, however, are often inconsistent and contradictory. In spite of such interest in ceria-based materials, there has not been any systematic research on the influence of yttria on the structure, microstructure, and consequently the electrical and mechanical properties of CeO_2-based materials. The microstructures of sintered samples, which are affected both by chemical composition and preparation conditions, have a strong influence on the material characteristics. Fine-grained, dense microstructures usually lead to an improvement of the mechanical and electrical properties. This is due to the role that grain boundaries play both in fracture propagation and the conductivity of materials.

The aim of this work was to study the influence of yttria concentration and preparation conditions on the microstructure of yttria-ceria based ceramics and hence on their mechanical and electrical properties.

2. Experimental

A co-precipitation method was used to prepare pure ceria and yttria-ceria solid solutions with the formula of $Ce_{1-x}Y_xO_2$, where $0< x <0.30$. Aqueous solutions of cerium nitrate with an appropriate amount of yttrium nitrate were introduced into the ammonia solution. The resulting gels were washed with water, dried, and calcined in the temperature range of 400–800 °C for 1 hour. The ground powders were cold pressed isostatically under 200 Pa and then sintered in air at 1250–1600 °C for 2 hours. The phase composition of all powders and sintered samples was characterized by X-ray diffraction analysis. The crystalline size of the powders was estimated by the line broadening analysis, using the reflection from (110) plane. The specific surface area of the powders was measured by the one-point BET technique. The Archimedean method was used to determine the apparent density of the studied samples. Scanning electron microscopy was used to observe the microstructure of the materials obtained. The Vickers hardness (*HV*) and fracture toughness (K_{IC}) were determined by the Vickers indentation method. The Palmquist crack model and Niihara equation were applied [7]. Specimens for three-point flexural tests were cut from the plates and their surface polished. The electrical properties of yttria-ceria-based solutions were investigated by ac impedance spectroscopy in the temperature range of 100–750 °C and at the frequencies from 1 Hz to 10 MHz.

3. Results and discussion

Phases of pure ceria and ceria-yttria solid solution with the formula of $Ce_{1-x}Y_xO_2$ (with $0< x <0.30$) were detected by the XRD analysis in the powders and samples sintered. The properties of pure and yttria-doped ceria powders are listed in Table 1.

Table 1. Average crystallite sizes of pure CeO_2 and $Ce_{1-x}Y_xO_2$ powders determined by XRD and BET specific surface measurements

x	D_{hkl}, nm	D_{BET}, nm
0	30.0	35.0
0.10	25.0	28.8
0.15	17.3	18.3
0.20	12.8	13.6
0.25	14.1	15.9

The data presented in Table 1 indicate a decrease in the crystallite size of the $Ce_{1-x}Y_xO_2$ solid solutions with increasing yttrium concentration. The consistency of sizes determined by X-ray diffraction analysis and BET specific surface measurements suggests that the powders are composed of isometric and not agglomerated crystallites. Generally, all samples sintered at temperatures 1400–1500 °C achieved a relative density exceeding 98% of the theoretical value. Concentrations of yttria higher than $x = 0.20$ in $Ce_{1-x}Y_xO_2$ solid solutions led to lower densities, because of an increase in close porosity. The unit cell parameter decreased with increasing yttria content (Fig. 1) in good agreement with effective ionic radii considerations, taking into account that $r_{Ce^{4+}} = 0.111$ nm and $r_{Y^{3+}} = 0.089$ nm [8].

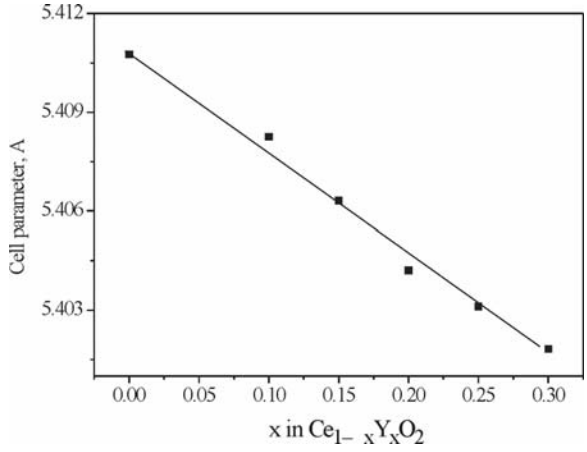

Fig. 1. Changes of cell parameters versus yttria concentrations in $Ce_{1-x}Y_xO_2$

Figure 2 shows a typical microstructure of a pure CeO_2 sample sintered at 1400 °C. The ceria average grain sizes decreased in the $Ce_{1-x}Y_xO_2$ materials sintered at this temperature from about 1.0 μm to 0.60 μm with increasing yttria content. Above 1500 °C, a significant grain growth was observed in all sintered samples. The samples sintered at temperatures of 1500–1600 °C exhibited average grain sizes in the range of 2.8–5.0 μm.

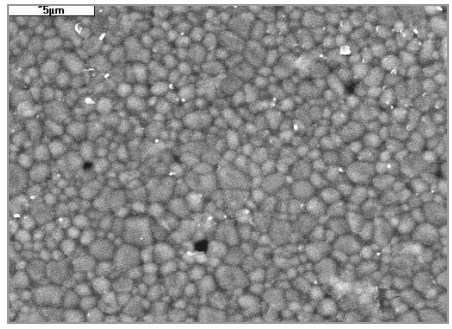

Fig. 2. Microstructure of pure CeO_2 sample sintered at 1400 °C

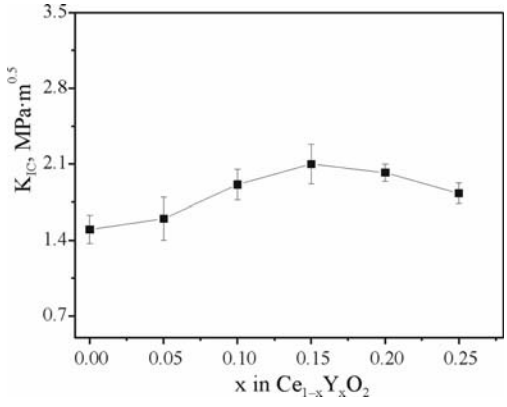

Fig. 3. Influence of yttria concentration on fracture toughness K_{IC} of $Ce_{1-x}Y_xO_2$ samples

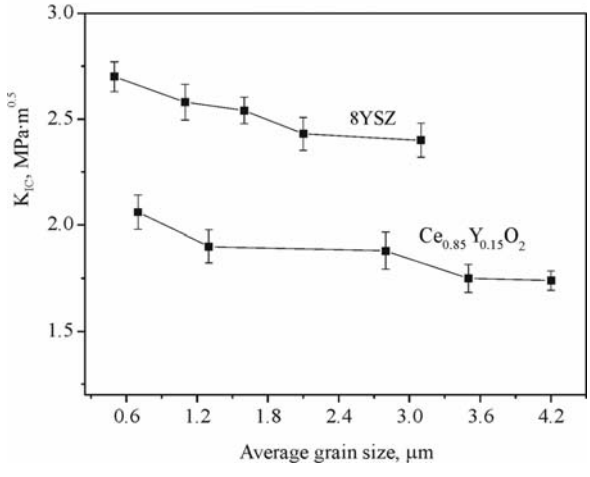

Fig. 4. Influence of grain size on fracture toughness K_{IC} of $Ce_{0.85}Y_{0.15}O_2$ and 8YSZ solid electrolyte

K_{IC} measurements revealed a small increase in fracture toughness with increasing yttria concentration in solid solutions for x = 0.15–0.20 (Fig. 3). For higher concentrations of yttria, a rather small decrease was observed, which could be attributed to the presence of small amounts of closed porosity in the investigated samples. The effect of grain size on the fracture toughness of the samples is also presented in Fig. 4. In order to compare the influence of microstructure on the changes in the fracture toughness of yttria-ceria based solid solutions, the diagram shows these changes together with the grain size for the 8YSZ sample, which up to now has been in common use as a solid electrolyte in oxide fuel cells. In both cases, one can observe a very slight increase in fracture toughness along with a decrease in grain size to about 0.5–0.7 μm. Without going into further details of the microscopic observations, one can state that the cracks propagate along grain boundaries and across grain interiors in the investigated materials. The very small increase in the fracture toughness of the fine-grained microstructure was caused by a slight deflection in the fracture course through the inter-granular boundaries. Table 2 presents other mechanical properties (hardness and flexural strength) which are important in the usage of yttria-doped ceria as a solid electrolyte in SOFC. A comparison of the data indicates a slight improvement of the mechanical characteristics with increasing yttria content in the $Ce_{1-x}Y_xO_2$ solid solutions which, however, have slightly worse mechanical properties than the 8YSZ electrolyte.

Table 2. Mechanical properties of selected materials based on ceria and zirconia

Material	*HV*,GPa	σ, MPa
CeO_2	7.80 ±0.15	101 ± 14
$Ce_{0.9}Y_{0.1}O_2$	8.13 ±0.11	130 ± 12
$Ce_{0.85}Y_{0.15}O_2$	8.90 ±0.16	144 ± 11
8YSZ	12.83 ±0.16	212 ± 17

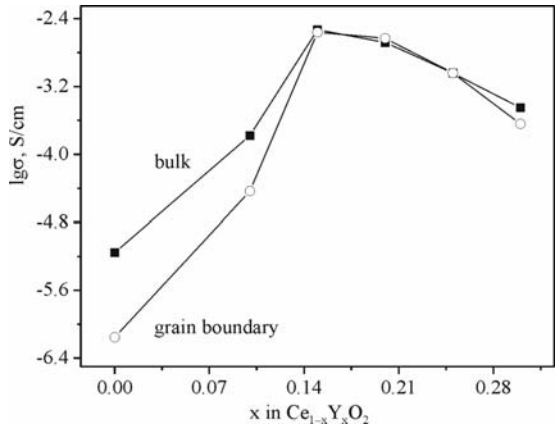

Fig. 5. The bulk conductivity and grain boundary conductivity of $Ce_{1-x}Y_xO_2$ as a function of dopant concentration x

Figure 5 shows the dependence of the bulk conductivity and grain boundary conductivity of the $Ce_{1-x}Y_xO_2$ system on dopant concentration x at 500 °C. The analysis of the conductivities of all investigated samples shows that the bulk conductivity reaches a maximum of $3.0 \cdot 10^{-3}$ S/cm at 500 °C for $x = 0.15$. This is in good agreement with the results reported in [9]. Other data, however, indicate a maximum conductivity corresponding to $x = 0.2$ or even $x = 0.08$–0.12 [10, 11].

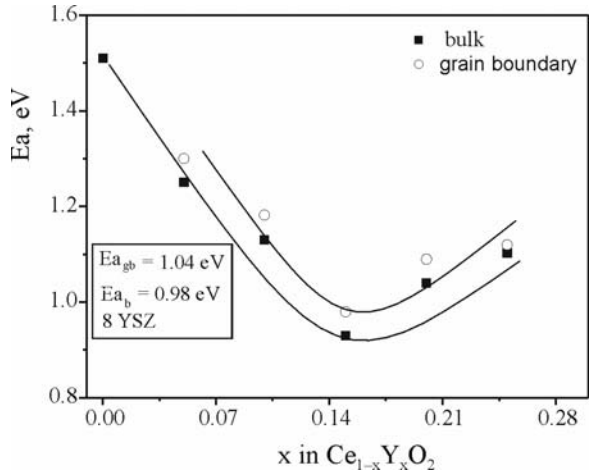

Fig. 6. The energy activation of bulk and grain boundary conductivity of $Ce_{1-x}Y_xO_2$ samples

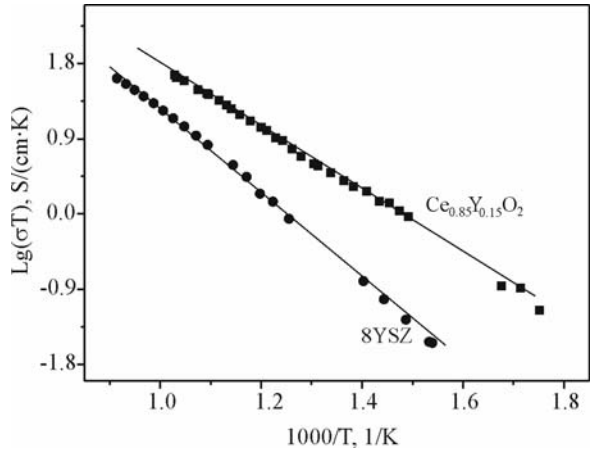

Fig. 7. Temperature dependence of the total conductivity of $Ce_{0.85}Y_{0.15}O_2$ and 8YSZ samples

The grain boundary conductivities of $Ce_{1-x}Y_xO_2$ also increase with Y_2O_3 content and reach a maximum for $x = 0.15$ in the investigated temperature range. In both cases, the maximum in grain boundary and bulk conductivity corresponds to a mini-

mum energy activation of electrical conductivity (Fig. 6). The temperature dependences of the total conductivity for a sample with $x = 0.15$ as well as for 8YSZ are shown in Figure 7. A single straight line represents the Arrhenius plot of total conductivities for both samples. The total conductivity of $Ce_{1-x}Y_xO_2$ reaches a maximum (6.0×10^{-2} S/cm at 700 °C) for $x = 0.15$. This value is nearly 50% higher than the total conductivity of 8 YSZ at 700 °C (1.2×10^{-2} S/cm). The obtained values of electrical conductivity and activation energy indicate that $Ce_{0.85}Y_{0.15}O_2$ can be a suitable electrolyte for solid oxide fuel cells operating in the temperature range of 600–700 °C. In both investigated electrolytes, an increase in the sintering temperature led to a decrease in the total electrical conductivity. This can be related to microstructural changes in ceria and zirconia samples, consisting in grain size and porosity development.

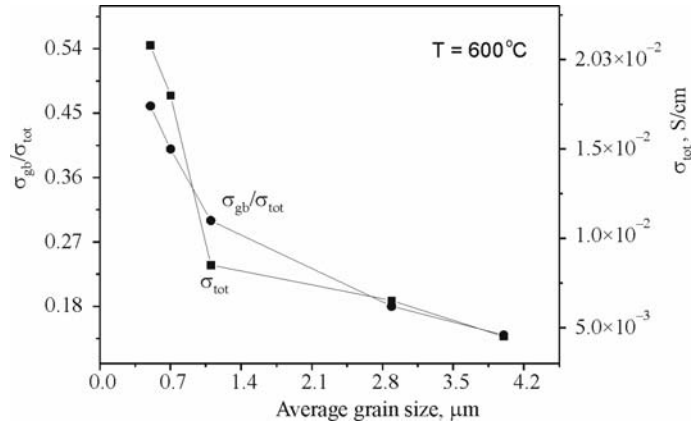

Fig. 8. Changes of the grain boundary conductivity to total conductivity and total conductivity as a function of grain size in $Ce_{0.85}Y_{0.15}O_2$ sample

The plot in Figure 8 shows the ratio of grain boundary and total conductivity (σ_g/σ_t) versus average grain size for the $Ce_{0.85}Y_{0.15}O_2$ sample. As expected, an increase in grain size caused a decrease in the relative fraction of grain boundary conductivity and total electrical conductivity.

4. Conclusions

Pure ceria and yttria-doped ceria solid solution powders with thea formula of $Ce_{1-x}Y_xO_2$ ($0 < x < 0.30$) were successfully synthesized by the calcination-coprecipitaion method. It was found that the electrical conductivity, fracture toughness and flexural strength of the investigated materials increase with the yttria doping concentration and reaches a maximum for $Ce_{0.85}Y_{0.15}O_2$. Contrary to mechanical properties, the electrical conductivity of ceria-based electrolytes can be improved simply by controlling the grain size. The obtained values of electrical conductivity and energy acti-

vation for $Ce_{0.85}Y_{0.15}O_2$ with an average grain size of 0.5 μm show that the prepared material is a promising solid electrolyte for IT-SOFC systems operating in the temperature range 600–700 °C.

Acknowledgement

This work was financially supported by the Polish Committee for Scientific Research under grant No. T08 D 016 28. One of the authors (M. Dudek) acknowledges the financial support grant of the Foundation for Polish Science, awarded for young scientists in 2004.

References

[1] MINH N.J., Am. Ceram. Soc., 76 (1993), 563.
[2] TIETZ F., BUCHKREMER H., STOVER D., Solid State Ionics, 152–153 (2002), 373.
[3] STEELE B.C., Solid State Ionics, 86–88 (1996), 1223.
[4] SOSINA M., Acta Materialia, 51 (2003), 5981.
[5] INABA H., TAGAWA H., Solid State Ionics, 83 (1996), 1.
[6] ANDERSON H , NOWICKI A., Solid State Ionics, 5 (1981), 547.
[7] NIHIHARA K.J., Mater. Sci. Lett., 21 (1983), 221.
[8] SHANNON R., PREWITT T., Acta Cryst. B, 25 (1969), 925.
[9] MA J., ZHANG T., J. Europ. Ceram. Soc., 24 (2004), 2641.
[10] ZHANG T.S., MA J., KILNER J.A., Solid State Ionics, 170 (2004), 209.
[11] WANG D.Y., PARK J., Solid State Ionics, 2 (1981), 95.

Received 28 December 2004
Revised 17 January 2005

Materials Science-Poland, Vol. 24, No. 1, 2006

Electrical properties of Nb-doped titanium dioxide TiO_2 at room temperature

A. TRENCZEK-ZAJĄC, M. REKAS*

AGH University of Science and Technology,
Faculty of Materials Science and Ceramics, al. Mickiewicza 30, 30-059 Cracow, Poland

Nb-doped TiO_2 (0–15 at. % Nb) polycrystalline specimens were prepared by the sol-gel method. Below 10 at. % of Nb, materials were homogeneous and exhibited rutile structure, their lattice parameters changing with Nb concentration according to the Vegard's law. Above 10 at. % of Nb, the second phase $TiNb_2O_7$ was formed, detected by X-ray diffractometry. Materials were heated at 1273 K for 3 h in air (p_{O2} = 210 kPa) and in flow of Ar + 3 vol. % H_2 gas mixture ($p_{O2} = 10^{-15}$ Pa) and then cooled down. Electrochemical impedance spectroscopy within the frequency range 0.01 Hz–2 MHz has been used to determine electrical properties of the materials. An equivalent circuit composed of a resistor R_{gb}, a capacitor C connected parallel and a resistor R_b connected in series, well represents the electrical properties of reduced samples. On the other hand, non-Debye elements should be taken into account in construction of the equivalent circuit of oxidized materials. The mechanism of the Nb incorporation has been proposed.

Key words: *titanium dioxide; Nb-doping; solid solution; defect structure; impedance spectroscopy*

1. Introduction

Titanium dioxide (rutile) has a wide range of applications due to its interesting electrical and photo-electrical properties [1, 2] determined by nonstoichiometry and related point defect structure. Metal ion doping (by both acceptor- or donor-type elements) can significantly modify these properties [1, 3–5]. High-temperature semiconducting properties of undoped [6, 7], acceptor- [3, 7, 8] or donor- [7, 9] doped TiO_2 have been the subject of numerous reports. On the other hand, little is known about the electrical properties of these materials at room temperature (i.e., at the conditions in which they are used as electrodes, electronic devices, etc.). The purpose of the pre-

*Corresponding author, e-mail: rekas@uci.agh.edu.pl

sent paper is to examine the effect of Nb doping on structural and electrical properties of polycrystalline TiO_2 at room temperature.

2. Experimental

Sample preparation. Materials were prepared by thermal decomposition of oxide precursors. Titanium tetraisopropoxide, $Ti[OCH(CH_3)_2]_4$, (Aldrich, 97 %) and niobium pentachloride, $NbCl_5$, (Aldrich, 99 %) were used as starting materials. Anhydrous C_2H_5OH was mixed with H_2O and HCl (as a catalyst) at 273 K and then added drop by drop to solution of $Ti[OCH(CH_3)_2]_4$ in C_2H_5OH under continuous stirring at room temperature. The molar composition of the solution was $Ti[OCH(CH_3)_2]_4$ $/C_2H_5OH/H_2O/HCl$ = 1/8/5/0.02. The Nb-containing solution was prepared by dissolution of 4 g of $NbCl_5$ in 100 cm^3 of anhydrous ethanol.

Both solutions were mixed by dropping a suitable amount of $NbCl_5$ solution into stirred tetraisopropoxide solution at temperature close to 273 K. Time of sol-gel transformation varied from 1 day to 3 weeks, for undoped specimen and 15 at. % Nb-doped, respectively. After the evaporation of solvents, the remaining powders were dried in air (273–373 K), ground in an agate mortar and then calcined at 873 K during 2 h. Pellets were formed by uniaxial pressing under 100 MPa followed by isostatic pressing under 250 MPa and then sintered at 1600 K during 5 h in air.

Impedance measurements. The impedance measurements were performed using a frequency response analyser Solartron 1294. Frequency range was 1 Hz–2 MHz, the amplitude of the sinusoidal voltage signal was 20 mV. The best-fit values of the equivalent circuit components were determined using the ZPLOT software included in the Solartron impedance equipment.

3. Results and discussion

XRD analysis. X-ray diffraction was done using Philips X'Pert Pro diffractometer with CuK_α filtered radiation in the 2θ range from 10° to 80°. Phase identification was performed using the data base ICDD. The analysis revealed that the samples containing 10 at. % of Nb and less are homogeneous and crystallize in the rutile phase. On the other hand, apart rutile phase, the traces of the $TiNb_2O_7$ have been detected in the specimen TiO_2 + 15 at. % of Nb. The lattice parameters were determined by means of Rietveld's method using the Fullprof program [10]. Figure 1 illustrates calculated lattice parameters *a* and *b* of the rutile unit cell as a function of the concentration of Nb. As it can be seen, a linear dependence is observed within the range 0–10 at. % of Nb, predicted by Vegard's law. The increase of both parameters, *a* and *b*, can be explained by substitution of smaller Ti^{4+}ions (r_{Ti4+} = 68 pm) by larger Nb^{5+} (r_{Nb5+} = 69 pm [11]). Departure from the linearity presented in Figure 1 indicates that the Nb-solubility limit is between 10 and 15 at. % of Nb.

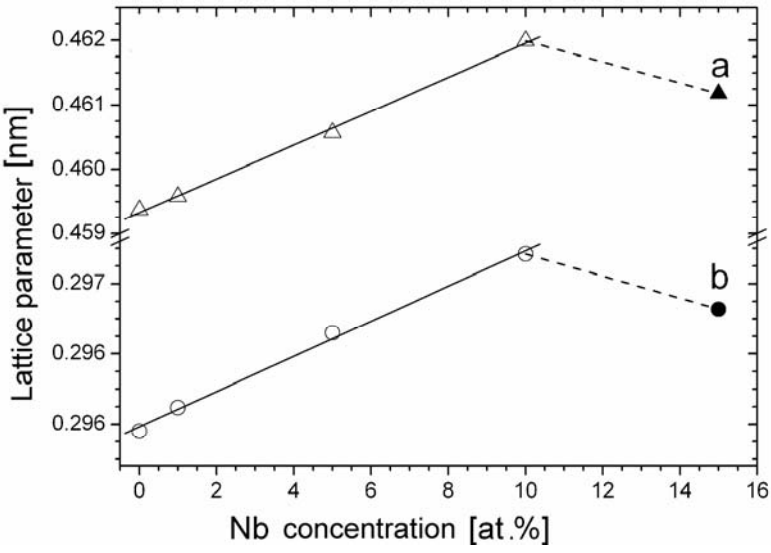

Fig. 1. Lattice parameters *a*, *b* of the Nb–TiO_2 rutile cell as a function of the concentration of Nb

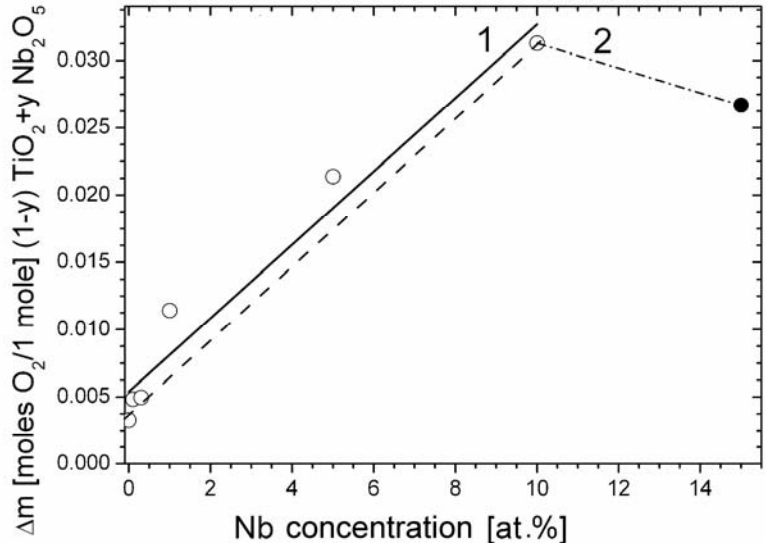

Fig. 2. Maximum reversible weight change of Nb-doped TiO_2 accompanying $p(O_2)$ changes between 210 kPa and 10^{-15} Pa as a function of the concentration of Nb. The dashed line 2 illustrates the best linear dependence; the solid line 1 corresponds to the theoretical dependence resulting from the reaction (3)

Thermogravimetric studies. Figure 2 shows weight changes of the samples, accompanying their reduction at 1273 K for 3 h. The observed weight losses may be ex-

plained by the existence of two forms of Nb-doped TiO_2 resulting from different reactions of the Nb incorporation into TiO_2 lattice occurring either in oxidizing or reducing conditions. In Kröger and Vink [12] notation, the following reaction occurs at oxidizing conditions:

$$2Nb_2O_5 \Rightarrow 4Nb_{Ti}^{\bullet} + V_{Ti}^{''''} + 10O_O \tag{1}$$

where $V_{Ti}^{''''}$ denotes titanium vacancy having the charge 4– with respect to the lattice. At reducing conditions:

$$Nb_2O_5 \rightarrow 2Nb_{Ti}^{\bullet} + 2e' + 4O_O + \frac{1}{2}O_2 \tag{2}$$

Transition between the above forms may be described by the following equation:

$$4Nb_{Ti}^{\bullet} + V_{Ti}^{''''} + 10O_O \rightarrow 4Nb_{Ti}^{\bullet} + 4e' + 8O_O + O_2 \tag{3}$$

Solid line 2 in Figure 2 illustrates the weight change corresponding to reaction (3) ("theoretical dependence"). As can be seen, there is a good agreement between the experimental data and the theoretical dependence.

Impedance measurements. Figures 3 and 4 illustrate impedance spectra presented in a complex impedance plane of undoped TiO_2 reduced and oxidized, respectively. In

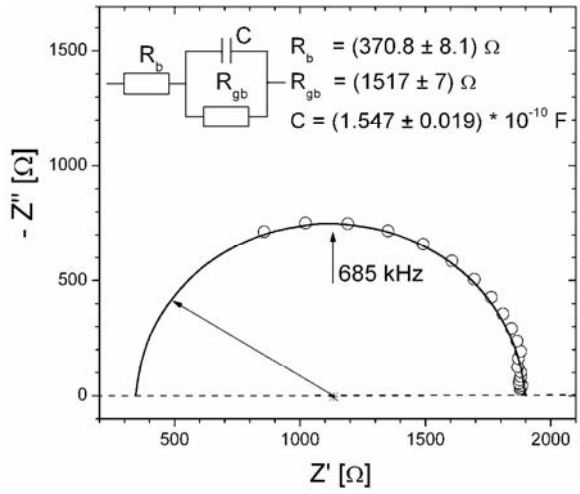

Fig. 3. Complex impedance spectrum and the equivalent circuit of reduced undoped TiO_2. The asterisk shows the centre of the semicircle

Figures 5 and 6, analogous spectra are shown for TiO_2 containing 10 at. % of Nb reduced and oxidized, respectively. For other compositions the impedance spectra are similar. The experimental points of reduced samples (Figs. 3 and 5) lie on semicircles

with the centre placed on the Z' axis. The simplest equivalent circuit of such plots is composed with a resistor R_b and a parallel R_{gb}–C branch in series.

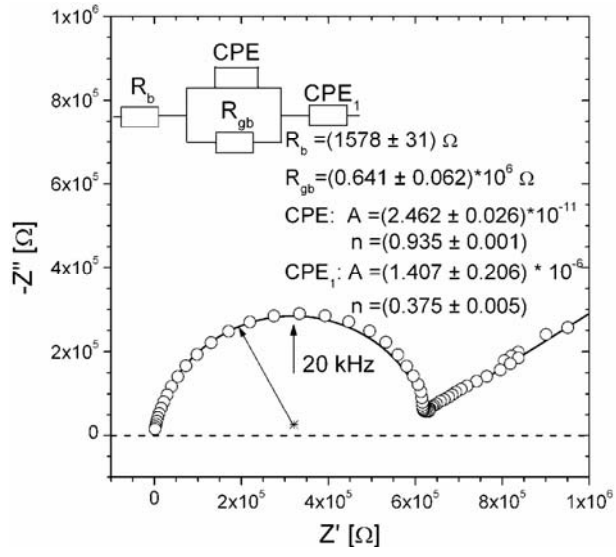

Fig. 4. Complex impedance spectrum and the equivalent circuit of oxidized undoped TiO_2.
The asterisk shows the centre of the semicircle

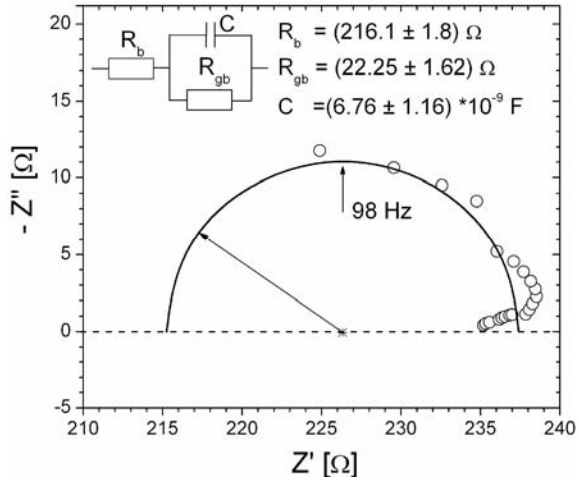

Fig. 5. Complex impedance spectrum and the equivalent circuit of reduced TiO_2 + 10 at. % Nb. The asterisk shows the centre of the semicircle

Based on general rules [13], we can ascribe R_b to the bulk resistivity, R_{gb} and C to the grain boundaries parameters. The impedance spectra of the oxidized samples show a more complex character. The centres of the arcs are placed below the Z' axis. More-

over, spur is observed at higher frequencies. The non-Debye constant phase elements (CPE) defined by the admittance formula:

$$Y_{\mathrm{CPE}} = A(j\omega)^n \tag{4}$$

had to be included into an equivalent circuit in order to describe properly the experimental results. Similar behaviour was observed for polycrystalline TiO_2 materials prepared by coprecipitation method [14].

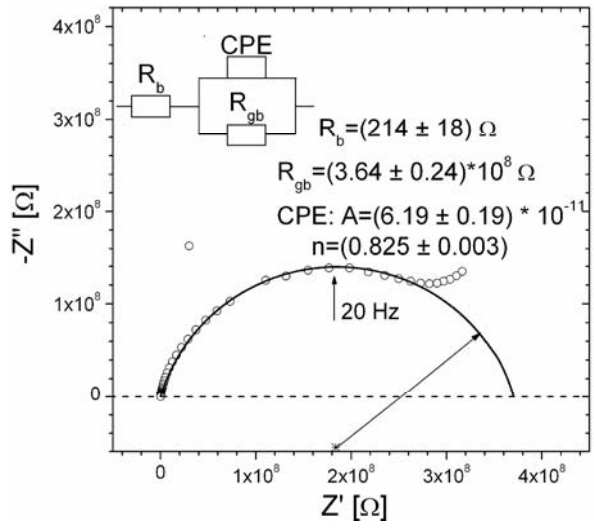

Fig. 6. Complex impedance spectrum and the equivalent circuit of oxidized TiO_2 + 10 at. % Nb. The asterisk shows the centre of the semicircle

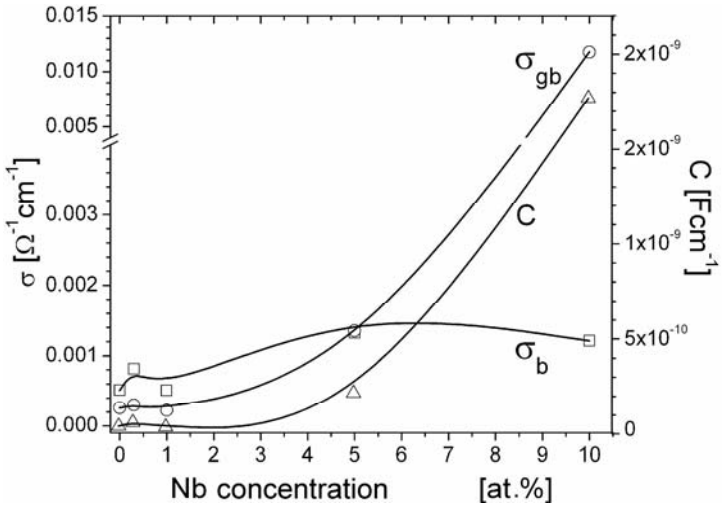

Fig. 7. Dependences of the electrical conductivity (left axis) and capacitance (right axis) of the Nb–TiO_2 system on the concentration of Nb

Figure 7 shows the compositional dependences of the electrical conductivity σ_b (bulk) and σ_{gb} (grain boundaries) (left axis), and capacitance C (right axis) of the reduced samples. Below 5 at. % of Nb, the electrical conductivity of grain boundaries is lower than that of the bulk. Poor conductivity of grain boundaries can results from enrichment of the grain boundaries with niobium. There are two possible explanations of this enrichment resulting from very slow rate of incorporation of Nb in TiO_2 lattice due to extremely low diffusion of Nb [14] or by the occurrence of segregation processes [16].

4. Conclusions

Polycrystalline Nb-doped TiO_2 specimens (0–15 at. % Nb) were the subject of this study. Below doping level of 10 at. % of Nb, materials exhibit rutile structure and lattice parameters change with Nb concentration according to Vegard's law. Above dopant concentration of 10 at. % of a second phase, $TiNb_2O_7$, was detected.

Electrochemical impedance spectroscopy within the frequency range 0.01 Hz–2 MHz has been used to determine electrical properties of the studied materials at room temperature. The impedance spectra differ substantially from those of oxidized ones. The equivalent circuit of the reduced materials is composed of a resistor R_{gb}, a capacitor C connected in parallel and a resistor R_b connected in series, well represents the impedance of studied samples. On the other hand, non-Debye elements should be taken into account in construction of the equivalent circuit of oxidized materials.

Acknowledgements

The authors gratefully acknowledge a helpful discussion with Professor Marta Radecka. This work was supported by the Polish State Committee for Scientific Research (KBN) in the Grant AGH No. 11.11.160.247.

References

[1] KOFSTAD P., *Electrical Conductivity, Nonstoichiometry, Diffusion in Binary Metal Oxides*, Wiley, New York, 1972.
[2] FINKLEA H.O., *Semiconductor Electrodes*, Elsevier, Amsterdam, 1988.
[3] BERNASIK A., RADECKA M., REKAS M., SLOMA M., Appl. Surf. Sci., 65–66 (1993), 240.
[4] RADECKA M., WIERZBICKA M., KOMORNICKI S., REKAS M., Physica B, 348 (2004),160.
[5] RADECKA M., SOBAS P., TRENCZEK A., REKAS M., Pol. J. Chem., 78 (2004), 1925.
[6] NOWOTNY J., RADECKA M., REKAS M., J. Phys. Chem. Solids, 58 (1997), 927.
[7] BAK T., NOWOTNY J., REKAS M., SORRELL C.C., J. Phys. Chem. Solids, 64 (2003), 1043, 1057,1069.
[8] CARPENTIER J.L., KEBRUN A., PERDU F., J. Phys. Coll., 47 (1986), C1 819.
[9] EROR N.G., J. Solid State Chem., 38 (1981), 281.
[10] http:\\www-llb.cea.fr\fullweb.
[11] *Handbook of Chemistry, Physics*, R.C. Weast, M.J. Astle (Eds.), CRC Press Inc., Boca Raton, 1980, F-214.

[12] KRÖGER F.A., VINK H.J. [in:] *Solid State Physics*, F. Seitz, D. Turnbull (Eds), Academic Press, New York, 1956, p. 307.
[13] MACDONALD J.R., FRANCESCHETTI D.R., [in:] *Impedance Spectroscopy*, J.R. Macdonald (Ed.), Wiley, 1987, 84.
[14] KOMORNICKI S., RADECKA M., REKAS M., J. Mater. Sci. Mater. Electron.,12 (2001),11.
[15] RADECKA M., REKAS M., J. Phys. Chem. Solid, 56 (1995), 1031.
[16] KOWALSKI K., IJJAALI M., BAK T., DUPRE B., NOWOTNY J., REKAS M., SORRELL C.C., J. Phys. Chem. Solids, 62 (2001), 531.

Received 10 December 2004
Revised 12 January 2005

Materials Science-Poland, Vol. 24, No. 1, 2006

Lithium-ion batteries – state of art
Novel phospho-olivine cathode materials

J. MOLENDA*

Faculty of Materials Science and Ceramics,
AGH University of Science and Technology, al. Mickiewicza 30, 30-059 Cracow, Poland

This work is a brief review of physicochemical properties of modern cathode materials for Li-ion batteries. These intercalated transition metal compounds of layered, spinel or olivine-type structure exhibit a correlation between their microscopic electronic properties and the efficiency and mechanism of lithium intercalation. The recently reported metallic-type conductivity of doped phospho-olivine $LiFePO_4$, being a novel promising cathode material, is discussed in more detail, and some fundamental arguments are presented against the bulk nature of the observed high electronic conductivity.

Key words: *Li-ion battery; cathode material; phospho-olivine; $LiFePO_4$; intercalation*

1. Introduction

The enormous technological progress and common use of portable electronic devices call for batteries with high energy densities per unit mass and volume, a high number of charge-discharge cycles, safe operation, non-toxicity and low price. In the widely used technologies of reversible Ni–Cd and NiMH batteries, no further improvements can be anticipated. A prospective technology under intensive development is that of reversible lithium batteries (Li-ion batteries). These are based on the reversible intercalation of lithium into the transition metal compounds M_aX_b (X = O, S). The effectiveness of intercalation in a $Li_xC_6/Li^+/Li_{1-x}M_aX_b$ cell, where the anode reaction is

$$C_6 + xLi^+ + xe^- \leftrightarrow Li_xC_6 \tag{1}$$

and the cathode reaction is

$$Li_1M_aX_b \leftrightarrow Li_{1-x}M_aX_b + xLi^+ + xe^- \tag{2}$$

*E-mail: molenda@uci.agh.edu.pl

depends on the transport properties of ions and electrons in both electrode materials and on the availability of sites for Li^+ ions, as well as on the density of electron states near the Fermi level in both materials [1, 2]. The graphite anode does not limit the useful parameters of such batteries. Potential improvements in the operation of the Li-ion batteries can be sought after in the cathode material.

In today's Li-ion batteries, $LiCoO_2$ cathodes have been replaced by other materials, such as $LiCo_{1-y}Ni_yO_2$ and $LiMn_2O_4$. These cathodes have a number of limitations. With $LiCoO_2$ it is possible to use merely half of its theoretical capacity, because the electrochemical deintercalation/intercalation process is reversible only within a limited compositional range, i.e. $LiCoO_2$–$Li_{0.5}CoO_2$, resulting in a low capacity of 130 mAh/g. Moreover, $LiCoO_2$ is toxic and relatively expensive. On the other hand, the capacity of $LiNiO_2$ is higher than the capacity of $LiCoO_2$, but its thermal stability is lower and the compound cannot be used in Li-ion batteries for safety reasons. The delithiation of $LiNiO_2$ leads to the exothermic oxidation of the liquid organic electrolyte. Therefore, the development of solid electrolytes (e.g., polymeric ones), which might replace the commonly used EC/DMC-$LiPF_6$, is a very important research direction. This would extend the service life of Li-ion batteries and increase their safety of operation. In the case of manganese spinel, $LiMn_2O_4$, capacity losses are observed on cycling and battery parameters degrade at elevated temperatures.

2. Iron oxide-based cathode materials

Some investigations under way are focused on cathode materials based on iron oxides. The interest in iron compounds arises from the fact that iron is cheap, abundant in the earth crust, and friendlier to the environment than cobalt, nickel, or manganese. Unfortunately, the iron-containing layered compound $LiFeO_2$, isostructural with $LiCoO_2$ and $LiNiO_2$, appears to be metastable. The stability of ABO_2 oxides with layered structures of the α-$NaFeO_2$ ($R3m$) type can be estimated from Pauling's rule [3], according to which the r_B/r_A ratio should be less than 0.86. In the case of $LiCoO_2$ and $LiNiO_2$, this ratio is 0.77 and 0.78, respectively. For $LiFeO_2$, $r_{Fe^{3+}}/r_{Li^+}$ equals 0.88, and the structure is unstable. Another important reason, which excludes $LiFeO_2$ from being applied in batteries, is the unfavourable position of the redox potentials of iron in relation to those of lithium [4] (Fig. 1). The Fe^{3+}/Fe^{4+} potential is too distant from that of Li/Li^+ and located beyond the electrochemical window of the electrolyte, which cannot guarantee the neutrality of the electrolyte versus the cathode. On the other hand, the Fe^{3+}/Fe^{2+} potential is too close to that of Li/Li^+, which results in a voltage of the cell that is too low. Such behaviour is related to the high-spin configuration of Fe^{3+} and strong interactions between d electrons.

It seems that the problems associated with structural instability and the unfavourable position of the redox potentials of iron versus lithium can be overcome by using a new series of iron compounds, e.g. $LiFeXO_4$, proposed by Goodenough [5], whose

large polyanions $(XO_4)^{y-}$ (X= S, P, As, Mo, W; y = 2 or 3) might stabilize the structure. The presence of such polyanions $(XO_4)^{y-}$, with a strong covalent X–O bond,

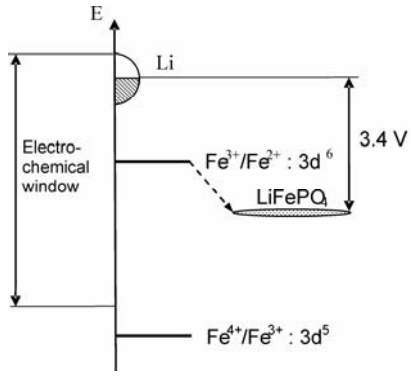

Fig. 1. Energy diagram showing the Fe^{4+}/Fe^{3+} and Fe^{3+}/Fe^{2+} potentials in the cathode materials based on iron in octahedral coordination

stabilizes the anti-bonding state, Fe^{3+}/Fe^{2+}. The Fe–O bond becomes less covalent due to the induction effect in the Fe–O–X system, which raises the electrode potential. The stronger the X–O bond, the weaker the Fe–O bond and the higher is the cell voltage. A shift of the Fe^{3+}/Fe^{2+} potential in $LiFePO_4$ (Fig. 1) results in a high voltage (3.4 V) of the $Li/Li^+/Li_xFePO_4$ cell.

3. Phospho-olivine – a new cathode material

$LiFePO_4$ with the olivine structure belongs to the family of NASICON-type compounds (NASICON – sodium super-ionic conductor), known to be fast ionic conductors and used as solid electrolytes in electrochemical cells. In $LiFePO_4$, the hexagonal close-packed lattice of oxygen has two-dimensional channel network being potential fast diffusion paths for lithium ions. Structural limitations (in the FeO_6 octahedra joined by corners, the Fe–Fe distances are larger than 4 Å, while in simple oxides M–M distances do not exceed 3 Å), however, make the material practically an insulator. Its electrical conductivity at room temperature is extremely low compared to typical cathode materials and equals 10^{-10} S·cm^{-1}. Thus, the observed LiFePO4 delithiation is not really a diffusional deintercalation process, described by the following equation:

$$LiFePO_4 - xLi^+ - xe^- \longleftrightarrow Li_{1-x}FePO_4 \tag{3}$$

which yields a homogeneous material with varying lithium content. The data reported in the literature [6] and our own studies [11] indicate that lithium extraction from $LiFePO_4$ in the discharge cycle leads to the decomposition of the cathode material into two phases, of which one contains lithium and the other is lithium-free:

$$LiFePO_4 - xLi^+ - xe^- = xFePO_4 + (1 - x)LiFePO_4 \quad (4)$$

and a similar reverse reaction (discharging cycle):

$$FePO_4 + xLi^+ + xe^- = xLiFePO_4 + (1 - x)FePO_4 \quad (5)$$

The reversibility of the charge–discharge processes is related to the great similarity of the structures of $LiFePO_4$ and $FePO_4$ (the same space group), which have a volume difference of only 6,81%. The described behaviour of the cathode material is not at all beneficial – only the grain surfaces of the cathode are effectively used and the current density of the cell is low. The reason for reactions (4) and (5) to occur is low electronic conductivity. Some attempts have been made to improve microscopic conductivity by the grain refinement of $LiFePO_4$, coated with carbon during synthesis. The applied procedures do not, however, increase the electronic conductivity within the grains and therefore affect neither the chemical diffusion coefficient of lithium nor the current density.

In spite of this, $LiFePO_4$ has some important advantages: the highest theoretical capacity of all known cathode materials (170 mAh/g), and the highest thermal stability, which guarantees safety of use and stable capacity after numerous work cycles. The most challenging issue in the search for a cathode material based on phospho -olivine is to get a mixed ionic-electronic conductivity, which should activate the diffusional mechanism of the deintercalation/intercalation process of reaction (3).

The first reports by Chiang [7] on the metallic-type conductivity of $LiFePO_4$, achieved by doping, evoked great interest and intensified studies on the influence of dopants on the electrical conductivity of this material.

Chiang [7] obtained a spectacular increase in electrical conductivity – by a factor of 10^7 – by introducing Nb^{5+}, Zr^{4+}, or Mg^{2+} ions into the lithium sublattice. Activation energies were of the order of 0.05 eV at room temperature. Figures 2 and 3 present the results of electrical conductivity and thermoelectric power measurements of phospho -olivine samples doped with W^{6+}, Ti^{4+}, and Al^{3+}. Conductivities of 10^{-2}–10^{-3} S/cm, together with low activation energies ranging from 0.02 to 0.1 eV, can be interpreted as metallisation at the border of carrier localization. The low absolute value of thermoelectric power – about 10 μV/K – and the lack of its dependence on temperature are characteristic of the metallic state. The described behaviour might be related to the formation of a narrow dopant band. Such a semiconductor–metal transition upon doping is known as a Mott's-type transition [8]. At some critical concentration, N_c, the electron wave functions of the dopant overlap, which leads to the formation of a dopant conduction band. Systematic analyses of the electrical properties of phospho-olivine doped with different concentrations of W, Ti or, Al, however, raise doubts about the bulk conductivity mechanism. The basic objections originate from a minor and rather random influence of the dopant type and concentration on conductivity. Moreover, an inhomogeneous distribution of the dopant (EDS) also leads to the same "metallic" behaviour of the material, and even for the highly conductive samples the deintercalation proceeds by a two-phase mechanism as in the case of pure $LiFePO_4$.

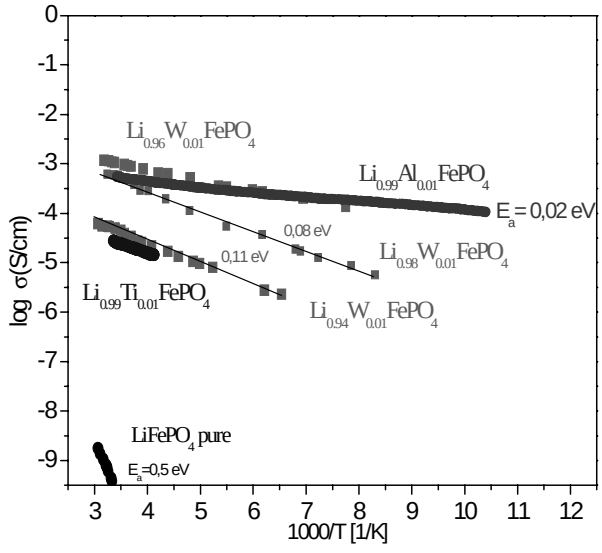

Fig. 2. Electrical conductivity of the pristine phospho-olivine samples and doped with W^{6+}, Ti^{4+} and Al^{3+}

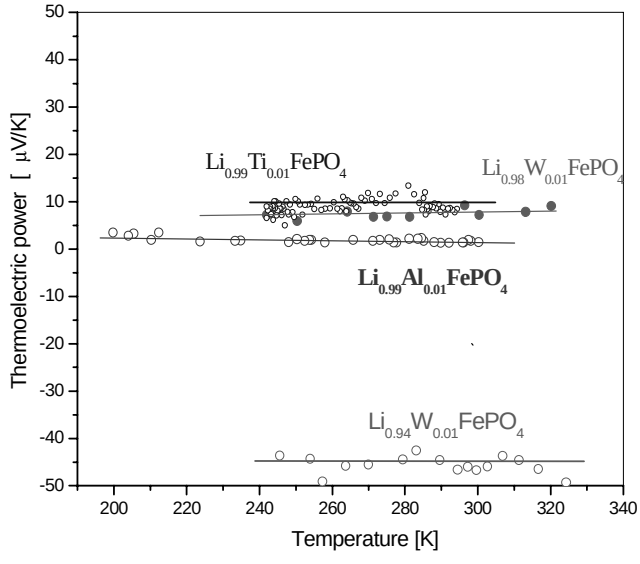

Fig. 3. Thermoelectric power measurements of the phospho-olivine samples doped with W^{6+}, Ti^{4+} and Al^{3+}

Results obtained by Nazar et al. [9], who by using a specific synthesis route arrived at phospho-olivine samples with lithium deficit $Li_{1-x}FePO_4$ and also stoichiometric $LiFePO_4$ with metallic-type conductivity, give strong arguments against the hypothesis about dopant atoms contributing to bulk metallic conductivity. Even if it is assumed that the obtained stoichiometric samples have a slight lithium

deficit, and consequently a mixed valency of iron, the presence of the Fe^{2+}–Fe^{3+} pair cannot account for the observed high electronic conductivity, since the iron–iron distance (~4 Å) in the olivine structure is too large. In numerous M–O oxides, metallic-type conductivity appears when the M–M distances are smaller than 3 Å. Therefore, what is the reason for the observed increase in conductivity by as much as seven orders of magnitude? Two possibilities should be considered: the appearance of conductive paths formed by residual carbon from the organic precursors used in synthesis, or by iron phosphides on phosphate grains. Traces of iron phosphides (estimated as ~4%) were observed by surface sensitive CEMS [11] or TEM [9]. Such a composite material consists of highly resistive grains and conductive surface of grains lined with iron phosphides, which play the role of conductive paths within the whole sample. The origin of iron phosphides on the surface of grains may be associated with the presence of internal reducing agents such as Fe, $Fe_x(CO)_y$, C, CO, and NH_3, which are released during synthesis from substrates such as $FeC_2O_4 \times H_2O$, $NH_4H_2PO_4$, and Li_2CO_3. As a result, a partial reduction of phosphates to phosphides may take place. For this reason, the real influence of the dopant seems to be restricted only to the assumed lithium deficit of the doped compound, which leads to the presence of the Fe^{2+}/Fe^{3+} redox couple, which in turn catalyses the reduction of $LiFePO_4$ to Fe_2P and forms a thin conductive layer over the sample.

Investigations aimed at improving the transport properties of phospho-olivine [12] indicate that the desired electronic-ionic mixed conductivity can be achieved by substituting a different transition metal for iron, generating a transfer of electrons from one ion to another. As an illustration, Mn^{+2} ($3d^5$) in Fe^{+2} ($3d^6$) sites in phospho-olivine $LiFe_{0.4}Mn_{0.6}PO_4$ introduces 0.6 moles of holes localized on manganese, and activates electronic conductivity through charge transfer between Fe and Mn. Charge transport becomes easier owing to the markedly increased concentration of effective carriers, whereas the Fe–Mn distance in $Li_xFe_{0.4}Mn_{0.6}PO_4$ remains the same as the Fe–Fe distance in $LiFePO_4$, i.e. 4 Å. Pure $LiFePO_4$, with all iron ions at the oxidation state Fe^{+2}, is an insulator. Charge carriers are created by lithium nonstoichiometry, which produces Fe^{3+} (electron holes), their concentration being, however, as low as 0.001 moles. It has been stated that at a composition of $Li_xFe_{0.4}Mn_{0.6}PO_4$ lithium deintercalation proceeds according to a diffusional mechanism. Similar observations have been reported by Yamada [10] for the chemical delithiation of phospho-olivine. This problem is discussed thoroughly in Refs. [11] and [12].

4. Conclusions

In the case of the discussed phospho-olivine cathode material, the formation of phosphides on grain surfaces during synthesis can be regarded as an *in situ* formation of a composite material.

Acknowledgement

The work is supported by the Polish Committee Scientific Research under the grant 4T08A 020 25. Author would like to thank Dr. M. Dudek for the results on $Li_xW_yPO_4$ samples.

References

[1] MOLENDA J., *Electronic structure in relation to the reactivity nonstoichiometric A_xMX_2 layered compounds*, Phys. Stat. Sol. (b), 165 (1991), 419.
[2] MOLENDA J., MARZEC J., SWIERCZEK K., OJCZYK W., ZIEMNICKI M., MOLENDA M., DROZDEK M., DZIEMBAJ R., Solid State Ionics, 171 (2004), 215.
[3] PAULING L., *The nature of the Chemical Bond*, Cornell University Press, Ithaca, NY (1960).
[4] PADHI A.K., NANJUNDASWAMY K.S., MASQUELIER C., OKADA S., GOODENOUGH J.B., J. Electrochem. Soc., 144 (1997), 1609.
[5] GOODENOUGH J.B., [in:] *Lithium Ion Batteries*, M. Wakihara, O. Yamamoto (Eds.), Chap. I, Kodansha, Tokyo (1998).
[6] YANG S., SONG Y., ZAVALIJ P.Y., WHITTINGHAM M.S., Electrochemistry Comm., 4 (2002), 239.
[7] CHUNG S.-Y., BLOKING J.T., CHIANG Y.-M., Nature Mater., 1 (2002), 123.
[8] MOTT N.F., DAVIS E.A., *Electron Processes in Non-Crystalline Materials*, Clarendon Press, Oxford 1979.
[9] HERLE P.S., ELLIS B., COOMBS N., NAZAR L.F., Nature Mater., 3 (2004), 147.
[10] YAMADA A., KUDO Y., LIU K.-Y., J. Electrochem. Soc., 148 (2001), A747.
[11] MARZEC J., OJCZYK W., MOLENDA J., Mater. Sci.-Poland, 24 (2006), 69.
[12] OJCZYK W., MARZEC J., DYGAS J., KROK F., RU- SHI LIU, MOLENDA J. Mater. Sci.-Poland, 24 (2006), 103.

Received 10 December 2004
Revised 17 February 2005

Materials Science-Poland, Vol. 24, No. 1, 2006

Delithiation of olivine – structured $LiFe_xMn_{1-x}PO_4$ cathode materials. Mössbauer studies

J. MARZEC*, W. OJCZYK, J. MOLENDA

AGH University of Science and Technology,
Faculty of Materials Science and Ceramics, al. Mickiewicza 30, 30-059 Cracow, Poland

This paper presents the results of applying the ^{57}Fe Mössbauer effect technique to studies of the delithiation mechanism of $Li_xMn_{0.55}Fe_{0.45}PO_4$ olivine samples, and also investigations of the origin of the widely discussed, astonishing high electronic conductivity of tungsten-doped $LiFePO_4$ samples, providing evidence of the presence of a residual, iron-containing and highly conductive phase. The delithiation process is perceived by iron ions as a change of their valence and symmetry of the local surroundings upon lithium extraction. The $Li_xMn_{0.55}Fe_{0.45}PO_4$ compound, which belongs to a novel group of cathode materials for Li-ion batteries, exhibits a single-phase deintercalation region, in contrast to $LiFePO_4$ exhibiting two-phase mechanism of electrochemical lithium extraction/insertion in the entire lithium concentration range, as well as to $LiMnPO_4$, for which the deintercalation process is practically irreversible. The range of deintercalation mechanism in $Li_xMn_{0.55}Fe_{0.45}PO_4$ was found to be exactly related to the content of Fe^{2+} ions in the cathode material. A surface sensitive technique, Conversion Electron Mössbauer Spectroscopy (CEMS), was used to prove the presence of traces of iron phosphides on the grain surfaces of tungsten-doped $LiFePO_4$ samples, pointing to the minor phase as being responsible for the high electronic conductivity of these samples.

Key words: *$LiMn_yFe_{1-y}PO_4$; lithium deintercalation; cathode material for lithium cells; Mössbauer spectroscopy*

1. Introduction

$LiFePO_4$ belongs to the group of $LiFeXO_4$ compounds containing large polyanions $(XO_4)^{y-}$ (where X = S, P, As, Mo, W; y = 2 or 3) and has been pointed out already by Goodenough [1, 2] as a promising cathode material for Li-ion batteries. The novel, olivine structured $LiFePO_4$-based group of cathode materials are stable, environmentally benign, and of potentially high stored energy density, but with one serious drawback – insulating properties (electrical conductivity of the order of 10^{-10} S/cm. Advantageous

*Corresponding author, e-mail: jotem@uci.agh.edu.pl

operational parameters of a Li-ion battery such as achievable high current density or a fast and fully reversible charge process, require an electronically conductive cathode material. Therefore, efforts have been concentrated on a significant improvement of its conductivity by a selective substitution of Li or Fe in $LiFePO_4$ with other metals. The goal is to overcome the limitations caused by electronic structure and its limiting influence on the transport properties of cathode materials.

The extraction of lithium from $LiFePO_4$ or $LiMnPO_4$ in the charging process of a lithium cell leads to the coexistence of two phases: one with an unchanged initial composition and another with zero lithium content [3, 4]. Moreover, in the case of $LiMnPO_4$, the process is almost irreversible. Substitution of Fe with Mn, yielding $LiMn_yFe_{1-y}PO_4$, substantially changes the nature of the lithium extraction process [5, 6]. For some compositions y, the initial delithiation process ($x = 1$ down to y) commences according to the deintercalation mechanism (related to $Fe^{2+} \rightarrow Fe^{3+}$ oxidation):

$$LiMn_yFe_{1-y}PO_4 - xLi^+ - xe^- \rightarrow Li_{1-x}Mn_yFe_{1-y}PO_4 \quad (1)$$

which means that a single-phase cathode material is observed with homogenous, gradually falling lithium content. A further lithium extraction ($0 < 1 - x < y$), related to subsequent $Mn^{2+} \rightarrow Mn^{3+}$ oxidation and accompanied by a 0.5 V voltage rise in the charge curve, leads to a two-phase system:

$$Li_yMn_yFe_{1-y}PO_4 - xLi^+ - xe^- \rightarrow x/y\ Mn_yFe_{1-y}PO_4 + (y - x)/y\ Li_yMn_yFe_{1-y}PO_4 \quad (2)$$

This phenomenon was observed by Yamada et al. [5] who used a chemical method for lithium extraction from $LiMn_yFe_{1-y}PO_4$.

In this work, the results of ^{57}Fe Mössbauer spectroscopy performed on samples obtained by electrochemical lithium extraction in $Li/Li^+/Li_xMn_{0.55}Fe_{0.45}PO_4$ cells are presented, as are the CEMS results obtained for tungsten-doped and pristine $LiFePO_4$ samples.

2. Experimental details

The $LiMn_{0.55}Fe_{0.45}PO_4$ samples were synthesized by a high-temperature (750 °C) reaction from Li_2CO_3, $MnCO_3$, $FeC_2O_4 \cdot 2H_2O$ and $NH_4H_2PO_4$; the samples were XRD-confirmed to be single-phase with an orthorhombic olivine structure (*Pmna*). The substitution of smaller Fe^{2+} ions by larger Mn^{2+} ions leads to an evident increase of all cell parameters.

The tungsten-doped samples were obtained by high-temperature solid-state reaction of Li_2CO_3, $FeC_2O_4 \cdot 2H_2O$, $NH_4H_2PO_4$, and H_2WO_4 under a flow of purified argon.

The lithium-deficient $Li_xMn_{0.55}Fe_{0.45}PO_4$ samples were obtained by the electrochemical extraction of lithium in $Li/Li^+/Li_xMn_{0.55}Fe_{0.45}PO_4$ cells with a lithium metal anode, Selectipur LP71 electrolyte (EC:DEC:DMC 1:1:1, 1M $LiPF_6$, from Merck),

and composite cathode material. Due to the high resistance (> 10^7 Ω/cm) of the cathode material samples, an electronically conductive additive (graphite) was required to assure proper cell operation. The added graphite formed a highly electronically conductive matrix, in which low-conductive grains of $LiMn_{0.55}Fe_{0.45}PO_4$ were sited.

In the case of the $LiMn_{0.55}Fe_{0.45}FePO_4$ materials, the Mössbauer effect measurements were performed at 300 K with a spectrometer working in constant acceleration mode in transmission geometry with a ^{57}Co(Rh) source. The Conversion Electron Mössbauer Spectroscopy (CEMS) measurements for tungsten-doped $LiFePO_4$ samples were done with a ^{57}Co(Cr) source. The presented isomer shifts are given relative to the sources. The effect is set to be 100% for the background CEMS spectra as commonly done for the sake of comparing with transmission spectra.

3. Results and discussion

$Li_xMn_{0.55}Fe_{0.45}PO_4$. Figure 1 presents the OCV curve of the $Li/Li^+/Li_xMn_{0.55}Fe_{0.45}PO_4$ cell. The accompanying OCV curves of the $Li/Li^+/Li_xMnPO_4$ and $Li/Li^+/Li_xFePO_4$ cells are shown for comparison. The jump in the OCV curve for the $Li_{0.55}Mn_{0.55}Fe_{0.45}PO_4$ cathode material can be ascribed to the difference in redox potentials between Fe^{2+}/Fe^{3+} (~3.5V) and Mn^{2+}/Mn^{3+} (~4.0V) [1]. The lower voltage range reflects the iron content of $LiMn_yFe_{1-y}PO_4$, while the higher one corresponds to the manganese concentration. The dashed vertical line positioned at x_{Li} = 0.55 separates sections where iron and manganese ions are oxidized.

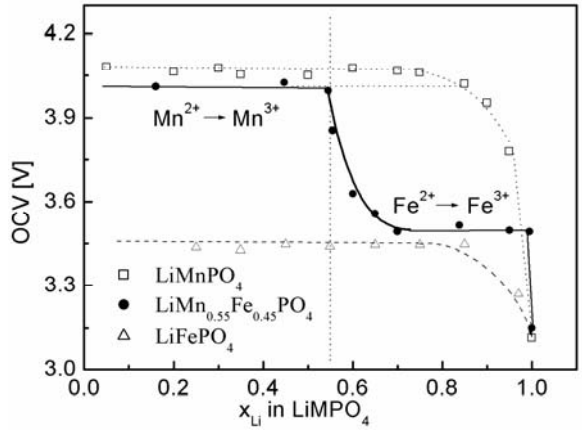

Fig. 1. OCV curves of $Li/Li^+/Li_xMnPO_4$, $Li/Li^+/Li_xMn_{0.55}Fe_{0.45}PO_4$ and $Li/Li^+/Li_xFePO_4$ cells. The dashed vertical line placed at x_{Li} = 0.55 separates regions where iron and manganese ions are oxidized in the $Li/Li^+/Li_xMn_{0.55}Fe_{0.45}PO_4$ cell. The lines connecting points are only to guide the eyes

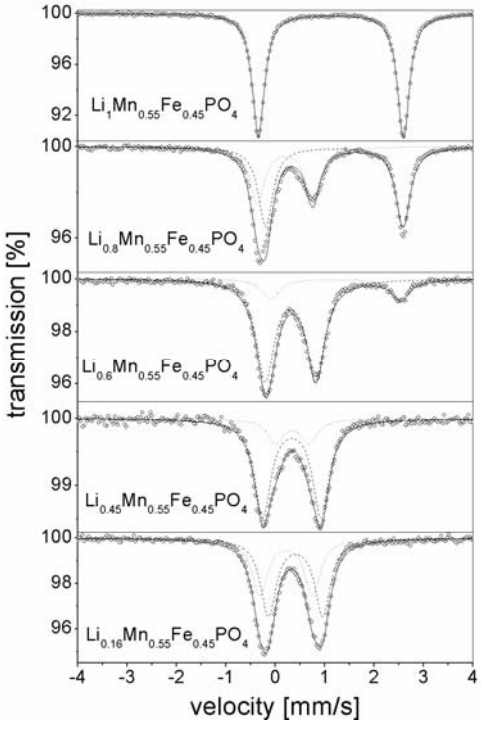

Fig. 2. Mössbauer spectra of $Li_xMn_{0.55}Fe_{0.45}PO_4$ samples obtained by deintercalation in a $Li/Li^+/Li_xMn_{0.55}Fe_{0.45}PO_4$ cell. The dashed lines represent the fitted components (quadruple doublets), while the solid lines are their sums

In the case of the starting $LiMn_{0.55}Fe_{0.45}FePO_4$ cathode material, only one quadruple doublet with a natural linewidth, originating from a single-valence state of iron (Fe^{2+}) occupying a unique crystallographic site, was necessary to fit the observed absorption pattern in the Mössbauer transmission spectrum (Fig. 2). For the subsequent electrochemically deintercalated samples, $Li_xMn_{0.55}Fe_{0.45}FePO_4$, the spectra were unambiguously fitted with two doublets with different isomer shifts (IS) and quadruple splittings (QS), indicating the presence of Fe^{2+} and Fe^{3+} ions with a relative ratio r varying with and matching the lithium content x ($r = x - 0.55/0.55$, $1 \geq x \geq 0.55$). As expected, the spectrum of $Li_{0.45}Mn_{0.55}Fe_{0.45}FePO_4$ consists of components originating only from Fe^{3+}, as at this stage only Fe^{3+} ions are present in the sample. Further deintercalation results in a successive oxidation of Mn^{2+} and, as a consequence, changes in the local symmetry of the iron site, which is confirmed by an increasing quadruple split of the doublets in the Mössbauer absorption pattern.

$Li_{0.98}W_{0.01}FePO_4$. Metallic conductivity of $LiFePO_4$ achieved by doping [7] has attracted great attention and intensified studies on the influence of dopants on the electrical conductivity of this material. Some following attempts of this substitution reported in literature [8], however, yield unclear results due to the observed negligible and rather random influence of the dopant type and its concentration on conductivity. One of the possible explanations of the observed increase in conductivity considers the formation of a nano-sized, conductive path, created by iron phosphides on the phosphate grains.

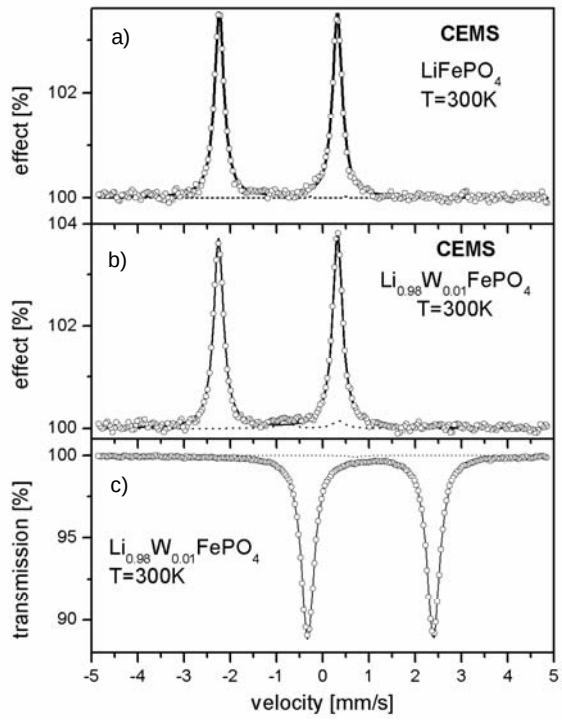

Fig. 3. CEMS spectra of pristine $LiFePO_4$ (a) and tungsten-doped $Li_{0.98}W_{0.01}FePO_4$ samples (b), together with a classical, "transmission" spectrum of the same doped sample (c)

In the case of the tungsten-doped $Li_{0.98}W_{0.01}FePO_4$ sample, which is found to be electronically conductive, only one quadruple splitted (QS) doublet, originating from a single valence state of iron (Fe^{2+}), was necessary to fit the observed absorption pattern in the transmission spectra (Fig. 3c). The CEMS technique, however, being a rather "surface sensitive" method, yields a slightly asymmetric pattern for the same sample (Fig. 3b), which was unambiguously fitted with two doublets with different isomer shifts (IS) and quadruple splittings (QS), indicating the presence of another phase containing iron. The isomer shifts of the component point to Fe_2P as the supplementary phase. A comparison of the relative contributions to the spectra enables the estimation of the content of the minor phase at a 4% level. A similar CEMS measurement, but carried out for an undoped and non-conductive $LiFePO_4$ sample (Fig. 3a), exhibits a symmetrical spectrum, and an attempt to fit it with two components, as in the previous case, fails since the second component vanishes. Therefore, the high conductivity of doped $LiFePO_4$ samples should be ascribed to the formation on a surface iron phosphide layer, which creates a conductive path over the whole sample. The iron phosphide on the surface of the grains may originate from the presence of internal reducing agents, since during the synthesis process species like Fe, $Fe_x(CO)_y$, C, CO and NH_3 are released. For this reason, the real influence of the

dopant seems to restrict only to the assumed lithium deficiency during the synthesis of the doped compound, which leads to the presence of a Fe^{2+}/Fe^{3+} redox couple, catalysing the reduction of $LiFePO_4$ into Fe_2P and forming a thin conductive layer over the sample.

4. Conclusions

Among a large number of papers devoted to the novel phospho-olivine cathode materials, only few [5, 6] take advantage of Mössbauer spectroscopy, which enables the direct and quantitative observation of the Fe^{3+}/Fe^{2+} pair in the $Li_xMn_{0.55}Fe_{0.45}PO_4$ cathode material upon lithium deintercalation and its variation with changing lithium content. The measured spectra yield information on the valence states of iron atoms and on the variation in the symmetry of their local surroundings.

In the case of the tungsten-doped $Li_{0.98}W_{0.01}FePO_4$ sample, the spectra obtained by CEMS prove the presence (4%) of another phase (Fe_2P) containing iron. Since an analogous measurement carried out for the undoped (and non-conductive) $LiFePO_4$ sample indicates no presence of the foreign phase, the high conductivity of doped $LiFePO_4$ samples should be ascribed to occurrence of a highly conductive phase on the surface of $LiFePO_4$ grains.

Acknowledgment

The work was supported by the Polish Committee for Scientific Research, under grant 4T08A 020 25.

References

[1] GOODENOUGH J.B., [in:] *Lithium Ion Batteries*, Chapt. I, M. Wakihara, O. Yamamoto (Eds.), Kodansha, Tokyo, 1998.
[2] PADLI A.K., NANJUNDASWAMY K.S., GOODENOUGHT J.B., J. Electrochem. Soc., 144 (1997), 1188.
[3] LI G., AZUMA H., TOHDA M., Electrochem. Solid-State Letters, 5 (2002), A135.
[4] PADLI A.K., NANJUNDASWAMY K.S., MASQUELIER C., OKADA S., GOODENOUGH J.B., J. Electrochem. Soc., 144 (1997), 1609.
[5] YAMADA A., KUDO Y., K.-Y. K.-Y., J. Electrochem. Soc., 148 (2001), A747.
[6] YAMADA A., KUDO Y., CHUNG S.CH., J. Electrochem. Soc., 148 (2001), A960.
[7] CHUNG S.-Y., BLOKING J.T., CHIANG Y.-M., Nature Mater., 1 (2002), 123.
[8] HERLE P.S., ELLIS B., COOMBS N., NAZAR L.F., Nature Mater., 3 (2004), 147.

Received 10 December 2004
Revised 17 February 2005

Materials Science-Poland, Vol. 24, No. 1, 2006

Transport and electrochemical properties of orthorhombic $LiMnO_2$ cathode material for Li-ion batteries

J. MOLENDA[1*], M. ZIEMNICKI[1], M. MOLENDA[2], M. BUĆKO[1], J. MARZEC[1]

[1]Faculty of Materials Science and Ceramics, AGH University of Science and Technology, al. Mickiewicza 30, 30-059 Cracow, Poland

[2]Jagiellonian University, Faculty of Chemistry, ul. Ingardena 3, 30-060 Cracow, Poland

The aim of this paper was to determine the temperature range of thermal stability of orthorhombic $LiMnO_2$, together with its electrical and electrochemical characterization. High-temperature studies of the electrical properties of orthorhombic $LiMnO_2$ point to structural instability of the phase at temperatures over 400 °C. Annealing above 400 °C leads to its decomposition into a two-phase mixture (Li_2MnO_3 + $LiMn_2O_4$). Stoichiometric $LiMnO_2$ has a very low conductivity at room temperature, which limits the effectiveness of intercalation at the initial stage. The temperature dependences of the electrical conductivity and thermoelectric power of deintercalated Li_yMnO_2 samples indicate a dominant electronic conductivity over the ionic one. A remarkable increase in electronic conductivity accompanied by a drop of activation energies is observed upon deintercalation. It was shown that the deintercalation of lithium from Li_yMnO_2 makes the structure less stable, leading to a two-phase mixture (Li_zMnO_2 + $Li_xMn_2O_4$).

Key words: *orthorhombic $LiMnO_2$; thermal stability; electrical properties; intercalation; Li-ion battery*

1. Introduction

The present technology of Li-ion batteries is based on $LiCoO_2$ oxide. Manganese oxide, $LiMnO_2$, with its higher capacity (280 mAh/g), lower price, and environmental friendliness, seems to be an attractive alternative cathode material. This material, however, is structurally unstable, which implies insufficient cyclability of manganese oxide-based batteries. There have been numerous attempts to improve its structural stability by manganese substitution with iron or nickel $LiM_xMn_{1-x}O_2$ (M = Fe, Ni) [1, 2]. The studies were limited to the determination of lattice parameters and electrochemical

*Corresponding author, e-mail: molenda@uci.agh.edu.pl

characteristics. Transport properties of manganese oxide are not sufficiently known, even though they determine to a great extent functional properties of the cathode material. The first aim of this work was to examine structural and electrical properties of $LiMnO_2$ over a wide temperature range, 230–1070 K, as well as changes in these properties upon lithium deintercalation. The other aim was to find a relationship between the electronic properties of the material and its electrochemical behaviour.

2. Experimental

CH_3COOLi and $(CH_3COO)_2Mn{\cdot}4H_2O$ were used as precursors. The substrates in stoichiometric proportions were dissolved in deionised water. The solution was alkalised by dropwise addition of the concentrated ammonia (25%); the amount of ammonia was sufficient for complete precipitation of manganese(II) hydroxide. After condensation, the obtained sol was dried at 90 °C to yield a xerogel, which was subsequently calcined in air, in the temperature range of 250–300 °C, for 24 h. The brownish-black product was powdered, again calcined in argon at 850 °C for 20 h and quenched in order to preserve the structure stable at high temperatures. The calcination parameters (temperature and the composition of the gas atmosphere) were established on the basis of thermogravimetric studies [3].

The structure of the obtained materials was determined using a PHILIPS X'pert X-ray diffractometer (Cu monochromatic radiation, ICDD data base). The electrical conductivity and thermoelectric power were measured at 230–350 K in vacuum. A four-probe AC method was used in the conductivity measurements, and a dynamic method in the thermoelectric power measurements.

The high-temperature measurements of electrical conductivity were performed in air and in argon, using the same methods as mentioned above. The electrochemical behaviour of $LiMnO_2$ was studied with a $Li\,|\,Li^+\,|\,Li_yMnO_2$-type cell using a Kest electronics 32K electrochemical amperostat.

3. Results and discussion

The specimens of $LiMnO_2$ obtained by quenching the high-temperature structure (see experimental) are single-phase and orthorhombic (Fig. 1). Figure 2 presents the electrical conductivity of $LiMnO_2$ in argon ($p_{O_2} = 10^{-5}$ atm) in the temperature range 150–800 ºC, measured in heating and cooling cycles. The variations of electrical conductivity are complex. Structural examination of specimens in the characteristic points of the conductivity hysteresis indicates that the orthorhombic structure is unstable at elevated temperatures. In the range 200 – 350 ºC, the orthorhombic phase is stable and its conductivity is thermally activated, the activation energy being 0.7 eV. At 350 ºC, the conductivity suddenly increases by three orders of magnitude, which is associated with the decomposition of $LiMnO_2$:

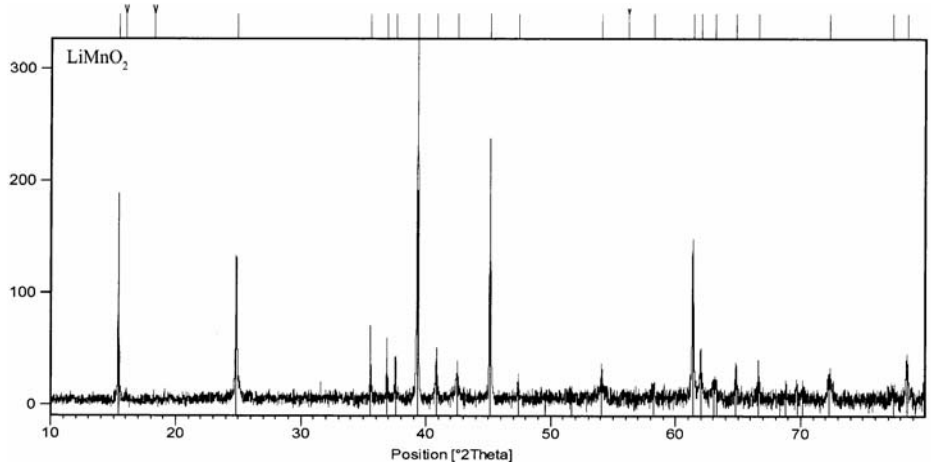

Fig. 1. XRD pattern of lithium manganese oxide $LiMnO_2$

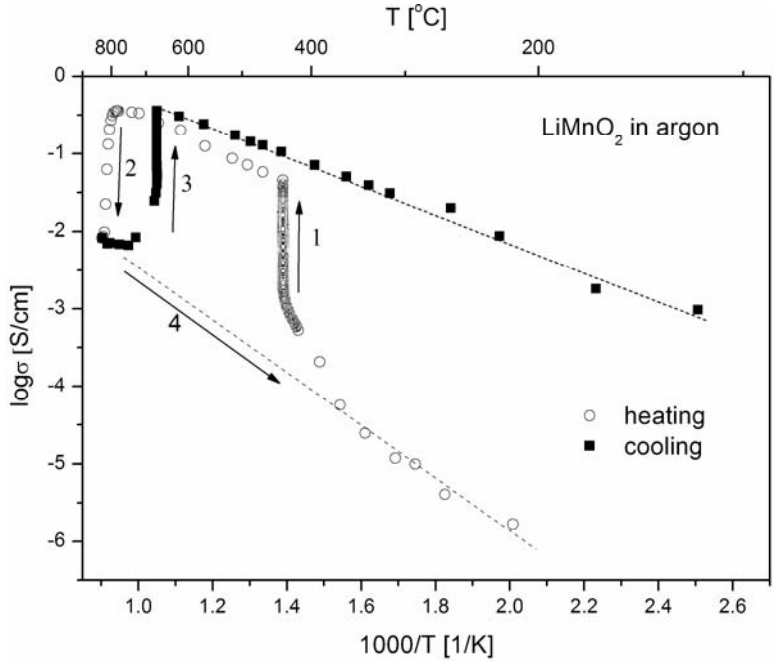

Fig. 2. High-temperature electrical conductivity of $LiMnO_2$ under argon atmosphere

$$3LiMnO_2 + 1/2O_2 = LiMn_2O_4 + Li_2MnO_3 \quad (1)$$

Higher conductivity of the spinel phase ($LiMn_2O_4$) is the reason for the observed significant conductivity increase (Fig. 2, arrow 1). The high conductivity of 10^{-1} $S \cdot cm^{-1}$ and the activation energy of conductivity of 0.1 eV, observed in the temperature range of 400–800 ºC, are characteristic of manganese spinel $LiMn_2O_4$ [4] (the conductivity

of Li_2MnO_3 is lower by several orders of magnitude). Manganese spinel, however, is not stable at 800 ºC and at low oxygen pressure (10^{-5} atm) [4], and reaction (1) proceeds to the left, which is reflected in a sudden drop of conductivity (arrow 2 in Fig. 2). This drop is related to the formation of $LiMnO_2$, the orthorhombic phase stable

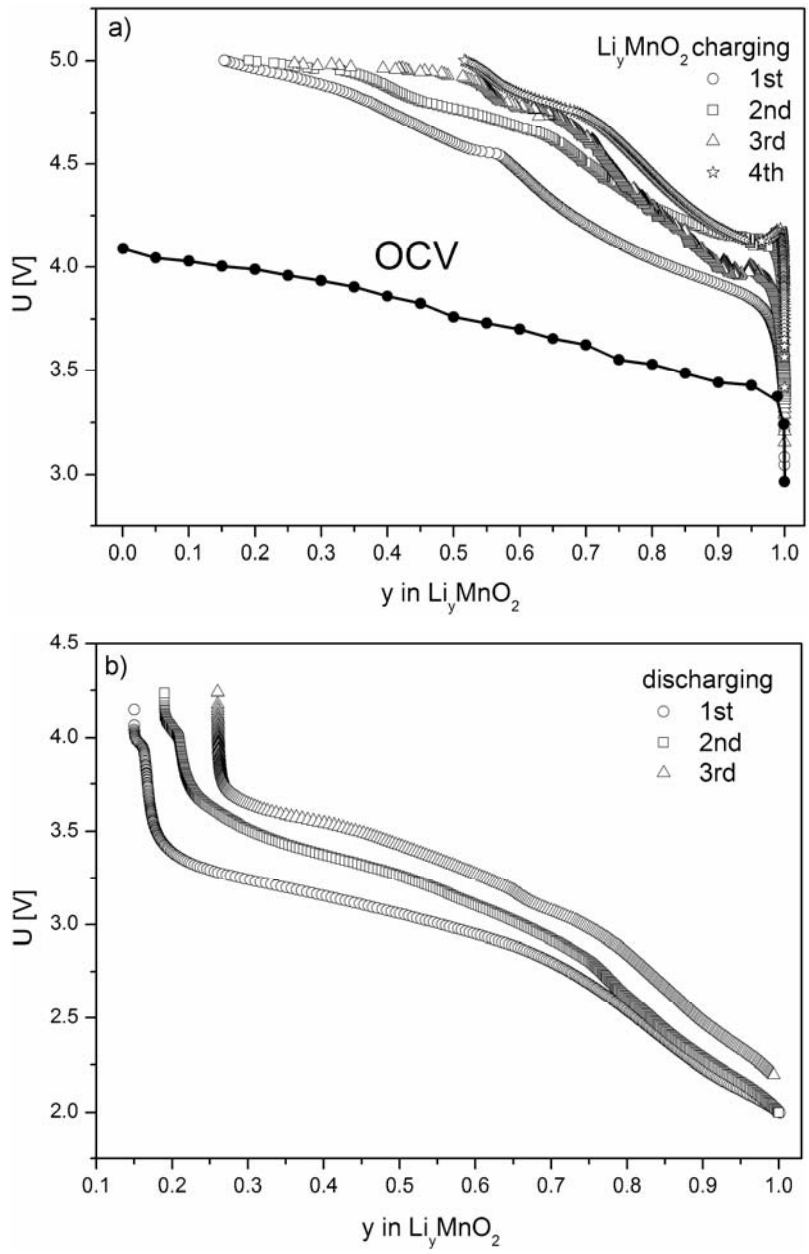

Fig. 3. The charge (a) and discharge (b) curves of the Li | Li^+ | Li_yMnO_2 cell

under these conditions, having much lower conductivity. Quenching of the orthorhombic phase causes the high-temperature structure to be preserved and the conductivity variations to follow arrow 4 in Fig. 2. Slow cooling of the high-temperature orthorhombic phase leads again to the decomposition of $LiMnO_2$ at about 650 ºC into manganese spinel $LiMn_2O_4$ and Li_2MnO_3 via reaction (1).

Figures 3a, b show the charge/discharge curves of a $Li \mid Li^+ \mid Li_yMnO_2$-type cell at the current density of 100 μA/cm^2. A comparison of the charge curve of the loaded cell with the corresponding OCV curve (Fig. 3a) indicates a significant resistivity of the cathode material Li_yMnO_2. It is worthwhile to note that the discharge curves shift toward higher voltages in consecutive cycles (Fig. 3b). Such behaviour can be explained by a gradual transformation of the orthorhombic $LiMnO_2$ into spinel, with a characteristic voltage of 4 V in a wide range of y_{Li}. X-ray studies confirm the increasing contribution of spinel with progressing lithium deintercalation [3]. This indicates that orthorhombic $LiMnO_2$, unstable at temperatures exceeding 350 ºC, is also not stable at room temperature, at which the deintercalation/intercalation of lithium takes place.

High resistivity of the cathode material Li_xMnO_2 implies a low chemical diffusion coefficient of lithium, estimated to be 10^{-9} cm^2/s (Fig. 4).

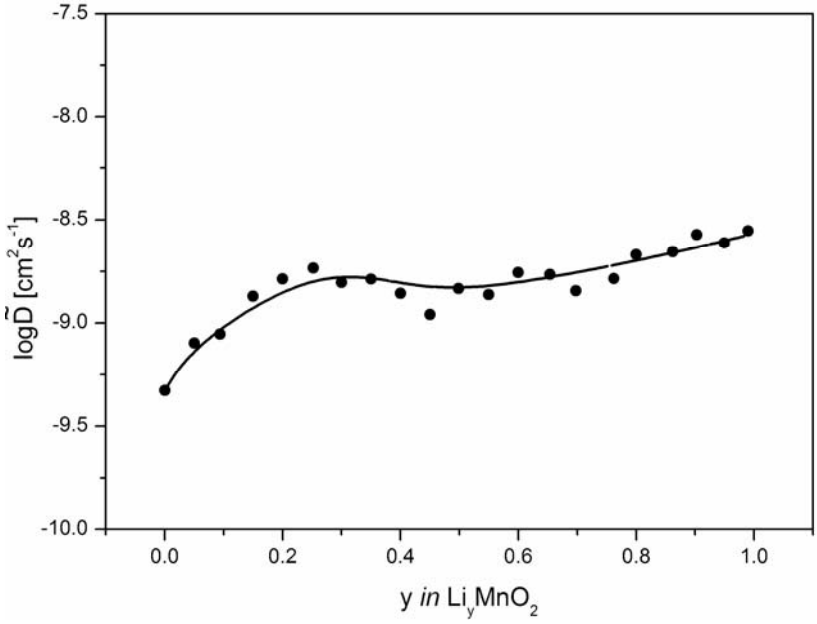

Fig. 4. Chemical diffusion coefficient of lithium in $LiMnO_2$ attained by GITT

Figures 5 and 6 demonstrate the temperature dependences of electrical conductivity and thermoelectric power for the starting compound, $LiMnO_2$, and after the stepwise deintercalation of lithium. Stoichiometric $LiMnO_2$ shows hardly measurable conductivity at room temperature. At 70 ºC, its conductivity is 10^{-8} S/cm and rapidly

increases during the deintercalation of lithium, reaching 10^{-5} S/cm at room temperature at a composition of $Li_{0.2}MnO_2$.

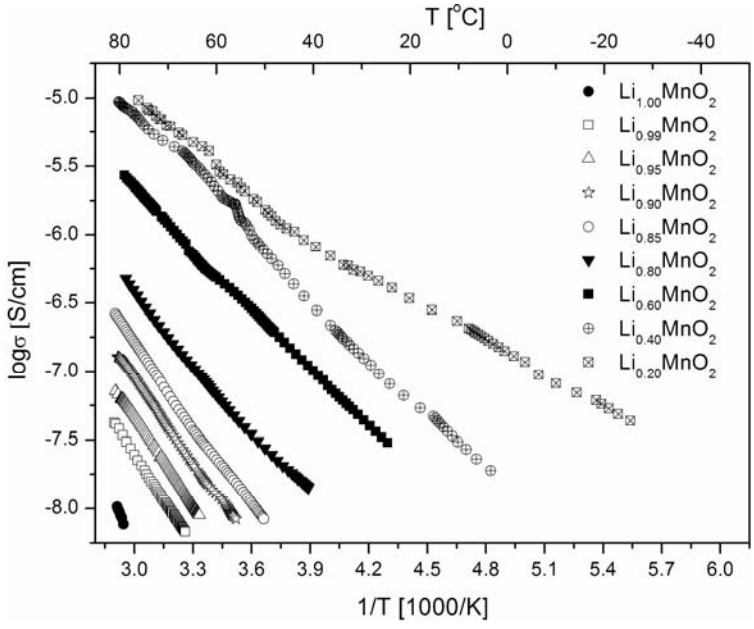

Fig. 5. Electrical conductivity of deintercalated Li_yMnO_2 samples

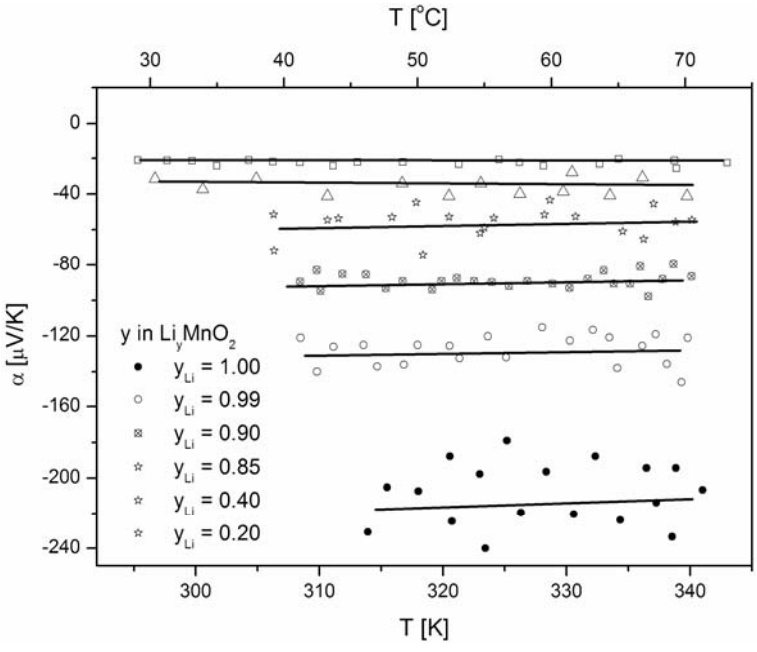

Fig. 6. Thermoelectric power of deintercalated Li_yMnO_2 samples

The activation energy of conductivity decreases in this process from 0.7eV for stoichiometric $LiMnO_2$ to 0.15 eV for $Li_{0.2}MnO_2$ (Fig. 7). The observed temperature characteristics of conductivity and thermoelectric power (Figs. 5 and 6), as well as the high-temperature dependence recorded in argon (Fig. 2) point to dominant electronic conductivity in $LiMnO_2$.

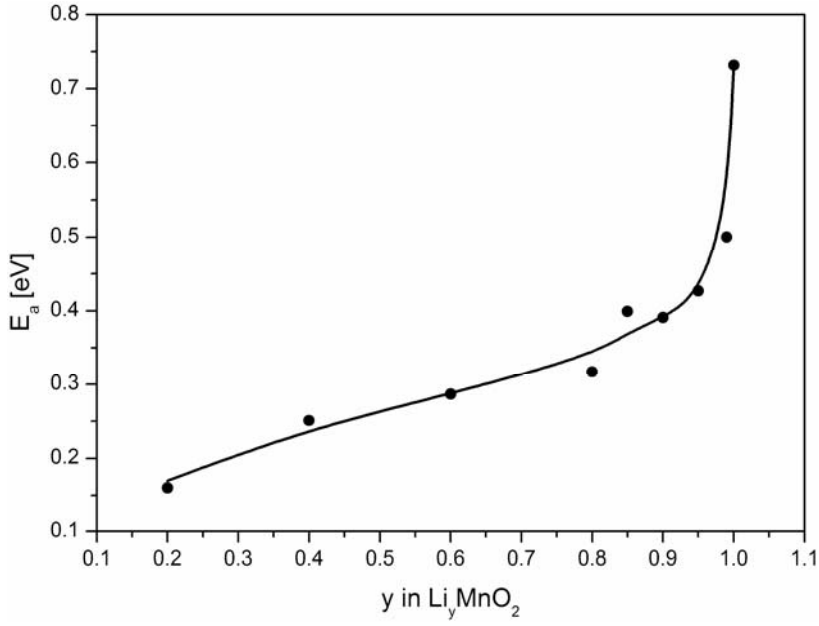

Fig. 7. Conductivity activation energy in deintercalated Li_yMnO_2

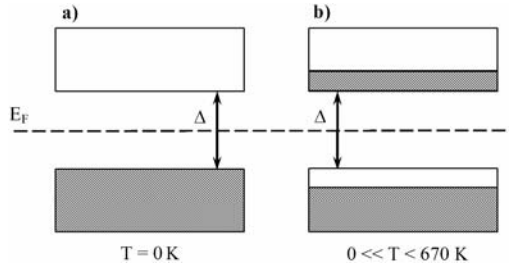

Fig. 8. The electronic structure of $LiMnO_2$ a) at 0 K, b) above 0 K

These results were useful in the elaboration of a qualitative model, which might explain the observed electrical and electrochemical properties. In stoichiometric $LiMnO_2$, a high-spin electron configuration (t_{2g}^3 e_g^1) is favoured. Due to strong interactions between electrons, the effective band e_g^1 splits into two sub-bands with opposite spins (Fig. 8). At 0 K, the lower band is completely filled and the upper one is empty (Fig. 8a). The number of carriers increases with temperature (electrons are generated in the upper sub-band and holes in the lower sub-band). An activation en-

ergy of conductivity of 0.7 eV determined for $LiMnO_2$ in the range of 200–350 ºC can be interpreted as the energy gap between the split sub-bands. An analysis of electrical properties of the deintercalated compound Li_yMnO_2 (Figs. 5 and 6) indicates that its electronic structure undergoes modifications at low temperatures (250–350 K). The energy gap becomes smaller, as a consequence of lattice parameter reduction during the deintercalation of lithium (a shortening of the Mn–Mn distance) [3] as is schematically drawn in Fig. 9. The variation in thermoelectric power (Fig. 6) in the direction of positive values with increasing deintercalation degree is consistent with the variation of conductivity (Fig. 5) in so far as the narrowing of the energy gap is concerned. Lack of temperature dependence for thermoelectric power at different compositions y_{Li} indicates that charge transport takes place simultaneously in both split sub-bands (holes in the lower sub-band and electrons in the upper sub-band, Fig. 9).

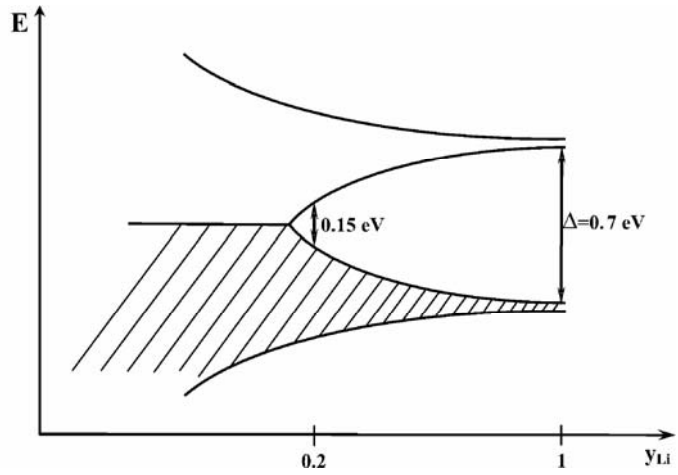

Fig. 9. Modification of the electronic structure of Li_yMnO_2 upon lithium deintercalation

The observed variation in the $Li^+ | Li_yMnO_2$ cathode potential (OCV curve in Fig. 3a) of about 0.7 V within the composition range $0.99 < y_{Li} < 0.05$, are quite complex. They can be associated with changes in the electrochemical potential of electrons (Fermi level) due to a decreasing concentration of electrons upon lithium deintercalation, and also with shifts in the Fermi level brought about by a shortening of the Mn–Mn distance in the Li_yMnO_2 structure (Fig. 9). A detailed analysis of correlations between the electronic and electrochemical properties calls for supplementary studies (e.g., XPS, UPS) and an extension of the composition range to lower values of y_{Li}.

Acknowledgements

This work was supported by the AGH Statutory Contract No. 11.11.160.109.

References

[1] CHEN C.J., GREENBLATT M., WASZCZAK J.V., J. Solid State Chem., 64 (1986), 24.
[2] WU Q., LI X., YAN M., JIANG Z., Electrochem. Commun., 5 (2003), 878.
[3] MOLENDA J. (in preparation).
[4] MOLENDA J., SWIERCZEK K., KUCZA W., MARZEC J., STOKŁOSA A., Solid State Ionics, 123 (1999), 155.

Received 12 November 2004
Revised 17 March 2005

Materials Science-Poland, Vol. 24, No. 1, 2006

Structural, thermal and electrical properties of lithium–manganese spinel with a sulphur-substituted oxygen sublattice

M. MOLENDA[1], R. DZIEMBAJ[1,2*], A. KOTWICA[1], W. ŁASOCHA[1]

[1]Faculty of Chemistry, Jagiellonian University, ul. Ingardena 3, 30-060 Cracow, Poland

[2]Regional Laboratory of Physicochemical Analyses and Structural Research, ul. Ingardena 3, 30-060 Cracow, Poland

Sulphur substituted $LiMn_2O_{4-y}S_y$ spinels were obtained using the sol-gel method followed by calcination at 300 °C. The crystallinity of the samples was improved by further calcination at 800 °C. The monophase system was formed up to $y = 0.20$. At higher sulphur concentrations an additional phase (Mn_2O_3) appeared. The sulphided spinels were thermally stable in air up to about 900 °C. They decomposed above this temperature, with the oxidation of sulphur to SO_2. The decomposition products, $LiMnO_2$ and Mn_3O_4, reacted during slow cooling and formed stoichiometric $LiMn_2O_4$. Sulphur substitution retarded the phase transition at room temperature, although a new one appeared at higher temperatures (540–580 °C). Such an effect does not exist in sulphur-free spinels.

Key words: *oxysulphide spinel; sol-gel method; Li-ion battery; thermal stability*

1. Introduction

Lithium–manganese spinels, due to their economical and environmental friendly properties, are still of interest for lithium-ion battery developers [1, 2]. In the last decade, a large number of papers have been devoted to Li–Mn–O spinel systems as new cathodes for Li-ion batteries. Such an electrode, however, exhibits capacity fading during cell cycling. This is usually related to the structural instability of the cathode material [1, 3]. Stoichiometric $LiMn_2O_4$ spinel shows a reversible low-temperature phase transition from a cubic (*Fd*3*m*) to an orthorhombic (*Fddd*) structure near room temperature [4]. This phase transition is related to the Jahn–Teller distortion of Mn^{3+} ions [5, 6]. Structural stabilisation may be achieved by partially substitution Mn^{3+} ions

*Corresponding author, e-mail: dziembaj@chemia.uj.edu.pl

by *3d* metal ions (Cr, Fe, Ni, Co) [7, 8], Al^{3+} [9] ions, or excess of Li^{+} ions [10, 11]. These modifications, however, result in a decrease of the Mn^{3+}/Mn^{4+} ratio due to the substitution and/or charge compensation of the crystal lattice. This causes a remarkable decrease in 4 V capacity. In a recent paper, we have stressed that the appearance of the low-temperature phase transition is restricted to high-spin Mn^{3+} ions at high symmetric octahedral sites O_h [12] and to specific charge ordering in the manganese sublattice [4, 13].

The aim of this paper is to show the influence of isoelectronic substitution in the oxygen sublattice by sulphur on the structural and thermal stability of lithium–manganese spinels. Yang-Kook Sun et al. have reported an improvement in the cycling properties for lithium–manganese spinels doped with aluminium and sulphur ($LiAl_xMn_{2-x}O_{4-y}S_y$) in the 4 V region even at elevated temperatures [14–16]. Additionally, they found that these materials were more stable and less soluble in electrolytes than stoichiometric $LiMn_2O_4$.

In the present paper, a series of sulphided lithium–manganese spinels were prepared by the sol-gel method. The obtained samples, $LiMn_2O_{4-y}S_y$ with different sulphur content, were studied using XRD, MS-TGA, and DSC in relation to their influence on electrical properties. The results are discussed with reference to the properties of stoichiometric $LiMn_2O_4$.

2. Experimental

A set of sulphided lithium–manganese spinels $LiMn_2O_{4-y}S_y$ ($0.09 \leq y \leq 0.5$) was prepared by a modified sol-gel method [17] using solutions of CH_3COOLi, $(CH_3COO)_2Mn$, $(NH_4)_2S$, and concentrated ammonia as the alkalising agent. The synthesis was performed under a constant argon flow to prevent uncontrolled oxidation of Mn^{2+} ions. Condensation of the formed sol was performed at 90 °C for 2 days, and then the obtained xerogel was decomposed in air for 24 h at 300 °C with a heating rate of 1 °C/min. The obtained residue was reground in an agate mortar, providing a brown-black powder. Additional high-temperature calcination (800 °C for 24 h in air), followed by quenching, was performed to obtain better crystallised samples. The nominal compositions and preparation conditions of the obtained samples are presented in Table 1.

The crystal structure of the samples was examined by X-Ray powder diffraction on a PW3710 Philips X'Pert apparatus using $CuK_{\alpha 1}$ radiation (λ = 0.154178 nm) with a graphite monochromator. The phase analysis of the XRD patterns was performed by the Rietveld method using PDF-2 standards and the DBWS-9411 software package [18].

MS-TGA experiments were performed in Mettler-Toledo 851^e microthermobalance in 150 μl open platinum crucibles under a flow of air (60ml/min) within the temperature range 30–1200–30 °C. Evolved gas analysis (EGA) was performed simultaneously by a joined on-line quadruple mass spectrometer (Thermostar-Balzers).

Table 1. Nominal composition and preparation conditions of the sulphided spinel samples

Sample	Nominal composition	Preparation
S 9	$LiMn_2O_{3.91}S_{0.09}$	sol-gel method, condensation and drying at 90 °C, 48 h, calcination in air at 300 °C for 24 h
S 20	$LiMn_2O_{3.8}S_{0.2}$	
S 30	$LiMn_2O_{3.7}S_{0.3}$	
S 40	$LiMn_2O_{3.6}S_{0.4}$	
S 50	$LiMn_2O_{3.5}S_{0.5}$	
QS 9	$LiMn_2O_{3.91}S_{0.09}$	sol-gel method, condensation and drying at 90 °C, 48 h, calcination in air at 300 °C for 24 h, recalcination in air at 800 °C for 24 h then quenching
QS 20	$LiMn_2O_{3.8}S_{0.2}$	
QS 30	$LiMn_2O_{3.7}S_{0.3}$	
QS 40	$LiMn_2O_{3.6}S_{0.4}$	
QS 50	$LiMn_2O_{3.5}S_{0.5}$	

DSC experiments were performed in a Mettler-Toledo 821^e calorimeter, equipped with a Haake intracooler, in 40 μl aluminium crucibles under the flow of argon (80 ml/min) within the temperature range from –40 to 60 °C.

Electrical conductivity was measured using a four-probe AC method at 33 Hz within the temperature range from –20 to 50 °C. To improve the electrical contact, a silver paste with acrylic resin was used.

3. Results and disscussion

Powder diffraction patterns of the obtained sulphided lithium–manganese spinels are presented in Figure 1. The diffraction peaks for the samples (S9, S30, and S50) calcined at 300 °C are broad and of low intensity, typical of defected spinels obtained at low temperatures [17]. Additional calcination at 800 °C provides much better crystallized samples, with narrower and more intensive XRD peaks.

In Table 2, the results of the phase analysis performed using the Rietveld method are presented. For the low-temperature samples, the best fit to XRD patterns was achieved using a two-phase system: spinel (*Fd*3*m*) and hausmannite – Mn_3O_4 (*I*4/*amd*). The amount of spinel phase decreases with increasing sulphur content, simultaneously the lattice constant *a* for this phase increases above the value for the sulphur-free
Li–Mn spinel ($Li_{0.96}Mn_{1.92}O_4$) obtained at 300 °C, namely a = 8.1731 Å [10]. This is in accordance with the substitution of oxygen by larger sulphur anions. Sample QS9 ($LiMn_2O_{3.91}S_{0.09}$) shows only the spinel phase XRD-peaks with the lattice constant a = 8.2630 Å. This value is much higher than that for stoichiometric $LiMn_2O_4$ (a = 8.2517 Å) [10].

Samples calcined at 800 ºC and containing larger amounts of sulphur (QS30 and QS50) showed XRD patterns that need a two-phase system for fitting, with spinel (*Fd*3*m*) and bixbyite (*Ia*3) phases. The amount of spinel phase decreases with increasing sulphur content. Additionally, the bixbyite phase (Mn_2O_3) shows another Li:Mn

stoichiometry, which causes the appearance of lithium excess in the spinel phase. Such a Li-rich spinel phase should reveal a lower lattice constant, which is in fact observed (Table 2). The same influence of lithium excess was previously observed for so called δ-spinels ($Li_{1+\delta}Mn_{2-\delta}O_4$) [10, 11]. For samples with the highest sulphur content (S30, QS30, S50, QS50), a small amount (less than 3%) of $Li_2SO_4 \cdot H_2O$ was observed (peaks around 21.5° and 25°). This is consistent with the mass lost due to dehydration, observed on TG curves (30–100 °C).

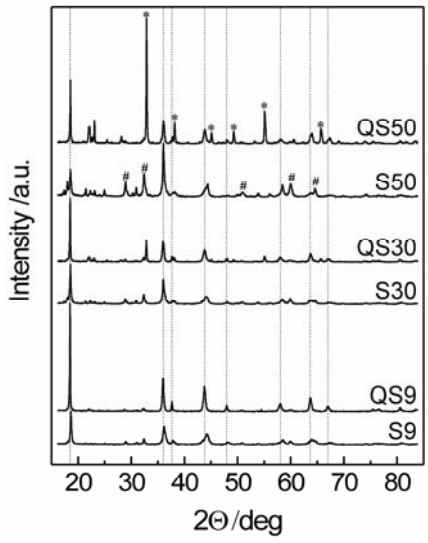

Fig. 1. XRD patterns of sulphided lithium–manganese spinels:
* – Mn_2O_3 bixbyite phase, # – Mn_3O_4 hausmannite phase

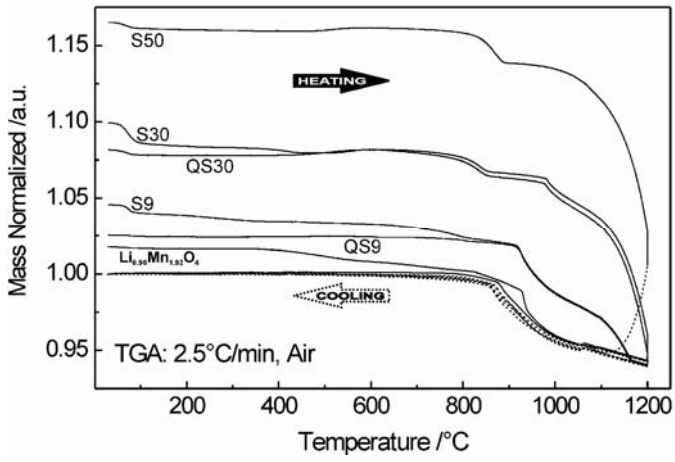

Fig. 2. Thermogravimetric analysis of sulphided lithium–manganese spinels

Table 2. Phase analysis of sulphided Li–Mn spinels

Sample	Nominal composition	Phase analysis
S 9	$LiMn_2O_{3.91}S_{0.09}$	76% spinel (a = 8.2136 Å) 24% hausmannite (a = 5.7573 Å, c = 9.4427 Å)
S 30	$LiMn_2O_{3.7}S_{0.3}$	54% spinel (a = 8.2272 Å) 46% hausmannite (a = 5.7615 Å, c = 9.4259 Å)
S 50	$LiMn_2O_{3.5}S_{0.5}$	29% spinel (a = 8.2356 Å) 71% hausmannite (a = 5.7640 Å, c = 9.4118 Å)
QS 9	$LiMn_2O_{3.91}S_{0.09}$	100% spinel (a = 8.2630 Å)
QS 30	$LiMn_2O_{3.7}S_{0.3}$	75% spinel (a = 8.2413 Å) 25% bixbyite (a = 9.4063 Å)
QS 50	$LiMn_2O_{3.5}S_{0.5}$	35% spinel (a = 8.2443 Å) 65% bixbyite (a = 9.4086 Å)

The results of thermogravimetric analysis (MS-TGA) are presented in Figure 2. The TG curves were recorded in dry air during heating up to 1200 °C and cooling to 30 °C. The TG curve for $Li_{0.96}Mn_{1.92}O_4$ has been added to compare with the curves for sulphur-free samples. Evolved gas analysis (EGA), performed simultaneously with TG measurements, proved that the sulphided spinel loses sulphur as SO_2 above 1000 °C (Fig. 3). The total process of the thermal decomposition of sulphided spinels, $LiMn_2O_{4-y}S_y$ (where $0 < y < 0.5$), may be described by following equation:

$$3LiMn_2O_{4-y}S_y + \left(\frac{9}{2}y - 1\right)O_2 \rightarrow 3LiMnO_2 + Mn_3O_4 + 3ySO_2\uparrow \qquad (1)$$

It should be stressed that the decomposition product reacts during slow cooling (2.5 °C/min) in air and forms the stoichiometric spinel phase ($LiMn_2O_4$).

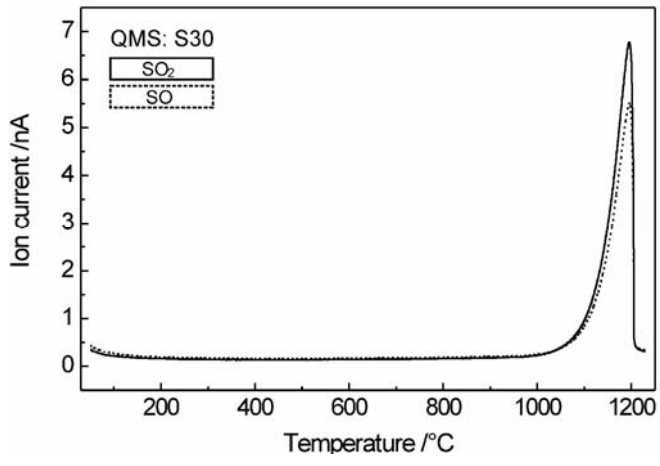

Fig. 3. EGA analysis of sample S30

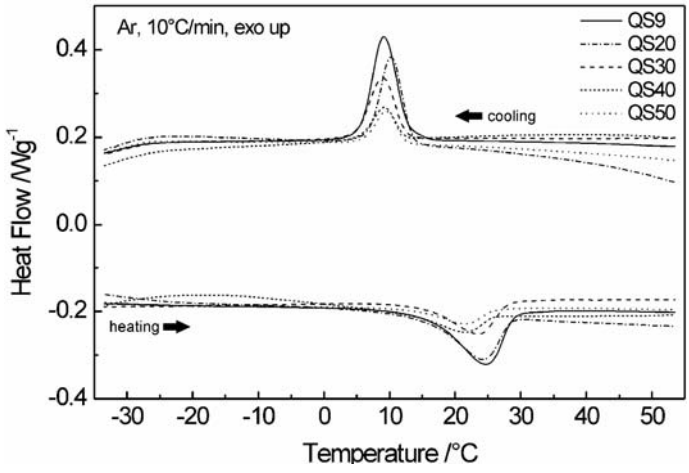

Fig. 4. DSC measurements of the QS-spinels from –30 to 50 °C

DSC measurements of QS samples near room temperature (from –30 to 50 °C) are presented in Figure 4. The thermal effects observed during cooling and heating on DSC curves are related to the phase transition from a cubic to orthorhombic structure. The measured enthalpies (ΔH) of this transformation for sulphided lithium –manganese spinels are collected in Table 3. The values are lower than that for the stoichiometric $LiMn_2O_4$, and they decrease with increasing sulphur concentration. This may suggest structural stabilisation owing to sulphur substitution.

Table 3. Enthalpies ΔH [J/g] of transformation for sulphided lithium–manganese spinel

Sample	Transition around	
	10–25 °C	540–580 °C
$LiMn_2O_4$	8.6	no heat effects
QS 9	6.5	7.0
QS 20	4.8	13.0
QS 30	3.9	24.3
QS 40	1.9	33.0
QS 50	1.7	42.1

The sulphided lithium–manganese spinels calcined at 800 °C reveal another reversible phase transition (with hysteresis about 40 °C) at very high temperatures, which was not observed for the sulphur-free $LiMn_2O_4$ phase (Fig. 5). The measured heat effects are collected in Table 3. This high temperature transformation intensifies with sulphur content. This is a first order phase transition, which needs additional XRD studies in order to explain its nature.

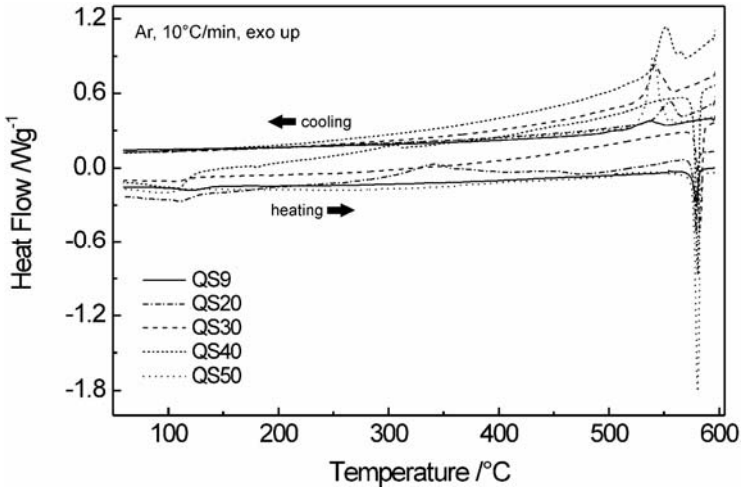

Fig. 5. DSC measurements of the QS-spinels within 25–600 °C

Measurements of the electrical conductivity of sulphided lithium–manganese spinels calcined at 800 °C are presented in Figure 6. The samples calcined at 300 °C reveal low electrical conductivity with a small activation energy (E_a = 0.13–0.28 eV, in the 10–40 °C temperature range). The calcination of these samples at 800 °C increases their electrical conductivity, but it is decreased with sulphur concentration, though the activation energy of electrical conductivity is slightly diminished (E_a = 0.24–0.30 eV, 10–40 °C). The activation energy for the stoichiometric $LiMnO_4$ is equal to 0.32 eV (10–40 °C). This may be explained by a strong distortion of the spinel network by sulphur substitution and in consequence lowering of Mn-Mn distances.

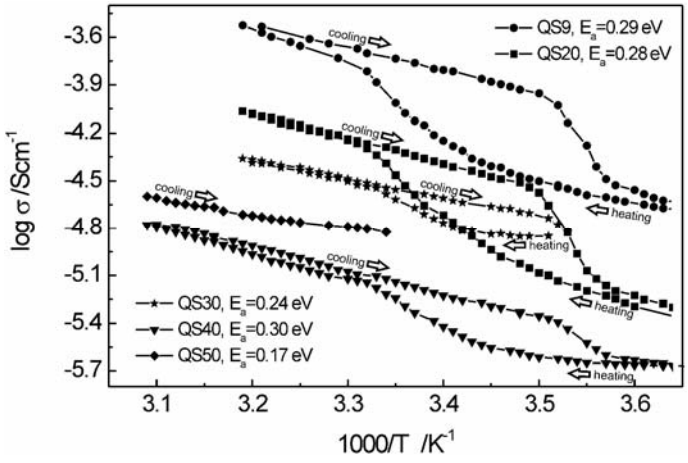

Fig. 6. Electrical conductivity of sulphided lithium–manganese spinels calcined at 800 °C

Data from electrical measurements suggest that the small polaron-conduction mechanism is preserved. The lowering of electrical conductivity with increasing sulphur concentration, which does not change the Mn^{3+}/Mn^{4+} ratio, is most probably caused by a decreasing number of effective carriers. This may suggest that effective electronic transport occurs only through manganese octahedra without sulphur substitution.

4. Conclusions

It is possible to obtain lithium–manganese spinels with partial sulphur substitution in an oxygen lattice. This can be effectively done using the sol-gel technique, followed by calcination at 800 °C in air. The single-phase material was obtained only for concentrations of sulphur less than 0.20 mole per spinel molecule.

The introduction of sulphur into the spinel lattice reduces the phase transition around room temperature, but another one appears at higher temperatures (540–580 °C). The explanation of the nature of the high-temperature transition demands further studies. The sulphided lithium–manganese spinels do not decompose up to 850 °C in air. Above this temperature, the spinels thermally decompose with the simultaneous oxidation of sulphur to SO_2.

The sulphur substitution of oxygen in the spinel lattice lowers electrical conductivity. Assuming the preservation of the small polaron mechanism, one may conclude that hopping is limited only to MnO_6 octahedra. The problem of cycling stability also requires additional studies.

Acknowledgements

The work is supported by the Polish Committee for Scientific Research under grant 3 T08D 010 28. One of the authors (M.M.) would like to acknowledge the Foundation for Polish Science for support in the form of The Annual Stipend for Young Scientists.

References

[1] TARASCON J.M., ARMAND M., Nature, 414 (2001), 359.
[2] WHITTINGHAM M.S., Solid State Ionics, 134 (2000), 169.
[3[AMATUCCI G.G., DU PASQUIER A., BLYR A., ZHENG T., TARASCON J.M., Electrochimica Acta, 5 (1999), 255.
[4] RODRIGUEZ-CARVAJAL J., ROUSSE G., MASQUELIER C., HERVIEU M., Phys. Rev. Lett., 81 (1998), 4660.
[5] YAMADA A., TANAKA M., Mat. Res. Bull., 30 (1995), 715.
[6] YAMADA A., TANAKA M., TANAKA K., SEKAI K., J. Power Sources, 81, 82 (1999), 73.
[7] WU Y.P., RAHM E., HOLZE R., Electrochim. Acta, 47 (2002), 3491.
[8] MOLENDA J., MARZEC J., SWIERCZEK K., OJCZYK W., ZIEMNICKI M., WILK P., MOLENDA M., DROZDEK M., DZIEMBAJ R., Solid State Ionics, 171 (2004), 215.
[9] CAPSONI D., BINI M., CHIODELL G., MASSAROTTI V., MUSTARELL P., LINATI L., MOZZATI M.C., AZZONI C.B., Sol. State Comm., 126 (2003), 169.

[10] DZIEMBAJ R., MOLENDA M., J. Power Sources, 119–121C (2003), 121.
[11] SWIERCZEK K., MARZEC J., MARZEC M., MOLENDA J., Solid State Ionics, 157 (2003), 89.
[12] MOLENDA M., DZIEMBAJ R., PODSTAWKA E., PRONIEWICZ L.M., J. Phys. Chem. Solids, 66 (2005), 1761.
[13] PISZORA P., J. Alloys and Compounds, 382 (2004), 112.
[14] SUN Y.K., JEON Y.S., Electrochem. Commun., 1 (1999), 597.
[15] PARK S.H., PARK K.S., SUN Y.K., NAHM K.S., J. Electrochem. Soc., 147 (2000), 2116.
[16] SUN Y.K., LEE Y.-S., YOSHIO M., Mat. Lett., 56 (2002), 418.
[17] DZIEMBAJ R., MOLENDA M., MAJDA D., WALAS S., Solid State Ionics, 157 (2003), 81.
[18] YOUNG R.A., DBWS-9411, Release 30.3.95, School of Physics, Georgia Institute of Technology, USA 1995.

Received 10 December 2004
Revised 13 March 2005

Materials Science-Poland, Vol. 24, No. 1, 2006

The effect of humidity on the electrical properties of Nasicon-type materials

A. IGNASZAK*, P. PASIERB, S. KOMORNICKI

AGH University of Science and Technology, Faculty of Materials Science and Ceramics,
al. Mickiewicza 30, 30-059 Cracow, Poland

Nasicon $Na_3Zr_2Si_2PO_{12}$ samples were prepared by coprecipitation and solid-state reaction. Both methods lead to materials consisting of monoclinic Nasicon phases with small admixtures of ZrO_2 or $ZrSiO_4$. The differences of their behaviours and stabilities in long-term ageing tests in humid atmospheres are discussed in terms of their microstructures. Model equivalent circuits are proposed to explain observed phenomena.

Key words: *Nasicon; relative humidity; impedance spectroscopy; microstructure*

1. Introduction

Nasicon-type (Na^+ Super Ionic Conductor) materials are known to exhibit high ionic conductivity and relatively high chemical stability. These materials have been proposed to be used as solid electrolytes in solid-state electrochemical cells such as gas sensors, ion sensors, and Na–S batteries [1–3]. The highest conductivities of Nasicon samples ($Na_{1+x}Zr_2Si_xP_{3-x}O_{12}$) were observed in the range $1.8 < x < 2.4$, hence most studies have concentrated on the composition of $x = 2.0$. Moreover, the total electrical conductivity strongly depends on the density and nature of the grain boundaries [4–6]; the microstructure of samples is usually affected by the preparation method.

Initially, Nasicon was considered to be insensitive to moisture and stable in contact with water, since its structure prevents water molecules from penetrating the lattice. Nearly 20 years ago, Ahmad et al. [7] revealed that Nasicon reacts with water solutions, regardless of composition and the processing route.

*Corresponding author, e-mail: ignaszak@uci.agh.edu.pl

The purpose of this work was to study the influence of humid air on the electrical properties of $Na_3Zr_2Si_2PO_{12}$ obtained by coprecipitation and the solid-state reaction method. The experimental conditions of synthesis and their correlation with the results obtained from accelerated ageing tests were also discussed.

2. Experimental

2.1. Sample preparation

Nasicon samples with a general formula of $Na_{1+x}Zr_2Si_xP_{3-x}O_{12}$, with a stoichiometric composition of $x = 2$, were prepared by coprecipitation and the solid-state reaction method. In the case of coprecipitation, aqueous solutions of $ZrO(NO_3)_2$, $NaOHSiO_2$, and $(NH_4)_2HPO_4$ were used. These solutions were mixed at room temperature and stirred until the gel-like coprecipitate was formed. This precipitate was then slowly evaporated at 70 °C for 48 h, then dried at 150 °C for 12 h, calcined in 24 h at 750 °C, and then in 900 °C for 24 h. Powders were formed into pellets, then isostatically pressed at 300 MPa. Sintering was done at $T = 1175$ °C for 5 h. In the case of solid-state reaction, the mixture $Na_3PO_4 \cdot 12H_2O$ and $ZrSiO_4$ powders in an appropriate stoichiometric ratio were pressed into pellets and calcined at 1150 °C for 24 h in one step. The obtained material was ground, pressed, and sintered under the same conditions as the material prepared by coprecipitation.

2.2 Measurements

X-ray Diffraction (XRD), and Scanning Electron Microscopy (SEM) were used to determine the structural and microstructural properties of the prepared pellets. Electrical properties were determined basing on AC Electrochemical Impedance Spectroscopy measurements (EIS). Measurements were done in a typical sample holder at room temperature in air atmosphere with controlled humidity. In order to obtain humid atmosphere, dry synthetic air was passed through a water bubbler. Air humidity was measured at the gas outlet. The gas flow was kept at constant level in all measurements. Pt blocking electrodes were deposited by screen-printing on both sides of the Nasicon pellets. Prior to each measurement, samples were equilibrated for 24 h after each change of conditions.

3. Results and discussion

3.1. Phase composition

The calcination at $T = 750$ °C of the primary gel/coprecipitate prepared by coprecipitation leads to the formation of tetragonal ZrO_2, and no traces of other phases are observed. Further calcination at $T = 900$ °C and $T = 1175$ °C leads to the formation of a monoclinic Nasicon phase with a slight admixture of monoclinic ZrO_2. The sample

prepared by the solid-state reaction method crystallises as a monoclinic phase just after calcination at 1150 °C for 24 h (with possible traces of tetragonal $ZrSiO_4$ and the usual slight admixture of monoclinic ZrO_2 phase).

3.2. Microstructure

Figures 1 A–D show the cross-section SEM micrographs of Nasicon samples, prepared by different methods; before (A, C) and after (B, D) ageing tests in a humid atmosphere. The samples obtained from powder prepared by the solid-state reaction method display much higher density (lower porosity) compared to the samples sintered from powders by coprecipitation. The grain boundaries are hardly visible in the case of Nasicon prepared by a solid-state reaction. This may suggest the presence of a liquid phase during sintering and a glassy-like phase after quenching. No significant difference in the microstructure before (C) and after (D) humidity treatment was observed.

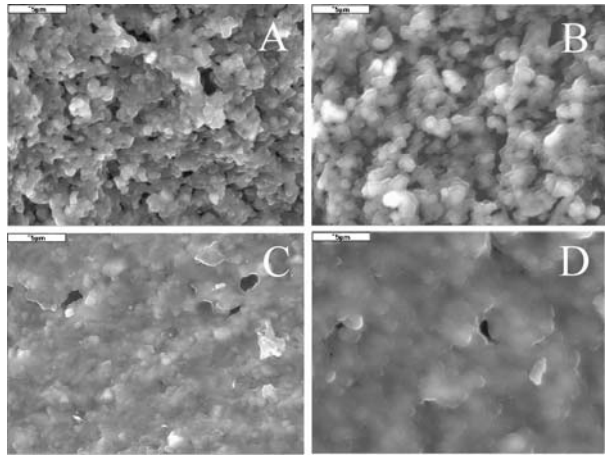

Fig. 1. SEM micrographs of $Na_3Zr_2Si_2PO_{12}$ sintered at 1175 °C for 5 h, prepared by coprecipitation before (A) and after (B) humidity treatment, and prepared by solid state reaction before humidity treatment (C)

As can be shown on the microstructure pictures of Nasicon obtained by coprecipitation (Fig. 1A, B), a smaller amount of glassy-like phase at the grain boundaries was visible, compared to the Nasicon prepared by the traditional method. Grains seem to be smooth and not uniform in size. After the ageing test, however, Nasicon prepared by coprecipitation looses its mechanical strength and easy crumbles. Similar behaviour was observed earlier by others [8, 9] and could be related to the dissolution of traces of glassy phase at grain boundaries or, on the contrary, to the formation of a hydronium Nasicon protonic conductor surrounding Nasicon particles. No additional Nasicon-like phase was found in our samples, so the first explanation of this phenomenon seems to be more feasible.

3.3. Electrical properties – the influence of humidity

Fig. 2 (A, B, C) shows examples of the admittance spectra of $Na_3Zr_2Si_2PO_{12}$ (prepared by coprecipitation) in dry and humid atmospheres, measured at room tempera-

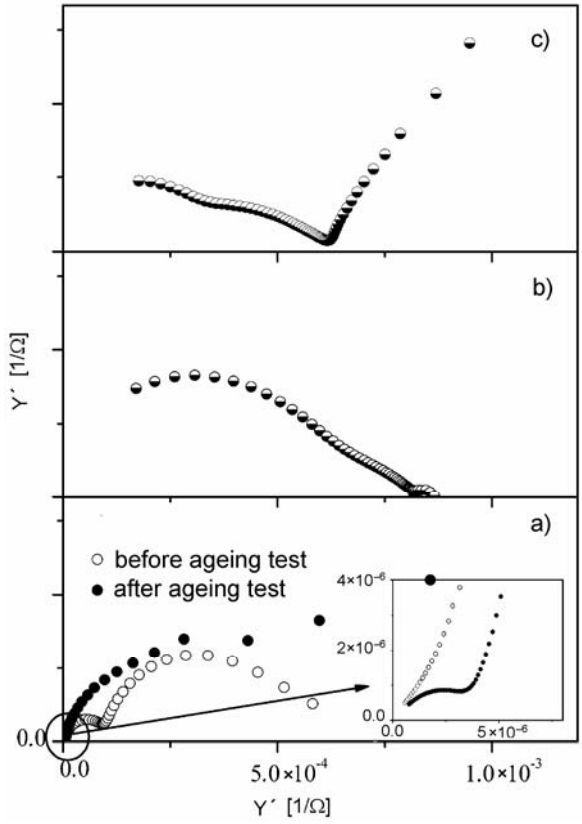

Fig. 2. The admittance spectra of $Na_3Zr_2Si_2PO_{12}$ prepared by coprecipitation:
a) 0% RH, b) ~90% RH, 400 h in wet air flow, c) ~90% RH, 768 h in wet air flow

ture. The proposed equivalent circuit is shown in Fig. 3a and consists of a CPE_{dl} element (double layer capacitance at the surface), R_b (bulk resistance), R_{gb} and CPE_{gb} (grain boundary resistance and capacitance), and R_g and CPE_g (glass resistance and capacitance). The diagram for Nasicon prepared by coprecipitation before the ageing test in a humid atmosphere (Fig. 2a) is represented by two semicircles (in the Y″(Y′) representation). On the left, a low frequency semicircle corresponds to electrode polarisation, and on the right, a high frequency semicircle reflects the grain boundary polarisation (the semicircles related to $RCPE_{gb}$ and $RCPE_{glass}$ are not separated due to similar R and CPE values). Additionally, to illustrate the difference between the low and high frequency ranges of the spectra, impedance diagrams were also used. The

electrical equivalent circuit taken to fit Nasicon spectra in a dry air flow, proposed earlier for samples prepared by solid state reaction [10], is typical of ceramic samples.

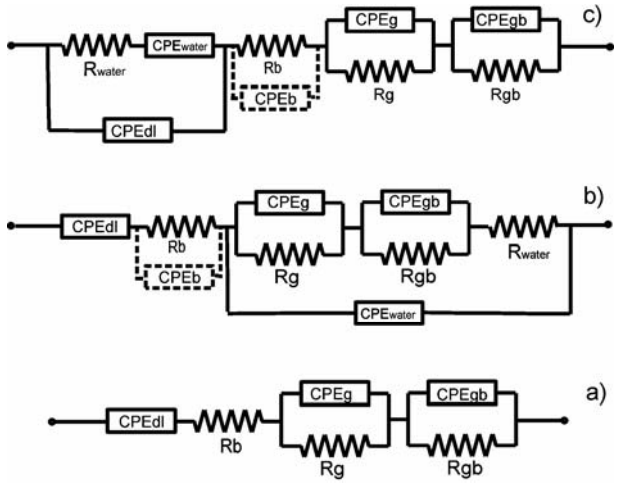

Fig. 3. Equivalent circuits proposed to fit the data obtained in dry (a) and humid atmospheres (b, c)

The presence of water vapour in an ambient atmosphere leads to a modification of the measured spectra (Fig. 2b, c) as compared to those obtained in dry air (Fig. 2a). Namely, the spectrum is shifted towards higher values of electrical conductivity; this effect can be attributed to the formation of conductive pathways along the ceramic pores due to water condensation, and was observed in Nasicon prepared by both methods. The shape of the spectra taken in a humid atmosphere (Fig. 2b) is the same for Nasicon prepared by both methods (Fig. 4b, c), but in the case of sample prepared by coprecipitation the spectrum is different after 500 h in a wet air flow (Fig. 2c). As can be seen in Fig. 3b and c, two possible circuits have to be taken into account to properly fit the obtained spectra. An additional electrode component related to water condensed at the electrode surface can be represented as a series-connected resistor and capacitor (R_{water}, CPE_{water}), connected in parallel with the double layer capacitance (CPE_{dl}). On the other hand, water condensation at grain boundaries has been considered, and the corresponding resistance and capacitance (R_{water} and CPE_{water}) may be included in series to the elements describing the bulk and grain boundary properties.

As can be seen on the spectra in wet flow for electrolytes obtained by coprecipitation, the grain boundary resistance (R_{gb}) decreases about one order of magnitude and the double layer capacitance (CPE_{dl}) is about two orders of magnitude higher compared to that of the sample in a dry atmosphere. The bulk resistance was initially lower, but after 700 h in a humid flow increased, probably due to the formation of new phase around Nasicon particles. To properly fit the spectra for Nasicon prepared by coprecipitation and measured after 500 h in a humid air flow, an additional CPE element connected with bulk capacitance is required (drawn by the dashed line and included in equivalent circuits describing measurements in a wet atmosphere in Fig. 3b and c). Additionally,

higher values of grain boundary and glassy phase resistances suggest that longer humidity treatment leads to the formation of a so-called hydronium Nasicon surrounding the main Nasicon particles [9].

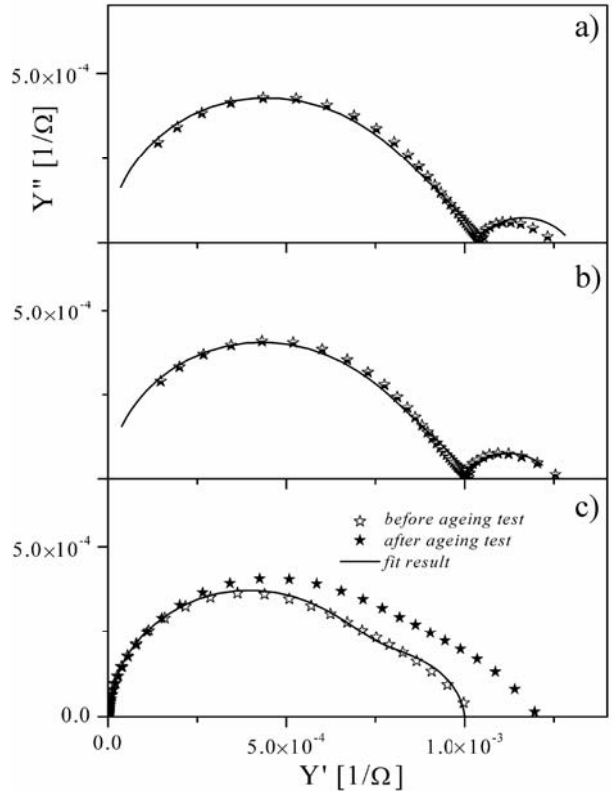

Fig. 4. The admittance spectra of $Na_3Zr_2Si_2PO_{12}$ prepared by solid state reaction: a) 0% RH, b) ~90% RH, 420 h in wet air flow, c) ~90% RH, 768 h in wet air flow

Figure 4 illustrates the admittance spectrum of a sample prepared by solid state reaction measured at room temperature in a dry air flow, before and after the ageing test. The shape of the spectrum does not change and the absolute value of electrical conductivity is only slightly higher after long humidity treatment, probably as a consequence of additional conductive pathways due to water condensed at the Nasicon/Pt-electrode surface or along ceramics pores.

The influence of humidity on the electrical properties of Nasicon prepared by both methods is summarised in Figure 5. The presence of water vapour leads to an increase in electrical conductivity for times shorter than 200 h. This effect appeared for the more porous samples prepared by coprecipitation, and after 500 h their resistance increases again. The resistivity of Nasicon prepared by solid-state reaction remained unchanged even after 1000 h in a wet atmosphere. These observations may be attrib-

uted to differences in the microstructures, densities, and other properties of grain boundaries.

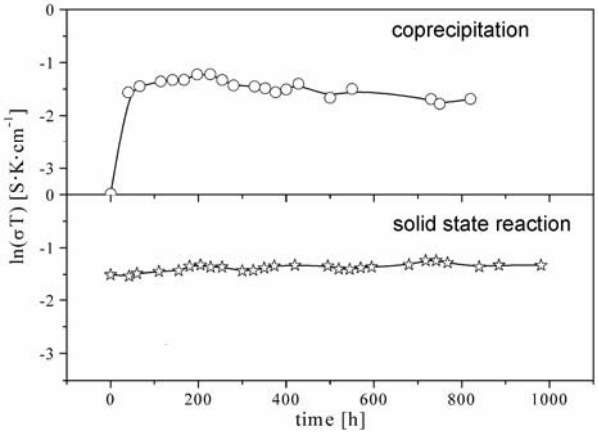

Fig. 5. The time dependence of the total conductivity of $Na_3Zr_2Si_2PO_{12}$, prepared by solid state reaction and coprecipitation in a humid atmosphere

4. Conclusions

The microstructure and phase composition of $Na_3Zr_2Si_2PO_{12}$ are strongly affected by the preparation method. Long-term measurements in a humid atmosphere indicate important differences in the stabilities of $Na_3Zr_2Si_2PO_{12}$ samples in contact with water vapour. In the case of Nasicon obtained by solid state reaction, the reversible modification of the admittance spectra after humidity treatment was noticed, contrary to the sample prepared by coprecipitation. This effect is strongly dependent on microstructure. No evidence of changes, such as the formation of a new phase, reduction of the glassy phase, or differences in the grain sizes, were detected after humidity treatment. Samples prepared by the solid-state reaction seem to be well-densified Nasicon and are more stable under a humid atmosphere. A behaviour typical of porous ceramics in contact with water vapour appeared in the case of Nasicon prepared by coprecipitation. The proposed equivalent circuits explain the effect of humidity on the Nasicon electrolyte. For samples obtained by solid state reaction, the wet atmosphere seems to modify rather the electrode/electrolyte surface, so an additional R-CPE_{water} element should be connected to the low frequency part of the admittance spectra. On the contrary, for samples prepared by coprecipitation, when water may also condense inside, the modification can also be seen in the high frequency part of the spectra.

Acknowledgements

The financial support of the Polish State Committee for Scientific Research (KBN), Project No. 7 T08A 030 21 is acknowledged.

References

[1] LEE D.D., CHOI S.D., LEE K.W., Sens. Actuators B, 24–25 (1995), 607.
[2] KIDA T., MIYACHI Y., SHIMANOE K., YAMAZOE N., Sens. Actuators B, 80 (2001), 28.
[3] TRAVERSA E., AONO H., SADAOKA Y., MONTANARO L., Sens. Actuators B, 65 (2000), 204.
[4] VON ALPEN U., Mat. Res. Bull., 14 (1979), 1317.
[5] PERTHUIS H., COLOMBAN P., Ceramics International, 12 (1986), 39.
[6] BOHNKE O., RONCHETTI S., MAZZA D., Solid State Ionics, 122 (1999), 127.
[7] AHMAD A., WHEAT T.A., KURIAKOSE A.K., CANADAY J.D., MCDONALD A.G., Solid State Ionics, 24 (1987), 89.
[8] MAUVY F., SIEBERT E., FABRY P., Talanta, 48 (1999), 293.
[9] FUENTES R.O., SMIRNOVA O.A., KHARTON V.V., FIGUEIREDO F.M., MARQUES F.M., J. Eur. Ceram. Soc., 24 (2004), 3049.
[10] BOGUSZ W., KROK F., PISZCZATOWSKI W., Solid State Ionics, 119 (1999), 165.

Received 10 December 2004
Revised 31 January 2005

Materials Science-Poland, Vol. 24, No. 1, 2006

Structural and transport properties of $LiFe_{0.45}Mn_{0.55}PO_4$ as a cathode material in Li-ion batteries

W. OJCZYK[1], J. MARZEC[1], J. DYGAS[2], F. KROK[2], R. S. LIU[3], J. MOLENDA[1*]

[1]Faculty of Materials Science and Ceramics, AGH University of Science and Technology, al. Mickiewicza 30, 30-059 Cracow, Poland

[2]Faculty of Physics, Warsaw University of Technology, pl. Politechniki 1, 00-661 Warsaw, Poland

[3]Department of Chemistry, National Taiwan University, Roosevelt Road, Taipei 106, Taiwan, R.O.C.

The paper presents investigations on structural, electrical and electrochemical properties of phospho-olivine, $LiFe_{0.45}Mn_{0.55}PO_4$, synthesized at high temperatures. Moessbauer spectroscopy measurements confirmed the occurrence of iron(II), and X-ray absorption near edge structure (XANES) measurements evidenced manganese(II) and iron(II). Impedance spectroscopy enabled the separation of electrical conductivity into electronic and ionic components. The substitution of manganese for iron led to a noticeable increase in the electronic component of conductivity and only to a slight increase in the ionic component, compared to pure $LiFePO_4$. Also, the chemical diffusion coefficient of lithium measured by GITT turned out larger in $Li_xFe_{0.45}Mn_{0.55}PO_4$. It has been stated that the increased electronic conductivity in manganese-doped phospho-olivine activates the diffusional mechanism of lithium deintercalation.

Key words: *$LiMn_yFe_{1-y}PO_4$; lithium diffusion; cathode material; Li-ion battery; intercalation*

1. Introduction

In the large group of compounds that can reversibly react with lithium, phosphates in particular draw the attention of researchers [1, 2]. The most promising ones are phosphates with a general formula of $LiMPO_4$ (M = Fe, Mn, Co, Ni) and the olivine structure. $LiFePO_4$ is characterized by high voltage (3.5 V) and capacity (170 mA·h/g), outstanding chemical stability, low cost, and environmental friendliness. The electrochemical charging of a $Li\,|\,Li^+\,|\,LiFePO_4$ cell yields a two-phase product, according to the following equation:

*Corresponding author, e-mail: molenda@uci.agh.edu.pl

$$Li_{1-x}FePO_4 - xLi^+ - xe^- \rightarrow xFePO_4 + (1-x)LiFePO_4 \quad (1)$$

Yamada et al. [3–5] reported that the chemical delithiation of phospho-olivine, $LiMn_{0.6}Fe_{0.4}PO_4$, at a voltage of 3.5V, proceeds as follows:

$$LiFe_{1-y}Mn_yPO_4 - xLi^+ - xe^- \rightarrow Li_{1-x}Fe_{1-y}Mn_yPO_4 \quad (0 < 1-x < y) \quad (2)$$

This voltage accounts for the oxidation of iron, $Fe^{2+} \rightarrow Fe^{3+}$. At 4 V, where manganese oxidation takes place ($Mn^{2+} \rightarrow Mn^{3+}$) the mechanism of reaction changes and a two-phase product is obtained according to the reaction [3–5]:

$$Li_yFe_{1-y}Mn_yPO_4 - xLi^+ - xe^- \rightarrow x/y\ Fe_{1-y}Mn_yPO_4 + (y-x)/y\ Li_yFe_{1-y}Mn_yPO_4 \quad (3)$$

The goal of this work was to investigate structural, electrical, and electrochemical properties of manganese-doped phospho-olivine, $LiFe_{0.45}Mn_{0.55}PO_4$, and the properties of this compound after electrochemical deintercalation in a $Li \mid Li^+ \mid LiFe_{0.45}Mn_{0.55}PO_4$ cell in order to asses the delithiation mechanism.

2. Experimental details

$LiFe_{0.45}Mn_{0.55}PO_4$ and $LiFePO_4$ olivines were synthesized by a high temperature reaction using Li_2CO_3 (POCh, pure p.a.), $MnCO_3$ (Aldrich, pure p.a.), $FeC_2O_4{\cdot}2H_2O$ (Aldrich, pure), and $NH_4H_2PO_4$ (POCh, pure p.a.). The substances were thoroughly ground in an agate mortar with some acetone added, then dried and pressed into pellets. Initial heating and synthesis were performed under argon of high purity, with the following sequence of time/temperature regimes: 1.5 h at 100 ºC (to remove water from the system), 2h at 260 ºC (to decompose iron oxalate), 3h at 350 ºC (to remove gaseous products and initiate the synthesis). The final heating was performed at 750 ºC for 24 h. This complex procedure was developed in order to avoid the oxidation of Fe^{2+} and to minimize the formation of phosphides and $Mn_yFe_{1-y}P_2O_7$ [6]. The colour of the samples varied from dark grey for samples with high iron content to light grey for samples with 55 at. % of manganese.

In the electrochemical studies, composite cathodes were used containing 85 wt. % of $LiFe_{0.45}Mn_{0.55}PO_4$, 7.5 wt. % graphite, and 7.5 wt. % of carbon obtained from the decomposition of a phenol-formaldehyde resin. The additives, being electronic conductors, were necessary because of the high resistivity of the samples ($> 10^9\ \Omega{\cdot}cm$). The additives constituted a highly conductive matrix, in which the much less conductive olivine dispersions were imbedded. This microstructure allowed the olivine capacity to be taken advantage of [7–9].

The samples were characterized by XRD (Phillips X'Pert Pro), SEM (JEOL JSM 5400), and EDS. The X-ray spectra were analysed using the Rietveld method. Iron oxidation state and its local surroundings were characterized by ^{57}Fe Moessbauer spectroscopy at 300 K, with the spectrometer operating in constant acceleration mode

in transmission geometry and with a ^{57}Co(Rh) source. The oxidation states of Fe and Mn were also characterized by X-ray absorption near edge structure (XANES) measurements. XANES was carried out at the Wiggler beam line BL 17C of National Synchrotron Radiation Research Center (NSRRC), Taiwan. The electron storage ring was operated at the energy of 1.5 GeV with a beam current of 100–200 mA. A Si(111) double-crystal monochromator was employed for energy selection, with a resolution ($\Delta E/E$) of ca. 2×10^{-4}. The XANES spectra at the Fe and Mn K-edges were recorded at room temperature in a transmission mode, using gas-filled ionisation chambers to measure the intensities of the incident and transmitted X-ray spectra, which were normalized with respect to edge jump.

The specimens for impedance spectroscopy measurements were shaped into flat pellets, ground with abrasive papers of up to 2400 grit No. Electrodes were made of thin layers of gold deposited on flat surfaces of the pellets by plasma spraying. Thus prepared specimens were inserted between two mounting plates in a spring holder. Measurements were performed in flowing argon, purity N5. The impedance was recorded with a laboratory set-up comprising a Solartron 1260 analyser and Keithley 428 current amplifier operating in the frequency range 10^{-2}–10^{7} Hz with an alternating voltage excitation (rms value of 30 mV). The specimens were thermostated by means of an electric furnace with a constant voltage supply. Measurements within the temperature range 300–600 K were repeated in each case when the measuring algorithm detected impedance drift during 30 min of data acquisition (spectrum consisting of 160 frequencies).

The electrochemical extraction of lithium was performed in $Li\,|\,Li^+\,|\,Li_{1-x}Fe_{0.45}Mn_{0.55}PO_4$ cells using a lithium metal anode, Selectipur LP71 electrolyte (EC:DEC:DMC 1:1:1, 1 M $LiPF_6$, Merck), and a composite cathode, as described above. The charging curves of the cells, OCV, and lithium diffusion coefficient were determined as a function of lithium concentration in the cathode material. Lithium diffusion was measured by GITT (Galvanostatic Intermittent Titration Technique), as described by Weppner and Huggins [10], with a current impulse of 300 $\mu A/cm^2$ lasting 130 s.

3. Results and discussion

According to the X-ray analyses, the $LiFe_{0.45}Mn_{0.55}PO_4$ material, synthesized at high temperatures, is single-phase and has the olivine structure (space group *Pnma*) (Fig. 1). Its X-ray spectrum is shown in Fig. 2. Lattice constants were determined by the Rietveld method. An example of the specimen's microstructure is given in the SEM micrograph in Fig. 3a. The size of agglomerates is 10–50 μm, and they are built of crystallites about 1 μm long. The distribution of elements over the grain surface was analysed by EDS (Fig. 3b). The analysis was taken at different points within the same grains, and showed a homogeneous distribution of elements and absence of im-

purities such as iron or manganese phosphides and carbophosphides [11]. The EDS spectrum of $LiFe_{0.45}Mn_{0.55}PO_4$ confirmed the assumed iron-to-manganese ratio. The small amount of carbon detected locally originates from the decomposition of the starting reagents.

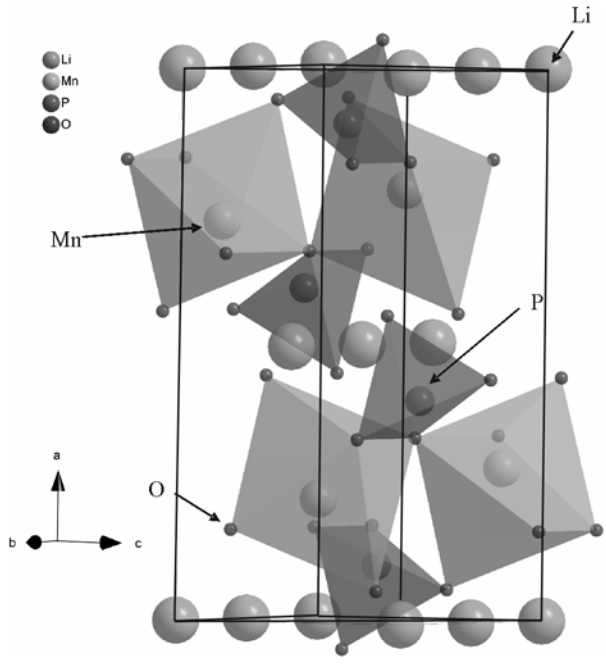

Fig. 1. The olivine structure of $LiMnPO_4$

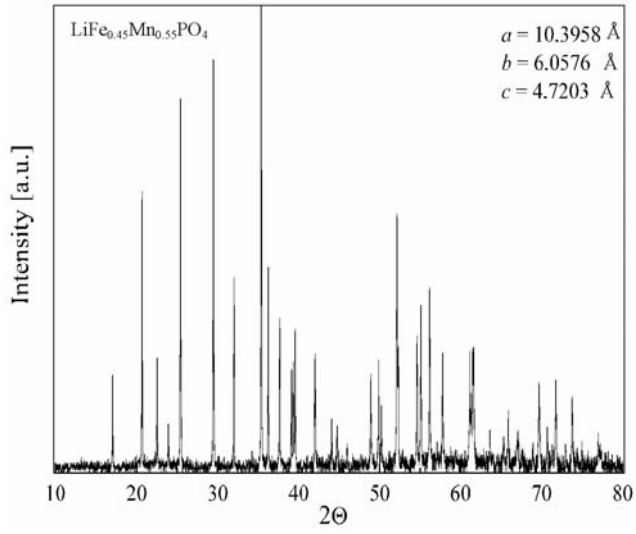

Fig. 2. X-ray diffraction pattern of $LiFe_{0.45}Mn_{0.55}PO_4$

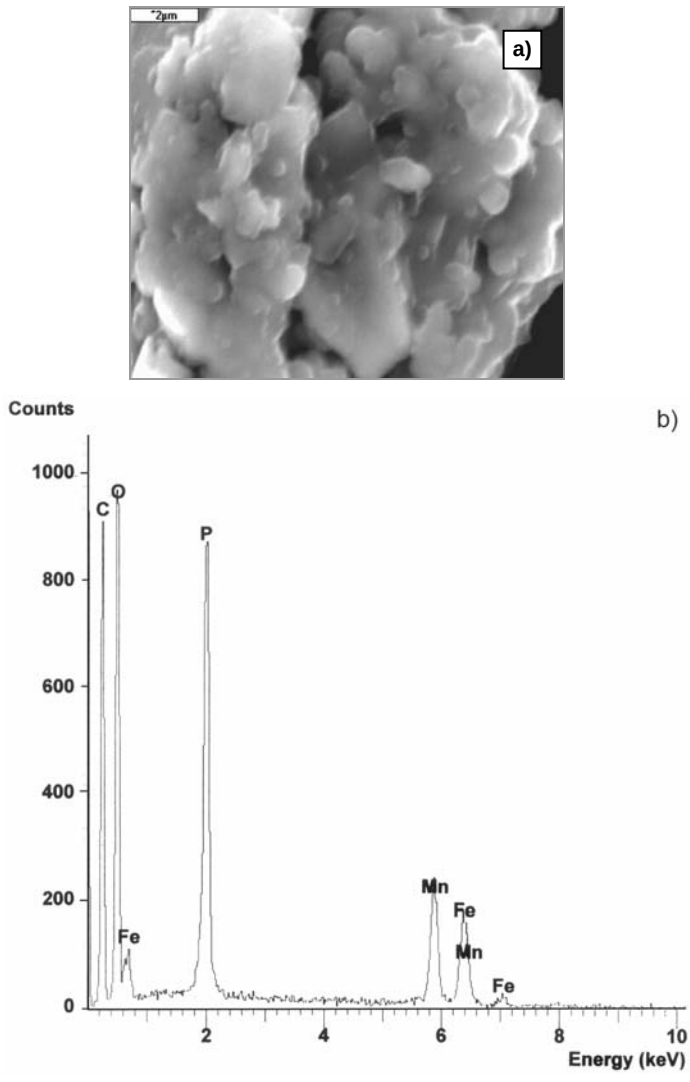

Fig. 3. Powder microstructure of $LiFe_{0.45}Mn_{0.55}PO_4$ (a) and its point EDS spectra (b)

The results of Moessbauer spectroscopy studies are presented in Fig. 4. The quadrupole doublet indicates iron(II) atoms in one crystallographic site. The oxidation numbers of manganese and iron could be determined by means of XANES (Fig. 5a, b). At different compositions of $LiFe_{1-y}Mn_yPO_4$ (y = 0, 0.25, 0.55, 0.75), the oxidation numbers of both these elements were always 2+. A detailed description of the determination mode of the oxidation state for Fe in $LiFePO_4$ has been published by Prince et al. [12]. These results indicate that the synthesis route followed in this work prevents the appearance of impurities containing Fe^{3+} [5].

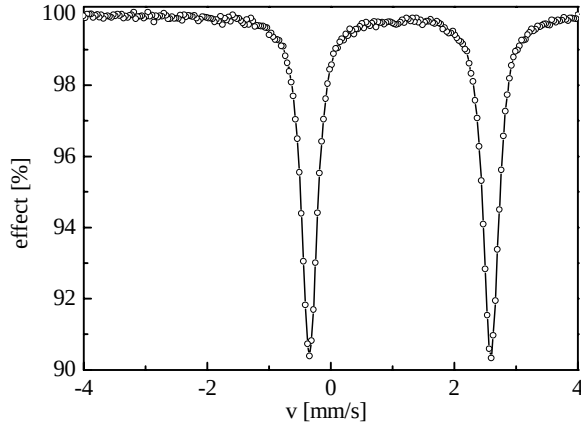

Fig. 4. Moessbauer spectrum of the $Li_1Fe_{0.45}Mn_{0.55}PO_4$ cathode material

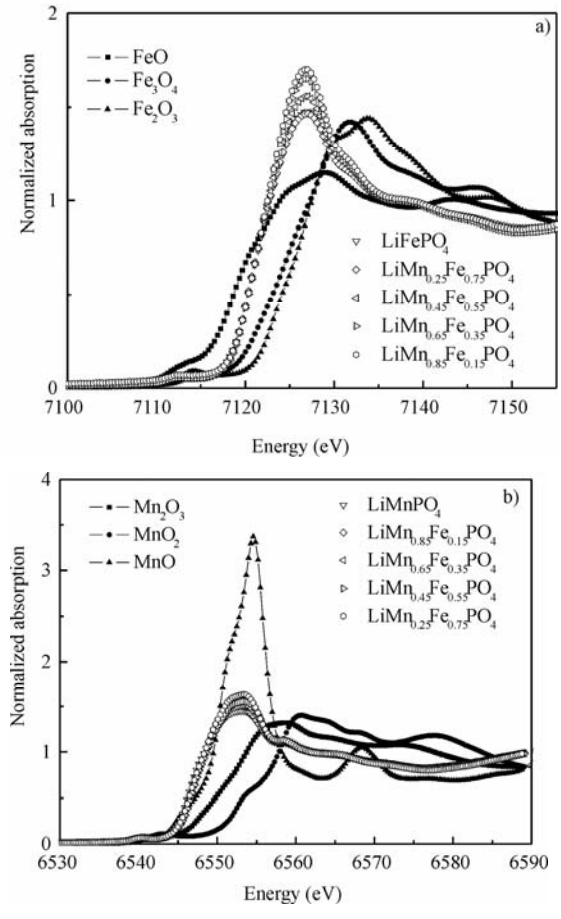

Fig. 5. The Fe K-edge (a) and Mn K-edge XANES spectra (b) of $LiFe_{1-y}Mn_yPO_4$ (y = 0, 0.25, 0.55, 0.75)

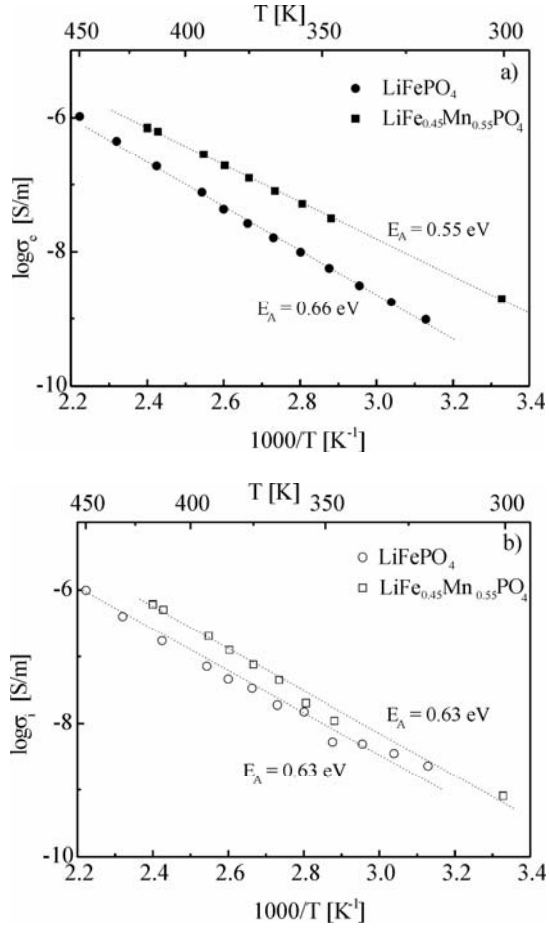

Fig. 6. The temperature dependences of the electronic (a) and ionic (b) conductivities of $LiFePO_4$ and $LiFe_{0.45}Mn_{0.55}PO_4$

The temperature dependences of the electronic and ionic conductivities of $LiFePO_4$ and $LiFe_{0.45}Mn_{0.55}PO_4$ are shown in Fig. 6a and b. The electronic conductivity of iron-manganese phospho-olivine is one order of magnitude higher than that of undoped $LiFePO_4$. The activation energies of electronic conductivities for $LiFe_{0.45}Mn_{0.55}PO_4$ and $LiFePO_4$ are 0.55 eV and 0.66 eV, respectively. The lower activation energy of electronic conductivity for the iron-manganese phospho-olivine is related to the presence of Fe^{2+}–Mn^{2+} pairs. The electronic configuration of manganese(II) is $3d^5$, while that of iron(II) is $3d^6$, which facilitates charge transport between these two types of ions. Structural relationships in phospho-olivine (Fig. 1) seem to favour charge transport via Fe–O–Mn bonds, where the interionic distance between Mn^{2+} and Fe^{2+} is about 4 Å. The lower electronic conductivity of $LiFePO_4$ is related to the presence of only one type of transition metal ion, namely Fe^{2+} ($3d^6$). The room-temperature ionic conductivities of both compounds are similar, a slightly higher value, however, has been

recorded for iron-manganese phospho-olivine. The activation energies of ionic conductivities have the same value for pure and manganese-doped phospho-olivine and close to the values calculated by numerical methods [13, 14]. In spite of increasing electronic conductivity, the ionic conductivity of $LiFe_{0.45}Mn_{0.55}PO_4$ remains practically unchanged. This may indicate that one-dimensional diffusion paths in the olivine structure are insufficient for fast lithium transport.

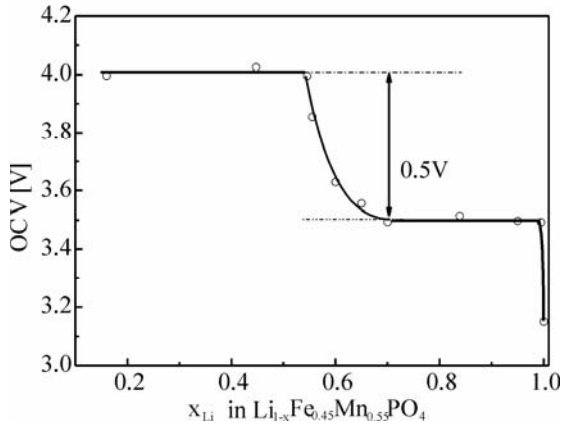

Fig. 7. OCV curve for a $Li\,|\,Li^+\,|\,Li_{1-x}Fe_{0.45}Mn_{0.55}PO_4$ cell as a function of lithium concentration

Figure 7 presents the OCV curve of the $Li\,|\,Li^+\,|\,Li_{1-x}Fe_{0.45}Mn_{0.55}PO_4$ cell with two characteristic plateaus. The first one, at 3.5V versus the lithium electrode, is related to iron oxidation ($Fe^{2+} \rightarrow Fe^{3+}$), and the second one at 4 V to manganese oxidation ($Mn^{2+} \rightarrow Mn^{3+}$). The sudden change in voltage by about 0.5 V is observed at $x_{Li} = 0.45$. In the composition range where the voltage is equal to 3.5 V and iron oxidation takes place, a linear variation of the lattice parameters of phospho-olivine with lithium content is observed. The lattice constants of $Li_{1-x}Fe_{0.45}Mn_{0.55}PO_4$, calculated by the Rietveld method, are given in Figure 8. The *a*, *b*, *c* lattice constants change linearly as lithium deintercalation proceeds, up to $x_{Li} = 0.45$. When lithium concentration becomes lower than 0.45, the X-ray spectrum indicates a single-phase material but the lattice parameters remain constant. It seems that such a behaviour can be explained on the basis of some earlier studies [15]. It has been stated that during lithium deintercalation at the voltage of 4 V, phospho-olivine phases with different lithium concentrations are formed. This observation seems to be in accordance with the model developed by Andersson [16], according to which the delithiation of phospho-olivines does not proceed in a radial mode, but by a mosaic mode, involving the appearance of microregions with and without lithium in the cathode material. Yamada [3–5] has shown that lithium deintercalation is a diffusional process at 3.5 V, while at 4 V manganese oxidation ($Mn^{2+} \rightarrow Mn^{3+}$) leads to the formation of two phases (Eq. (3)). The different delithiation mechanisms of phospho-olivine, observed by the authors at 4 V,

may be related to the fact that in Yamada's experiments lithium was extracted chemically in NO_2BF_4 solution. It has been demonstrated earlier [17] that the electrochemical and chemical deintercalation of lithium from manganese spinel yields products with different physical and chemical properties.

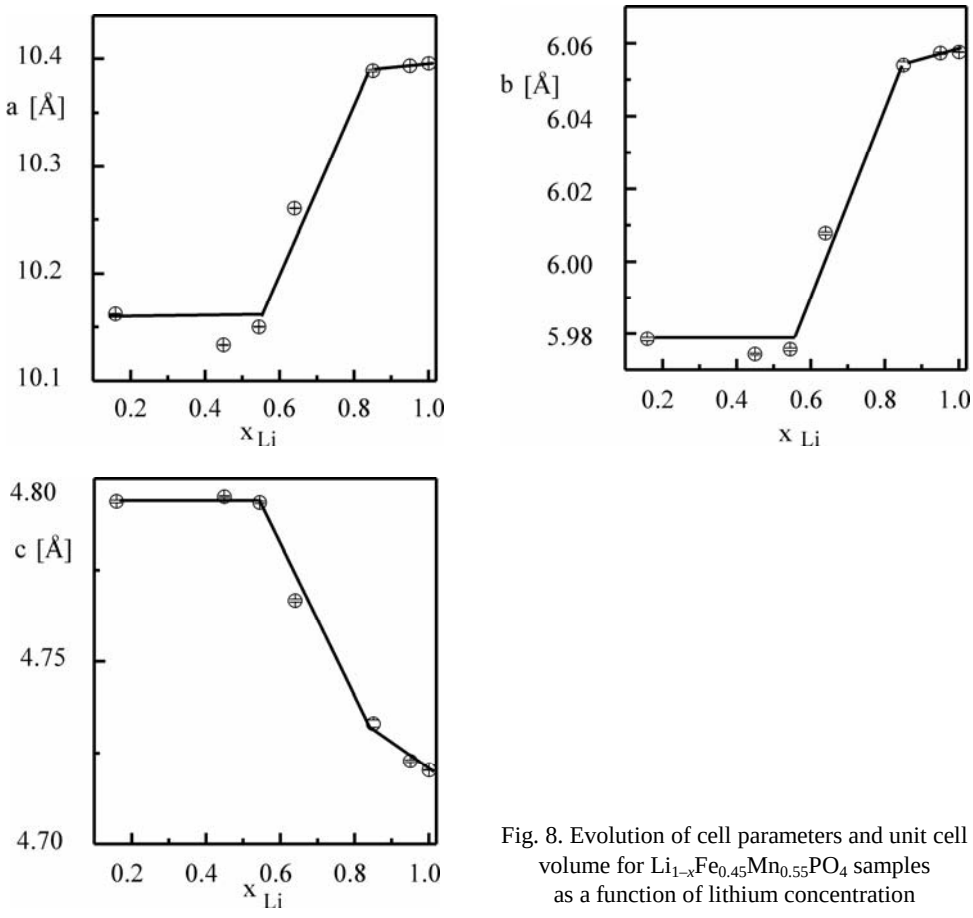

Fig. 8. Evolution of cell parameters and unit cell volume for $Li_{1-x}Fe_{0.45}Mn_{0.55}PO_4$ samples as a function of lithium concentration

Figure 9 presents the chemical diffusion coefficient of lithium as a function of lithium concentration in the cathode material, with a maximum of D_{Li} at $x_{Li} = 0.45$. The significant increase (about two orders of magnitude) in the diffusion coefficient can be related to the increased number of sites available for lithium diffusion in the $Li_{1-x}Fe_{0.45}Mn_{0.55}PO_4$ structure. At a lower concentration of lithium, the chemical diffusion coefficient D_{Li} decreases, which reflects some change in the relaxation mechanism of the cathode material. Despite the slight improvement in electronic conductivity, the chemical diffusion coefficient of lithium in $LiFe_{0.45}Mn_{0.55}PO_4$ remains low and increases only at a lithium concentration of about 0.45. The observed diffusion coefficients do not exceed $10^{-11}cm^2/s$, and are about 3–5 orders of magnitude lower than in the case of $LiMn_2O_4$ [18] or $LiNi_{1-y}Co_yO_2$ [19]. This may indicate that not only the

crystallographic structure, but also low electronic conductivity limits the effectiveness of $LiFe_{0.45}Mn_{0.55}PO_4$ in the electrode process.

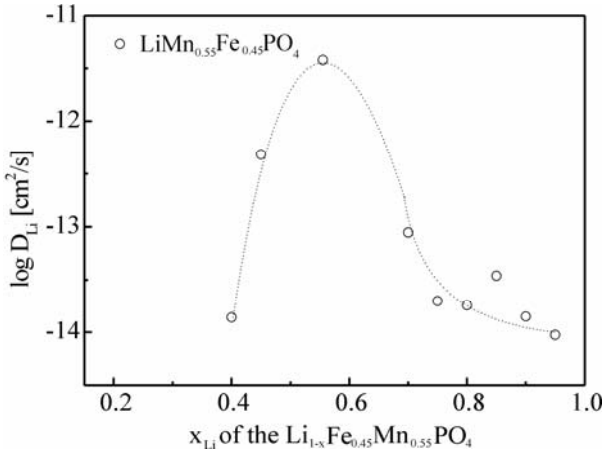

Fig. 9. Effective diffusion coefficient of lithium measured in a $Li\,|\,Li^+\,|\,Li_{1-x}Fe_{0.45}Mn_{0.55}PO_4$ cell. The line serves as a guide for the eyes

It seems that the one-dimensional diffusion paths, which can be easily blocked, disable fast lithium migration in this material. The phenomenon of cation mixing may additionally decrease the effective diffusion of lithium. A 3d metal substituted for lithium in the olivine structure blocks the diffusion path. It seems that a better effectiveness of the cathode process in the case of olivines ($LiFe_{1-y}Mn_yPO_4$) might be attained by microstructure optimisation, e.g. by using nanopowders with high specific surfaces.

4. Conclusions

Impedance spectroscopy studies of electrical conductivity in the temperature range 300–460 K have shown an increased electronic conductivity of $LiFe_{1-y}Mn_yPO_4$ as compared to $LiFePO_4$, while the ionic conductivity and chemical diffusion coefficient of lithium were only slightly higher than those of $LiFePO_4$. It seems that the increased electronic conductivity activates the diffusional mechanism of deintercalation, whereas it does not change the chemical diffusion coefficient of lithium to any significant degree.

Acknowledgement

This work was supported by the State Committee for Scientific Research, Poland under grant No. 4 T08A 020 25.

References

[1] PADLI A.K., NANJUNDASWAMY K.S., GOODENOUGH J.B., J. Electrochem. Soc., 144 (1997), 1188.
[2] PADLI A.K., NANJUNDASWAMY K.S., MASQUELIER C., OKADA S., GOODENOUGH J.B., J. Electrochem. Soc., 144 (1997), 1609.
[3] YAMADA A., KUDO Y., LIU K.-Y., J. Electrochem. Soc., 148 (2001), A747.
[4] YAMADA A., KUDO Y., LIU K.-Y., J. Electrochem. Soc., 148 (2001), A1153.
[5] YAMADA A., KUDO Y., CHUNG. S.CH., J. Electrochem. Soc., 148 (2001), A960.
[6] HONG Y.-S., RYU K.S., PARK Y.J., KIM M.G., LEE J.M., CHANG S.H., J. Mater. Chem., 12 (2002), 1870.
[7] OKADA S., SAWA S., EGASHIRA M., YAMAKI J.I., TABUCHI M., KAGEYAMA H., KONISHA T., YOSHINO A., J. Power Sources, 97–98 (2001), 430.
[8] YAMADA A., HOSOYA M., CHUNG. S.CH., KUDO Y., HINOKUMA K., LIU K.-Y., NISHI Y., J. Power Sources, 119–121 (2003), 232.
[9] FRANGER S., LE CARS F., BOURBON C., ROUAULT H., J. Power Sources, 119–121 (2003), 252.
[10] WEPPNER W., HUGGINS R.A., J. Electrochem. Soc., 124, (1977), 1569.
[11] HERLE S., ELLIS B., COOMBS N., NAZAR L.F., Nature Materials, **2** (2004), 147.
[12] PRINCE A.A.M., MYLSWAMY S., CHAN T.S., LIU R.S., HANNOYER B., JEAN M., SHEN C.H., HAUNG S.M., LEE J.F., WANG G.X., Solid State Commun., 132 (2004), 455.
[13] MORGAN D., VAN DER VEN A., CEDER G., Electrochem. Solid State Lett., 7 (2004), A30.
[14] RISSOULI K., BENKHOUJA K., RAMOS-BARRADO J.R., JULIEN C., Mater. Sci. Eng., B98 (2003), 185.
[15] OJCZYK W, MARZEC J., ŚWIERCZEK K., MOLENDA J., Defect Diffusion Forum, 237–240 (2005), 1299.
[16] ANDERSSON A.S., THOMAS O.J., J. Power Sources, 97–98 (2001), 498.
[17] MOLENDA J., OJCZYK W, MARZEC M., MARZEC J., PRZEWOŹNIK J., DZIEMBAJ R., MOLENDA M., Solid State Ionics, 157 (2003), 73.
[18] MOLENDA J., ŚWIERCZEK K., MOLENDA M., MARZEC J., Solid State Ionics, 135 (2000), 53.
[19] MOLENDA J., WILK P., MARZEC J., Solid State Ionics, 157 (2003), 115.

Received 10 December 2004
Revised 18 March 2005

Materials Science-Poland, Vol. 24, No. 1, 2006

$La_{1-x}Sr_xCo_{1-y-z}Fe_yNi_zO_3$ perovskites – possible new cathode materials for intermediate-temperature solid-oxide fuel cells

K. ŚWIERCZEK*, J. MARZEC, J. MOLENDA

Faculty of Materials Science and Ceramics, AGH University of Science and Technology,
al. Mickiewicza 30, 30-059 Cracow, Poland

$La_{1-x}Sr_xCo_{1-y-z}Fe_yNi_zO_3$ perovskites have been synthesized with hexagonal *R*-3*c* structures by a modified citric acid method and determined their structural and transport properties. Structural instabilities for samples with high Ni and Sr content heated to 1270 K were observed, leading to the appearance of secondary phases with spinel structures. Moessbauer studies revealed the presence of two different, clearly distinguishable surroundings of Fe ions, despite single crystallographic positions of iron ions. Low-temperature (77–300 K) dc conductivity and thermoelectric power measurements suggest an activated charge transport mechanism with the activation energy strongly dependent on the chemical composition of the material. Electrical conductivity as a function of temperature suggests the appearance of a hopping mechanism. The observed high-temperature (870–1070 K) dc electrical conductivity of $La_{1-x}Sr_xCo_{1-y-z}Fe_yNi_zO_3$ samples is relatively high and strongly depends on chemical composition. It seems possible to optimise the transport properties of $La_{1-x}Sr_xCo_{1-y-z}Fe_yNi_zO_3$ by chemical composition, which may lead to a new, attractive cathode material in terms of possible applications in intermediate -temperature solid-oxide fuel cells (IT-SOFCs).

Key words: *perovskite; solid-oxide fuel cell; cathode material; transport properties*

1. Introduction

Lowering the working temperature of high-temperature solid-oxide fuel cells (to the 600–800 ºC range) seems to be very important with respect to further developing the SOFC technology. Beneficial results will be a decrease in high-temperature corrosion and chemical degradation, usage of cheaper and more environmentally friendly materials for cell stack construction, as well as reduction of problems with cell stack

*Corresponding author, e-mail: xi@uci.agh.edu.pl

sealing. State of the art materials used in high temperature SOFCs, however, do not perform well in the intermediate temperature region.

New materials, which can replace currently used ZrO_2-based electrolytes and $La_{1-x}Sr_xMnO_{3\pm\delta}$ or other manganese-based perovskite cathodes, have been studied. Among the possible candidates for the cathode material, Co and Fe-based perovskites seem interesting due to their high catalytic activities and electrical conductivities [1, 2]. Ni-based perovskites have also been studied due to the high, metallic-like conductivity of $LaNiO_3$; these, however, suffer from lower thermal stability [3]. Perovskites with mixed composition, i.e. $La_{1-x}Sr_xCo_{1-y}Fe_yO_3$, exhibit even better properties in terms of their possible applications [4, 5].

The aim of this study was to investigate materials from a La–Sr–Co–Fe–Ni perovskite system in terms of their possible applications as cathodes for IT-SOFCs.

2. Experimental

$La_{1-x}Sr_xCo_{1-y-z}Fe_yNi_zO_3$ perovskites were synthesized using precursors obtained by the modified citric acid method; details of the synthesis procedure can be found elsewhere [6]. Final heating was conducted at 1270 K in air for 24 h with an initial step at 1070 K for 12 h. The obtained samples were characterized by XRD studies (Phillips X'Pert Pro). The X-ray spectra were analysed using the Rietveld method. For $La_{1-x}Sr_xCo_{0.4}Fe_{0.4}Ni_{0.2}O_3$ samples, the local structure of iron ions was characterized by ^{57}Fe Moessbauer spectroscopy. Scanning electron microscopy, together with EDS spectroscopy, was performed on perovskite powders. dc electrical conductivity was measured by a pseudo 4-probe method, and electrodes were made using silver paint. Thermoelectric power was calculated from the slope of the dependence of thermoelectric voltage on the variable temperature gradient ($\Delta T \approx 0$–3K).

3. Results

The results of X-ray measurements performed for various $La_{1-x}Sr_xCo_{1-y-z}Fe_yNi_zO_3$ perovskites obtained by the citric acid route are presented in Table 1. We were able to obtain single phase $La_{1-x}Sr_xCo_{1-y-z}Fe_yNi_zO_3$ perovskites with small amounts of Sr and Ni. For all samples with $x + z > 0.6$, secondary phases appear. The observed secondary phases possess spinel structures and most likely have a La_2NiO_4-like composition for materials with higher Ni content or a Sr_2FeO_4-like composition for materials with higher Sr content. For some two-phase samples, a lowering of the final heating temperature from 1270 K to 1070 K leads to a single-phase system. This temperature is too low, however, in terms of possible application in the IT-SOFCs. X-ray results suggest that the La–Sr–Co–Fe–Ni system is complicated and that the allowed solid solution range is relatively small. It is worth noting that in La_2NiO_4 the valence of

nickel ions is 2+. This suggests that the $La_{1-x}Sr_xCo_{1-y-z}Fe_yNi_zO_3$ instability for $x + z > 0.6–0.7$ is strongly linked to the valence of 3d metals.

Table 1. Structural properties of $La_{1-x}Sr_xCo_{1-y-z}Fe_yNi_zO_3$ perovskites

Composition	Structure	*a* [Å]	*c* [Å]	Cell volume [Å]^3
$La_{0.9}Sr_{0.1}Co_{0.2}Fe_{0.6}Ni_{0.2}O_3$	*R*-3*c*	5.5097(2)	13.3101(7)	349.92(3)
$La_{0.8}Sr_{0.2}Co_{0.2}Fe_{0.6}Ni_{0.2}O_3$	*R*-3*c*	5.4963(2)	13.3179(6)	348.42(2)
$La_{0.7}Sr_{0.3}Co_{0.2}Fe_{0.6}Ni_{0.2}O_3$	*R*-3*c*	5.4814(2)	13.3180(7)	346.54(3)
$La_{0.6}Sr_{0.4}Co_{0.2}Fe_{0.6}Ni_{0.2}O_3$	two phase	–	–	–
$La_{0.9}Sr_{0.1}Co_{0.4}Fe_{0.4}Ni_{0.2}O_{3-\delta}$	*R*-3*c*	5.4818(2)	13.2423(5)	344.62(2)
$La_{0.8}Sr_{0.2}Co_{0.4}Fe_{0.4}Ni_{0.2}O_{3-\delta}$	*R*-3*c*	5.4745(2)	13.2584(5)	344.12(2)
$La_{0.7}Sr_{0.3}Co_{0.4}Fe_{0.4}Ni_{0.2}O_{3-\delta}$	*R*-3*c*	5.4620(2)	13.2732(7)	342.93(3)
$La_{0.9}Sr_{0.1}Co_{0.2}Fe_{0.4}Ni_{0.4}O_{3-\delta}$	*R*-3*c*	5.4866(2)	13.2576(5)	345.62(2)
$La_{0.8}Sr_{0.2}Co_{0.2}Fe_{0.4}Ni_{0.4}O_{3-\delta}$	*R*-3*c*, traces of spinel phase	5.4769(2)	13.2764(6)	344.89(2)
$La_{0.9}Sr_{0.1}Co_{0.5}Fe_{0.4}Ni_{0.1}O_3$	*R*-3*c*	5.4777(2)	13.2335(5)	343.88(2)
$La_{0.8}Sr_{0.2}Co_{0.5}Fe_{0.4}Ni_{0.1}O_3$	*R*-3*c*, traces of spinel phase	5.4709(3)	13.2578(7)	343.65(3)

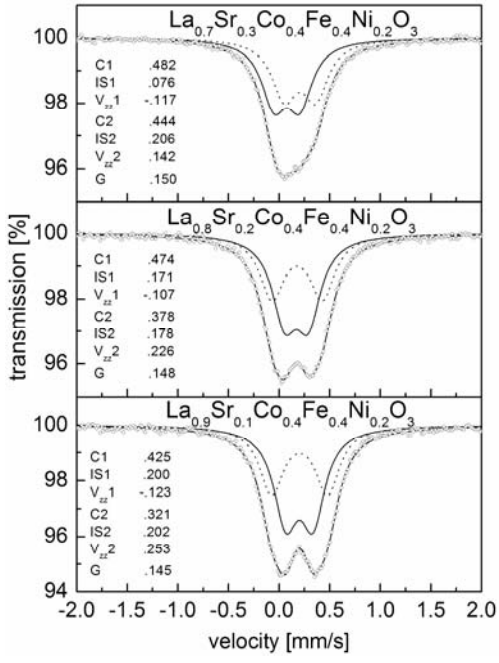

Fig. 1. Moessbauer spectra of $La_{1-x}Sr_xCo_{0.4}Fe_{0.4}Ni_{0.2}O_3$ perovskites

Moessbauer studies for $La_{1-x}Sr_xCo_{0.4}Fe_{0.4}Ni_{0.2}O_3$ samples (Fig. 1) revealed the presence of two different, clearly distinguishable surroundings of Fe ions, despite

a single crystallographic position of iron ions (6b). A comparison of these results with previous studies for $La_{1-x}Sr_xCo_{0.2}Fe_{0.6}Ni_{0.2}O_3$ compositions [6] leads to the conclusion that this differentiation is driven by the La–Sr sublattice. The first coordination sphere of Fe in the *R*-3*c* perovskite structure is the FeO_6 octahedron, the second coordination sphere is cube-shaped, with Fe in the centre and La and Sr ions randomly occupying the corners. It seems that the observed Moessbauer spectra may originate from a superstructure formed by the possible ordering of La and Sr ions within this sublattice.

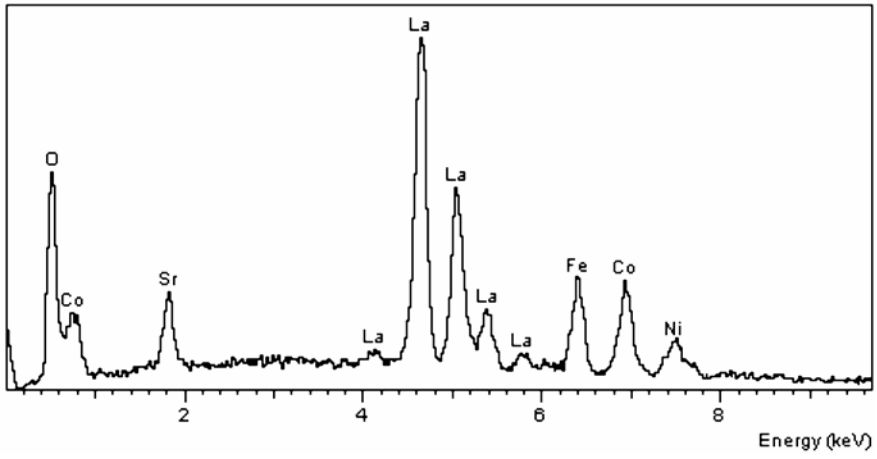

Fig. 2. Exemplary EDS spectrum of a $La_{0.8}Sr_{0.2}Co_{04}Fe_{0.4}Ni_{0.2}O_3$ sample

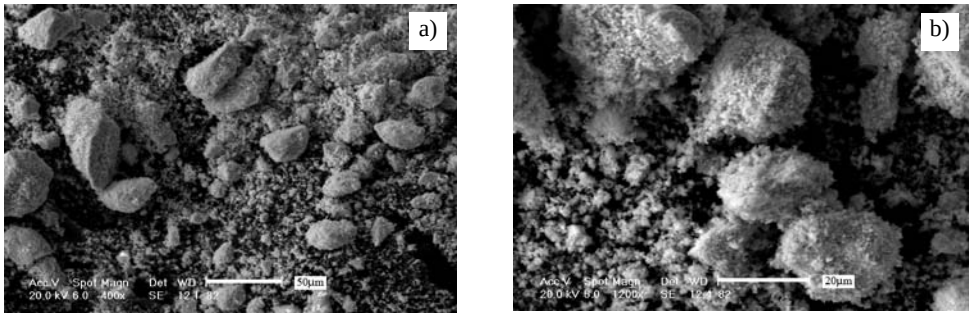

Fig. 3. SEM images of $La_{0.8}Sr_{0.2}Co_{0.4}Fe_{0.4}Ni_{0.2}O_3$ powder: a) 400×, b) 1200×

The exemplary EDS measurement of a $La_{0.8}Sr_{0.2}Co_{0.4}Fe_{0.4}Ni_{0.2}O_3$ sample presented in Figure 2 shows an even distribution of elements, with appropriate La/Sr and Co/Fe/Ni ratios. This confirms that the citric acid method is suitable for obtaining perovskites in the La–Sr–Co–Fe–Ni system. Traces of Cu, probably from nitrides and carbon, coming from the decomposition of citric acid, can also be detected. Scanning electron microscopy images of $La_{0.8}Sr_{0.2}Co_{0.4}Fe_{0.4}Ni_{0.2}O_3$ powder, presented in Figure 3, show rather a typical microstructure of the ceramic material obtained by heating

of the low temperature precursor. Agglomerates with sizes in the 5–50 μm range, consisting of < 1 μm crystallites, are observed. Similar microstructures were observed for other compositions.

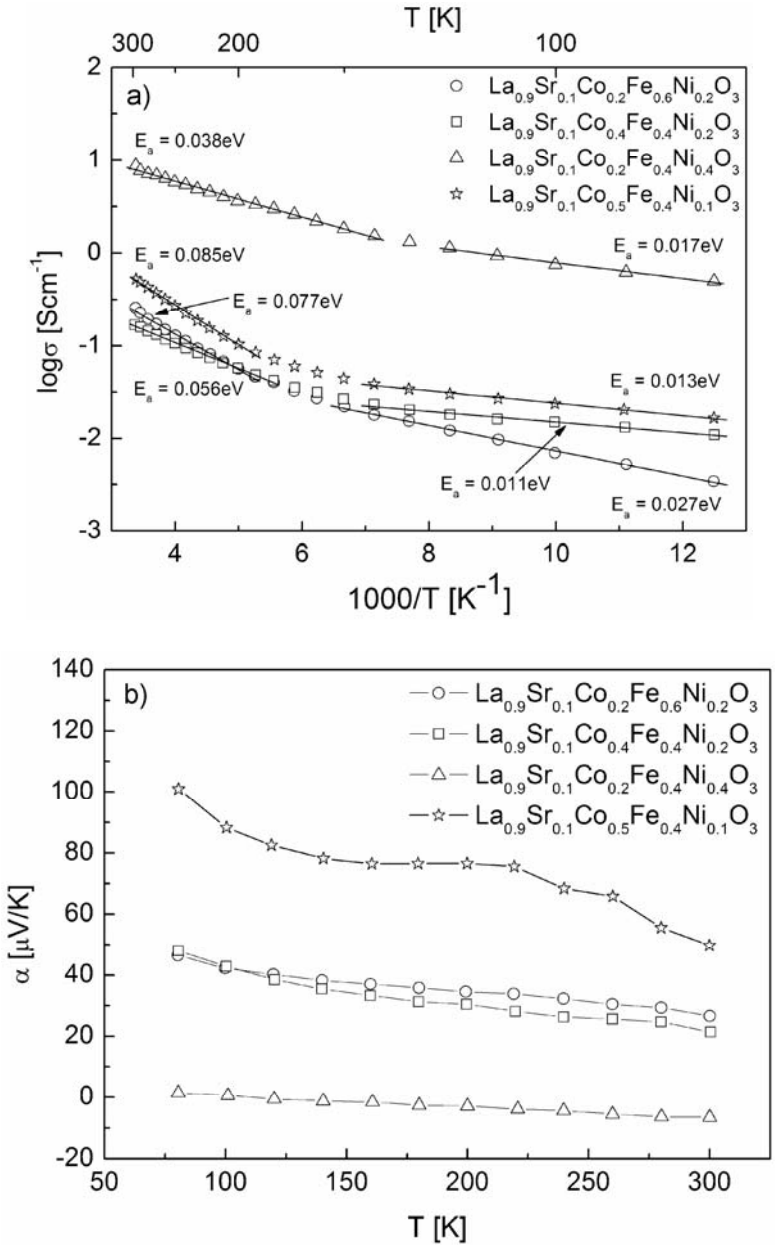

Fig. 4. Low-temperature (77–300 K) transport properties of $La_{0.9}Sr_{0.1}Co_{1-y-z}Fe_yNi_zO_3$ perovskites: a) electrical conductivity, b) thermoelectric power

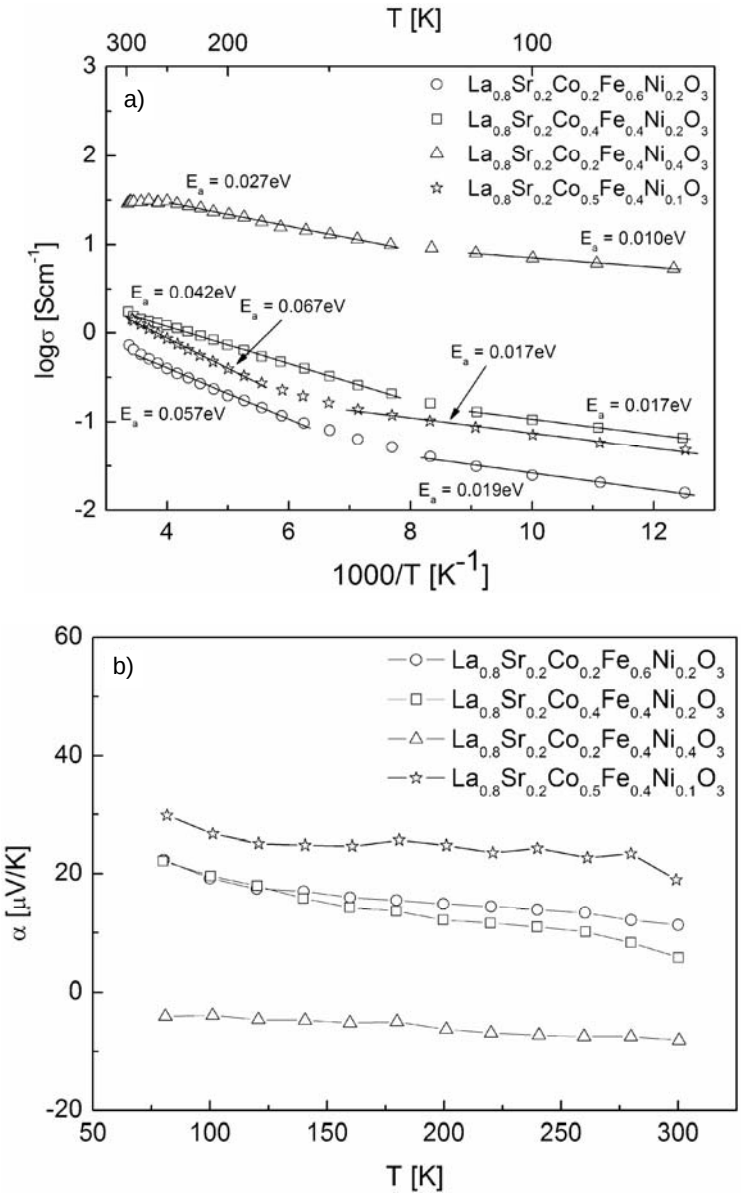

Fig. 5. Low-temperature (77–300 K) transport properties of $La_{0.8}Sr_{0.2}Co_{1-y-z}Fe_yNi_zO_3$ perovskites; a) electrical conductivity, b) thermoelectric power

The results of transport property measurements at low temperatures (77–300K) for $La_{0.9}Sr_{0.1}Co_{1-y-z}Fe_yNi_zO_3$ and $La_{0.8}Sr_{0.2}Co_{1-y-z}Fe_yNi_zO_3$ samples are presented in Figures 4 and 5. The observed dependence of electrical conductivity in a logσ–1/T plot cannot be fitted linearly in the entire temperature range. Two regions appear, one with a lower activation energy in the lower temperature range, and the other with a higher

activation energy in the higher temperature range. The highest electrical conductivity and low activation energies are observed for $La_{1-x}Sr_xCo_{0.2}Fe_{0.4}Ni_{0.4}O_3$ samples. This

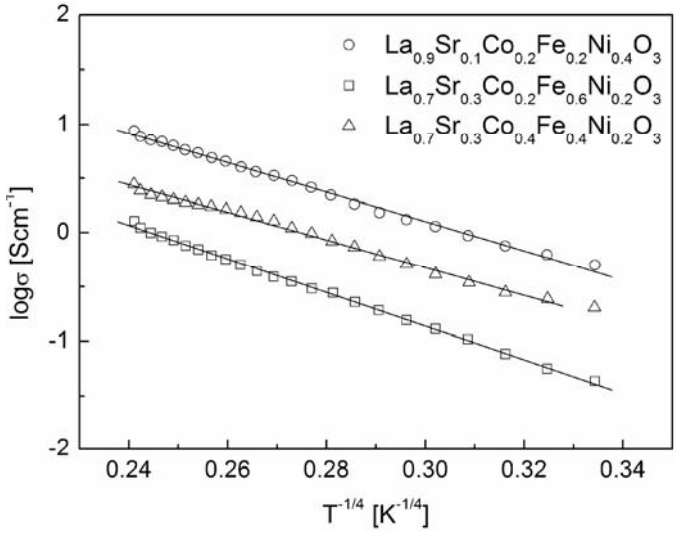

Fig. 6. Electrical conductivities of selected $La_{1-x}Sr_xCo_{1-y-z}Fe_yNi_zO_3$ perovskites in the low-temperature range (77–300 K), presented in a $\log\sigma - T^{-1/4}$ plot

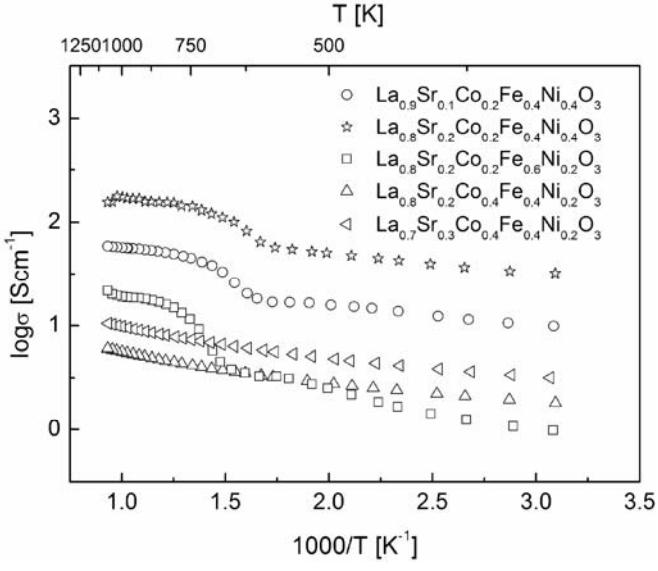

Fig. 7. Electrical conductivities of selected $La_{1-x}Sr_xCo_{1-y-z}Fe_yNi_zO_3$ perovskites at high temperatures

may be attributed to a higher Ni concentration, which leads to more metallic-like characteristics [7]. The influence of Co concentration on transport properties in the examined composition range is rather small. Similar effects can be observed in the

dependence of thermoelectric power on temperature. For $La_{1-x}Sr_xCo_{0.2}Fe_{0.4}Ni_{0.4}O_3$ samples, the thermoelectric power is negative in almost the entire temperature range, contrary to other samples. A negative TEP means that electrons are the dominant charge carriers. In Figure 6, the dependences of the electrical conductivity of selected $La_{1-x}Sr_xCo_{1-y-z}Fe_yNi_zO_{3-\delta}$ samples in a $\log\sigma$–$T^{-1/4}$ plot are presented. The observed linear dependence in these coordinates may be explained by using the 3D variable hopping range approach, which has also been observed in other perovskites [8].

High-temperature dc electrical conductivity measurements for selected $La_{1-x}Sr_xCo_{1-y-z}Fe_yNi_zO_3$ perovskites are presented in Figure 7. The change in the slope of the electrical conductivity, observed in the 600–750 K temperature range, can be related to a structural phase transition from hexagonal symmetry to a structure with higher symmetry. Relatively high electrical conductivity for samples with higher Sr and Ni content (175 $S \cdot cm^{-1}$ for $La_{0.8}Sr_{0.2}Co_{0.2}Fe_{0.4}Ni_{0.4}O_3$ at 1023 K) points to the necessity of further studies of perovskites from the (La, Sr)(Co, Fe, Ni)O_3 system.

4. Conclusions

The measured high-temperature (870–1070 K) dc electrical conductivity is relatively high for samples with high Sr and Ni content and needs further studies of perovskites belonging to the (La, Sr)(Co, Fe, Ni)O_3 system. The results of measurements suggest that optimised $La_{1-x}Sr_xCo_{1-y-z}Fe_yNi_zO_3$ samples in terms of chemical composition may possess attractive properties as cathode materials for IT–SOFCs.

Acknowledgements

This work is supported by the Polish Committee for Scientific Research under grant No. 3 T08A 013 26. One of the authors (K. Ś.) would like to thank the Foundation for Polish Science for financial support in the form of The Annual Stipends for Young Scientists program.

References

[1] SKINNER S.J., Fuel Cells Bull., 33 (2001), 6.
[2] IVERS-TIFFEE E., WEBER A., HERBSTRITT D., J. European Ceramic Soc., 21 (2001), 1805.
[3] CHIBA R., YOSHIMURA F., SAKURAI Y., Solid State Ionics, 124 (1999), 281.
[4] JIANG S.P., Solid State Ionics, 146 (2002), 1.
[5] KHARTON V.V., VISKUP A.P., BOCHKOV D.M., NAUMOVICH E.N., REUT O.P., Solid State Ionics, 110 (1998), 61.
[6] ŚWIERCZEK K., MARZEC J., OJCZYK W., MOLENDA J., Defect and Diffusion Forum, 237–240 (2005) 1293.
[7] CHAINANI A., SARMA D.D., DAS I., SAMPATHKUMARAN E.V., J. Phys.: Condens. Matter, 8 (1996), L631.
[8] JUNG W.-H., Physica B, 304 (2001), 75.

Received 10 December 2004
Revised 10 January 2005

Materials Science-Poland, Vol. 24, No. 1, 2006

The effect of aluminium on the electrical and electrochemical properties of phospho-olivine – a cathode material for Li-ion batteries

W. ZAJĄC, J. MARZEC, J. MOLENDA*

Faculty of Materials Science and Ceramics, AGH University of Science and Technology,
al. Mickiewicza 30, 30-059 Cracow, Poland

The structure, electrical and electrochemical properties of phospho-olivine ($LiFePO_4$) doped with aluminium were investigated. Some of the obtained samples had much higher electrical conductivities than the undoped material (10^{-4} S/cm compared to 10^{-10} S/cm). It has been stated that the enhanced conductivity is caused by a thin layer of reduced material that has metallic properties (probably iron phosphide), formed on the grain surfaces of phospho-olivine.

Key words: *$LiFePO_4$; phospho-olivine; lithium-ion battery; electrochemical properties*

1. Introduction

Contemporary portable electronic devices require very efficient energy supplies, such as Li-ion batteries. Lithium iron phosphate ($LiFePO_4$) with an olivine structure is potentially a very good cathode material for such batteries. Its major advantage is high theoretical capacity, approaching 170 mA·h/g, the voltage of about 3.5 V versus the metallic lithium anode, chemical stability, low price and nontoxicity. Goodenough et al. [1] have reported that it is possible to reversibly insert up to 0.8 mole of lithium per 1 mole of the compound at a current density of 0.05 mA/cm^2. In spite of its unquestioned advantageous characteristics, the material will not gain commercial importance unless some drawbacks are overcome. For instance, lithium iron phospho-olivine has low electrical conductivity, which is responsible for the low chemical diffusion coefficient of lithium and low current densities supplied by the battery. It has been reported that the conductivity of $LiFePO_4$ can be improved by doping, e.g.,

*Corresponding author, e-mail: molenda@uci.agh.edu.pl

by substituting lithium with Mg, Al, Cr, Ti, Nb, or W [2, 3]. Besides, compounds containing lithium and aluminium have also been tested as anode materials [4].

2. Experimental

The materials investigated were prepared from Li_2CO_3, $FeC_2O_4 \cdot 2H_2O$, $NH_4H_2PO_4$, and aluminium acetylacetate at high temperatures. The reactants were mixed in stoichiometric proportions in a mortar with addition of propanol. Thermal treatment was performed in two stages under flowing highly pure argon. The first stage, decomposition of the reactants at 350 °C, was continued for 12 h, the second stage, the synthesis at 800 °C, was continued for the next 12 h. After the first stage, the reactants were cooled down to room temperature and again mixed in a mortar. The phase composition of the products was analysed using an X'Pert Pro Philips X-ray diffractometer. Microstructures were examined by scanning electron microscopy (JEOL JSM – 5400 microscope equipped with EDS).

Electrical conductivity was measured by a four-probe ac method, and thermoelectric power was measured by a dynamic method with an increasing temperature gradient. The chemical diffusion coefficient of lithium was measured by GITT [5].

3. Results and discussion

The synthesized materials were: $Li_xAl_{0.01}FePO_4$ (x = 0.99–0.97) and $Li_{0.95}Al_{0.05}FePO_4$. These compositions were selected in order to examine the influence of lithium non-stoichiometry on the properties of aluminium-doped phospho-olivine.

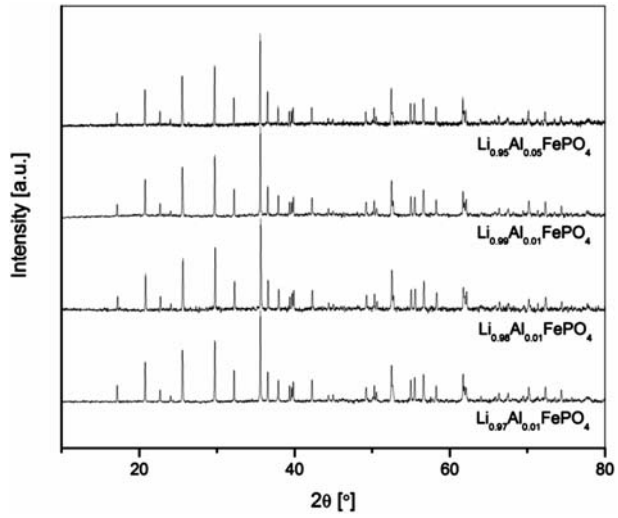

Fig. 1. X-ray diffraction patterns of the investigated samples of phospho-olivines

Figure 1 presents X-ray diffractograms of the investigated samples. The obtained materials are single-phase and consist of tryphyllite ($LiFePO_4$).

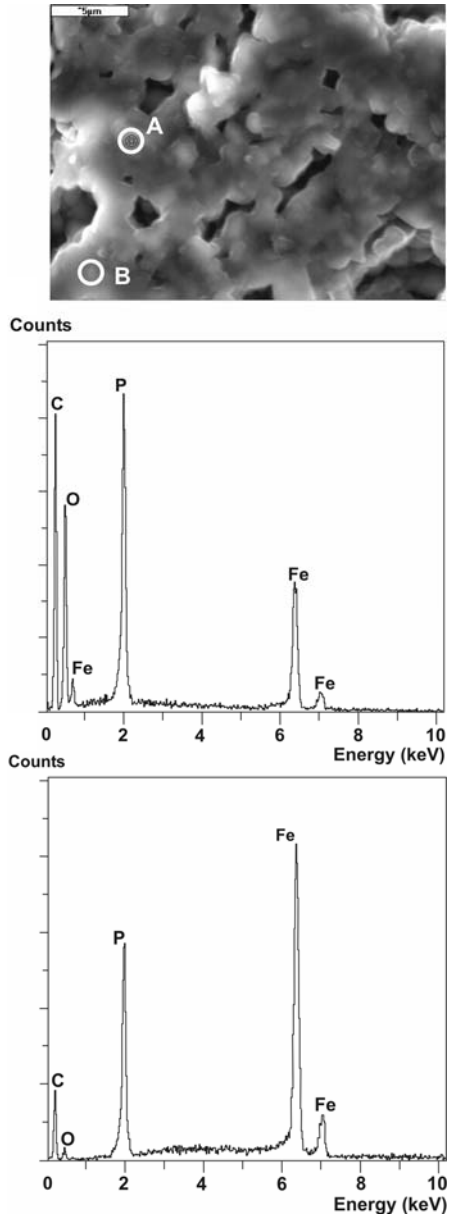

Fig. 2. Point EDS spectra for the sample with composition $Li_{0.99}Al_{0.01}FePO_4$

The analysis of SEM images indicates that the microstructures in all the samples are similar, independent of chemical composition. Examples SEM images of the frac-

tured samples are shown in Figures 2 and 3 (samples with the composition of $Li_{0.99}Al_{0.01}FePO_4$). The distribution of elements in all samples was examined by EDS.

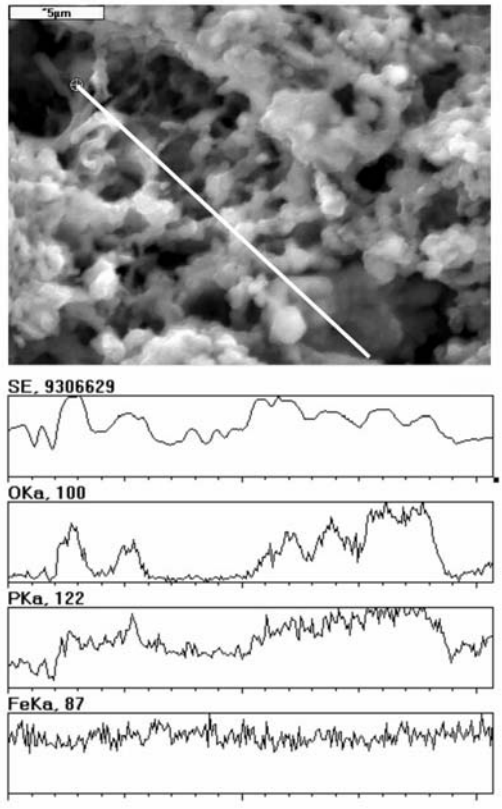

Fig. 3. Line EDS spectra for the sample with composition $Li_{0.99}Al_{0.01}FePO_4$

The results were also similar. Figures 2 and 3 illustrate EDS spectra for the sample with a composition of $Li_{0.99}Al_{0.01}FePO_4$. Carbon – visible in the plot – was purposely deposited on the surface of samples prior to analysis. These results indicate that the samples are not homogeneous. There are regions with lower concentrations of oxygen and simultaneously higher concentrations of iron and phosphorus, which suggests that the phosphate phase might locally reduce to phosphide, e.g. iron phosphide (the Fe/P ratio observed on the sample surface might result from the presence of FeP and Fe_2P). A similar hypothesis has been put forward by Canadian researchers [6] on the basis of EELS and TEM studies. Using a more advanced analytical tool they have stated that the grain boundary region is much richer in phosphorus, iron, and carbon (coming from the decomposition of substrates) than the bulk of grains.

With the selected substrates (Li_2CO_3, $FeC_2O_4{\cdot}2H_2O$, $NH_4H_2PO_4$, aluminium acetyl -acetate) and synthesis parameters, it is possible that several reducing agents (Fe, $Fe_x(CO)$, C, CO, NH_3) might be present in the reaction environment and partly reduce

$LiFePO_4$ to phosphides. The role of aluminium may be limited to raising lithium non-stoichiometry. As a result, the redox pairs Fe^{2+}/Fe^{3+} form and catalyse the reduction of

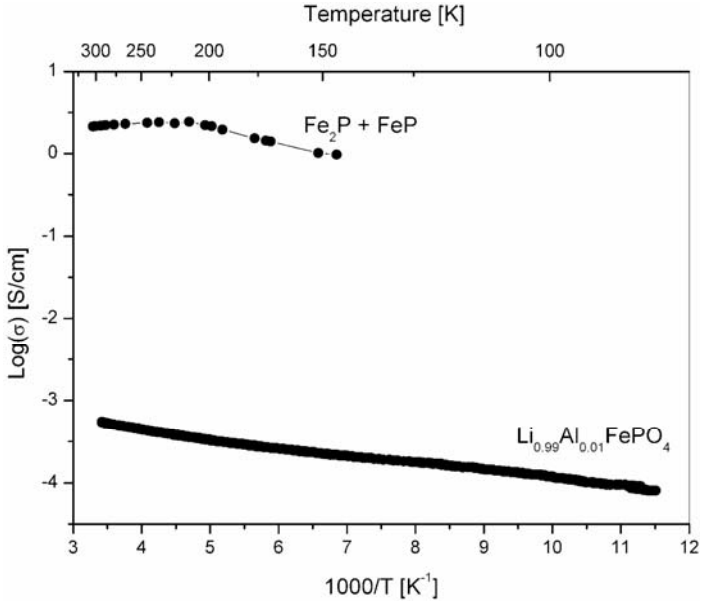

Fig. 4. Electrical conductivity of $Li_{0.99}Al_{0.01}FePO_4$ sample. For comparison data for a (FeP, Fe_2P) mixture are shown

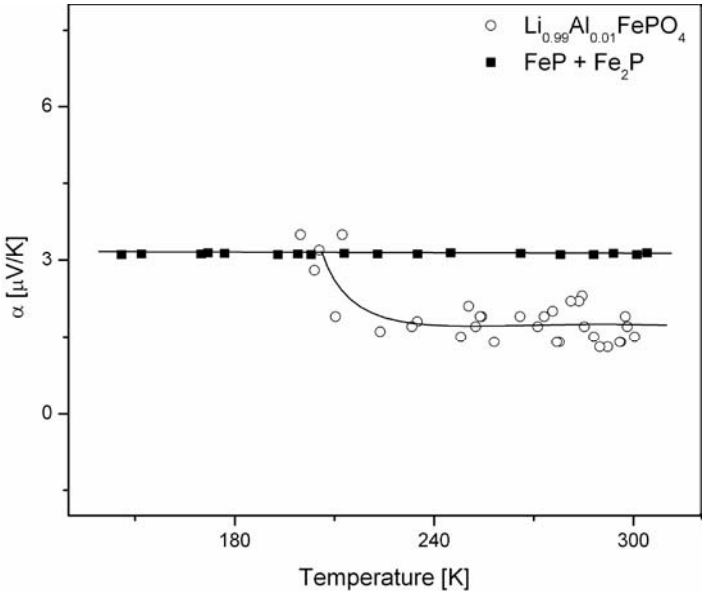

Fig. 5. Thermoelectric power of $Li_{0.99}Al_{0.01}FePO_4$ sample. For comparison data for a (FeP, Fe_2P) mixture are shown

phosphate. During the synthesis, this process occurs locally and does not disturb the overall stoichiometry of the sample, which according to XRD analysis does not contain any foreign phases.

The consequences of the mentioned processes are important for the electrical properties of the materials obtained. The electrical conductivity varied from $<10^{-7}$ to about 10^{-4} S/cm at room temperature. The conductivity could not be correlated with chemical composition. Figures 4 and 5 present the conductivity and thermoelectric power of $Li_{0.99}Al_{0.01}FePO_4$ (the sample with the highest conductivity). For comparison, the characteristics of the material received by a complete reduction of phosphoolivine to Fe_2P and FeP are also given [7]. Depending on whether a continuous conductive path is formed during synthesis or merely local precipitates, the conductivity may change by several orders of magnitude. This is probably the reason for inconsistent results obtained in different laboratories [2, 8] and for the irreproducibility of synthesis carried out under the same experimental conditions.

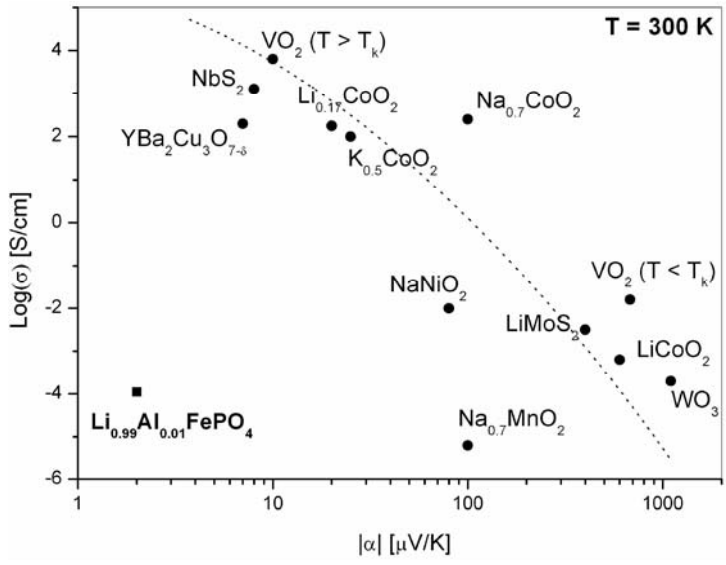

Fig. 6. Comparison between electrical conductivity and thermoelectric power for different transition metal compounds

It is interesting to note the non-typical electronic properties, i.e. a very low thermoelectric power (characteristic of metals) at room temperature of about 3 μV/K and at the same time a relatively low room-temperature conductivity of about 10^{-4} S/cm. The results obtained for many transition-metal compounds by Molenda et al. [9–12] indicate a corrrelation between conductivity and thermoelectric power. As follows from Figure 6, the properties of $LiFePO_4$ do not obey this relation. To explain this behaviour, it is suggested that a thin layer of iron phosphides with low resistivity creates a percolation path on the surface of the grains of the material, which has a much

higher resistivity ($LiFePO_4$). The low electrical conductivity may be caused by a low thickness of this layer, and thermoelectric power – independent of size effects – assumes values characteristic of the component responsible for this parameter.

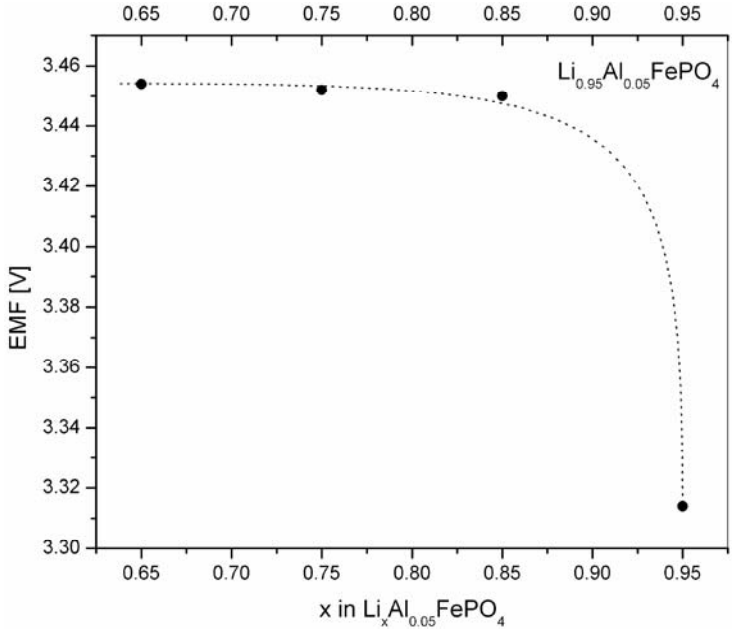

Fig. 7. EMF of the Li / Li^+ / $Li_{0.95}Al_{0.05}FePO_4$ cell as a function of lithium concentration

Figure 7 shows the EMF of a $Li/Li^+ \mid Li_{0.95}Al_{0.05}FePO_4$ cell as a function of lithium concentration. Except for the initial sudden jump, there are no variations in EMF during the charging cycle. Such behaviour can be explained by a two-phase operation mechanism of the cathode material:

$$LiFePO_4 - xLi^+ - xe^- \rightarrow (1-x)LiFePO_4 + xFePO_4 \qquad (1)$$

The coexistence of the two phases, $LiFePO_4$ and $FePO_4$, in equilibrium during the whole process maintains a constant value of the voltage. This statement is supported by XRD analysis of the cathode material based on the conductive phospho-olivine with an initial composition of $Li_{0.99}Al_{0.01}FePO_4$ after 50% delithiation (Fig. 8). Two phases can be identified in this diffractogram, one with the structure of tryphyllite, $LiFePO_4$, and another with the structure of heterosite, $FePO_4$. The two-phase mechanism has been previously reported for undoped phospho-olivines with low bulk conductivities [1], but in the samples obtained in this work, with conductivities of about 10^{-4} S/cm, the diffusional mechanism of deintercalation has been anticipated.

The chemical diffusion coefficients of lithium in the obtained materials measured by GITT were very low (10^{-12}–10^{-17} cm^2/s), close to that of pure phospho-olivine $LiFePO_4$ [13].

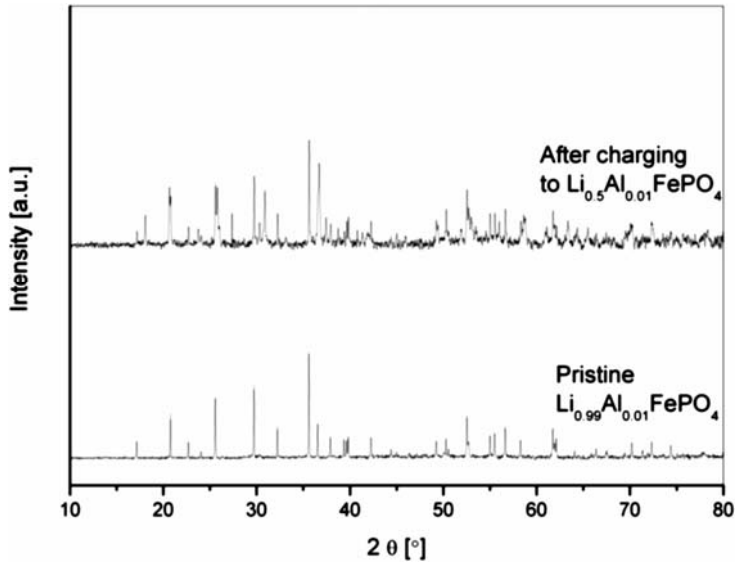

Fig. 8. X-ray diffraction patterns of the cathode material based on the conductive phospho-olivine with the initial composition $Li_{0.99}Al_{0.01}FePO_4$ before and after 50% delithiation

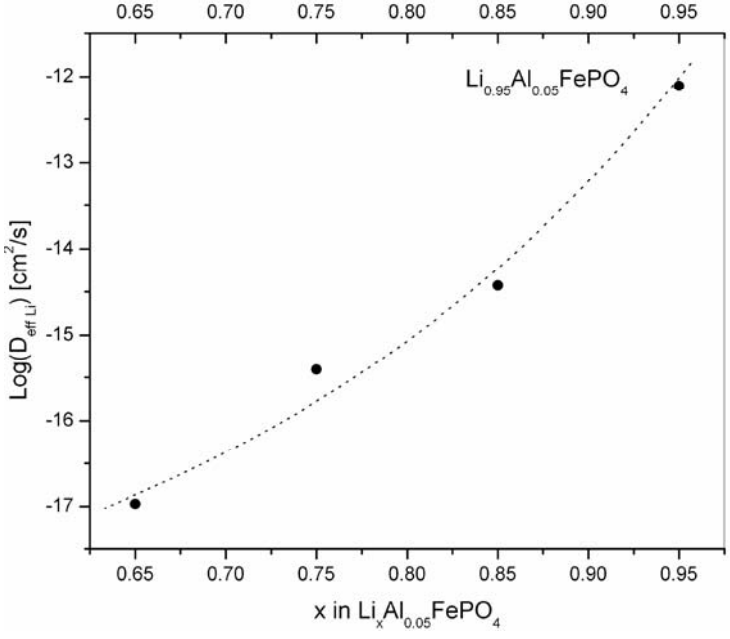

Fig. 9. Dependence of the chemical diffusion coefficient of lithium as a function of lithium concentration in the cathode material $Li_{0.95}Al_{0.01}FePO_4$

Figure 9 shows an example of the dependence of the lithium chemical diffusion coefficient on lithium concentration in the cathode material $Li_{0.95}Al_{0.05}FePO_4$. Should

the conductive samples of doped phospho-olivine have some bulk conductivity, the increasing electronic conductivity would enhance the mobility of the lithium ions. This, however, is not the case. The quasi-metallic conductivity is related to the phosphide layer that covers the non-conducting phospho-olivine grains. Aluminium doping, in spite of the apparently metallic type of conduction, did not change the mechanism of lithium intercalation/deintercalation during the operation cycle of the cell, i.e. it did not activate the diffusional mechanism of intercalation. This is another strong argument against the bulk metallic properties of aluminium-doped phospho-olivine.

4. Conclusions

The distribution of elements in the obtained samples is not uniform. EDS reveals regions with lowered concentrations of oxygen, which indicate the partial reduction of $LiFePO_4$ to iron phosphides.

EMF variations for $Li\,|\,Li^+\,|\,Li_xAl_{0.01}FePO_4$ cells and X-ray diffractograms of the conductive cathode material after partial delithiation allow the conclusion that the reaction taking place in the charging cycle of the cell proceeds according to a two -phase mechanism. In the cathode material, which has a relatively high conductivity, the diffusional mechanism of lithium does not operate, meaning that aluminium as a dopant does not improve the bulk electronic properties of $LiFePO_4$. It catalyses the reduction of phosphate and the formation of a thin surface layer composed of iron phosphides.

Acknowledgements

The work supported by the Polish Committee for Scientific Research under the grant No. 4T08A 020 25.

References

[1] PADHI A.K., NANJUNDASWAMY K.S., GOODENOUGH J.B., J. Electrochem. Soc., 144 (1997), 1188.
[2] CHUNG S.-Y., BLOKING J.T., CHIANG Y.-M, Nature Mater., 1 (2002), 123.
[3] SHI S., LIU L., OUYANG C., WANG D.-S., WANG Z., CHEN L., HUANG X., Phys. Rev., B 68 (2003), 195108.
[4] JORGENSEN J.E., Solid State Ionics, 18–19 (1986), 852.
[5] WEPPNER W., HUGGINS R.A., J. Electrochem. Soc., 124 (1977), 1569.
[6] HERLE P.S., ELLIS B., COOMBS N., NAZAR L.F., Nature, 3 (2004), 147.
[7] DUDEK M., MOLENDA J., Private communication.
[8] RAVET N., ABOUIMRANE A., ARMAND M., Nature Mater. Correspondence from our readers, 2 (2003).
[9] MOLENDA J., BĄK T., MARZEC J., Phys Stat Sol., 156 (1996), 159.
[10] MOLENDA J., KUBIK A., Solid State Ionics, 117 (1999), 57.
[11] MOLENDA J., BĄK T., STOKŁOSA A., Physica, C 207 (1993), 147.
[12] MOLENDA J., KRZYWANEK K., Solid State Phenomena, 39–40 (1994), 127.
[13] PROSINI P.P., LISI M., ZANE D., PASQUALI M., Solid State Ionics, 148 (2002), 45.

Received 10 December 2004
Revised 17 February 2005

Materials Science-Poland, Vol. 24, No. 1, 2006

Li-ion conducting organic–inorganic hybrid electrolytes

E. ŻELAZOWSKA[1*], M. BORCZUCH-ŁĄCZKA[2],
E. RYSIAKIEWICZ-PASEK[3], T. ZDUNIEWICZ[1]

[1]Institute of Glass and Ceramics, Cracow Branch, ul. Lipowa 3, 30-702 Cracow, Poland

[2]Faculty of Materials Science and Ceramics, University of Mining and Metallurgy,
al. Mickiewicza 30, 30-059 Cracow, Poland

[3]Institute of Physics, Wrocław University of Technology,
Wybrzeże Wyspiańskiego 27, 50-370 Wrocław, Poland

Lithium ion conducting, sol-gel derived, amorphous, organic–inorganic hybrid electrolytes were obtained from tetraethoxysilane, poly(ethylene oxide), propylene oxide, propylene carbonate, acetonitrile and $LiClO_4$ precursors, and were investigated for their morphological and structural properties by scanning electron microscopy equipped with energy dispersive X-ray spectroscopy (SEM/EDX), X-ray diffraction (XRD), infrared spectroscopy, and nitrogen adsorption at 77 K. A room-temperature conductivity of *ca.* 10^{-4}–10^{-3} $S \cdot cm^{-1}$, attributed to an amorphous character and the organic addition, as well as results of testing in WO_3–based electrochromic thin-film systems, make the hybrid materials obtained promising as electrolytes for ambient temperature electrochemical and optoelectronic applications.

Key words: *organic-inorganic hybrid; sol-gel; solid ionic electrolyte; electrochromic coating*

1. Introduction

Solid materials with high ionic conductivities at ambient temperatures have attracted much attention in recent years, because of their possible application as electrolytes in advanced optoelectronic and electrochemical devices, such as rechargeable lithium batteries, and electrochromic windows and displays [1-3]. Electrolytes for applications in electrochromic windows are additionally required to be colourless and transparent. Polymer electrolytes at ambient temperatures have large contents of crystalline regions, causing a decrease in ionic conductivity [3-7]. On the other hand, due to the process starting from solutions of precursors prepared at room temperature, the sol-gel route has been successfully employed for producing amorphous transparent

*Corresponding author, e-mail: ezelazowska@isic.krakow.pl

materials, including organically modified gels [8–10]. Among others, Park and Nagai [10] have reported on sol-gel derived organic-inorganic hybrid proton-exchange membranes for fuel cells application.

In this work, sol-gel derived, lithium ion conductive organic-inorganic hybrid electrolytes were synthesized and investigated by scanning electron microscopy equipped with energy dispersive X-ray spectroscopy SEM/EDX, X-ray diffraction (XRD), infrared spectroscopy (FTIR) and nitrogen adsorption at 77 K. D.c. conductivity was measured using a four-electrode cell. Photometric and current–voltage characteristics were observed in WO_3 - based thin film electrochromic systems, at (±) polarized dc potential applied through a potentiostat/galvanostat.

2. Experimental

Silica components of organic- inorganic hybrids, and silica gels prepared for comparison, were produced from TEOS [$Si(OC_2H_5)_4$] and distilled water with the molar ratio of TEOS : H_2O = 1 : 4. As a catalyst, 36.6 % HCl was added, up to pH = 2. Organic parts were prepared from PEO, $–(CH_2\ CH_2O)_n–$ ($M_w \approx 600\ 000$), propylene oxide (PO, C_3H_6O, M_w = 58.08), propylene carbonate (PC, C_4H_6O), dichloromethane (CH_2Cl_2), ethanol (C_2H_5OH) and acetonitrile (CH_3CN) (Table 1). As a salt for doping at weight ratio of about 0.02 and 0.03 with respect to the mass of fresh gels, $LiClO_4$ dissolved in PC or water (sample C) was employed. Solutions of TEOS, after stirring for 1 hour, were mixed with solution of PEO and/or PO and PC, and the resulting mixtures were stirred for 3–3.5 hours, up to the end of hydrolysis reaction. Mass fractions of organic additives were of *ca.* 20 mass% in gels, with a weight ratio of PEO: PO and/or PC equal to 1, and molar ratio of PO: PC equal to 1.

Table 1. Components of starting solutions for gels under investigation

Sample	Components	$LiClO_4$ weight fraction	Appearance, remarks
A	TEOS, PC	0.02	organic glass, colourless, transparent
B	TEOS, PEO/CH_2Cl_2, PC	0.03	
C	TEOS, PEO/CH_3CN	0.02	
K	TEOS, PEO/CH_3CN, PC	0.02	
D	TEOS, PO, PC	0.02	organic glass, slightly opalescent
F	TEOS	0.03	transparent silica glass

Fresh gels were stored for two weeks with a small surplus of ethanol and/or dichloromethane and then dried for a week at ambient temperature and for 3–5 h at temperatures of 80–230 ºC. The hybrid gels to be used as electrolytes were spread onto glass sheets with thin films of: (SnO_2:F) and WO_3, and V_2O_5 and CeO_2/TiO_2, respectively, prepared by pyrolysis method, as was described earlier [11].

3. Results and discussion

The duration of sol-gel transformation ranged from several minutes for gel D to 1.5, 2, 3, 2–4 and 6 days, respectively for gels A, B, C, K, and pure or lithium doped silica gels. Hybrid gels remained transparent after 3-hour heating at temperatures 125–150 ºC and XRD patterns of all the gels obtained were typical of amorphous materials. SEM images of hybrid gels are shown in Figures 1a–d. FTIR spectra for hybrid gels B, C, D, K are shown in Figure 2. Assignments of the characteristic absorption bands in infrared are listed in Table 2.

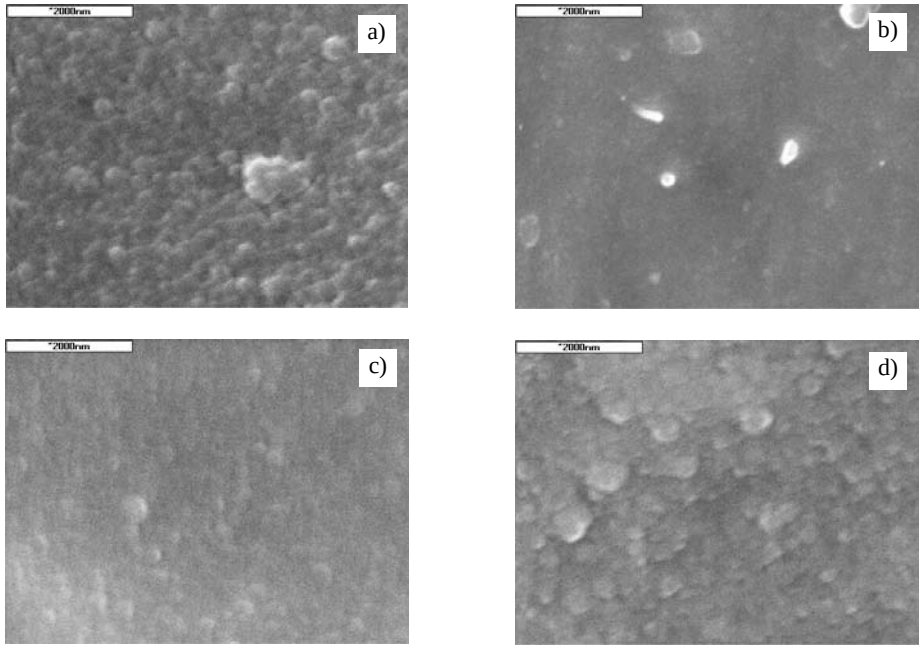

Fig. 1. SEM images (at magnification of 20 000×, the bar corresponds to 2000 nm) for samples of the hybrid gels heated at 125 ºC: a) gel C, b) gel K, c) gel D, d) gel B

In FTIR spectra of gels under investigation (Fig. 2), there can be seen absorption bands characteristic of water in molecular and adsorbed forms (ca. 3400 and 1620 cm^{-1}, respectively). Lithium incorporation into gel structures, resulting in breaking of the oxygen bridges, appears in splitting of the main absorption band, localized at ca. 1080 cm^{-1}. The absorption band at ca. 782 cm^{-1} is characteristic of the hybrid gels only. According to Gunzler and Gremlich [12], it can be ascribed to vibrations of O–Si–C_nH_m species, providing the evidence of formation of the hybrid structure in gels with organic additions, in which the organic and inorganic parts are connected by oxygen bridges. Heating at temperatures of ca. 200 ºC resulted in retaining vibrations of oxygen bridges Si–O–Si only, connected with disappearing of organic parts. Typical results of texture observations are shown in Table 3.

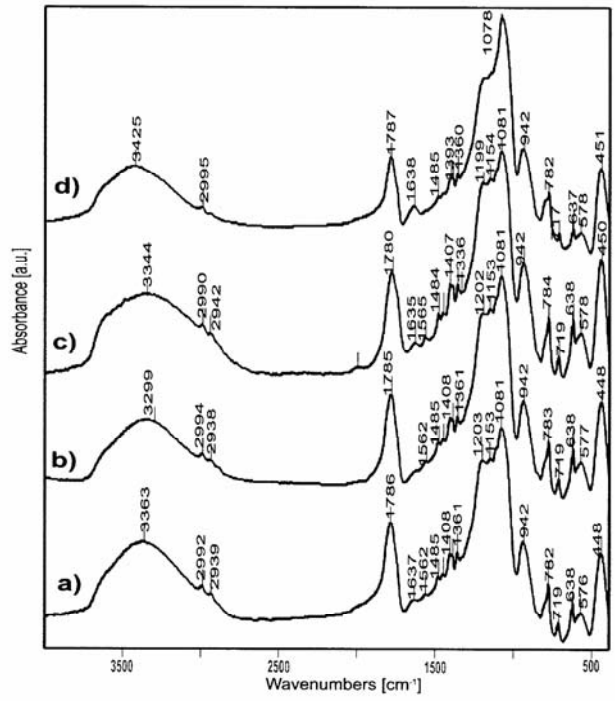

Fig. 2. FTIR spectra of organic-inorganic hybrid gels after heating at 80 ºC:
a) gel C, b) gel B, c) gel K, d) gel D

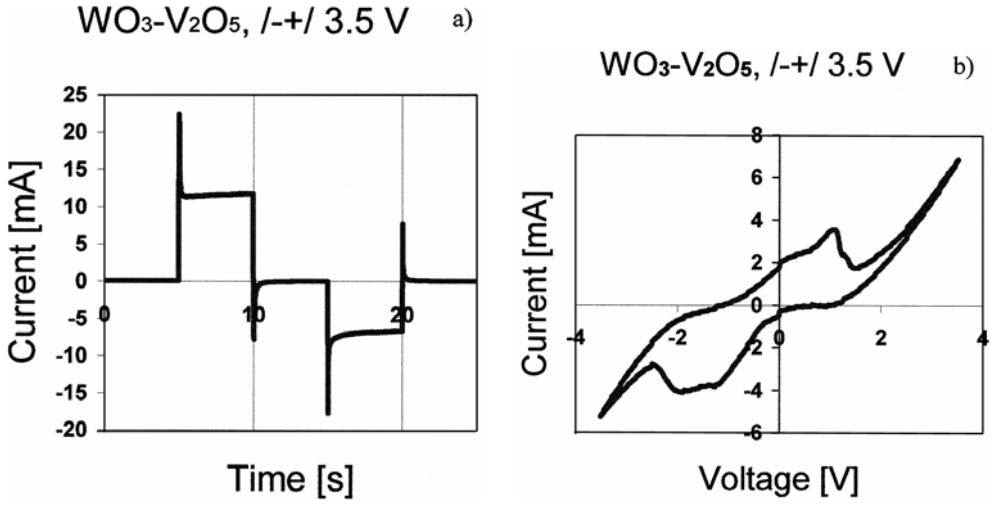

Fig. 3. Current response (a) and cyclic voltammogram (b) for tungsten oxide/hybrid electrolyte, $(LiClO_4)_{0.2}$ $(TEOS/PEO/PC)_{0.8}$/vanadium oxide/thin film electrochromic system on glass coated with fluorine doped SnO_2, after cycling with voltage of ± 3.5 V (cycled area ca. 2 cm^2, scan rate 50 mV/s)

Table 2. Assignments of the characteristic infrared absorption bands [cm^{-1}] [12–15]

B	C	D	K	F	Assignment
448	448	451	450	468	ρ Si-O
576	576	578	576	554	Li in $LiClO_4$ Li with organics
628–638	628–638	637	628	628-638	ClO_4, Li – organics,
719	719	717	720		ν SiO–C_2H_5, organics
783	782	782	783	802	ν_s Si–O–Si, ν_{as} Si–C Si–O–Si–C_nH_m
942	942	942	942	941	ν_{as} Si–OH
1081	1081	1078	1081	1090	ν_{as} Si–O–Si
1153	1153		1154	1110 1147	ν Si–O–Si,
1202	1203		1199		ν C–C, –OR (C_2H_5), organics
1361	1361	1360	1392		organics, ν CH_3
1393	1393	1393	1407		ν CH_2 –O in ethers
1408	1408	1407 1485	1450		
	1562 1637	1638	1565 1635	1639	H–O–H, molecular
1785	1786	1787	1780		organics, C–O
2938	2939	2995	2942		ν_{as} CH_2, ν C–H_x organic groups
3362	3363 3375	3425	3299	3458	ν OH, adsorbed H–O–H,

Table 3. Typical results of texture examination

Material	F	A	B
BET surface area [m^2/g]	248.96	61.84	336.97
Langmuir surface area [m^2/g]	347.87	99.34	484.59
Micro-pore area [cm^3/g]	2.6048	45.82	118.79
BJH meso-pores volume [cm^3/g]	0.4311	–	0.1866
BET micro-pore diameter [nm]	6.7103	1.9357	2.9993
BJH average pore diameter [nm]	5.6562	–	3.7225

dc conductivities at 25 ºC (σ_{25}) for the species A, B, C, D, K and F were of (1.31; 8.29; 1.37; 1.58; 4.26;) $\times 10^{-3}$ $S \cdot cm^{-1}$ and 5.6×10^{-5}, respectively. The SEM/EDX, nitrogen adsorption and ionic conductivity examination results have shown that the obtained hybrid materials were porous, with morphologies and conductivities strongly influenced by organic additives and lithium salt doping [16]. In silica glass and silica gel derived materials, both organic additions and doping with lithium, are expected to change coordination of oxygen atoms around silicon and lithium, causing partial dissociation of immobile species from the non-bridging oxygen atoms and also expansion of the silica host, resulting in enlargement of pathways available for lithium ions

migration [6–7, 16]. In all of the hybrid gels obtained in this work, both textures and ionic conductivities were generally observed to increase with content of low-molecular-weight organic additives. The enhancement of conductivity was observed especially in samples containing PEO together with addition of PC. These results can be explained in frame of a free-volume model as well as the percolation model, used for fast ion conductive glasses and polymers [4–7].

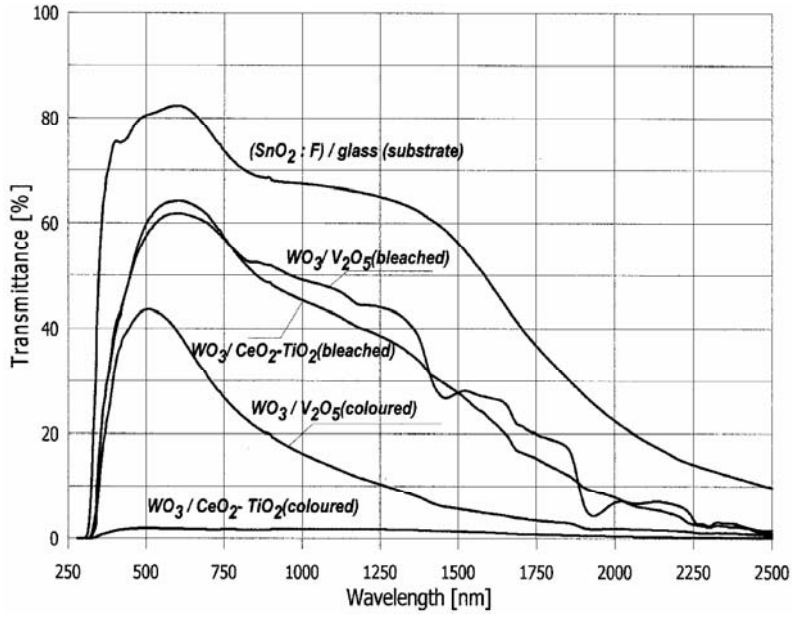

Fig. 4. Transmittance as a function of the wavelength for electrochromic cells with thin films of WO_3 as active electrode and V_2O_5 or CeO_2 –TiO_2 as counter-electrodes, coated by spray pyrolysis onto (SnO_2: F) substrate, and the hybrid organic-inorganic electrolytes examined: C and G, respectively. The spectra were taken for the cells in both lithium intercalated (coloured) and lithium deintercalated (bleached) states, at dc voltage of (±)1.5V and (±)2.5 V, applied to the cells with V_2O_5 or CeO_2–TiO_2 counter electrodes, respectively

Accordingly to relatively large ionic conductivity, of about 10^{-4}–10^{-3} S·cm^{-1}, all hybrid gels obtained in this work, when examined in thin film electrochromic WO_3 -based cells have proved to be able to take effective part in reversible electrochromic reactions depending on intercalation/deintercalation of lithium ions associated with injection/extraction of electrons under cycling with low, ± polarized dc voltage and resulting in deeply blue or colourless state of the tungsten oxide layer. A typical current response to a signal of a rectangular shape as well as a cyclic voltammogram (CV) for a cell with electrolyte under investigation are shown in Fig. 3a, b. The symmetric situation and shape of cathodic and anodic peaks for active- and counter-electrode due to ion insertion and extraction respectively, indicate materials under investigation to be kinetically favoured insertion hosts. On the other hand, relatively sharp peaks at the highest values of the voltage applied (in Fig. 3 b, at voltages higher than ca. ± 2.5–3.5 V) makes

possible the association of lithium and proton conductance, connected with the presence of water, which has been revealed by infrared spectroscopy in all gels under investigation. Typical photometric transmission characteristics for WO_3-based electrochromic systems with hybrid gels as electrolytes and two different materials of the counter-electrode are given in Fig. 4. The double insertion of lithium ions and electrons into the WO_3 film with active electrochromic properties was accompanied by a significant optical absorption phenomenon which lead to a deep blue colouration due to formation so called tungsten bronze and such electrochromic reactions were reversible.

4. Conclusion

Sol-gel derived, lithium-conducting, organic–inorganic hybrid gel materials obtained in this study from TEOS, PEO, PO and PC precursors, have proved to be electrochemically effective in reversible electrochromic reactions, which make them to be prospective electrolytes for ambient temperature electrochemical and optoelectronic applications. Relatively high room-temperature ionic conductivity, of about 10^{-4}–10^{-3} $S \cdot cm^{-1}$ can be attributed to amorphous character and organic additions. The hybrid structure of the gels obtained in this work, which has been revealed by FTIR investigation, can be ascribed to the formation of bonds between species of organic and inorganic components and incorporation of the organic groups into the silica gel host, resulting in development of structure more accessible for lithium ions migration. With aim to determine exactly a conductance mechanism in electrolytes prepared in this work, further investigations have been undertaken.

Acknowledgement

Financial support of this work provided by the Ministry of Education and Science, Department of Scientific Research, Poland, Grant No 4 T08D 001 25 is gratefully acknowledged.

References

[1] GREENBERG CH.B., Thin Solid Films, 251 (1994), 81.
[2] GLÄSER, H.J., *Large Area Glass Coating*, Von Ardenne, Dresden, 2000, pp. 378–380.
[3] AIHARA Y., APPETTECCHI G.B., SCROSATI B., J. Electrochem. Soc., 147 (2002), A849.
[4] FAN J., MARZKE R.F., SANCHEZ E., ANGELL C.A., J. Non-Cryst. Solids, 172-174 (1994), 1178.
[5] HUNT A., J. Non-Cryst. Solids, 175 (1994), 59.
[6] DOI A., J. Non-Cryst. Solids, 246 (1999), 155.
[7] KUUTTI L.M.A., SEPPÄLÄ J.V., PASSINIEMI P., Solid State Ionics, 39 (1990), 151.
[8] PAJONK G.M., J. Non-Cryst. Solids, 225 (1998), 307.
[9] PARK M., KOMARNENI S., CHOI J., J. Mater.Sci., 33 (1998), 3817.
[10] PARK Y.-IL, NAGAI M., J. Electrochem. Soc., 148 (2001), A616.
[11] ŻELAZOWSKA E., ZIEMBA B., LACHMAN W., Optica Appl., 30 (2000), 663.
[12] GUNZLER H., GREMLICH H.-U., *IR Spectroscopy, An Introduction*, Wiley–VCH, Weinheim, 2002.
[13] MARAGE P., LANGLET M., JOUBERT J.C., Thin Solid Films, 238 (1994), 218.

[14] YING J.Y., BENZIGER J.B., NAVROTSKY A., J. Am. Ceram. Soc., 76 (1993), 2571.
[15] MUNRO B., Glastech. Ber. Glass Sci. Technol., 68 (1995), 123.
[16] WAKAMATSU H., SZU S.-P., KLEIN L.C., GREENBLATT M., J. Non-Cryst. Solids, 147–148 (1992), 668.

Received 10 December 2004
Revised 24 January 2005

Materials Science-Poland, Vol. 24, No. 1, 2006

New composite materials prepared by high-pressure infiltration of superionic glasses into diamond powder compacts

M. FOLTYN[1], M. ZGIRSKI[1], J. GARBARCZYK[1*], M. WASIUCIONEK[1], B. PAŁOSZ[2], S. GIERLOTKA[2], J.L. NOWIŃSKI[1]

[1]Faculty of Physics, Warsaw University of Technology, ul. Koszykowa 75, 00-662 Warsaw, Poland

[2]High Pressure Research Center, Polish Academy of Sciences, ul. Sokołowska 29/37, 01-142 Warsaw, Poland

Glassy-crystalline composites have been prepared by infiltrating highly conducting silver vanadate glasses into diamond powder compacts. The process of infiltration was carried out at a high isostatic pressure (from 1.5 to 8 GPa) and temperatures up to 800 °C. The resulting composites have conductivities comparable to those of glasses used for infiltration, but exhibit a wider range of thermal stability (up to 300 °C) than glasses. Additionally, they have much better mechanical properties, in particular, being less brittle and exhibiting higher microhardness than glasses.

Key words: *glass-crystalline composite; impedance spectroscopy; ionic conductor; silver vanadate composite; high-pressure infiltration*

1. Introduction

In recent years, the focus in the area of solid-state ionics has been shifting towards composite materials, which have become frequently used as electrodes or solid electrolytes in batteries, gas sensors, fuel cells, and electrochromic windows [1]. The advantages of composite materials over single-phase systems are well-documented, e.g. often higher conductivity, better performance in operation, improved mechanical properties without substantial loss of good electrical or electrochemical performance. The quest for novel composite materials for electrodes or electrolytes is intensive and multidirectional [2].

In this work, we present the results of studies on the electrical properties of novel composite solid ionic conductors, also characterized by X-ray diffractometry (XRD) and

*Corresponding author, e-mail: jegar@mech.pw.edu.pl

scanning electron microscopy (SEM). These materials were prepared by the infiltration of liquefied silver conducting glasses of the $AgI–Ag_2O–V_2O_5$ system into diamond powder compacts. The process has been carried out at high pressures (1.5–8 GPa) and elevated temperatures (200–800 °C). Such an infiltration process has been found very effective for preparing composites with metals, magnetic, and semiconducting materials introduced into diamond, SiC or other hard powder matrices.

2. Experimental

Silver-vanadate glasses were prepared by a standard melt-quenching method [3]. The process of infiltrating ion-conducting glasses into hard powder compacts matrices has been described in [4]. The composites were obtained by infiltrating $40AgI·38Ag_2O·22V_2O_5$ glass into compacts of diamond powder consisting of 0.5 or 30–40 μm grains. A pre-pressed layer of diamond powder was covered with a layer of ground glass in a graphite tube serving as a furnace. These two layers, together with ceramic boron nitride plugs, were placed in a special pressure container. The container was mounted between the anvils of a hydraulic press and heated up to 200–800 °C under high pressure (1.5–8 GPa). Under these conditions, the liquefied glass penetrated into voids between the diamond grains. The final products had the form of compact and hard cylinders, 5 mm in diameter and 2 mm thick, much more resistant to fracture than the glasses.

X-ray diffraction (XRD) analyses were carried out using a Siemens D 5000 diffractometer with a CuK_α line. The XRD patterns of the as-received glasses confirmed their amorphousness. The glass transition temperature (T_g) of the glasses used for infiltration as determined by differential scanning calorimetry (DSC) was close to 100 °C. Scanning electron microscopy (SEM) observations were carried out using LEO 1530 equipment. Impedance measurements were carried out using a computer-controlled setup based on a Solartron 1260 impedance/gain phase analyzer in the temperature range 20–300 ºC and frequency range from 10 mHz to 10 MHz. Prior to measurements, gold electrodes were sputtered onto opposite polished faces of the samples. The fitting package FIRDAC [5] was used for the numerical analysis of the impedance spectra.

3. Results

Preparation. Before obtaining composites of good quality, multiple trials had to be carried out in order to optimise the experimental conditions for infiltration. The main adjustable experimental factors were pressure and temperature. The best composites of $AgI–Ag_2O–V_2O_5$ glasses were obtained when infiltration was carried out at $p \approx 1.5–3$ GPa and $T \approx 200–300$ °C. Samples prepared under other conditions, in particular at higher temperatures, were of poorer quality, they contained unfilled voids and easily decomposed when subject to external forces. In these cases it was obvious that infiltration was incomplete and the distribution of the glass phase in the composite was far from homogeneous.

Microstructure and mechanical properties. SEM pictures of the composites prepared at optimum conditions (specified above) have revealed that the amorphous phase, filling the space between grains of the matrix, forms many separate small "nodules" situated at the grains of the diamond matrix. When the composite was heated up to ca. 200 ºC and then cooled down to room temperature, the "nodules" disappeared and the amorphous phase formed a continuous layer over the grain surfaces.

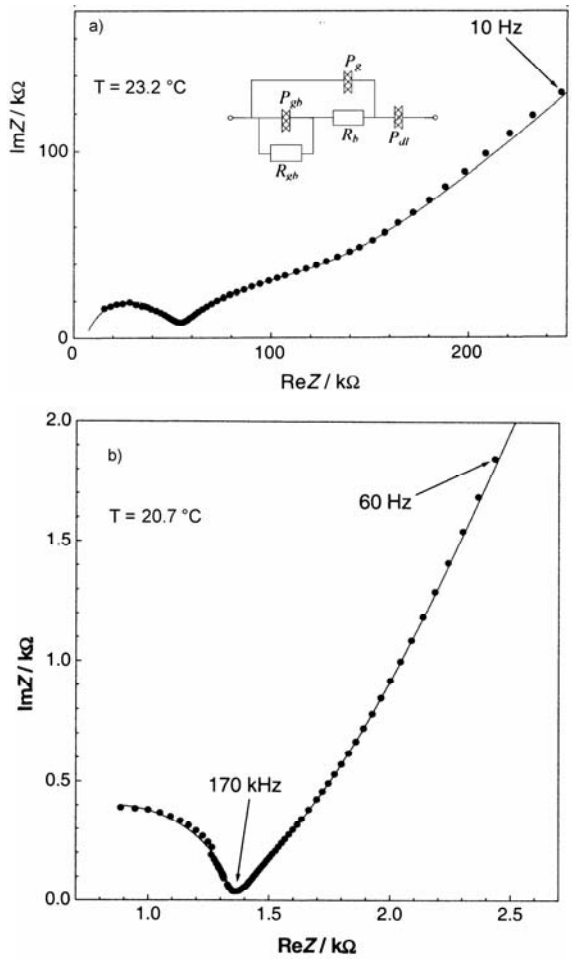

Fig. 1. Room-temperature impedance spectra of: a) composite $40AgI{\cdot}38Ag_2O{\cdot}22V_2O_5$ infiltrated in a diamond (30–40 μm) matrix, b) glass $40AgI{\cdot}38Ag_2O{\cdot}22V_2O_5$. The equivalent circuit, used for fitting the data, is shown as an inset in Fig.1a. Fits are represented by solid lines

Mechanical properties were sampled by measurements of microhardness by the Vickers method. It was found that the microhardness of the composites is more than twice higher than that of the glass (176 versus 72, respectively).

Electrical properties. Impedance spectra of the as-prepared composites were substantially different from those of the glasses used for infiltration (Fig. 1a, b, respectively). In the case of the composites, the spectra consisted of a high-frequency semicircle, followed by a suppressed arc at intermediate frequencies and a linear part inclined at about 45º to the real *Z* axis. This spectrum was fitted using the equivalent circuit shown in the inset of Figure 1a. The result of fitting (line in Fig. 1a) to the experimental spectra (points in Fig. 1a) was satisfactory. The spectra of the glasses used for infiltration (Fig. 1b) consisted of a semicircle at high frequencies and a linear

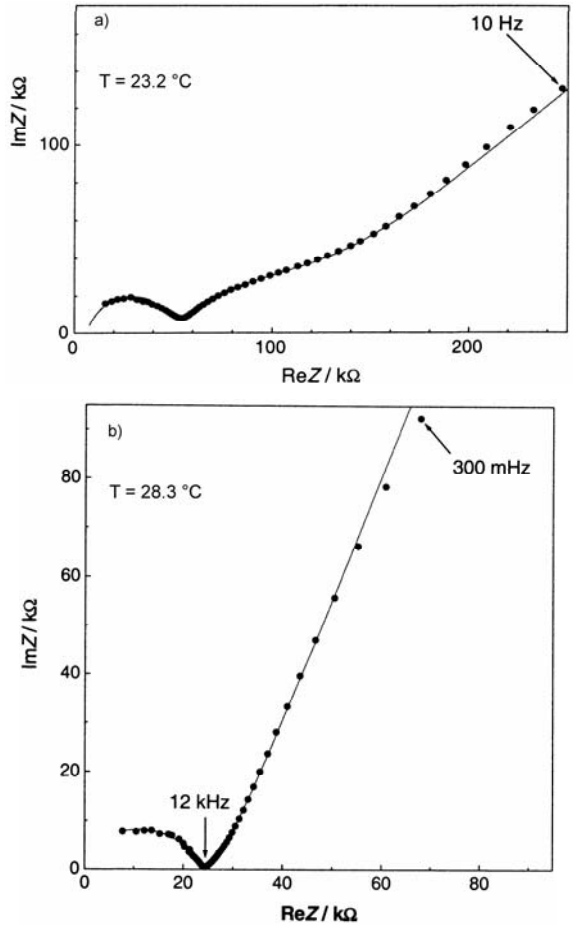

Fig. 2. Room-temperature impedance spectra of the composite $40AgI{\cdot}38Ag_2O{\cdot}22V_2O_5$ infiltrated in a diamond matrix a) before, b) after heating up to 200 ºC

spur at the low-frequency end, with a narrow intermediate region between these two main parts. Despite the differences in the shapes of the spectra of the composite and glass, the same equivalent circuit was successfully used to fit both. After a heating-cooling cycle, the impedance spectra of the composites at room temperature (Fig. 2b)

were different than those before the heat treatment (Fig. 2a). They were more similar to the spectra of the glasses used for infiltration (cf. Fig. 1b).

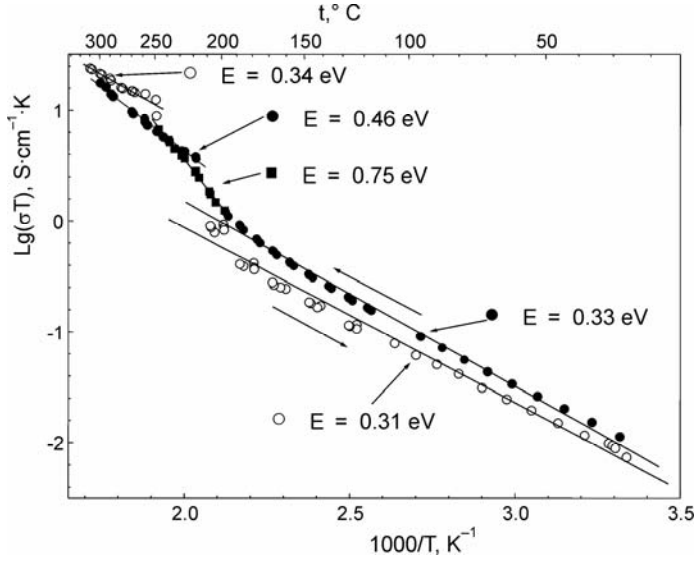

Fig. 3. Temperature dependences of the total ionic conductivity of the composite ($40AgI{\cdot}38Ag_2O{\cdot}22V_2O_5$ +diamond 30–40 μm) during heating (○) and cooling (•)

The temperature dependence of the total conductivity of the composites based on $40AgI{\cdot}38Ag_2O{\cdot}22V_2O_5$ glass in a diamond matrix with a grain size of 30–40μm (Fig.3) follows the Arrhenius formula from room temperature up to ca. 170ºC. On heating the activation energy in this range is equal to 0.31 eV, while on cooling it is slightly higher, 0.33 eV. In the range 180–250 ºC, the slope of the conductivity dependence visibly increases. The corresponding activation energy during cooling is 0.75 eV, and on heating it is even higher. Above 250 ºC, the activation energy decreases to 0.34 eV on heating, and to 0.46 eV on cooling. There is additionally some hysteresis between absolute conductivity values measured during heating and cooling.

4. Discussion

The differences in the shapes of impedance spectra observed for glasses and composites based on these glasses can be justified by the differences between the microstructures of the systems. The presence of a well-visible middle arc in the impedance spectra of composites (Fig. 1a) and its absence for bulk glasses (Fig. 1b) is related to a specific distribution of a glassy phase in the composites. As can be seen on the SEM micrographs of composites obtained by infiltration, glass forms a number of small round “nodules” in the space between grains of the ceramic matrix (in this case diamond). It was found that after heating the composites to above 200 ºC, these “nod-

ules" disappear and the glassy phase forms a continuous layer covering the grains of the matrix. This change in glass distribution following heating is accompanied by a modification of the impedance spectra (Fig. 2b), which are similar to those of bulk glasses (Fig. 1b). The reason for this similarity lies in a continuous distribution of the conducting phase in glasses and annealed composites. In the case of freshly prepared composites, the conducting phase contains many boundaries, mainly between glassy nodules, which can discernibly impede, or, more generally, modify ion transport conditions in the system. The presence of these boundaries may cause the appearance of an additional arc in the impedance spectrum like that in Fig.1a.

A linear temperature dependence of the conductivity in the (log σT vs. $1/T$) coordinates) observed at temperatures up to ca. 170 ºC means that the activation energy is constant in this range. Its value, close to 0.3 eV, is typical of bulk glasses containing considerable amounts of AgI. The increase in activation energy in the 180–250 ºC range and its decrease at higher temperatures point to the presence of some amount of crystalline AgI in the composites. Bulk crystals of AgI undergo a phase transition from a low conducting β to highly conducting α phase at 147 ºC [2]. The fact that for the composites under study the change in conductivity is observed at higher temperatures (ca. 170 C, Fig. 3) than for bulk AgI (147 ºC) should be ascribed to the dispersion of AgI in the composite and to its strong interactions with the glassy phase as well as diamond particles.

5. Conclusions

It has been demonstrated that it is possible to prepare attractive composites based on $AgI–Ag_2O–V_2O_5$ glasses infiltrated into diamond powder. Such composites exhibit improved thermal stability and better mechanical characteristics as compared to those of as-received glasses. The conductivities of these materials are comparable to that of the infiltrated glasses, in spite of a lower share of conductive phase in these composites compared to bulk glasses.

Acknowledgements

This work was financed by the State Committee for Research, Grant No. 4T08E 05223.

References

[1] MAIER J., Prog. Solid St. Chem., 23 (1995), 171.
[2] KEEN D.A., J. Phys. Cond. Matter., 14 (2002), R819.
[3] KRASOWSKI K., GARBARCZYK J.E., WASIUCIONEK M., Phys. Stat. Sol. (a), 181 (2000), 157.
[4] ZGIRSKI M., GARBARCZYK J., GIERLOTKA S., PAŁOSZ B., WASIUCIONEK M., NOWIŃSKI J.L., Solid State Ionics, 176 (2005), 2141.
[5] DYGAS J., PhD Thesis, Northwestern University, Evanston, 1986.

Received 10 December 2004
Revised 10 January 2005

Materials Science-Poland, Vol. 24, No. 1, 2006

Evaluation of transference numbers in mixed conductive lithium vanadate-phosphate glasses

P. JOZWIAK, J. E. GARBARCZYK*, M. WASIUCIONEK

Faculty of Physics, Warsaw University of Technology, ul. Koszykowa 75, 00-662 Warsaw, Poland

A method for evaluating the transference numbers in mixed electronic-ionic glasses of the Li_2O $–V_2O_5–P_2O_5$ system is proposed and tested, basing on the analysis of temperature dependences of the total conductivity of these glasses. The method consists of representing experimental non-Arrhenius temperature dependences of the total conductivity by a sum of two Arrhenius-like contributions. The latter ones were tentatively attributed to the electronic and ionic partial conductivities.

Key words: *mixed electronic-ionic conduction; conductive glasses; impedance spectroscopy; transference number*

1. Introduction

Lithium vanadate-phosphate glasses of the $Li_2O–V_2O_5–P_2O_5$ ternary system exhibit mixed electronic-ionic conduction [1, 2], which, depending on the proportions of the constituents, can be purely ionic (low V_2O_5 content), almost purely electronic (high amounts of V_2O_5) or intermediate electronic-ionic [3]. The relative ratio between the electronic and ionic components of the conduction can be controlled in a continuous way by appropriate changes in the glass composition. Ionic conduction in these glasses occurs via the motion of Li^+ ions, while electronic transport takes place by electron (polaron) hopping between aliovalent V^{4+} and V^{5+} centres present in vanadate glasses. The possibility of controlling the character of conductivity within the same system by adjusting chemical composition can be of interest for potential applications of these conductors as basic components in integrated microbatteries, solid electrolytes (ionic conducting glasses), or mixed electronic-ionic cathode materials.

*Corresponding author, e-mail: jegar@mech.pw.edu.pl

A closer look at the changes in slopes of the temperature dependences of the conductivity of lithium vanadate glasses, especially those with higher contents of V_2O_5, suggests that the character of the conductivity may depend not only on composition, but also on temperature, even at moderate temperatures [4]. In this work, we present the temperature dependences of the conductivity of mixed conductive glasses of the Li_2O–V_2O_5–P_2O_5 system and tentative analyses of these dependences in terms of temperature-dependent ionic and electronic transference numbers.

2. Experimental

The glasses were prepared by a standard melt-quenching method [4]. Reagent grade $LiNO_3$ (Aldrich), V_2O_5 (ABCR), and $NH_4H_2PO_4$ (POCh) were used in glass syntheses. A series of glasses was prepared, whose compositions are described by the formula: xLi$_2$O·(100 – 2x)V$_2$O$_5$·xP$_2$O$_5$, where x = 15, 25, 35, 40 and 45. Their compositions were additionally labelled as: A (x = 15), B (x = 25), C (x = 35), D (x = 40), and E (x = 45). The compositions of all these glasses corresponded to different values of the parameter $r = [Li_2O]/([V_2O_5] + [P_2O_5])$ which is a good measure of the extent of disruption of the glass network (formed by vanadate and phosphate polyhedra) by the glass modifier (Li_2O).

XRD measurements have confirmed the amorphous state of the as-prepared samples. Characteristic temperatures (glass transition and crystallization temperatures T_g and T_c) were determined from DSC traces taken on a Perkin-Elmer Pyris 1 apparatus, with the heating rate 20 K/min. The total electrical conductivity of the samples was determined by ac impedance spectroscopy (IS), i.e. by applying a small ac voltage and recording the current response [5]. The measurements were done in a wide temperature range (20–360 °C) using a Solartron 1260 analyzer and a temperature regulation and stabilization system [4]. Gold electrodes were sputtered onto polished opposite sides of the glasses. The electrodes were blocking for ions and reversible for electrons. The spectra were measured in the 100 mHz–10 MHz range, and the amplitude of the ac signal was set to 30 mV rms in two-electrode mode. All impedance spectroscopy measurements were fully automated and run under computer control, temperature programming included. The acquired spectra were numerically analyzed by the equivalent circuit approach [5] using the computer package [6].

3. Results and discussion

Figure 1 presents the dependence of the glass transition temperature T_g on the parameter r. It is seen that T_g values change with the composition in a step-like manner: glasses A and B with higher contents of V_2O_5 have lower values of T_g (260–280 °C), while other compositions (C, D, E) with lower amounts of V_2O_5 are characterized by a considerably higher T_g (360–370 °C). The step-like dependence of

T_g versus r indicates that there is a distinct difference in the structures of those two groups of glasses.

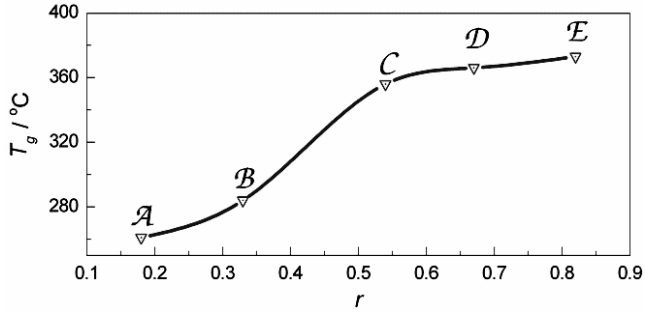

Fig. 1. Dependence of the glass transition temperature on the parameter r.
Solid line is a guide for the eye

Also, the character of the impedance spectra (not shown here – for more details and plots see Refs. [3, 4]) of the glasses under study depend on their chemical composition. The spectra of samples with a predominant electronic component consisted of a single semicircle, and predominantly ionic conducting glasses contained an additional spur at low frequencies. For intermediate cases (comparable ionic and electronic components), spectra consisted of two strongly overlapping semicircles. We also noticed that for glasses A and B the spectra change their character with temperature, from a single semicircle at room temperature to two overlapping arcs at higher temperatures.

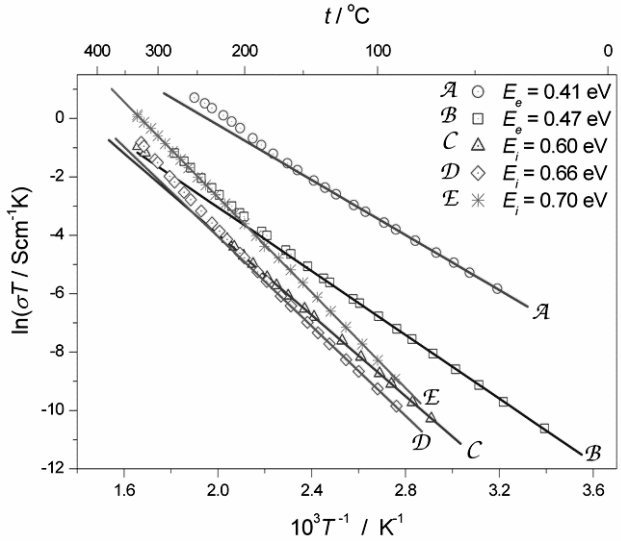

Fig. 2. Temperature dependences of conductivity for mixed conductive glasses of the composition $x\mathrm{Li_2O}\cdot(100 - 2x)\mathrm{V_2O_5} - x\mathrm{P_2O_5}$. Glass labels: A ($x$ = 15), B (x = 25), C (x = 35), D (x = 40), E (x = 45)

The temperature dependence of the total conductivity of the mixed conducting lithium vanadate glasses (Fig. 2) exhibit a discernible deviation from linearity at temperatures T_s well below the glass transition temperature determined from DSC. The temperature range, in which the change of slope occurs, depends on the chemical composition of the glass.

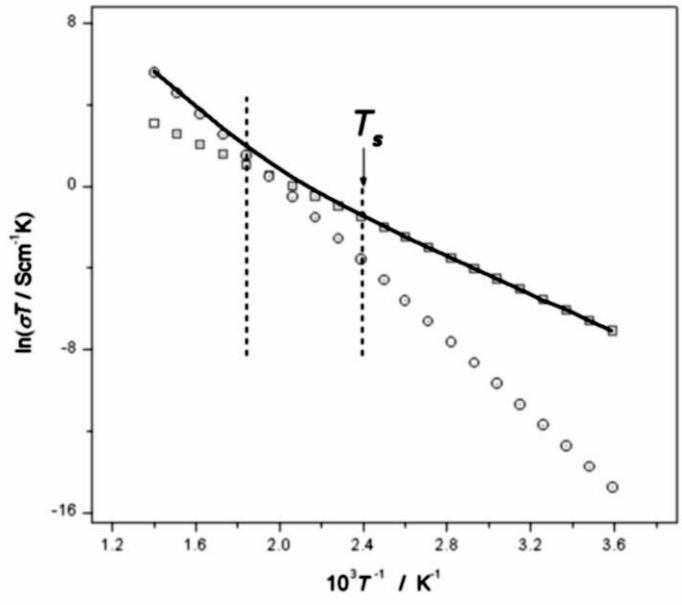

Fig. 3. Simulation of the effective conductivity of a mixed conductive glass based on the approach shortly explained in the text

In order to account for this feature, we have represented each of the experimental non-Arrhenius dependences shown in Fig. 2 by a sum of two Arrhenius-like ones with different activation energies. A model temperature dependence of that kind is shown in Fig. 3. To represent the experimental non-Arrhenius dependence by a sum of two Arrhenius-like ones, we used a standard least square fitting procedure that varies parameters of the Arrhenius formula (the preexponential factor σ_0 and activation energy E) to reach the best fit. An example of the results of such fits (for glass A; $x = 15$) is shown in Fig. 4.

We have attributed the observed effect (i.e. a gradual increase of the activation energy with temperature) to contributions of both electronic and ionic components to the total electrical conductivity. Due to different activation energies for electronic and ionic transport, the proportions between both components vary with temperature, resulting in a non-Arrhenius temperature dependence of the total conductivity.

It has been established for years that in the temperature range 20–300 °C the conductivity in electronically conducting vanadate-based solids follows the Arrhenius formula with a single activation energy E_e in the range 0.3–0.5 eV (e.g., [7]). On the

other hand, the ionic conductivity in purely ionically conducting lithium glasses also depends on temperature according to the Arrhenius formula. The activation energies E_i determined in this work are in the range 0.66–1 eV. They are close to $E_i = 0.6$ eV for the ionically conducting glass $40Li_2O{\cdot}20B_2O_3{\cdot}40P_2O_5$ [8] (similar to $E_i = 0.66$ eV found in this work for the glass $40Li_2O{\cdot}20V_2O_5{\cdot}40P_2O_5$) and $E_i = 0.74$ eV for another ionically conducting glass, $50Li_2O{\cdot}50B_2O_3$ [9].

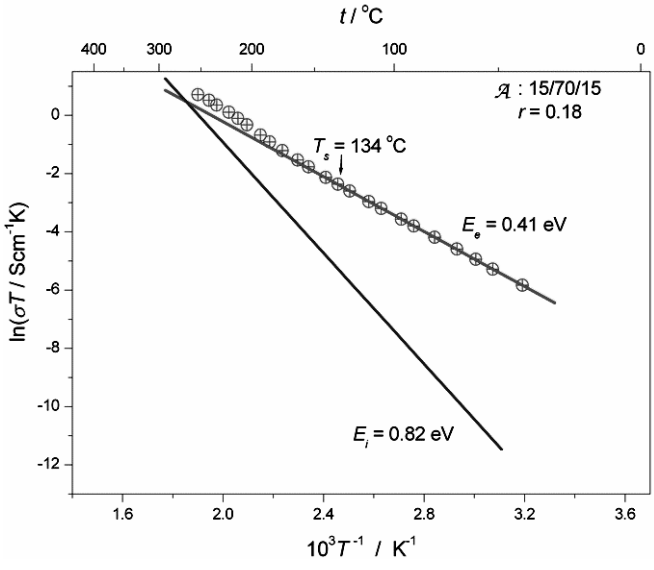

Fig. 4. Temperature dependences of the conductivities of glass A of the composition $15Li_2O{\cdot}70V_2O_5{\cdot}15P_2O_5$ (circles). The lines represent the calculated Arrhenius dependences for the electronic and ionic components of the total electrical conductivity

Since both components, electronic and ionic, are non-negligible in the glasses under study, it is natural to attribute the Arrhenius-like dependences used to reconstruct the experimental temperature dependences of conductivity to electronic and ionic components separately. We have assumed that both components are totally independent of each other.

Using the results of the aforementioned fitting procedure for the studied glasses, we determined the temperature dependences of the electronic and ionic conductivities, (σ_e and σ_i, respectively) for all glasses. Consequently, we were able to evaluate the transference numbers, electronic $t_e = \sigma_e/(\sigma_e + \sigma_i)$ and ionic $t_i = 1 - t_e$. The evaluated temperature dependences of the electronic and ionic transference numbers for glasses A, B, and D are shown in Fig. 5. Up to temperature T_s (the temperature where a change in activation starts, Figs. 2–4), one of the transference numbers (t_e for glasses A and B and t_i for glass D) is higher than 0.95 and the other is less than 0.05. Above this temperature, the difference between both transference numbers gradually decreases and they approach each other at temperatures close to T_g. Glass E, with 40

% Li_2O and only 10 % V_2O_5, exhibits a single activation energy in the whole temperature range. Due to a small content of V_2O_5, the predominance of V^{4+} centres [10], and strong disruption of the glass network, electron hopping is unlikely and the total conductivity is due to ionic transport alone ($t_i \approx 1$ and $t_e \approx 0$).

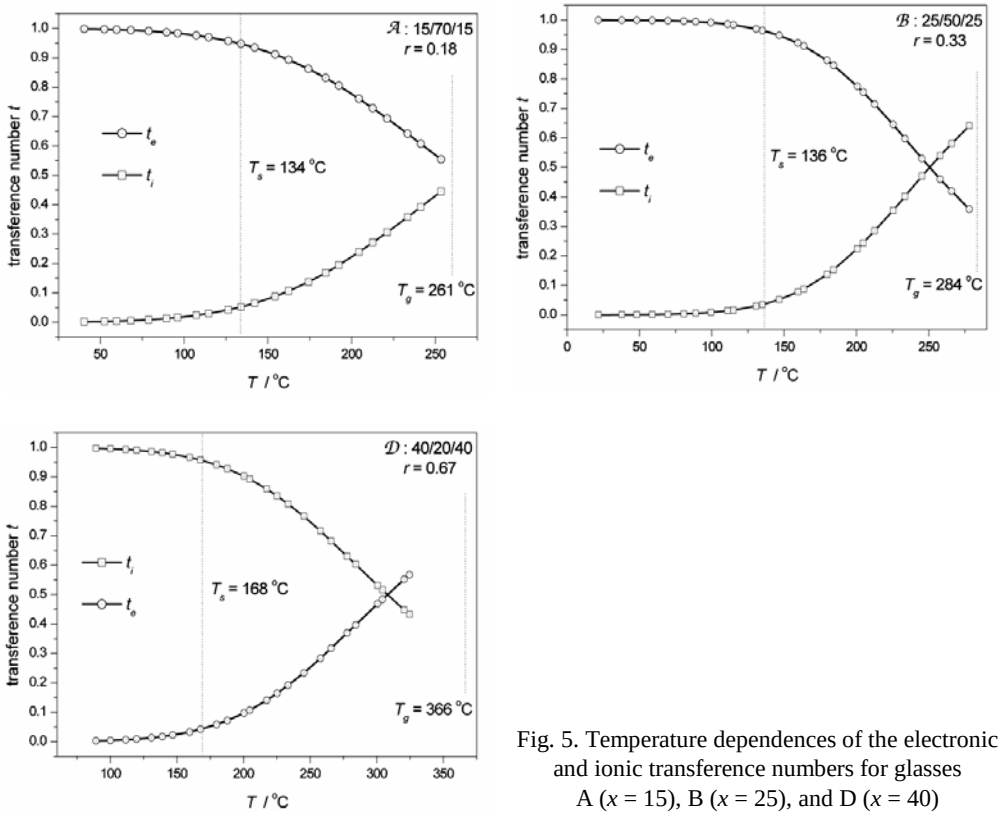

Fig. 5. Temperature dependences of the electronic and ionic transference numbers for glasses A (x = 15), B (x = 25), and D (x = 40)

Further studies on transference numbers in lithium vanadate-phosphate glasses using independent methods are planned.

4. Conclusion

A method for estimating electronic and ionic transference numbers in mixed electronic-ionic conductors from the temperature dependences of their total conductivity was proposed and applied to mixed conducting glasses of the Li_2O –V_2O_5–P_2O_5 system.

References

[1] SOUQUET J.L., KONE A., LEVY M., [in:] *Solid State Microbatteries*, J.R. Akridge, M. Balkanski, (Eds.), NATO ASI Series, Series B: Physics, 217, Plenum Press, New York, 1990, p. 301.

[2] GARBARCZYK J.E., WASIUCIONEK M., JOZWIAK P., TYKARSKI L., NOWIŃSKI J., Solid State Ionics, 154–155 (2002), 367.
[3] JOZWIAK P., GARBARCZYK J.E., Solid State Ionics, 176 (2005), 2163.
[4] JOZWIAK P., PhD Thesis, Warsaw University of Technology, 2003.
[5] MACDONALD J.R., Impedance *Spectroscopy: Emphasizing Solid State Materials and Systems*, Wiley, New York, 1987.
[6] DYGAS J., PhD Thesis, Northwestern University, Evanston, 1986.
[7] MURAWSKI L., Zeszyty Naukowe Politechniki Gdańskiej, 29 (1993), 1.
[8] SARRADIN J., CREUS R., PRADEL A., ASTIER R., RIBES M., [in:] *Solid State Microbatteries*, J.R. Akridge, M. Balkanski (Eds.), NATO ASI Series, Series B: Physics, 217, Plenum Press, New York, 1990, p. 41.
[9] KOSACKI I, MASSOT M., BALKANSKI M., TULLER H.L., Mat. Sci. Eng., B12 (1982), 345.
[10] SZÖRENYI T., BALI K., HEVESI I., Phys. Chem. Glasses, 23 (1982), 42.

Received 10 December 2004
Revised 17 February 2005

Materials Science-Poland, Vol. 24, No. 1, 2006

Effect of the microstructure on transport properties of doped SLS glasses

B. MACALIK*, M. SUSZYŃSKA, L. KRAJCZYK

Institute of Low Temperature and Structure Research,
Polish Academy of Sciences, ul. Okólna 2, 50-950 Wrocław, Poland

Results of thermally stimulated polarisation current measurements and transmission electron microscopy investigations of copper-exchanged soda lime silicate glasses are presented. During the ion exchange procedure, sodium ions are partially substituted by copper. It has been stated that, besides the formation of copper and copper oxide, the joint effect of chemical and thermal treatment is the modification of matrix morphology. Thus, the induced modification of transport properties could be related to mobility changes for Na^+ charge carriers.

Key words: *soda lime silicate glass; conductivity; ion exchange*

1. Introduction

Oxide glasses containing small particles of transiition metals can be used as resonant-type non-linear optical materials for photonic devices [1]. Ion implantation and ion exchange techniques are usually used to introduce metal ions into glass networks. Subsequent thermal treatment in an inert or reducing atmosphere results in the formation of metallic atoms and colloidal particles. Preliminary studies of copper-doped soda lime silicate glasses (SLSG) have shown that the thermally stimulated depolarisation current (TSDC) spectra of these materials are sensitive to ion exchange parameters and post-exchange thermal treatment [2].

To obtain a deeper insight into these phenomena, thermally stimulated polarisation (TSP) and depolarisation (TSD) current measurements and transmission electron microscope (TEM) observations were performed for commercial SLSG subject to chemical and thermal treatment.

*Corresponding author, e-mail: b.macalik@int.pan.wroc.pl

2. Experimental

The composition of the commercial multicomponent glass (determined by EDX) was as follows (in mole %): SiO_2 – 74, Na_2O – 13, CaO – 6.4, MgO – 4.5 and Al_2O_3 – 1.4. Ion exchange was performed in an air atmosphere by dipping the glass plates into molten Cu_2Cl_2 at 900 K for various time periods. Then the samples were annealed in a stream of dry hydrogen at 773 K for 5 hours under atmospheric pressure.

Measurements of thermally stimulated polarisation (TSP1 and TSP2) and thermally stimulated depolarisation (TSD) currents were performed in vacuum [3] as a function of temperature from 150 to 450 K. For the TSP runs, the samples were first cooled to 150 K, and then heated at a constant rate with a polarising field of 400 V/cm ON. The polarisation current (TSP1) was recorded as a function of temperature. After the first run, the sample was cooled again to 150 K with the electric field ON, reheated and the TSP2 current was measured. After TSP2, the sample was cooled to 150 K for the third time, short-circuited, and reheated while the TSD current was recorded with the external electric field OFF.

A Philips scanning microscope (SEM 515) with a microanalyser (EDX 9800) was used to determine the composition of the SLS glasses and the concentration of Cu ions as a function of the distance from the exchanged surface. Transmission electron microscopy (TEM) and selected area electron diffraction (SAED) were used to study the morphology of the exchanged layer by means of a PHILIPS CM 20 microscope. For these performances, shadowed and extraction replicas were prepared.

3. Results and discussion

Figure 1 shows the dependence of Cu and Na ion concentration on the distance from the glass surface as a function of the exchange time at 900 K. It can be seen that for exchange times longer than 2 h, the penetration profile has a step-like character with a constant Cu concentration. The thickness of the exchanged layer reaches a maximum value of about 80 μm. For shorter times, the amount of substituted Na ions is smaller. During reduction, performed at 773 K, sodium ions move towards the sample surface, while copper enters deeper into the glass and the original step-like profile becomes flatter [4]. The hydrogenation of the exchanged samples modifies the valence state of the copper ions and induces the formation of copper colloids.

For all samples, TSP1, TSP2, and TSD measurements were performed. In TSP1, two thermally stimulated polarisation bands are accompanied by a high temperature component (see Fig. 2). These two bands are better seen in the TSD spectrum, whose behaviour has been already described by Suszynska et al. [2]. In TSP2, only the high temperature component appears. Since TSP1 = TSP2 + TSD, the polarisation and transport properties of the investigated glasses can be separated. Moreover, TSP2 data can be used to calculate the dc conductivity and activation energy of the detected charge transport.

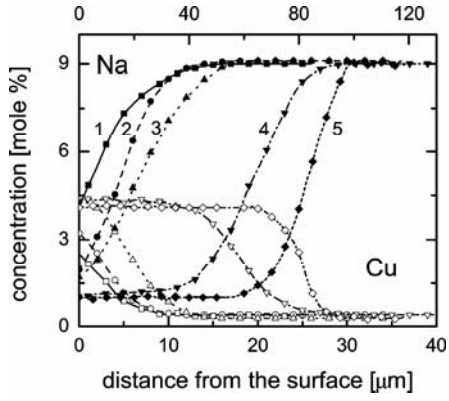

Fig. 1. Penetration profiles for Na (solid) and Cu (open symbols) ions in the surface layer of samples ion exchanged for 10 min (1), 1 h (2), 2 h (3), 6 h (4), and 24 h (5). The upper scale is used for curve 5 (open and solid diamonds)

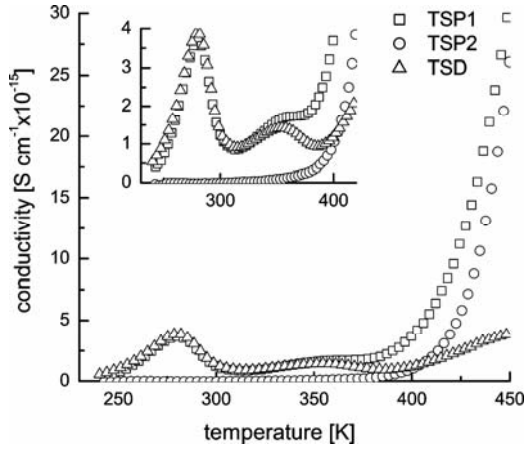

Fig. 2. An example of thermally stimulated polarisation (TSP1 and TSP2) and depolarisation (TSD) spectra (a hydrogenated sample ion-exchanged for 24 h)

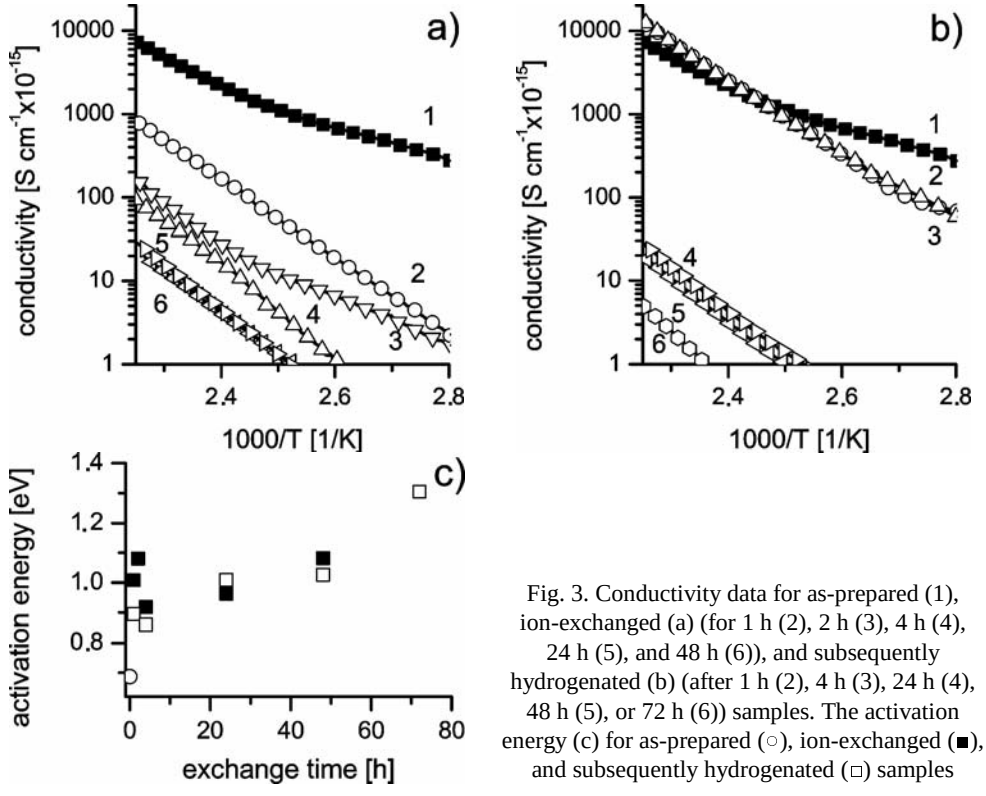

Fig. 3. Conductivity data for as-prepared (1), ion-exchanged (a) (for 1 h (2), 2 h (3), 4 h (4), 24 h (5), and 48 h (6)), and subsequently hydrogenated (b) (after 1 h (2), 4 h (3), 24 h (4), 48 h (5), or 72 h (6)) samples. The activation energy (c) for as-prepared (○), ion-exchanged (■), and subsequently hydrogenated (□) samples

It has been found that the annealing of as-prepared samples at 900 K for several hours and their hydrogenation does not modify the charge-transport properties of the investigated glasses. The dc conductivities and activation energies of such samples are similar to those obtained for as-prepared samples. On the other hand, for samples exchanged with copper, the dc conductivity monotonously decreases with increasing exchange time; for instance, a decrease of about three orders of magnitude was detected for the sample exchanged for 48 h (Fig. 3a). The decrease in the number and/or mobility of the main charge carriers (i.e. the Na^+ ions, [5]) might be responsible for the observed changes. Also, the hydrogenation of the samples modifies their conductivities. Namely, for hydrogenated samples previously exchanged shorter than 4 h, the recorded currents increase up to the value characteristic of the as prepared samples (Fig. 3b). For samples exchanged longer, the conductivity is similar to that obtained for glass before hydrogenation.

Figure 3c shows the behaviour of the calculated activation energy. It has been stated that the incorporation of copper results in an increase of the activation energy from 0.69 eV (that of an untreated sample) to nearly 1 eV and 1.1 eV for samples exchanged for 1 h and 2 h, respectively. For longer exchange times and for all hydrogenated samples, the activation energy increases nearly linearly with the exchange time. It seems probable that the joint effect of copper and annealing temperature either induces a new type of matrix morphology or modifies the existing one. The different mobilities of the main charge carriers inside the related matrix species affect the conductivity data. This hypothesis has been confirmed by direct TEM observations.

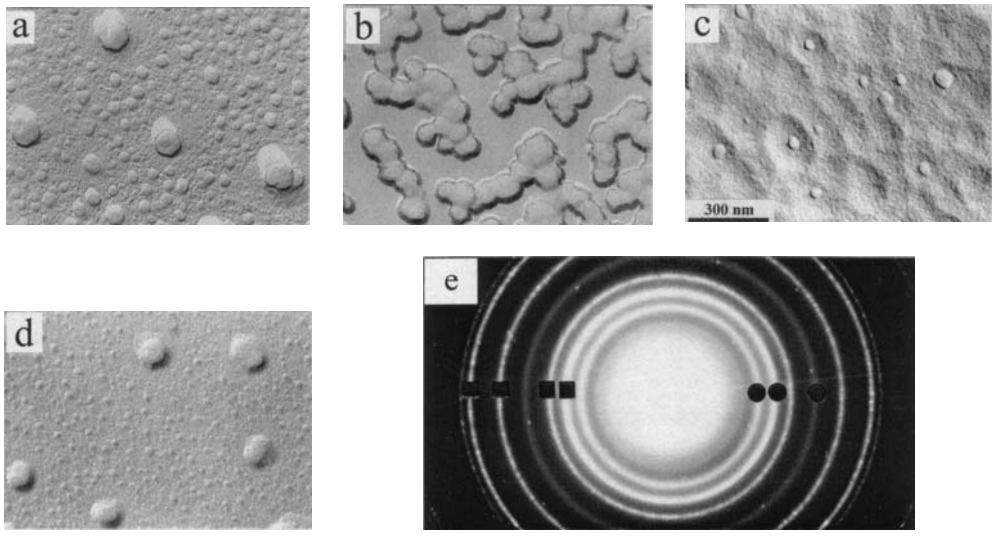

Fig. 4. TEM micrographs of the SLS glass surface of exchanged (a = 10 min, b = 1 h, c = 6 h, d = 24 h) and hydrogenated samples. The electron diffraction patterns (e) evidence the presence of Cu (■) and Cu_2O (●) crystallites

Changing matrix morphology with the exchange time is shown in Fig 4a–d; Figure 4e shows the presence of copper and copper oxide colloids. Phase separation, a highly connected structure, and secondary phase separation were observed. Unfortunately, the identification of these occlusions was not possible, because a corresponding crystalline form was not detected. Assuming that the originally separated phase is the Na_2O-rich one (as observed for silver doped SLS glass of a similar composition [6]), the incorporation of copper supposedly modifies the existing phase into another with continuously changing morphology and/or composition. These structural modifications affect the mobility of the charge carries and the resulting dc conductivity. The changed mobility of the charge carriers in the copper-rich layer may, however, result in the formation of a space charge between the exchanged and copper free part of the matrix, changing the internal electric field. Future investigations are necessary here.

4. Conclusions

dc electric conductivity measurements and TEM observations have been used to show the effect of copper incorporation on SLS glass microstructure. It has been shown that copper dispersed in the glass matrix in the form of ions, atoms, and colloidal particles of copper and copper oxide affect the conductivity in an indirect way by changing the quantity and mobility of the main charge carriers.

Acknowledgement

Financial support by KBN (project No. 7T08D 06021) is acknowledged.

References

[1] HACHE F., RICHARD D., FLYTZANIS C., KREIBIG U., Appl. Phys., A 47 (1988), 347.
[2] SUSZYŃSKA M., MACALIK B., KRAJCZYK L., CAPELLETTI R., J. Alloys Compounds, 378 (2004), 155.
[3] GUBAŃSKI A., MACALIK B., Bull. Acad. Pol. Sci., Ser. Tech., 35 (1987), 537.
[4] MACALIK B., KRAJCZYK L., OKAL J., MORAWSKA-KOWAL T., NIERZEWSKI K., SUSZYŃSKA M., Rad. Effect Defects Solids, (2002), 887.
[5] OWEN A.E., [in:] J.E. Burke (Ed.), *Progress in Ceramic Science*, vol. 3, Pergamon Press, New York, 1963, p. 77.
[6] SUSZYŃSKA M., KRAJCZYK L., CAPELLETTI R., BARALDI A., BERG K.-J., J. Non-Cryst. Solids., 315 (2003), 114.

Received 10 December 2004
Revised 6 April 2005

Materials Science-Poland, Vol. 24, No. 1, 2006

Crystallization processes in superionic $AgI–Ag_2O–P_2O_5$ ($[Ag_2O]/[P_2O_5] = 3$) glasses

J. L. NOWIŃSKI*, M. MROCZKOWSKA, J.E. GARBARCZYK, M. WASIUCIONEK

Faculty of Physics, Warsaw University of Technology, ul. Koszykowa 75, 00-662 Warsaw, Poland

Crystallization processes in superionic $AgI–Ag_2O–P_2O_5$ ($[Ag_2O]/[P_2O_5] = 3$) glasses were investigated by X-ray, DSC, SEM, and impedance spectroscopy. It was found that the crystallization process depended on the total concentration of the AgI dopant in the material and on the thermal treatment of the glass. During quenching of the glass melt, the following phases are successively formed with increasing total AgI concentration: pure glass without detectable (XRD) traces of crystalline phases, glasses containing β-AgI and some other, unidentified crystallites precipitated on the surface, and finally a composite material, namely a glass matrix in which β/γ-AgI inclusions are embedded. Glasses containing $x < 50$ mol % of AgI do not crystallize during annealing. Two bulk crystallization processes were identified in solid glasses with $50 < x < 75$ mol %. During annealing, the initial product of crystallization transforms to the final one. There is an evidence that crystallization is preceded by a pre-crystallization stage, in which the glass matrix becomes inhomogeneous, forming nano-sized volumes.

Key words: *crystallization; superionic phosphate glass*

1. Introduction

Glass-ceramic composites have been attracting attention of researchers for decades, because of their technological importance. In the case of superionic glassy composites, however, the interest has been very limited, resulting in poor knowledge of their properties and processes. Recently, some papers [1–3] reported an enhancement of ionic conductivity after introducing a crystalline phase into the superionic glass matrix. These observations highlighted the technological interest of superionic glassy composites pointing to the need for more fundamental investigations, of crystallization, in particular.

The investigated $AgI–Ag_2O–P_2O_5$ glasses are well known as useful and model materials for fundamental research of superionic processes in glasses. Due to their low

* Corresponding author, e-mail: nowin@if.pw.edu.pl

glass transition temperatures (60–120 °C), they also appear to be convenient for the observation of crystallization phenomena. According to our knowledge, crystallization in phosphate glasses ($[Ag_2O]/[P_2O_5] = 3$) has not been reported in the literature so far.

2. Experimental

Samples of the material were prepared by the method described elsewhere [4, 5]. Crystalline phases were formed inside a glassy matrix during the quenching of the molten glass or by annealing the solid glass. Depending on the goal, thermal processing consisted of several annealing steps, at temperatures and duration times selected to achieve the required stage of crystallization. X-ray diffraction was used for material characterization, both for as-received and thermally processed samples. A Philips X'Pert Pro ($CuK_{\alpha 1}$) diffractometer, equipped with an Anton Paar high-temperature diffraction oven, was employed for room and high temperature X-ray diffractometry. Field emission scanning electron microscopy was used for microstructure investigation, using the LEO 1530 model. Ion conductivity was determined by impedance spectroscopy (Solartron 1260). Calorimetric properties were investigated and differential scanning calorimetry (DSC) was applied (Perkin-Elmer, Pyris1 model). Depending on the particular investigation, the material was powdered in a mortar and pestle, or a thin surface layer was removed by fine sand paper; in some cases as-received samples were used.

3. Results and discussion

The shapes of the X-ray diffraction patterns for the as-received samples show a correlation with the total concentration of AgI dopant. When silver iodide concentration does not exceed about 65 mol %, the diffraction patterns exhibit a 'halo' profile typical of amorphous materials (Fig. 1). For higher dopant concentrations, some diffraction lines are visible on the patterns. Powdering or removing a thin surface layer about 30–40 μm thick from the material containing $65 \leq x \leq 70$ mol % of the dopant resulted in the disappearance of these lines (Fig. 2). This observation evidently indicates that the crystalline phase is located on the surface of the glass. For materials with $x > 70$ mol %, similar mechanical processing does not change the shape of the XRD profile, suggesting bulk crystallization (Fig. 3). Concluding, there is a sequence of crystallization events with increasing total AgI concentration in the material: a glassy matrix, free from crystalline inclusions (detectable by X-ray diffraction), surface crystallization, and, finally, crystallization in the bulk. Phase analysis based on the ICDD diffraction database attributes the β/γ-AgI crystal structure to bulk precipitates and identifies a mixture of β/γ-AgI and some unknown crystalline phase on the surface of the glass.

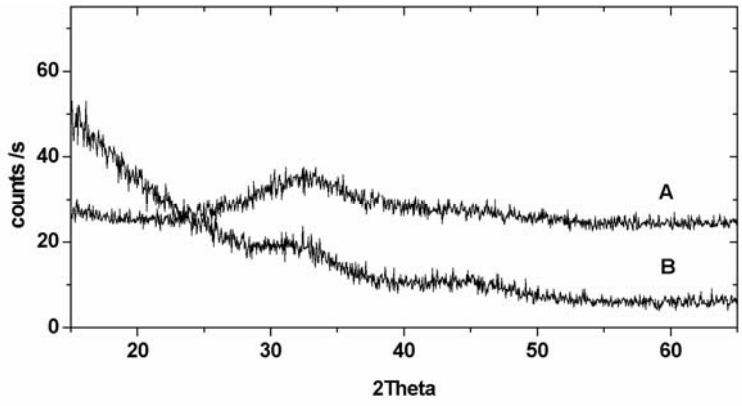

Fig. 1. X-ray diffraction patterns for the 60AgI–30Ag_2O–10P_2O_5 glass:
a) – as-received, solid sample, b) – as-received, powdered sample

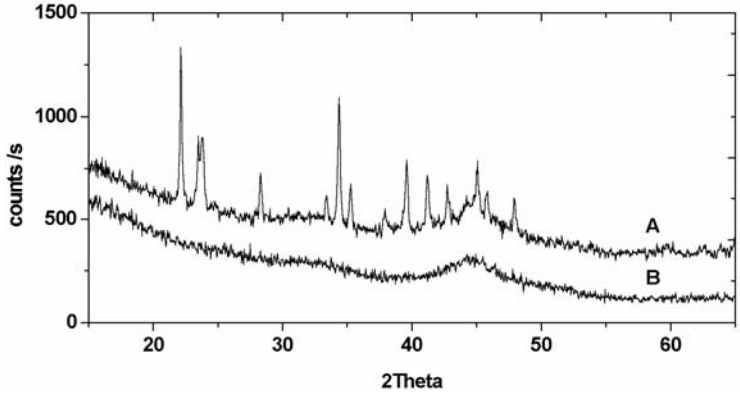

Fig. 2. X-ray diffraction patterns for the 70AgI–22.5Ag_2O–7.5P_2O_5 glass:
a) – as-received, solid sample, b) – as-received, powdered sample

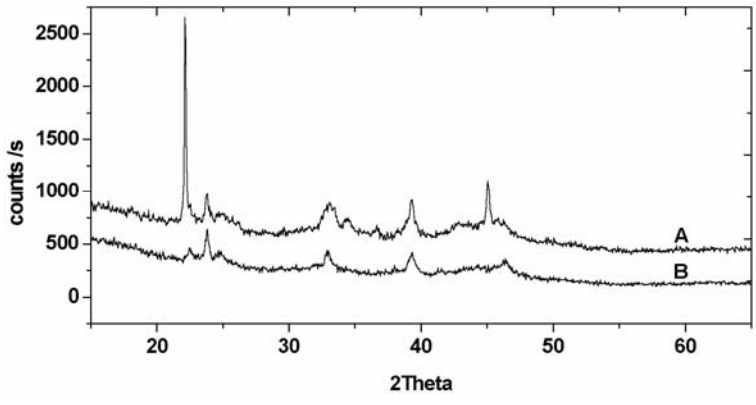

Fig. 3. X-ray diffraction pattern for the 75AgI–18.75Ag_2O–6.25P_2O_5 glass after preparation:
a) – as-received, solid sample, b) – as-received, powdered sample

It was found that crystallization in solid glasses containing more than 50 mol % of AgI could be initiated by annealing at elevated temperatures. Efforts to proceed with such crystallization for glasses with $x < 50$ mol % have not succeeded, even for long annealing (months) at various temperatures up to 160 °C. DSC investigations of glasses with $x \geq 50$ mol % revealed two crystallization processes: the first at about 62–90 °C and the second at 100–110 °C (depending on x). The glass transition temperature was found to be about 52–57 °C.

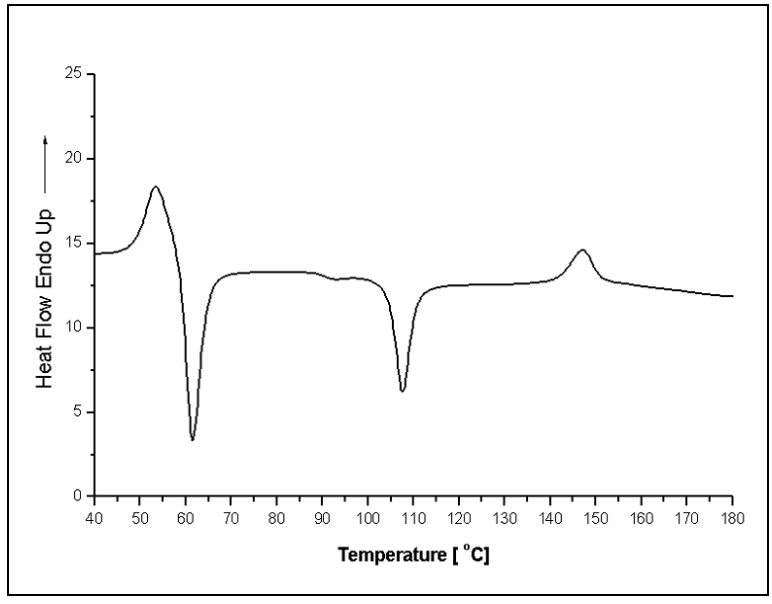

Fig. 4. DSC trace for the $75AgI–18.75Ag_2O–6.25P_2O_5$ as-received glass

Figure 4 presents, as an example, the DSC curve for the glass $75AgI–18.75Ag_2O–6.25P_2O_5$. XRD investigations also confirmed the existence of these two crystallizations. Figure 5 shows diffraction patterns for $60AgI–30Ag_2O\text{-}10P_2O_5$, recorded after various thermal treatments. Profile (d), obtained after annealing at 64 °C for 145 min, differs from profile (e), observed after annealing at 64 °C for 145 min and additionally at 66 °C for 418 min. None of the lines visible in profile (d) are repeated in pattern (e). Similarly, two characteristic shapes of the X-ray patterns exhibited other, thermally treated glasses, containing ca. 60–75 mol % of the dopant (Fig. 6). According to the ICDD database, the lines observed in both patterns represent unknown crystalline phases. Some of the weak reflections in Fig. 5e can be attributed to γ-AgI. Since during annealing the diffraction lines assigned to the first crystallization continuously decreased, whereas those ascribed to the second crystallization increased, it was concluded that the final product of crystallization was formed at the expense of the initial crystalline phase.

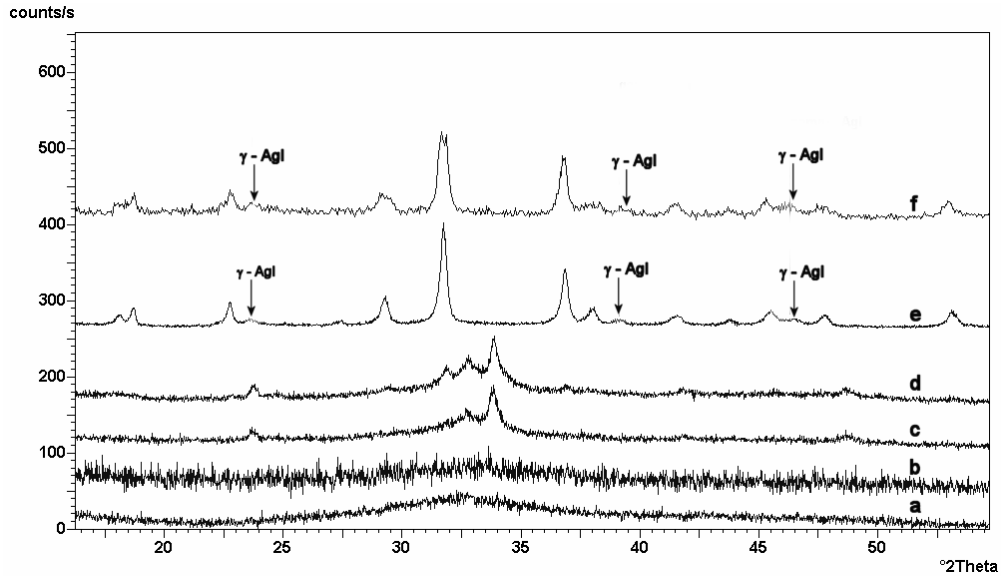

Fig. 5. X-ray diffraction patterns for the 60AgI–30Ag_2O–10P_2O_5 glass: as-received material (a) and after annealing at 60 °C for 12 min (b), at 60 °C for 12 min and additionally at 64 °C for 74 min (c), at 60 °C for 12 min and at 64 °C for 145 min (d), at 60 °C for 12 min, at 64 °C for 145 min, and at 66 °C for 418 min (e), at 60 °C for 12 min, at 64 °C for 145 min, at 120 °C for 12 min (f); the reflections attributed to γ-AgI are marked

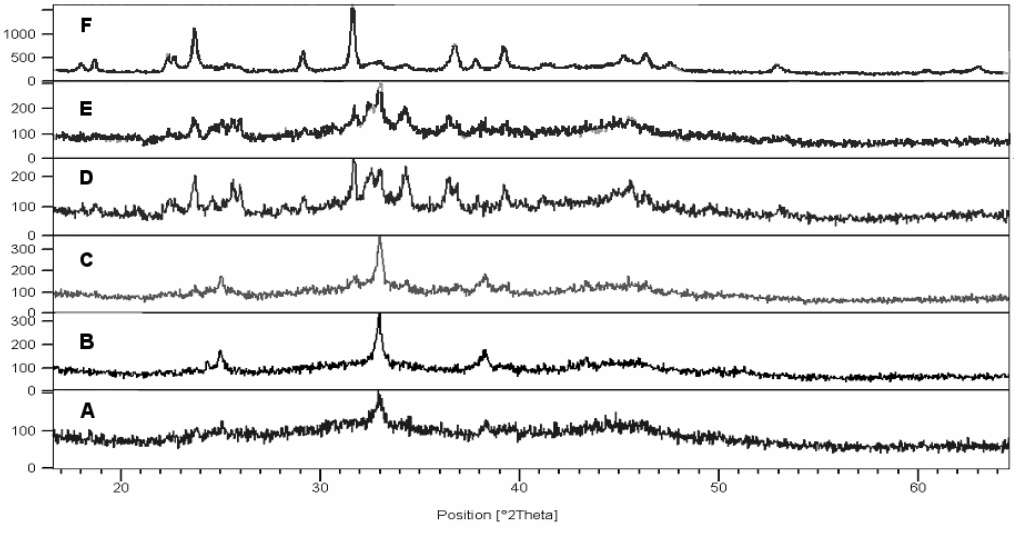

Fig. 6. X-ray diffraction patterns for the 70AgI–22.5Ag_2O–7.5P_2O_5 glass: as-received material (a); after annealing for 10 minutes at: 60 °C (b), 80 °C (c), 100 °C (d), 110 °C (e), and 120 °C (f)

Correlated XRD, SEM, and impedance spectroscopy revealed some interesting features of crystallization process in the glass. It was observed that ion conductivity in

$60AgI–30Ag_2O\text{-}10P_2O_5$ after annealing at 60 °C for 12 min increased about twice compared to that of the as-received glass. Further annealing at 64 °C resulted in an abrupt decrease of conductivity. The relevant diffraction patterns showed no lines after annealing at 60 °C, and no reflections characteristic of the first crystallization after annealing at 64 °C.

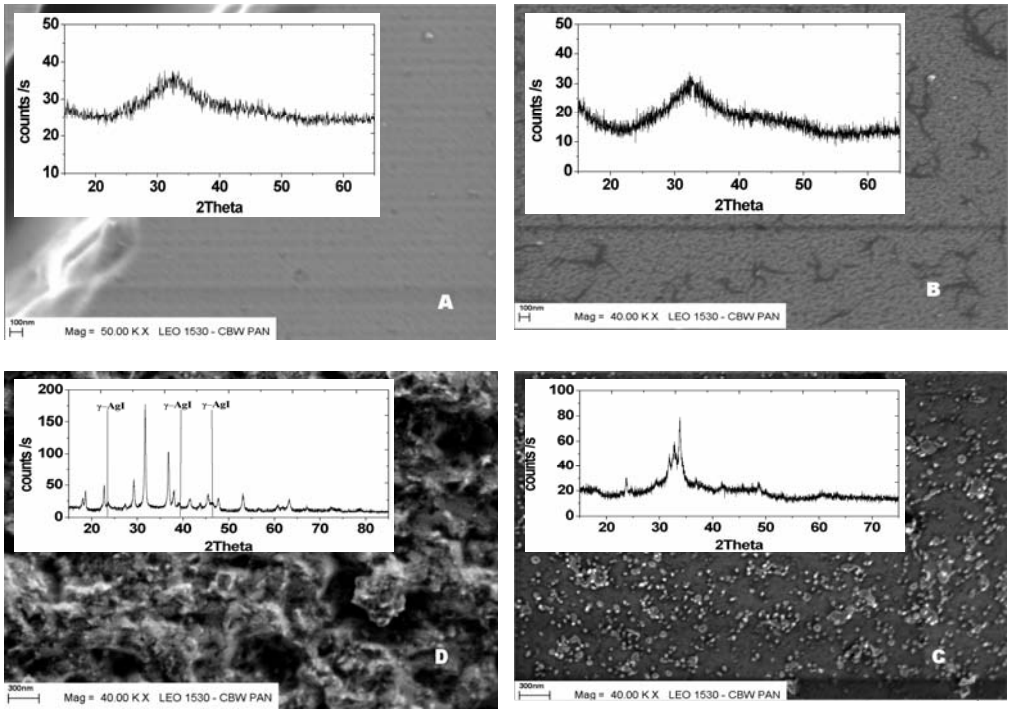

Fig. 7. SEM images of the $60AgI–30Ag_2O–10P_2O_5$ glass: a) as-received; after annealing at 60 °C for 12 min (b), at 60 °C for 12 min and at 64 °C for 145 min (c), at 60 °C for 12 min, at 64 °C for 145 min, and at 66 °C for 418 min (d)

The SEM image of the as-received glass bulk showed a uniform structure, in which few small inclusions are embedded (Fig. 7a). On the contrary, SEM images of the glass after annealing at 60 °C manifested a complex microstructure, whose shape suggests rather inhomogeneities of the glass phase (nano-sized) than the precipitation of some foreign inclusions (Fig. 7b). The presence of such inclusions was exhibited only by SEM images recorded for the glass annealed at 64 °C (Fig. 7c). It seems that annealing at 60 °C results in a phase separation in the glass and that such material appears to be a better ion conductor than the untreated one. These results suggest that mainstream crystallization is preceded by a pre-crystallization stage. It is very likely that during this stage elements of the glass structure, previously uniformly distributed, begin to regroup and form volumes or domains, enabling the further growth of crystallization seeds.

4. Conclusions

Crystallization processes in superionic AgI–Ag_2O–P_2O_5 ([Ag_2O]/[P_2O_5] = 3) glasses are determined by the total concentration of AgI dopant in the material and by thermal treatment of the glass. In as-received (thermally untreated) glasses, the following phases are successively formed with increasing total AgI concentration: pure glass without detectable (XRD) traces of crystalline phases, glasses containing β-AgI and some other, unidentified crystallites precipitated on the surface, and, finally, a composite material being a glass matrix with embedded β/γ-AgI. Two bulk crystallization processes were identified in solid glasses with $50 < x < 75$. During annealing, the initial product of crystallization transforms into the final one. There is an evidence that crystallization is preceded with a pre-crystallization stage, in which the glass matrix becomes inhomogeneous, forming some nano-size volumes.

Acknowledgements

The authors express their thanks to Dr. S. Gierlotka, High Pressure Research Center, UNIPRESS, Warsaw, for the assistance in SEM investigations.

References

[1] ADAMS ST., HARIHARAN K., MAIER J., Solid State Ionics, 86–88 (1996), 503.
[2] ADAMS ST., HARIHARAN K., MAIER J., Solid State Ionics, 75 (1995), 193.
[3] GARBARCZYK J.E., JOZWIAK P., WASIUCIONEK M., NOWIŃSKI J.L., Solid State Ionics, 175 (2004), 691.
[4] NOWINSKI J.L., WNETRZEWSKI B., JAKUBOWSKI W., Solid State Ionics, 28–30 (1988), 804.
[5] WNETRZEWSKI B., NOWIŃSKI J.L., JAKUBOWSKI W., Solid State Ionics, 36 (1989), 209.

Received 10 December 2004
Revised 15 March 2005

Materials Science-Poland, Vol. 24, No. 1, 2006

Crystallization processes in silver-ion conducting borate and phosphate glasses

J.L. NOWIŃSKI*

Faculty of Physics, Warsaw University of Technology, ul. Koszykowa 75, 00-662 Warsaw, Poland

Crystallization processes in silver-ion conducting superionic borate and phosphate glasses are presented. Experimental evidence indicates that these processes are determined by the dopant concentration *x*, glass former, molar ratio of modifier to former $\eta = [Ag_2O]/[P_2O_5]$, cooling rate of the molten glass during preparation, and by the thermal history of the glass. A crystal-free material is produced by the press-quenching method, in which the total concentration of AgI does not exceed 64–65 mol %. Rapid quenching of highly-doped borate glasses results in the formation of α-AgI crystallites in the glass. The phase deteriorates when stored for a long time or after pressure operation. Annealing prompts crystallization in solid glasses when they contain $40 < x < 65$ mol % of dopant. Only surface crystallization takes place when $0 < \eta < 1$. In the $1 < \eta < 2$ range, the surface crystallization of γ-AgI dominates, provided the annealing time is not too long. When the concentration of the modifier Ag_2O is high ($\eta > 2$), the crystalline phases precipitate in the glass bulk. Investigations point to the key role of a rigid substructure in crystallization. Some of the results indicate that primary crystallization is preceded by a pre-crystallization stage.

Key words: *crystallization; borate glass; phosphate glass; α-AgI*

1. Introduction

For a long time, crystallization effects in superionic glasses have not attracted much attention of researchers who have been mainly interested in ionic properties of this class materials. Therefore, only a limited number of papers considering the subject have been published. In consequence, details of the crystallization processes, mechanisms of crystallization, and their influence on the properties of superionic glasses are hardly known.

In one of the first papers devoted to crystallization, it has been shown that the solubility limit of silver iodide in Ag_2O–P_2O_5 glass matrix is about 60 mol % [1, 2].

*E-mail: nowin@if.pw.edu.pl

The excessive amount of dopant precipitated in the bulk of the glass as a mixture of β- and γ-AgI inclusions.

The properties of silver superionic glasses, prepared by rapid quenching, were reported by a group from the University of Osaka [3–14]. Their research revealed that in highly doped borate, vanadate, and germanate glasses, an α-AgI crystalline phase was formed. At normal conditions, its structure is stable above 147 °C and the compound exhibits superionic properties. Below this temperature, it transforms into a poor ion conducting β-AgI phase. The finding raised hopes for devising methods allowing the structure stabilization of compounds exhibiting superionic properties at high temperatures.

The influence of crystalline precipitates on the ion conductivity of silver iodide oxysalt glass was investigated by Adams et al. [15, 16]. An anomalous increase of conductivity was found, correlating with the interface area between the crystalline inclusion and glassy matrix. Garbarczyk et al. showed that nanocrystallization in $Li_2O–V_2O_5–P_2O_5$ glasses enhances the ion conductivity of the material [17].

The reported results advocate that crystalline nanoparticles embedded in a glassy matrix improve its ionic characteristics. Such glass–ceramic composites seem to be promising technologically, but their application calls for materials satisfying severe technical regimes. Therefore, the knowledge of how to design a material and control its properties is essential. To understand the nature of crystallization processes in superionic glasses is not only an academic, but also an urgent technological need.

The work aims to summarize experimental observations related to crystallization processes in silver ion conducting borate and phosphate glasses doped with silver iodide. Although the selected glasses are rather outside the interest of technology, they appear to be ideal model media, useful for fundamental investigations of ion and molecular processes in glasses.

2. Experimental

Phosphate glasses were prepared from AgI, $AgNO_3$, and $NH_4H_2PO_4$. NH_4NO_3 was added to some glasses as an additional substrate. AgI, $AgNO_3$, and H_3BO_3 were used as starting compounds in borate glass preparation. After grinding, stoichiometric amounts of the reagents were placed in a furnace. The crucible with the substrates was kept at 400 °C for about half an hour. During this stage of the reaction, the constituents melted and some ammonia and water evaporated from the melt. Next, the temperature was increased to about 650 °C, causing nitrogen oxide to be released. The melt was annealed for about 20 minutes and then, depending on the quenching method, an appropriate procedure was employed. In the case of the press-quenching method, the melt was quenched between two stainless steel plates. Disks of a cast glass, about 5 cm in diameter and 0.5 mm thick, were formed. The press-quenching method assures the cooling rate up to about 10^2 K/s. Square solid samples, with a

1 cm base, were cut out from the disks for further investigations or when necessary the glass was powdered in an agate mortar. A surface layer was removed from the sample with a very fine sand paper.

When a rapid quenching was required, the melt was heated at the temperature range 300–350 °C for about 10 minutes and then it was poured between two rollers rotating with the speed of 700–1000 rpm. Thin flakes of the material were produced. The twin-roller method allows the melt to be cooled with a rate of 10^3–10^5 K/s [4].

X-ray diffraction was carried out using a Philips X'Pert Pro diffractometer. An HTK 1200 Anton Paar X-ray diffraction camera oven, equipped with a temperature control attachment, was employed for the thermal treatment of the samples and high temperature X-ray diffraction.

Differential scanning calorimetry (DSC) measurements were performed using a Perkin-Elmer Pyris 1 instrument. A LEO 1530 field emission scanning electron microscope was used in glass microstructure investigations. Ion conductivity was measured by the impedance spectroscopy method.

3. Results and discussion

The course of the crystallization processes in phosphate and borate glasses, in general, depends on: chemical composition, i.e. dopant concentration *x*, the glass former, and the molar ratio of modifier to former $\eta = [Ag_2O]/[P_2O_5]$ (i), the thermal history of the glass, comprising the annealing sequences at various temperatures and of various duration(ii), the cooling rate υ of the molten glass during preparation (iii). The variety of the observed crystallization phenomena makes it difficult to specify the individual influence of each factor on the process. It is more convenient to consider separately the class of crystallization processes taking place during quenching of the glass melt and the class of crystallizations, which are initiated and proceeded by external factors (like temperature) in the glass.

3.1. Crystallization in molten glass

When the crystalline phase is formed during quenching, crystallization depends mainly on the total AgI concentration *x*, the chemical composition of the glass former, and on the cooling rate. Crystal-free phosphate glasses are produced when the total concentration of the dopant does not exceed about 64–65 mol % and when they are prepared by the press-quenching method [1, 2]. Increasing the cooling rate hardly affects the solubility limit of the silver iodide dopant. Also, the value of η does not influence the formation of the crystalline phase in the glass. The excess of the dopant precipitates as a mixture of β- and γ-AgI. The average size of a crystalline grain decreases with increasing cooling rate – as the broadening of the XRD lines of the rapid-quenched material suggests.

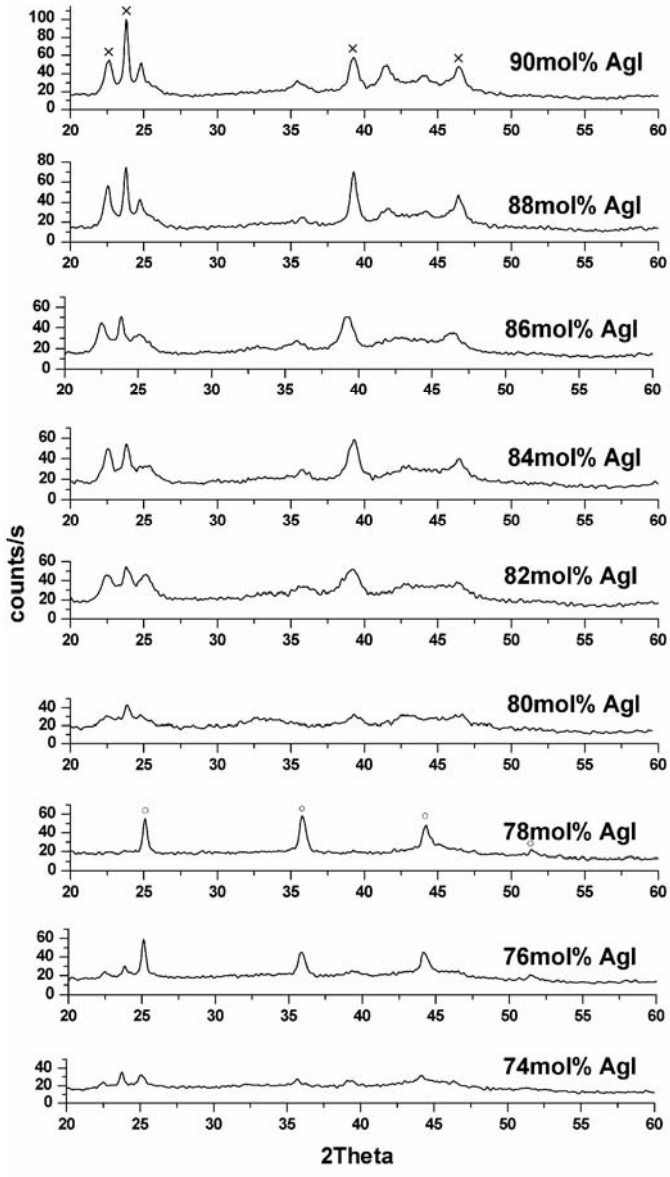

Fig. 1. X-ray patterns of xAgI–(100 – x)(0.75Ag_2O–0.25B_2O_3) glasses as a function of silver iodide content x; crosses denote reflections characteristic of β-AgI, open circles those characteristic of α-AgI

Crystallization in borate glasses is sensitive to the cooling rate. When the rate is relatively low, the dopant solubility limit and crystalline products are similar to those for phosphate glasses. For a high cooling rate, the crystallization route is different. Figure 1 presents the XRD patterns of borate glasses (η = 3) collected at room temperature, prepared by the twin-roller method, ordered as a function of x. The shape of

the profiles and the 2θ positions of the diffraction lines suggest that the investigated materials are glass–crystalline composites comprising α-, β-, and γ-AgI. The relative contents of each crystalline phase vary with the total silver iodide concentration in the material. For x = 78, the diffractograms indicate that only the cubic α-AgI phase is present in the glassy matrix. There was an attempt to prepare a single α-AgI, rapidly cooling AgI melt. Also, a part of the glass melt was cooled at a lower rate. In both cases, the obtained material contained only β/γ-AgI inclusions. In another experiment, highly doped phosphate glasses were subjected to the rapid quenched procedure, resulting in the production of the glass/β/γ-AgI composite.

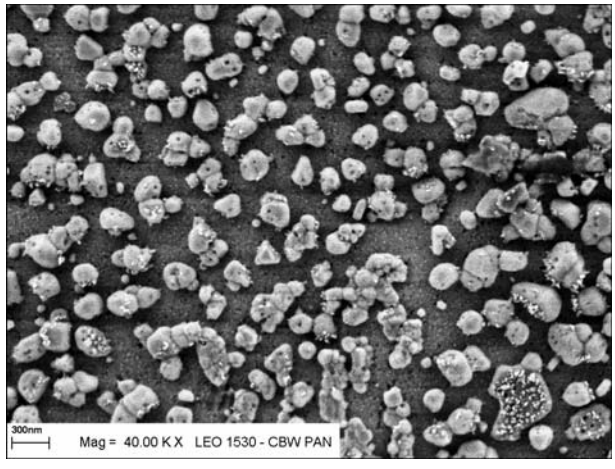

Fig. 2. SEM image of the 78AgI–16.5Ag_2O–5.5B_2O_3 rapid quenched glass

A detailed analysis of α-AgI crystallization reveals its complex nature. Figure 2 shows a SEM photograph of the material with x = 78. One can see the presence of oval inclusions, about 100 nm in diameter, dispersed in the glassy matrix. The inclusions are amorphous, as indicated by XRD patterns with no diffraction lines. When the inclusions break up, forming smaller objects 20–40 nm in diameter, the diffraction lines characteristic of α-AgI appear in the XRD pattern. Tatsumisago et al. [14] found that similar oval inclusions also grow during the annealing of highly doped borate glasses following the precipitation of α-AgI nanocrystals. Our observation and reports in the literature are in agreement, that the α silver iodide phase, stable at room temperature, can be formed only if it is embedded inside a glassy matrix of a suitable chemical composition. High total dopant concentration in the glass is essential for the process. When the cooling rate is too low, thermodynamic conditions are not far from equilibrium and concentration of the AgI dissolved in the glass matrix is not high enough to prompt the formation of oval inclusions. Rapid quenching, however, at conditions far from thermodynamic equilibrium, allows a much higher concentration of silver iodide to be introduced into the glass matrix, therefore the α phase crystallizes in glasses prepared with this method.

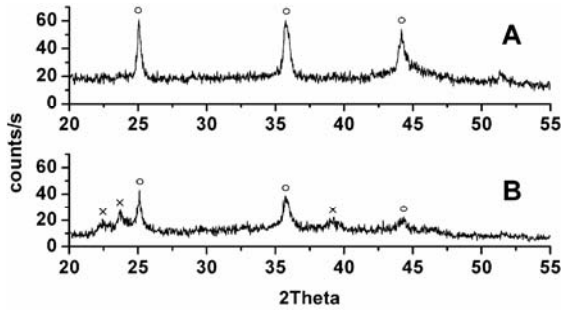

Fig. 3. X-ray patterns for the $78AgI–16.5Ag_2O–5.5B_2O_3$ glass:
a) just after rapid quenching, b) after storing at RT for 3 months; crosses denote reflections characteristic of β-AgI, open circles those characteristic of α-AgI

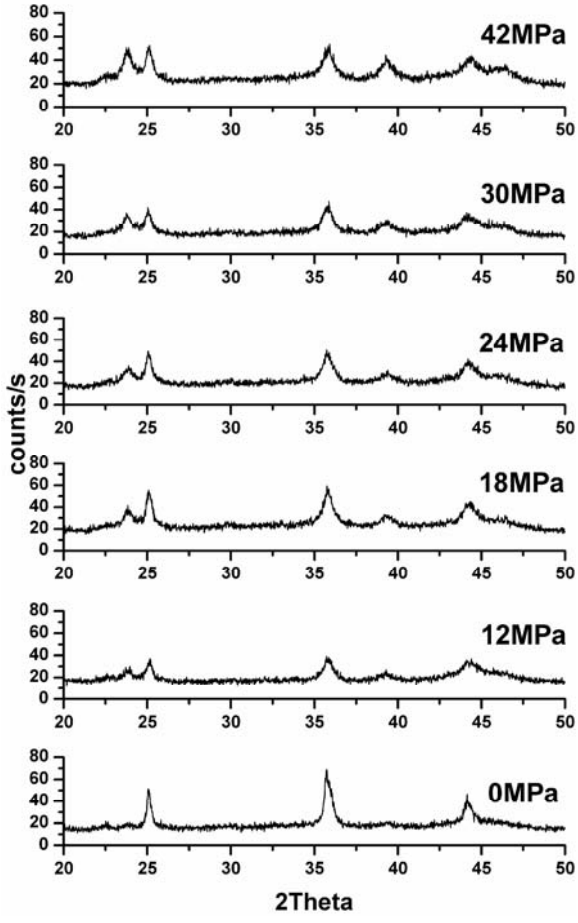

Fig. 4. X-ray patterns for the $78AgI–16.5Ag_2O–5.5B_2O_3$ glass after pressure application: a) as quenched, b) after storage at RT for 3 months; crosses denote reflections characteristic of β-AgI, open circles those characteristic of α-AgI

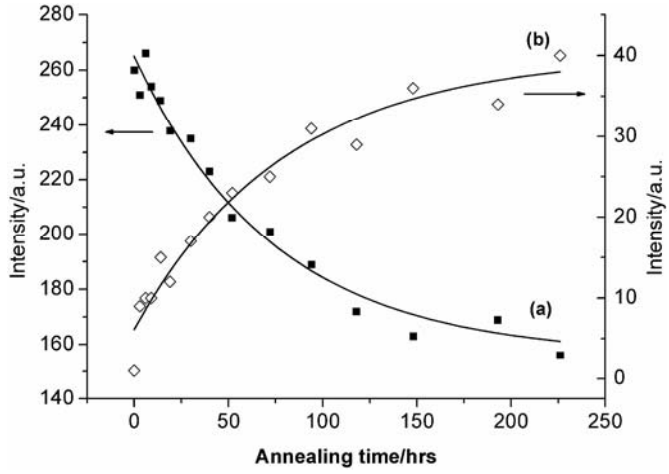

Fig. 5. The XDR intensity of the peak $2\theta = 35.8°$, characteristic of α-AgI (a), and the diffraction line $2\theta = 22.4°$ attributed to β-AgI (b) as a function of the annealing time at 60 °C for the $78AgI–16.5Ag_2O–5.5B_2O_3$ glass

The α-AgI crystalline precipitates deteriorate when the material is stored for several months at RT or subject to high pressure (Figs. 3 and 4). Annealing at elevated temperatures also causes the disappearance of the precipitates. It was observed that decreasing α-AgI content correlates with increasing γ-AgI content in the glass (Fig. 5), suggesting that this phase is formed due to the consumption of the former one.

3.2. Crystallization in solid glasses

Crystallization processes are relatively better recognized in phosphate glasses. For this reason, the discussion will be mainly focused on that group of crystallizations. Among various external and internal factors affecting the composite microstructure of the material, the most significant are: dopant concentration x, the parameter η, and thermal history. The influence of these factors on crystallization can be represented in the two-dimensional phase space of x and η (Fig. 6).

The most interesting phase volume for crystallization covers the $40 < x < 65$ mol % range. Below and above this range, the process is difficult to initiate by annealing. Generally, for this phase crystallization volume, experimental evidence indicates that the more AgI is dissolved in the glass, and the higher temperature and longer annealing time, the easier crystallization proceeds. The type of the crystallization, namely bulk (homogeneous) or surface (heterogeneous), is strongly governed by the parameter η. Employing the phase space approach, one can indicate the area of the most probable occurrence of the crystallization type (Fig. 6). Only surface crystallization takes place when $0 < \eta < 1$. For the $1 < \eta < 2$ range, the surface crystallization of γ-AgI dominates, provided the annealing time is not too long. When thermal treatment

lasts several days and the applied temperature does not exceed 20–50 °C above the glass transition temperature, the γ-AgI phase disappears and the bulk crystallization of $Ag_{16}I_{14}P_2O_7$ proceeds. [18]. Crystallization for glasses with $1 < \eta < 2$ can change if an additional NH_4NO_3 substrate is added during preparation. Usually, ammonia nitrate is used to prevent the decomposition of silver compounds. During annealing the molten substrate, NH_4NO_3 decomposes, producing gaseous ammonia and nitrogen oxides. The ionic properties of the glasses prepared with and without ammonia nitrate are identical, but their crystallization properties are different. While in the former precipitates crystallize on the surface, in the latter they locate inside the glassy matrix.

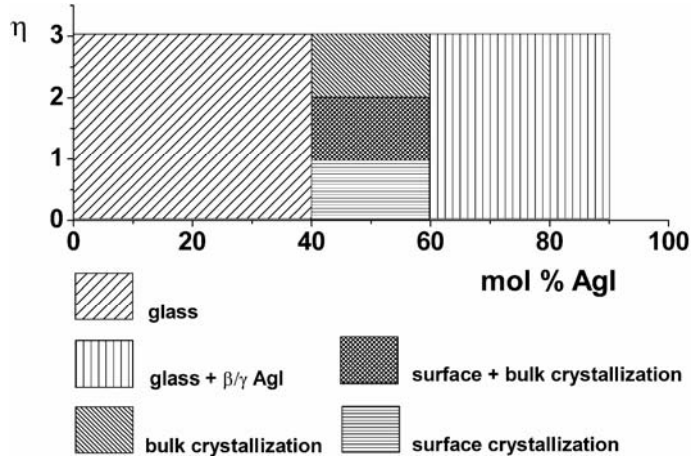

Fig. 6. Phase diagram of the crystallization process in the AgI–Ag_2O–P_2O_5 glasses; $\eta = [Ag_2O]/[P_2O_5]$

When the concentration of the modifier Ag_2O is high ($\eta > 2$), the crystalline phase precipitates in the glass bulk. The process exhibits a characteristic two-stage course. In the beginning, a transitional phase first precipitates, then during annealing it gradually disappears and a second crystalline phase is formed at the expense of the first one. Both phases have unknown structures, as the analysis of XRD patterns reveals [19].

The beginning of crystallization in this glass exhibits unusual features. Complementary XRD, SEM, and impedance spectroscopy investigations revealed that primary crystallization is preceded by a pre-crystallization stage, in which a uniform glass matrix transforms and produces a domain-like area, in which crystallization probably initiates; the details are presented in [19].

3.3. Mechanism of crystallization

Trying to understand the experimental evidence discussed earlier, it is necessary to consider the susceptibility of the glass structure to change under certain thermodynamics conditions. The rigid part of the glass structure comprises chains of PO_4 tetra-

hedra sharing corners. The length of a chain depends on the value of η. Very long chains are formed if $\eta \approx 1$. In the case of $\eta = 2$, short chains consisting of two tetrahedra are present, while for $\eta = 3$ only single PO_4 tetrahedra exist. Among these crystal units, Ag^+ and I^- ions locate in a disordered manner, constituting a so-called ionic substructure. During crystallization, the structure units exhibit a long-range order. One can assume that ordering proceeds only within one of the substructures or within the whole structure. According to the classical theory of crystallization [20], a foreign phase can grow only if crystallization seeds of suitable size are present in the material. In the case of the discussed glasses, in the molten state, local fluctuations could form some volumes occupied by silver and iodine ions only. For low and intermediate doping, the volumes are too small to reach a critical size. In contrary, in highly doped glasses, fluctuations can produce the appropriate volumes required for crystallization. Therefore, the ions order during quenching, forming AgI. Since the critical size of the crystallization seed is determined by the chemical composition of the volume, one could conclude that the critical size should be the same or similar in all silver oxysalt superionic glasses. That would explain why the solubility limit of AgI is practically the same in all these glasses [21–23].

In solid glasses at normal conditions, elements of the rigid substructure are immobile, inhibiting any crystallization. At elevated temperatures, they are more movable, depending on the lengths of polyhedron chains. Due to fluctuations in the local density of the chains, volumes containing silver and iodine ions, free of chains, can be formed in some places. Inside them, critical size seeds can be formed. The probability of forming such a seed increases with the total concentration of the dopant, with temperature, and with the annealing time. On the other hand, longer polyhedron chains are less mobile. Therefore, in agreement with our observations, it is difficult, if at all possible, to proceed with bulk crystallization for glasses with $\eta \approx 1$ and relatively easy for those with $x > 60$ mol % ($\eta \approx 3$). When chains are short enough and the dopant concentration is about 40–60 mol %, the chance to form a critical seed of AgI is rather low. The involvement of entire units of the structure is more favourable, first in the formation of volumes with an appropriate chemical composition, and next in their ordering. Such a mechanism would explain the presence of the pre-crystallization microstructure observed in glasses with $\eta = 3$ and the formation of some crystalline phases with unidentified structures. Also, crystallization in glasses with $\eta = 2$, where silver iodine phosphate was identified, firmly supports the suggested mechanism. $Ag_{16}I_{12}P_2O_7$ can be formed from $(P_2O_7)Ag_4$ chains, Ag^+ and I^- ions.

The nature of the process leading to the formation of α-AgI in borate glasses seems to be an intriguing and challenging problem. Evidence advocates the phase separation of glass. The nanometer size of the α silver iodide precipitate indicates an important role of the surface energy in stabilization. On the other hand, ordinary, nanocrystalline AgI exists only as a β structure [24]. Therefore, the glass matrix stabilizes the α structure also. Why, then, does the borate matrix stabilize and the phosphate one does not? What property of the matrix decides about stabilization? Pressure

investigations expose the role of internal friction as a stabilization factor. Unfortunately, the state of present knowledge does not give a satisfactory answer for these questions.

4. Conclusions

It was shown that crystallization processes in silver-ion conducting borate and phosphate glasses are governed by the chemical composition of the glass and its thermal history, including the quenching of the melt. It is difficult to suggest one universal crystallization scheme common for all glasses, because of the variety of crystallization routes and complex ordering mechanisms. An analysis of the experimental evidence points to the key role of the mobility of the rigid substructure during crystallization. Some of the results indicate that primary crystallization is preceded by a pre-crystallization stage.

α-AgI crystallization is interesting and technologically promising. Investigations revealed that under specific conditions, such as high pressure or long-lasting storage at room temperature, the phase deteriorated. The mechanism of this crystallization needs further investigations.

Acknowledgements

The author appreciates the assistance of colleagues and diploma students from the Superionic Glass Laboratory, Faculty of Physics, Warsaw University of Technology. The SEM photographs were made courtesy of dr St. Gierlotka, High Pressure Research Center, UNIPRESS, Warsaw.

References

[1] NOWIŃSKI J.L., WNĘTRZEWSKI B., JAKUBOWSKI W., Solid State Ionics, 28–30 (1988), 804.
[2] WNĘTRZEWSKI B., NOWIŃSKI J.L., JAKUBOWSKI W., Solid State Ionics, 36 (1989), 209.
[3] TATSUMISAGO M., SHINKUMA Y., MINAMI T., Nature, 354 (1991), 217.
[4] TATSUMISAGO M., SHINKUMA Y., SAITO T., MINAMI T., Solid State Ionics, 50 (1992), 273.
[5] TATSUMISAGO M., TANIGUCHI A., MINAMI T., J. Am. Ceram. Soc., 76 (1993), 235.
[6] TATSUMISAGO M., ITAKURA N., MINAMI T., J. Non-Cryst. Solids, 232–234 (1998), 267.
[7] SAITO T., TATSUMISAGO M., MINAMI T., J. Electrochem. Soc., 143 (1996), 687.
[8] ITAKURA N., TATSUMISAGO M., MINAMI T., J. Am. Ceram. Soc., 80 (1997), 3209.
[9] TATSUMISAGO M., TORATA N., SAITO T., MINAMI T., J. Non-Cryst. Solids, 196 (1996), 687.
[10] TANIGUCHI A., TATSUMISAGO M., MINAMI T., J. Am. Ceram. Soc., 78 (1995), 460.
[11] SAITO T., TORATA N., TATSUMISAGO M., MINAMI T., J. Phys. Chem., 99 (1995), 10691.
[12] TATSUMISAGO M., OKUDA K., ITAKURA N., MINAMI T., Solid State Ionics, 121 (1999), 193.
[13] TATSUMISAGO M., SAITO T., MINAMI T., Solid State Ionics, 71/72 (1994), 394.
[14] TATSUMISAGO M., SAITO T., MINAMI T., J. Non-Cryst. Solids, 293–295 (2001), 10.
[15] ADAMS ST., HARIHARAN K., MAIER J., Solid State Ionics, 86–88 (1996), 503.
[16] ADAMS ST., HARIHARAN K., MAIER J., Solid State Ionics,75 (1995), 193.
[17] GARBARCZYK J.E., JÓŹWIAK P., WASIUCIONEK M., NOWIŃSKI J.L., Solid State Ionics, 175 (2004), 691.

[18] NOWIŃSKI J.L., GOŚCINIAK R., MROCZKOWSKA M., GARBARCZYK J.E., WASIUCIONEK M., Glass Techn., 46 (2005), 125.
[19] NOWIŃSKI J.L., MROCZKOWSKA R.M., GARBARCZYK J.E., WASIUCIONEK M., Mater. Sci.-Poland, 24 (2006), 161.
[20] CHRISTIAN J.W., *The Theory of Transformation in Metals and Alloys*, Oxford, Pergamon Press, 1965.
[21] MINAMI T., J. Non-Cryst. Solids, 56 (1983), 15.
[22] MINAMI T., J. Non-Cryst. Solids, 73 (1985), 273.
[23] MINAMI T., NAMBU Y., TANANKA M., J. Am. Ceram. Soc., 60 (1977), 467.
[24] WANG Y., MO J., CAI W., YAO L., ZHANG L., Materials Letters, 56 (2002), 502.

Received 10 December 2004
Revised 15 March 2005

Materials Science-Poland, Vol. 24, No. 1, 2006

EXAFS/XANES studies of the local structure of amorphous ionic and electronic-ionic conductors

M. WASIUCIONEK*, J. GARBARCZYK, R. BACEWICZ, P. JÓŹWIAK, J. L. NOWIŃSKI

Faculty of Physics, Warsaw University of Technology, ul. Koszykowa 75, 00-662 Warsaw, Poland

X-ray absorption spectroscopy methods such as EXAFS (Extended X-ray Absorption Fine Structure) and XANES (X-ray Absorption Near Edge Structure) are sophisticated and effective tools for studying the local structure of many solids and liquids. Their use is particularly valuable in the case of amorphous systems, in which due to the absence of long-range order the possibilities of structure determination by diffraction methods are limited. EXAFS and XANES have been extensively used to study the local structure of many electrically conducting (via ions, electrons, or both electrons and ions) solids. The special merit of the latter studies is that their results reveal the short-range structure of these conductors, which is an important factor determining their transport properties. The paper reports recent results of EXAFS/XANES studies on the local structure of selected electrically conducting glasses of the Li_2O $–V_2O_5–P_2O_5$ system and their silver analogues. All spectra were acquired at the K-edge of vanadium.

Key words: *EXAFS; XANES; amorphous ionic conductor; local structure; vanadate glass*

1. Introduction

During over thirty years of progress in the field of solid-state ionics it has been established that the transport of ions and electrons in electrically conducting solids is strongly dependent on the structure of the conducting materials (cf. recent review by Hull [1]). Structural studies are relatively straightforward in the case of crystalline materials, where one can apply the powerful method of X-ray diffractometry (XRD). The structure determination of amorphous solids is more difficult due to absence of long-range order in these materials, which makes XRD much less efficient. There are, however, several spectroscopic methods, such as Raman scattering, infrared absorption (IR), and electron paramagnetic resonance (EPR), which can provide information on the local structure of these solids.

*Corresponding author, e-mail: mwas@mech.pw.edu.pl

An important group of such methods is X-ray absorption spectroscopy (XAS). The most widely applied of them are EXAFS (extended X-ray absorption fine structure) and XANES (X-ray absorption near edge structure), sometimes jointly called XAFS (X-ray absorption fine structure).

Throughout the years XAFS methods have been used to study a large number of systems: solid, liquid, and gaseous. The main advantages of the methods compared to other spectroscopies are: their selectivity (they probe the vicinity of a given central atom that absorbs X-rays up to a few Å), insensitivity to long-range order, the possibility of determining the basic parameters of several of the closest coordination shells (the number of atoms in each shell, distances, multiple scattering paths, etc.) [2]. Additionally, XANES spectra in the immediate proximity of the absorption edge are sensitive to the formal state of oxidation of transition metal atoms, to the symmetry of the cage formed around the central absorbing atom by its nearest neighbours, to details on atomic or molecular orbitals, to allowed and forbidden transitions of the central atom, etc. Among the systems investigated by XAFS methods, there have been also ionic and mixed electronic-ionic solid conductors, such as e.g., α- and β-AgI and silver borate glasses [3, 4], bismuth oxides, and BIMEVOX-es [5, 6] or V_2O_5, and vanadate glasses or gels [7, 8].

In this paper, we present the results of our XANES studies on lithium vanadate -phosphate glasses, which are known to be mixed electronic-ionic conductors (cf. e.g. Ref. [10]), and on their analogues with lithium replaced by silver.

2. Experimental

Lithium and silver vanadate and vanadate-phosphate glasses were prepared by a standard press-quenching technique [10] from dried reagent-grade chemicals: $AgNO_3$ (POCh), $LiNO_3$ (Aldrich), V_2O_5 (ABCR), $NH_4H_2PO_4$ (POCh). The compositions of the series of lithium-containing glasses may be described by the general formula $xLi_2O\cdot(100 - 2x)V_2O_5\cdot xP_2O_5$, where x = 15, 35, and 45. Silver glasses had the composition described by an analogous formula, namely $xAg_2O\cdot(100 - 2x)V_2O_5\cdot xP_2O_5$, where x = 15 and 35. Additionally, we carried out XAFS studies on a reference material – commercial crystalline V_2O_5 powder (ABCR, reagent grade).

As-received glasses, prior to XAFS measurements, were routinely characterized by X-ray diffractometry (XRD), which confirmed the absence of crystalline phases.

Before XAFS measurements, samples were ground in an agate mortar to a uniform powder. The powder was evenly distributed on a Scotch adhesive tape and covered with another piece of adhesive tape. The resulting "sandwiches" were mounted on a sample holder. All measurements were done at room temperature.

XAFS experiments were carried out on a A1 station at the Hasylab synchrotron facility in Hamburg. The X-ray energy range near the K-edge of vanadium (5465 eV) was used. The radiation was monochromatized by a Si (111) monochromator set

either in a standard 2-crystal mode or a in a special 4-crystal mode (for some runs of XANES). The latter mode was used to improve the energy resolution of the incident beam (below 0.5 eV). The studies were done in transmission mode using ionisation chambers as detectors of incident and transmitted radiation.

3. Results

Lithium vanadate-phosphate glasses. The XAFS spectra of glasses with a composition of $x\mathrm{Li_2O}\cdot(100 - 2x)\mathrm{V_2O_5}\cdot x\mathrm{P_2O_5}$ contain several characteristic features: a strong pre-peak, an absorption edge and an oscillatory part above the edge. The absorbance modulations are stronger close to the edge and are damped at higher energies. The fast decay of the oscillations in the EXAFS signals observed for most of the studied glasses led to difficulties in obtaining reliable values for interatomic distances of the secondary and further coordination shells as well as other parameters characterizing local structure. An overview of the EXAFS studies of these glasses will be presented in a separate paper. Herein, we focus on presenting the results of the absorption spectra in the XANES region, i.e. approximately in the 5460–5540 eV range.

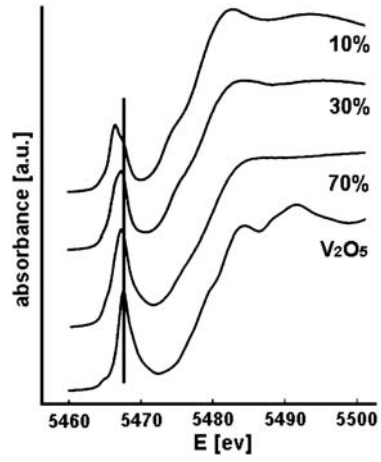

Fig. 1. XANES spectra of glasses with the composition of $x\mathrm{Li_2O}\cdot(100 - 2x)\mathrm{V_2O_5}\cdot x\mathrm{P_2O_5}$, where x = 15, 35, 45, taken at the K-edge of vanadium. The numbers next to the curves denote the molar fraction of $\mathrm{V_2O_5}$. The vertical line at the pre-edge peak serves to emphasize the position shift

Figure 1 shows the XANES region of the spectra for the studied lithium vanadate -phosphate glasses. As the amount of $\mathrm{V_2O_5}$ increases, several changes are observed: i) the pre-peak systematically shifts towards higher energies and visibly changes its shape, ii) there is some shift of the position of the absorption edge, iii) modulations above the edge, which are well discernible for crystalline $\mathrm{V_2O_5}$, are absent in the case of the investigated glasses.

Lithium vs. silver vanadate-phosphate glasses. In Figure 2, the XANES spectrum for the glass $15\mathrm{Li_2O}\cdot70\mathrm{V_2O_5}\cdot15\mathrm{P_2O_5}$ is presented, along with its silver analogue $15\mathrm{Ag_2O}\cdot70\mathrm{V_2O_5}\cdot15\mathrm{P_2O_5}$ and a reference sample – crystalline $\mathrm{V_2O_5}$. The spectra of

both glasses are identical. In both cases, the pre-peak has the same position, height, and shape. Also, above the absorption edge the spectra are similarly flat, without any discernible modulation, in opposition to the spectrum of crystalline V_2O_5, in which oscillations are well visible in this range.

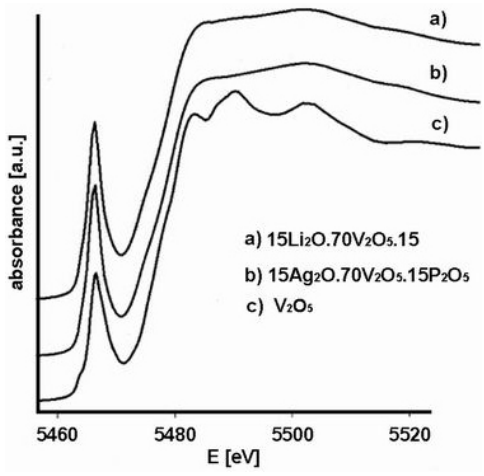

Fig. 2. XANES spectra of glasses with compositions of $15Li_2O{\cdot}70V_2O_5{\cdot}15P_2O_5$ and $15Ag_2O{\cdot}70V_2O_5{\cdot}15P_2O_5$, and of crystalline V_2O_5

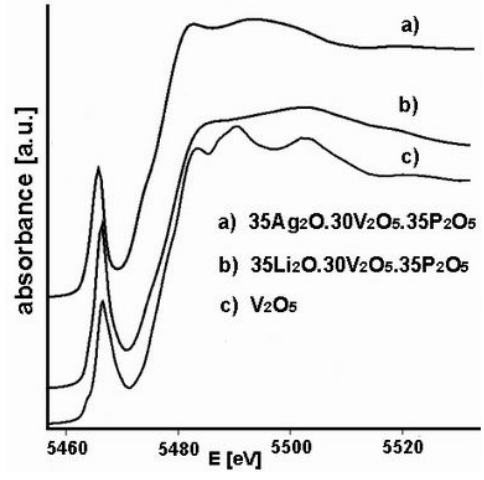

Fig. 3. XANES spectra of glasses with compositions of $35Li_2O{\cdot}30V_2O_5{\cdot}35P_2O_5$ and $35Ag_2O{\cdot}30V_2O_5{\cdot}35P_2O_5$, and of crystalline V_2O_5

The differences between the spectra obtained for lithium- and silver glasses appear when the amount of the modifier is higher (35 mol %) (Fig. 3). The position of the pre-edge peak for the $35Ag_2O{\cdot}30V_2O_5{\cdot}35P_2O_5$ glass is shifted towards lower energies compared to its lithium analogue. Additionally, there are weak, but discernible oscillations above the absorption edge for the silver glass, while a plateau is observed for the lithium glass.

4. Discussion

A strong pre-edge peak visible in all the spectra in Figure 1 is due to a 1s–3d electronic transition in the vanadium atom [7]. This transition is forbidden for the vanadium atom in an octahedral environment, but becomes allowed if the symmetry is lowered. In crystalline V_2O_5, the oxygen atoms around vanadium V^{5+} form a distorted pyramid with a square base [8]. The distances between the central vanadium atom and surrounding oxygens range from 1.58 Å (apical) to 1.78–2.04 Å (basal oxygens). The distance to the next-nearest oxygen atom below the pyramid base is much larger – 2.78 Å [8]. In our earlier EXAFS studies, we determined the first and second coordination shell radii in V_2O_5, corresponding to V–O distances of 1.68 Å and 1.98 Å, respectively. Similar values were obtained for some glasses, namely $45Li_2O{\cdot}10V_2O_5{\cdot}45P_2O_5$ [9].

The absorption edge is due to dipole-allowed 1s–4p transitions of vanadium [7, 8]. The "waves" visible on the XAFS curve of crystalline V_2O_5 just above the absorption edge have been ascribed to the multiple scattering of photoelectrons [7].

The observed systematic shift of the pre-edge peak towards lower energies for lower V_2O_5 contents (Fig. 1) reflects changes in the relative occupancy of aliovalent V^{4+} and V^{5+} states. For crystalline V_2O_5, where most of the vanadium atoms are in the V^{5+} state, the pre-peak is centred at 5467.6 eV, while for the glass $45Li_2O{\cdot}10V_2O_5{\cdot}45P_2O_5$, in which a considerable part of vanadium has V^{4+} valence due to the action of the modifier, its position is shifted to 5466.6 eV. Moreover, in the latter case the peak has a complex structure, which can be represented by a sum of two Gaussian maxima centred at 5466.6 and 5467.6 eV. The magnitudes of these component peaks reflect the occupancy of V^{4+} and V^{5+} states, respectively. By performing a best-fit deconvolution of the pre-edge peaks into their Gaussian components, it was possible to estimate the relative shares of vanadium in V^{5+} and V^{4+} states [11].

The absence or at least strong suppression of modulations just above the absorption edge observed for the studied glasses has been attributed to a relatively flat distribution of distances of neighbouring scattering atoms around vanadium in these complex amorphous systems.

The fact that the XANES spectra for lithium and silver glasses containing 15 mol % of the respective modifier (Fig. 2) are identical indicates that both modifiers (i.e. Li_2O and Ag_2O) act in the same way and introduce identical modifications to the local structure of vanadium. The absence of absorbance modulations above the edge of these glasses, contrasting with the clear oscillatory character of absorbance for crystalline V_2O_5, points to a disorder in the local structure of the former and precludes multiple scattering. This disorder in the local structure originates in part from the multitude of nearest-neighbour configurations in vanadate-phosphate glasses due to the mixed valence of vanadium, the presence of mixed vanadium-phosphate structural units, or broken V-O bonds.

When the amount of modifier is higher (35 mol %), one observes differences between the spectra of silver and lithium glasses in the XANES range. A shift of the

pre-edge peak to lower energies for the silver glass indicates an increase of the relative share of vanadium in the V^{4+} state. The presence of some structure in the XANES curve for $35Ag_2O{\cdot}30V_2O_5{\cdot}35P_2O_5$ just above the absorption edge (Fig. 3) suggests that the structural disorder in these glasses is smaller that of their lithium analogues. In particular, this may mean that the relative distances between absorbing and scattering atoms are better defined (or less distributed) in silver- than in lithium glasses.

5. Conclusions

It has been shown that XANES spectroscopy gives information on the population of aliovalent states of vanadium in glasses of the $Li_2O–V_2O_5–P_2O_5$ and $Ag_2O–V_2O_5–P_2O_5$ systems. An increase in modifier content leads to an increase of the number of vanadium atoms in the V^{4+} charge state. It has also been demonstrated that silver- and lithium glasses containing 15% of the respective modifier (Ag_2O or Li_2O) have very similar local structures. At higher contents (35%), however, there are discernible differences between the XANES curves for both glasses.

Acknowledgements

The authors are grateful to Dr. E. Welter from Hasylab for assistance in solving practical problems encountered during the experiments. Special thanks are addressed to Prof. P. Fornasini from Faculty of Physics, University of Trento, Italy for his encouragement and valuable discussions on the XAFS methodology and on the results of our experiments.

References

[1] HULL S., Rep. Prog. Phys., 67 (2004), 1233.
[2] REHR J.J., ALBERS R.C., Rev. Mod. Phys., 72 (2000), 621.
[3] DALBA G., FORNASINI P., MONTI F., ROCCA F., ADACHI M., MINAMI T., TATSUMISAGO M., TORATA N., KISHIMOTO S., Physica B, 208 209 (1995), 383.
[4] ŠIPR O., DALBA G., ROCCA F., Phys. Rev., B 69 (2004), 134201.
[5] CHADWICK A.V., COLLI C., MALTESE C., MORRISON G., ABRAHAMS I., BUSH A., Solid State Ionics, 119 (1999), 79.
[6] SAMMES N.M., TOMPSETT G.A., NÄFE H., ALDINGER F., J. Eur. Ceram. Soc., 19 (1999), 1801.
[7] WONG J., LYTLE F.W., MESSMER R.P., MAYLOTTE D.H., Phys. Rev., B 30, (1984), 5596.
[8] ŠIPR O., ŠIMUNEK A., BOCHAROV S., KIRCHNER TH., DRÄGER G., Phys. Rev., B 60 (1999), 14115.
[9] STIZZA S., DAVOLI I., GZOWSKI O., MURAWSKI L., TOMELLINI M., MARCELLI A., BIANCONI A., J. Non-Cryst. Sol., 80 (1986), 175.
[10] GARBARCZYK J.E., WASIUCIONEK M., JÓŹWIAK P., TYKARSKI L., NOWIŃSKI J., Solid State Ionics, 154–155 (2002), 367.
[11] BACEWICZ R., WASIUCIONEK M., TWARÓG A., FILIPOWICZ J., JÓŹWIAK P., GARBARCZYK J., J. Mat. Sci., 40 (2005), 4267.

Received 10 December 2004
Revised 10 January 2005

Materials Science-Poland, Vol. 24, No. 1, 2006

Ionic conductivity of polymer electrolytes comprising acrylonitrile–butyl acrylate copolymer and a lithium salt

A. ŁASIŃSKA[1], J. R. DYGAS[1*], F. KROK[1], M. MARZANTOWICZ[1], Z. FLORJAŃCZYK[2], A. TOMASZEWSKA[2], E. ZYGADŁO-MONIKOWSKA[2]

[1]Faculty of Physics, Warsaw University of Technology, ul. Koszykowa 75, 00-662 Warsaw, Poland

[2]Faculty of Chemistry, Warsaw University of Technology, ul. Noakowskiego 3, 00-664 Warsaw, Poland

New polymer electrolytes were prepared by mixing random copolymers of acrylonitrile and butyl acrylate (poly(AN-*co*-BuA)) with lithium bis(trifluoromethanesulfone) imide (LiTFSI). Electrical properties were studied by the impedance spectroscopy. The glass transition temperature was studied by DSC. Presented results concern a broad range of compositions, from a pristine copolymer to the system with 98 wt. % of salt. Correlation was established between the glass transition temperature, ionic conductivity, and salt content in the system. Mixtures of poly(AN-*co*-BuA) and LiTFSI exhibit much lower glass transition temperatures than the parent copolymer. Effects of ageing were observed for electrolytes with high salt content.

Key words: *polymer electrolyte; acrylonitrile–butyl acrylate copolymer; lithium bis(trifluoromethanesulfone)imide; polymer-in-salt electrolyte*

1. Introduction

Polymer electrolytes have received much attention in the past two decades. There has been a persistent interest in the development of highly efficient energy sources for applications such as cellular phones, mobile computers, and vehicles with electrical propulsion. Polymer electrolytes with high salt content are investigated in search for obtaining electrolytes characterised by effective anion immobilisation, which combine good mechanical properties of the polymer and high ionic conductivity of solid electrolytes. Such systems, named “polymer-in-salt” electrolytes, were first described by

[*]Corresponding author, e-mail: jrdygas@if.pw.edu.pl

Angell et al. [1]. After this pioneering work, many papers were published concerning mainly polyacrylonitrile (PAN)-based systems [2–4]. For these systems it was proposed that ion mobility is not directly connected to the segmental relaxation of the polymer matrix but that it results from the high degree of ion aggregation. PAN is, however, soluble only in a small number of aprotic solvents, such as DMSO, which are very difficult to remove during membrane preparation.

We propose the use of random copolymers of acrylonitrile (AN) and butyl acrylate (BuA) as the polymeric matrix. These copolymers are well soluble in acetonitrile, a volatile solvent that can easily be removed. In this work, we describe electrical properties of rubbery solids obtained by mixing lithium bis(trifluoromethanesulfone)imide (LiTFSI) and random copolymers poly(AN-*co*-BuA). Compositions ranging from a pure copolymer, through low salt content systems (corresponding to traditional "salt-in-polymer" electrolyte), to "polymer-in-salt" electrolytes with high salt content up to 98 wt. %, were investigated by DSC and impedance spectroscopy.

2. Experimental

2.1. Sample preparation

Lithium bis(trifluoromethanesulfone)imide $LiN(CF_3SO_2)_2$ (Aldrich) was dried under vacuum at 120 °C. Acetonitrile (Aldrich) was dried and distilled under an argon atmosphere prior to use. The copolymers of butyl acrylate (BuA) (Aldrich, reagent grade) and acrylonitrile (AN) (Aldrich, reagent grade) were obtained by radical polymerisation in the presence of azo-bis-isobutyronitrile (AIBN) as an initiator. Copolymerisation was carried out from 3 to 5 hours in the temperature range 60–70 ºC in an oil bath. For this study, a copolymer with an average molar ratio of AN m.u. (monomeric units) to BuA m.u. equal to 2:1 was prepared (67 mol % of acrylonitrile).

$LiN(CF_3SO_2)_2$ was combined with the copolymer in an acetonitrile solution in the appropriate ratio. Electrolyte membranes were obtained by casting the solution on Teflon dishes and drying in two stages under vacuum. Acetonitrile was first removed under 2500 Pa for 50 h, and then drying was carried out at 0.1 Pa for about 140 h. The salt was added in the amount of 10–98 wt. % of the electrolyte, thus in a molar ratio between 0.045:1 and 20:1 with respect to AN m.u. of the copolymer.

2.2. Differential scanning calorimetry

DSC experiments were performed on a Perkin-Elmer Pyris 1 scanning calorimeter equipped with a low-temperature measuring head. The samples were placed in hermetically closed aluminium pans. DSC traces were recorded with a heating rate of 20 °C/min after rapid cooling from 120 °C to –100 °C. The glass transition temperature was determined from the second heating run.

2.3. Impedance spectroscopy

The cells for impedance measurements were prepared in a glove box under an argon atmosphere. Circular samples (16 mm in diameter) were cut from films of thicknesses between 0.3 and 0.6 mm and mounted between gold-plated stainless steel electrodes in a gas tight holder. The holder was placed in a thermostat, and heated or cooled by Peltier elements between –60 °C and 145 °C. Temperature was controlled by an Eurotherm 2408. Impedance spectra were recorded at a constant temperature during heating and cooling runs. A computer-controlled set-up based on a Novocontrol Alpha-N dielectric analyser or a Solartron 1260 impedance analyser and a Keithley 428 current amplifier [5] was used in the frequency range 10^7–10^{-2} Hz. The amplitude of the AC signal was 20 or 100 mV rms. The stability of impedance, measured for a selected set of frequencies, was tested over the period of acquisition of an impedance spectrum. Measurements at a given temperature were automatically repeated until the drift of impedance was below a specified limit (e.g., 1% of the relative change per hour) [6].

3. Results and discussion

3.1. DSC studies

The physical properties of the obtained polymer electrolytes depend on the share of the lithium salt and the matrix used. Systems comprising poly(AN-*co*-BuA) and about 20 wt. % of the salt are a stiff rubber. With increasing salt content, the films become more flexible. At 74 wt. % of the salt, the membranes are flexible. At salt contents above 90 wt. %, the membranes exhibit the properties of a metastable, very viscous liquid.

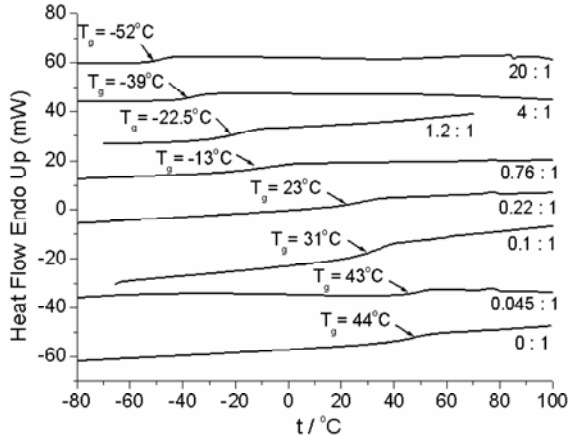

Fig. 1. DSC traces recorded during heating at a rate of 20 °C /min, after a rapid cooling from 120 °C. The glass transition is seen on the plot as a deviation in the endothermic direction. The value of T_g for each sample was taken at the centre of the slope

Table 1. Results of DSC and the electrical characterisation of the system poly(AN-*co*-BuA) with LiTFSI *

Molar ratio Li:AN	Weight % of LiTFSI	σ at 50 °C [S·cm^{-1}]	T_g [°C]	T_0 [°C]	$T_g - T_0$ [°C]	log(R_τ)
0:1	0	1.2×10^{-11}	44	–40	84	2.5
0.045:1	10	1.28×10^{-10}	43	–23	66	3.5
0.1:1	19.7	1.2×10^{-10}	31	–38	69	1.5
0.22:1	35	2.1×10^{-8}	23	–90	113	4.2
0.76:1	65	9.4×10^{-6}	–13	–100	87	5.5
1.2:1	74.6	7.3×10^{-6}	–22	–95	73	3.3
4:1	91	5.2×10^{-6}	–39	–94	55	1.2
20:1	98	1.2×10^{-4}	–52	–102	50	3.9

*Composition is given as a molar ratio of LiTFSI to AN m.u. The content of the salt is also given in weight percent. The glass transition temperature, T_g, measured by DSC, is compared with the ideal glass transition temperature, T_0, obtained by fitting the VTF function to the temperature dependence of conductivity. The logarithm of the de-coupling index, log(R_τ), is based on Eq.(3)

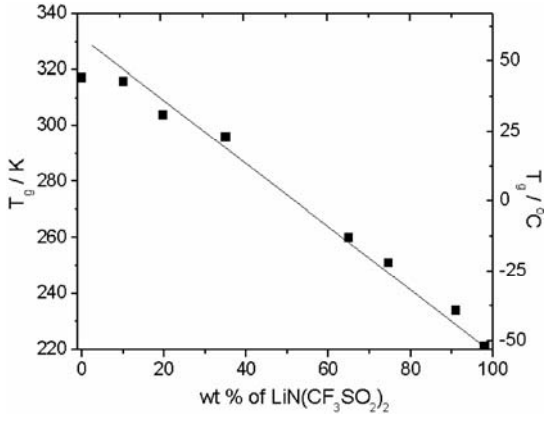

Fig. 2. Dependence of the glass transition temperature, T_g, measured by DSC, on the content of $LiN(CF_3SO_2)_2$ in the systems with poly(AN-*co*-BuA) comprising 67 mol % of acrylonitrile m.u.

The dependence of the mechanical properties of the systems on salt content is correlated with the glass transition temperature. Figure 1 shows the DSC traces for all samples with glass transition temperatures, T_g, marked. The values of the glass transition temperatures are given in Table 1. The main observation is that the salt operates like a plasticiser and that T_g for composites is lower than that of the parent copolymers. In addition, the dependence of the glass transition temperature T_g on the content of salt appears to be linear (Fig. 2). By extrapolating the dependence of T_g on salt content, the value of T_g for pure LiTFSI was estimated to be about –52 °C. The plasticising effect of lithium salts was already observed in other polymer-in-salt electrolytes comprising polyacrylonitrile or its copolymers [7, 8], but the mechanism of this phenomenon is not fully understood yet.

3.2. Ionic conductivity

Figure 3 shows the temperature dependences of the conductivity of poly(AN-*co*-BuA) with LiTFSI for the compositions listed in Table 1. The presented conductivity data were collected during cooling after first heating the cast film to about 100 °C.

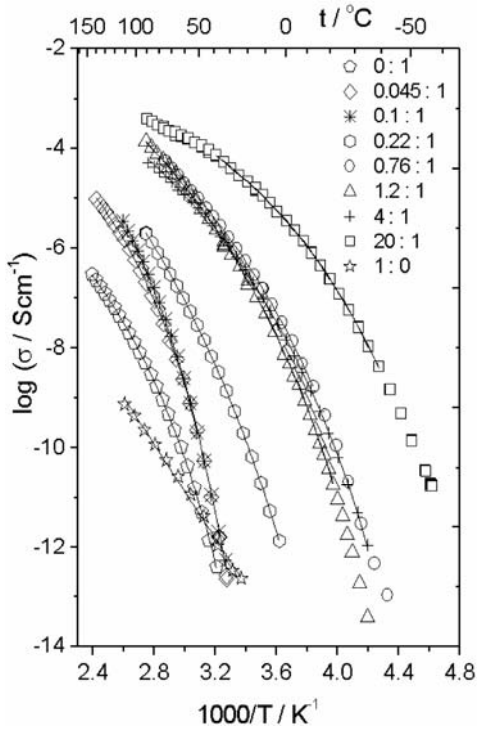

Fig. 3. Temperature dependence of the ionic conductivity of the electrolytes composed of LiTFSI and poly(AN-*co*-BuA) copolymer containing 67 mol % AN m.u. The composition of each sample is given by its respective molar ratio LiTFSI:AN m.u. The continuous lines represent the VTF function, fitted for temperatures above the glass transition temperature. The conductivity of the pristine LiTFSI salt (marked as 1:0) is fitted with a straight line representing the Arrhenius dependence

Figure 3 shows also the variation of ionic conductivity with temperature for the pristine LiTFSI salt placed between blocking electrodes, which after heating to 120 °C gives a reproducible Arrhenius-type dependence:

$$\sigma(T) = A\exp[\,-E_A/(k_B T)\,] \tag{1}$$

The conductivity of the crystalline salt at 50 °C was measured to be about 3×10^{-12} S/cm, and the activation energy in the temperature range 30–90 °C was about 1 eV.

The temperature dependence of ionic conductivity for amorphous electrolytes composed of LiTFSI and AN-*co*-BuA copolymers (Fig. 3) is well fitted by the Vogel –Tamman–Fulcher function:

$$\sigma(T) = A\,\exp[-B/(T - T_0)] \tag{2}$$

In this equation, A is the pre-exponential factor, proportional to the concentration of charge carriers, B is the pseudo-activation energy for conduction, and T_0 is the ideal

glass transition temperature. The electrical conductivity of the studied electrolytes depends on the content of lithium salt in the system. Conductivity at 50 °C ranged from 10^{-11} to 10^{-4} S/cm, showing an increase with increasing lithium salt content. Figure 4 shows the dependence of conductivity on the content of $LiN(CF_3SO_2)_2$. The ideal glass transition temperature, T_0, obtained from the fit of the VTF function is considerably lower than the T_g obtained from DSC. The difference between T_g and T_0 is also included in Table 1. The value of $T_g - T_0$ ranges from 50 °C to 113 °C.

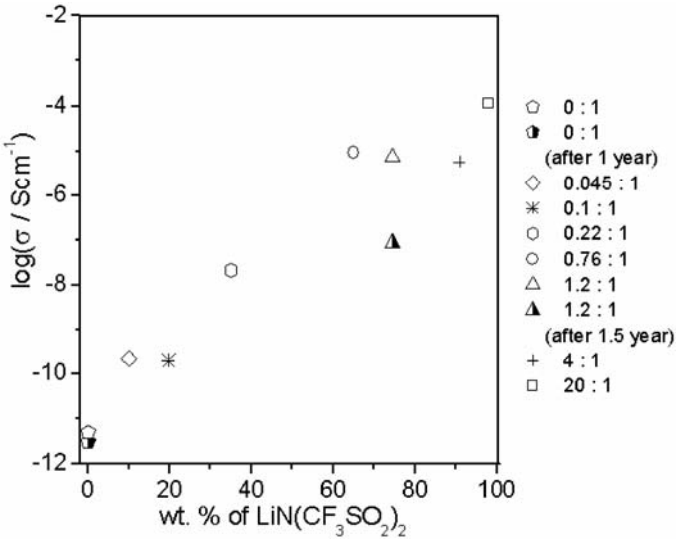

Fig. 4. Dependence of conductivity measured at 50 °C on the content of $LiN(CF_3SO_2)_2$ in the system with poly(AN-*co*-BuA) copolymer containing 67 mol % m.u. of AN. A decrease in electrical conductivity for LiTFSI:AN (1.2:1) was observed over a period of several months

The conductivity measured at the glass transition temperature, σ_{Tg}, allows the estimation of the de-coupling index R_τ, which is defined as the ratio of the shear relaxation time to the conductivity relaxation time [9]. The de-coupling index reflects the level of freedom of mobile ions from the interference by the immobile elements. At the glass transition temperature, T_g, the decimal logarithm of the de-coupling index can be obtained from an approximate relation [9]:

$$\log(R_\tau) = 14.3 + \log(\sigma_{Tg}) \tag{3}$$

For the LiTFSI/AN-*co*-BuA system, the logarithm of de-coupling index is between 1.2 and 5.5 (Table 1), generally higher than that for the poly(ethylene oxide)–LiTFSI system, in which $\log(R_\tau)$ is usually between 1 and 2 [10]. The values obtained for the studied system, however, are much lower than $\log(R_\tau)$ equal to 9.8 reported for poly(vinylsulfonic) acid lithium salt, in which the backbone oxygen is absent [11]. For comparison, typical values of $\log(R_\tau)$ for highly conducting inorganic glasses are close to 12 [9, 12–13].

For prospective applications, it is important to test the long-term stability of the obtained polymer electrolytes. The cast films were examined after over one year of storage at room temperature in a dry box with circulating argon. Changes in the physical properties were noticed. Films with a high content of the salt became less flexible or even brittle, and opaque instead of transparent. Impedance measurements on samples cut from the aged films were made under the same conditions as previously made on samples cut from freshly cast films. A comparison of the effect of ageing on the temperature dependence of ionic conductivity in the pure copolymer and polymer-in-salt system with the molar ratio of 1.2:1 LiTFSI to AN m.u. is presented in Figure 5.

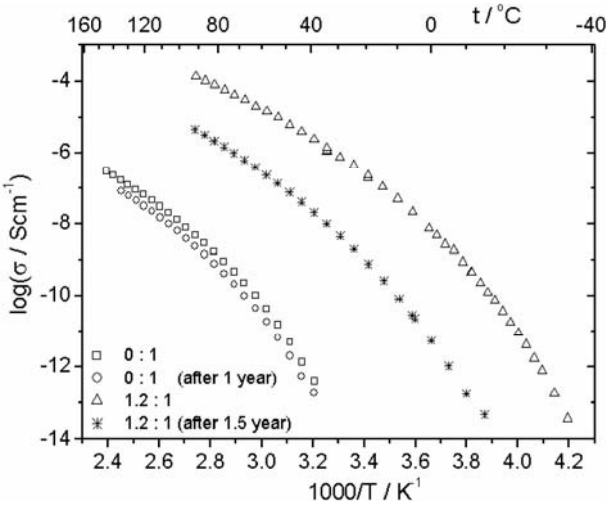

Fig. 5. The effect of ageing on the ionic conductivity of pristine poly(AN-*co*-BuA) and a polymer-in-salt electrolyte of molar ratio 1.2:1 LiTFSI to AN m.u. in poly(AN-*co*-BuA). Temperature dependence of conductivity, measured for samples from freshly cast film and for the same films after 1 or 1.5 years of storage at room temperature in an argon atmosphere

Conductivity in the polymer-in-salt system decreased by about two orders of magnitude after 1.5 years of storage, whereas the conductivity of the pristine copolymer decreased by only about 4 times after 1 year. The glass transition temperature of the pristine copolymer did not change, whereas in the case of the 1.2:1 Li:AN m.u. electrolyte it increased significantly. The nature of the changes is not clear yet. Possible phase segregation in systems with high salt content should be taken into account. A loss of volatile remnants, left from the technological process, may cause a decrease in the conductivity of the pristine copolymer.

4. Conclusions

AN-*co*-BuA copolymers with LiTFSI form flexible membranes exhibiting a glass transition temperature significantly lower than that of the parent copolymer. The glass

transition temperature, T_g, decreases with increasing lithium salt content. The conductivities of these systems increase with increasing salt content. The temperature dependence of conductivity in these systems may be described by a VTF equation. Values of the de-coupling index are considerably lower in comparison to typical values for highly conducting inorganic glasses, but higher than values for PEO-LiTFSI systems. After long-lasting storage at the room temperature in an argon atmosphere, a considerable decrease in conductivity was observed for some systems. The nature of this lack of stability is not understood yet and is presently subject to further investigations.

References

[1] ANGELL C.A., LIU C., SANCHEZ E., Nature, 362 (1993), 137.
[2] FERRY A., EDMAN L., FORSYTH M., MACFARLANE D.R., SUN J., Electrochim. Acta, 45 (2000), 1237.
[3] FORSYTH M., SUN J., MACFARLANE D.R., HILL A.J., J. Polym. Sci., Part B: Polym. Phys., 38 (2000), 341.
[4] BUSHKOVA O.V., ZHUKOVSKY V.M., LIROVA B.I., KRUGLYASHOV A.L., Solid State Ionics, 119 (1999), 217.
[5] DYGAS J.R., BREITER M.W., Electrochim. Acta, 41 (1996), 993.
[6] KUREK P., DYGAS J.R., BREITER M.W., J. Electroanal. Chem., 378 (1994), 77.
[7] WANG Z., GAO W., CHEN L., MO Y., HUANG X., Solid State Ionics, 154–155 (2002), 51.
[8] FORSYTH M., SUN J., MACFARLANE D.R., Solid State Ionics, 112 (1998), 161.
[9] ANGELL C.A., Annu. Rev. Phys. Chem., 43 (1992), 693.
[10] FLORJAŃCZYK Z., ZYGADŁO-MONIKOWSKA E., AFFEK A., TOMASZEWSKA A., ŁASIŃSKA A., MARZANTOWICZ M., DYGAS J.R., KROK F., Solid State Ionics, 25–28 (2005), 2123.
[11] XU K., ANGELL C.A., Electrochim. Acta, 40 (1995), 2401.
[12] ANGELL C.A., Solid State Ionics 18–19 (1986), 72.
[13] ANGELL C.A., [in:] T. Takahashi (Ed.), *High Conductivity Solid Ionic Conductors*, World Scientific, Singapore, 1989, p. 89.

Received 10 December 2004
Revised 10 January 2005

Materials Science-Poland, Vol. 24, No. 1, 2006

In-situ study of the influence of crystallization on the ionic conductivity of polymer electrolytes

M. MARZANTOWICZ[1*], J. R. DYGAS[1], F. KROK[1],
E. ZYGADŁO-MONIKOWSKA[2], Z. FLORJAŃCZYK[2]

[1]Faculty of Physics, Warsaw University of Technology, ul. Koszykowa 75, 00-662 Warsaw, Poland

[2]Faculty of Chemistry, Warsaw University of Technology, ul. Noakowskiego 3, 00-664 Warsaw, Poland

Simultaneous impedance measurements and optical observations of polymer electrolytes were conducted in an automated experimental setup, combining an impedance analyser, polarizing microscope with a heating stage and a digital camera. The polymer film was placed between glasses with indium tin oxide conductive layers, forming a transparent cell mounted in a custom-designed holder, which preserved an argon atmosphere. Results of *in-situ* studies for various compositions of poly(ethylene oxide) (PEO) with $LiN(CF_3SO_2)_2$ salt (LiTFSI), as well as pure PEO, are presented. In the investigated systems, crystallization had a strong impact on ionic conductivity. It was found that the initial growth of crystalline structures caused only a small fraction of the total decrease of conductivity. A large decrease in conductivity was observed during the second stage of crystallization, when no significant changes in microscope picture were observed. In pure PEO and the PEO:LiTFSI 6:1 system, a dense crystalline structure developed, resulting in a decrease in conductivity of over two orders of magnitude. In dilute PEO:LiTFSI systems, a "loose" structure was formed, with amorphous areas preserved between crystallites, and conductivity decreased by only a factor of about 6.

Key words: *poly(ethylene oxide); LiTFSI; polymer electrolyte; conductivity; crystallization*

1. Introduction

After early reports that the crystalline phase of PEO-based electrolytes is poorly conductive [1], various efforts have been taken to prevent the polymer electrolyte from crystallizing [2]. A lithium salt with a large and flexible anion, $LiN(CF_3SO_2)_2$ (lithium bis(trifluoromethanesulfone)imide – LiTFSI), was proposed as an inhibitor for crystallization. In the PEO:LiTFSI system, crystalline PEO coexists with the

[*]Corresponding author, e-mail: marzan@mech.pw.edu.pl

amorphous phase for dilute compositions [3], For a range of PEO:LiTFSI compositions between 12:1 and 6:1, a "crystallization gap" region has been reported for low-molecular-weight PEO [3], and very slow crystallization kinetics were observed for a molecular weight of about 10^6 g/mol [4,5]. For higher salt contents, crystalline complexes of PEO and salt are formed with a defined stoichiometry of 6:1, 3:1, and 2:1 EO:Li [3, 4].

The question of the influence of microstructure on ion transport in the electrolyte remains open. It has been evidenced in recent years, that in some systems the crystalline structure can support conductivity [6]. In polymer films with a structure oriented by stretching [7] or by casting in strong magnetic fields [8], much higher conductivities were obtained in the direction of chain ordering than in the perpendicular direction.

Previously, we described the influence of inhomogeneity caused by crystallization on the electrical properties of PEO and PEO with dissolved salts [9]. Polarizing microscope observations of the electrolyte were used as an additional technique, giving information on electrolyte morphology [10, 11]. Recently, simultaneous impedance measurement and microscope observations were introduced for detailed investigation of the influence of crystallization on ion transport [12, 13]. Here, we present an overview of the results obtained for PEO-based electrolytes of different compositions by *in-situ* studies. The discussion is focused on changes in the ionic conductivity of the electrolyte during crystallization.

2. Experimental

PEO:LiTFSI electrolytes were prepared by mixing $LiN(CF_3SO_2)_2$ (Fluka) and PEO (Aldrich, $M_W = 5{\cdot}10^6$ g/mol) in acetonitrile solution. The obtained solution was poured onto a glass dish, and a thin foil was formed after vacuum drying. The samples for *in-situ* measurement were cut from the foil in the form of discs, about 16 mm in diameter.

The polymer sample was placed between two glass plates covered with conductive indium tin oxide (ITO) films, which served as electrodes. The lower glass was glued to the bottom of a copper cylinder, the upper one to a piston made of Nylon®. The piston was centred inside the cylinder by an o-ring and was free to slide along the axis of the cylinder. Spring loading ensured good electrical contact between the sample and ITO electrodes. A screw mechanism limited the distance between the electrodes and maintained the parallel alignment of the plates. The holder was mounted on a custom-designed microscope stage, heated or cooled by Peltier elements. Due to moisture condensation on the glasses, most of the measurements were performed above room temperature.

Impedance measurements were made with a Novocontrol Alpha-N impedance/dielectric analyser from 10^{-2} (or 10^{-1}) to 10^7 Hz using an ac signal of 20 mV rms. Temperature was stabilized prior to the measurement of the impedance spectrum. The

drift in impedance was detected by a special algorithm, comparing impedance values measured at test frequencies at intervals of several minutes [14]. When the value of the root-mean-squared drift exceeded a specified threshold (typically 2% per hour), measurements at constant temperature were repeated, allowing for the automated detection of phase transitions.

For microscope observation, a polarizing microscope Biolar PI (PZO Warszawa, Poland) was used. The pictures were acquired using a digital camera Coolpix 4500 (Nikon). The basic functions of the camera (shutter, zoom) were controlled by a PC serial port and integrated with the measurement software written under LabView (National Instruments).

3. Results and discussion

The conductivity as a function of time during crystallization for the studied systems is depicted in Figure 1. The values of dc conductivity were calculated from the fit of an equivalent circuit to the measured impedance spectra, done with a custom-written program Firdanov [15]. Details regarding the equivalent circuit and fitting procedure have been described elsewhere [9, 13].

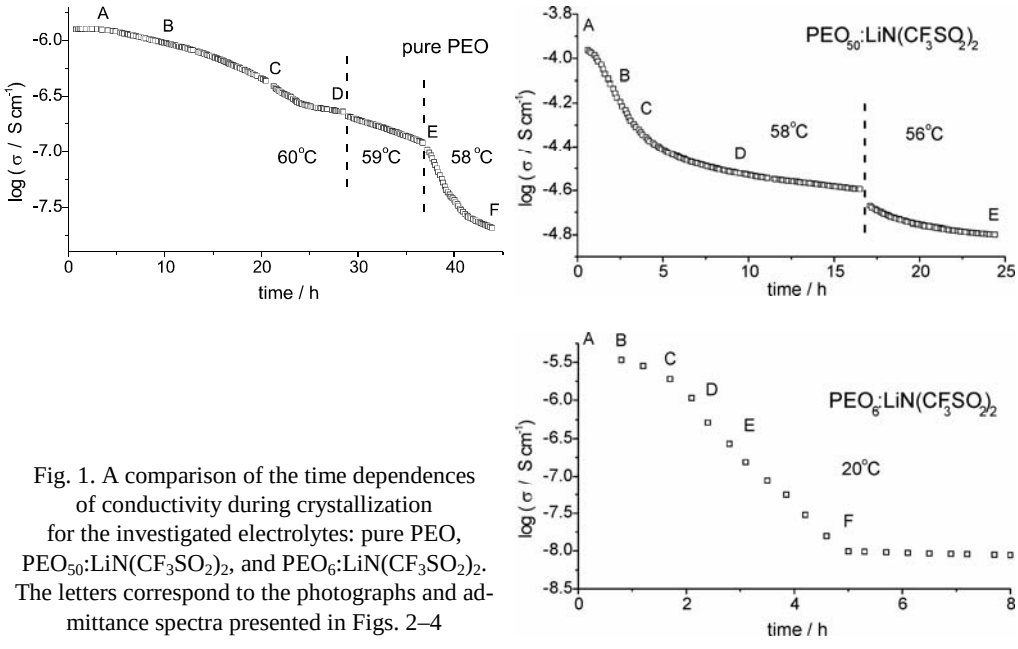

Fig. 1. A comparison of the time dependences of conductivity during crystallization for the investigated electrolytes: pure PEO, PEO_{50}:$LiN(CF_3SO_2)_2$, and PEO_6:$LiN(CF_3SO_2)_2$. The letters correspond to the photographs and admittance spectra presented in Figs. 2–4

3.1. Pure PEO

Prior to the described crystallization process, the PEO sample was fused at 80 ºC and cooled stepwise to 60 ºC. Measurements were performed with a small tempera-

ture step and a strict drift detection criterion in order to obtain stable impedance spectra during crystallization. At 60 ºC, spherulites appeared in the microscope picture.

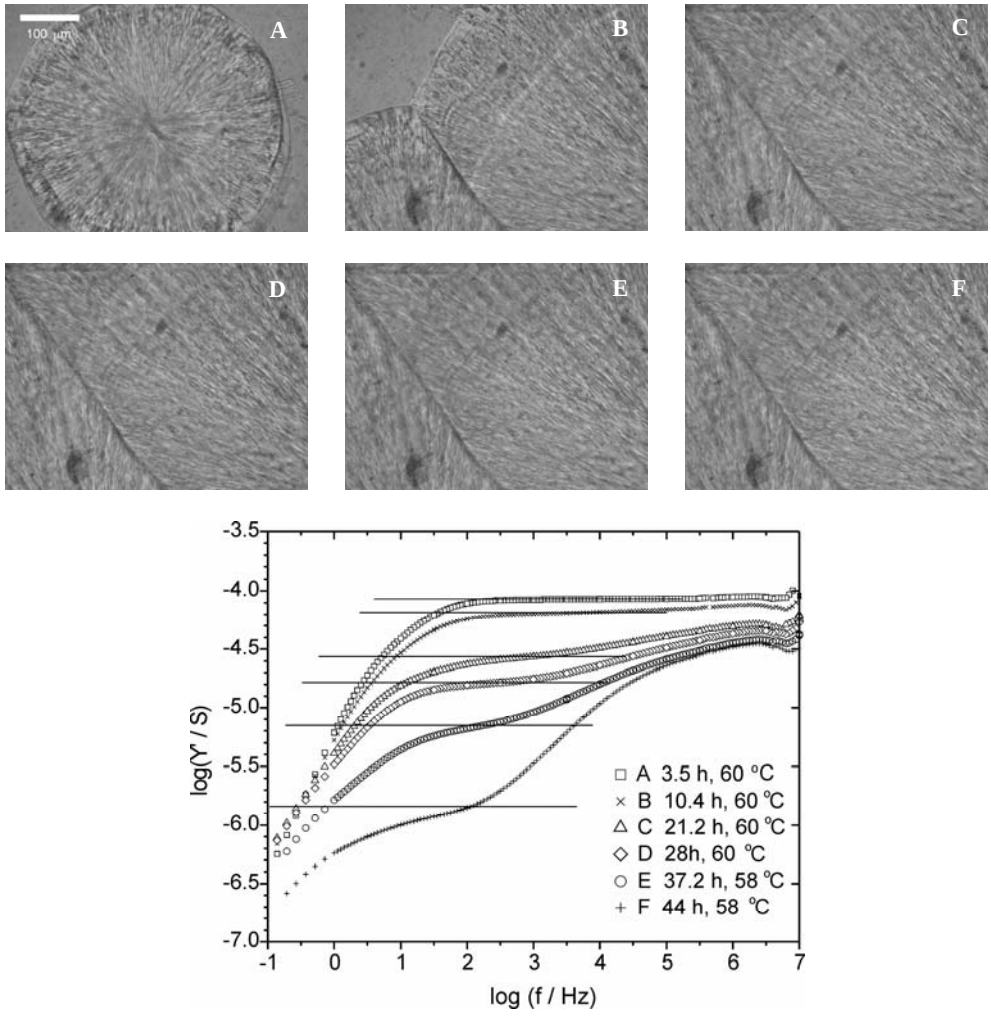

Fig. 2. Polarizing microscope photographs and corresponding spectra of the real part of admittance for pure PEO during crystallization, after cooling to 60 °C. Solid lines mark the dc conductivity estimated by a fit of an equivalent circuit to the data. The time elapsed after cooling to 60 ºC and actual temperature are indicated

Two different stages could be distinguished in the process of PEO crystallization. On cooling to 60 ºC, nucleation followed by a growth of spherulites was observed. The growth of spherulites, which was evident in the microscope pictures, had a relatively small effect on the conductivity, until the crystallites began to constitute a large fraction of the polymer (Fig. 2B). At an early stage of crystallization, when large areas of amorphous phase were still visible around spherulites (Fig. 2A), the plot of log(Y')

versus log(*f*) (Fig. 2, spectrum A) exhibited a single plateau, which extended over four decades of frequency, between 10^2 and 10^6 Hz, and corresponded to the dc conductivity. When the spherulite borders met each other, this single plateau in the log(Y') vs. log(*f*) plot became inclined (Fig. 2, spectrum B) and eventually split into two regions of mild slope divided by a range with a steeper slope around 10^4 Hz (Fig. 2, spectrum C). After about 20 h from the moment of cooling to 60 °C, the entire observation area was filled with spherulites. A decrease of conductivity was still observed. In the second stage of crystallization, upon cooling to 59 °C, and further to 58 °C, no changes in the microscope picture were detected. In contrast, at this stage significant changes in the admittance spectra were observed. These changes are mostly seen in the low frequency region, while only a slight decrease of conductance in the high frequency region may be ascribed to the temperature dependence of conductivity. A constant rate of increase in resistance with time was recorded at 59 °C (Fig. 1). Further cooling to 58 ºC caused an enormous increase in resistance.

To explain the origin of the change in electrical properties, several phenomena should be considered. In the crystallization stage, which occurred after the entire observation area was filled by the spherulites, an additional crystallization process took place within the spherulites, and this process might be responsible for blocking the conductivity pathways. Charge carriers became trapped within the structure, so they no longer could be involved in conductivity or electrode polarization. A second major effect was the hardening of the electrolyte, which could cause deterioration in the electrical contact with the electrodes. A roughening of the surface of the semicrystalline polymer might cause a decrease of the effective contact area. Some areas, like spherulite boundaries, might recess from the electrode when the density of the electrolyte increases.

3.2. PEO_{50}:$LiN(CF_3SO_2)_2$

On cooling the sample from 90 ºC to 57.5 ºC, the nucleation and gradual growth of spherulites were observed in the optical pictures (Fig. 3A–C). High concentration of nucleation centres can be explained by the fact that, despite heating to 90 ºC, the sample was not fully homogeneous. Inhomogeneities probably result from an initial phase separation, or the salt itself acts as a nucleation agent. Due to the high density of nucleation centres, the spherulites impinge on each other relatively early. This process limits the size of spherulites to less than the sample thickness (230 μm). Therefore, a 3-dimensional grain-like structure is formed (Fig. 3D, E). After the impingement of spherulites, the growth slowed down. On photographs taken in regular intervals, only slight changes can be noticed. As one of the possible causes of this phenomenon, an accumulation of non-crystallisable material at the crystallization front was proposed. The salt accumulated at the crystallization front may act as a plasticiser. This would also lead to a higher salt content in the areas between spherulites, which may require heating to higher temperatures than the melting point of PEO in order to homogenize (dissolve) the salt-rich fractions.

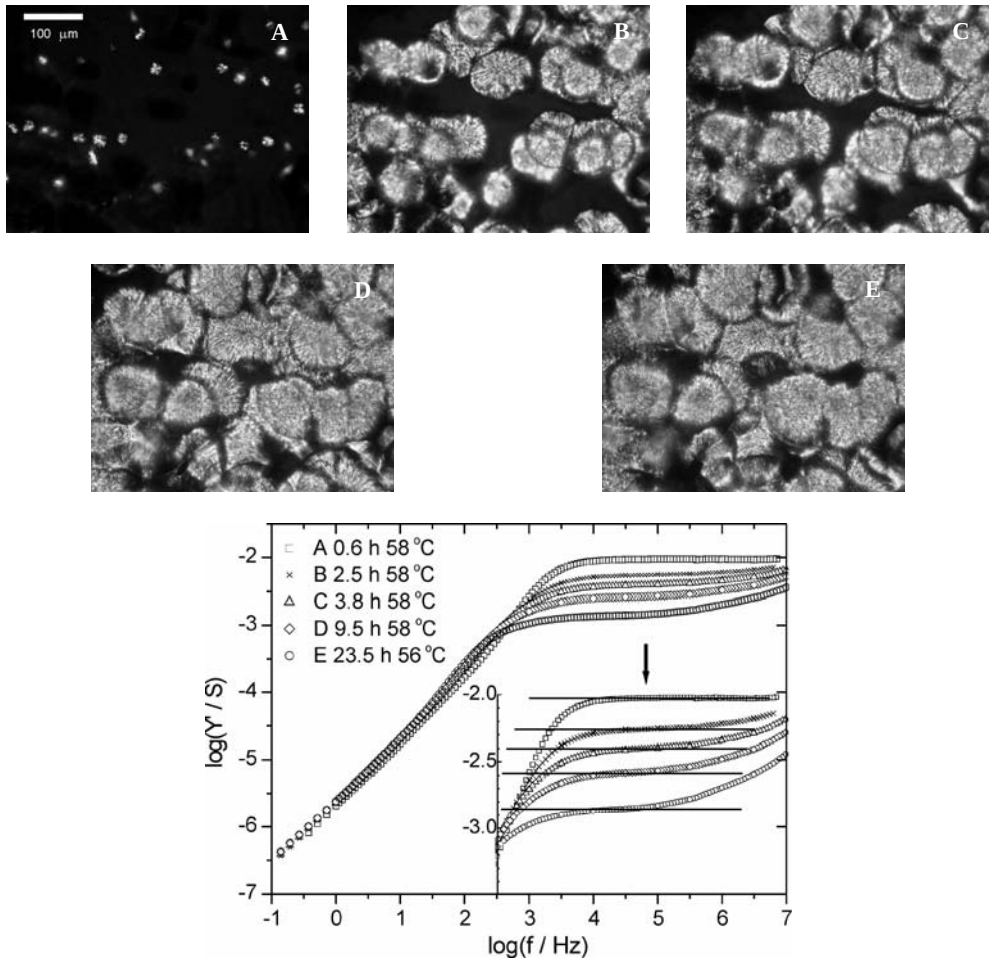

Fig. 3. Polarizing microscope photographs and corresponding spectra of the real part of admittance for PEO_{50}:$LiN(CF_3SO_2)_2$ during crystallization, after cooling to 58 °C. In the insert, the *Y* scale was magnified for clarity. Solid lines mark the dc conductivities obtained from a fit. The time elapsed after cooling to 58 ºC and temperature are indicated

At the early stages of crystallization, changes in the admittance spectra were quite similar to those described for pure PEO. The much higher conductivity values and somewhat different electrode properties, however, caused the characteristic features of the impedance spectrum to shift to higher frequencies. Even during the late stage of crystallization at 58 °C and at 56 °C, no separation of the plateau in the log(*Y′*) versus log(*f*) plot into high and a low frequency regions of mild slope was observed. Following an initial drop with a sigmoidal shape, after about 6 hours from setting the temperature to 58 °C, the conductivity changes slowed down (Fig. 1). A slow decrease of the ionic conductivity was recorded for another 10 hours, until the drift of impedance finally fell below 1% per hour threshold, which was the limit for repeating the meas-

urement. Lowering the temperature to 56 °C caused a further decrease of conductivity with time, which, however, did not affect electrode properties. Despite a grain-like structure developed during crystallization, the PEO:LiTFSI system retained good contact with the electrodes.

3.3. PEO_6:$LiN(CF_3SO_2)_2$

For the investigation of crystallization in isothermal conditions, the $P(EO)_6$:$LiN(CF_3SO_2)_2$ sample was melted at 80 ºC and then fast cooled to 20 ºC (cooling time was about 5 minutes). At this temperature, the measurements were repeated.

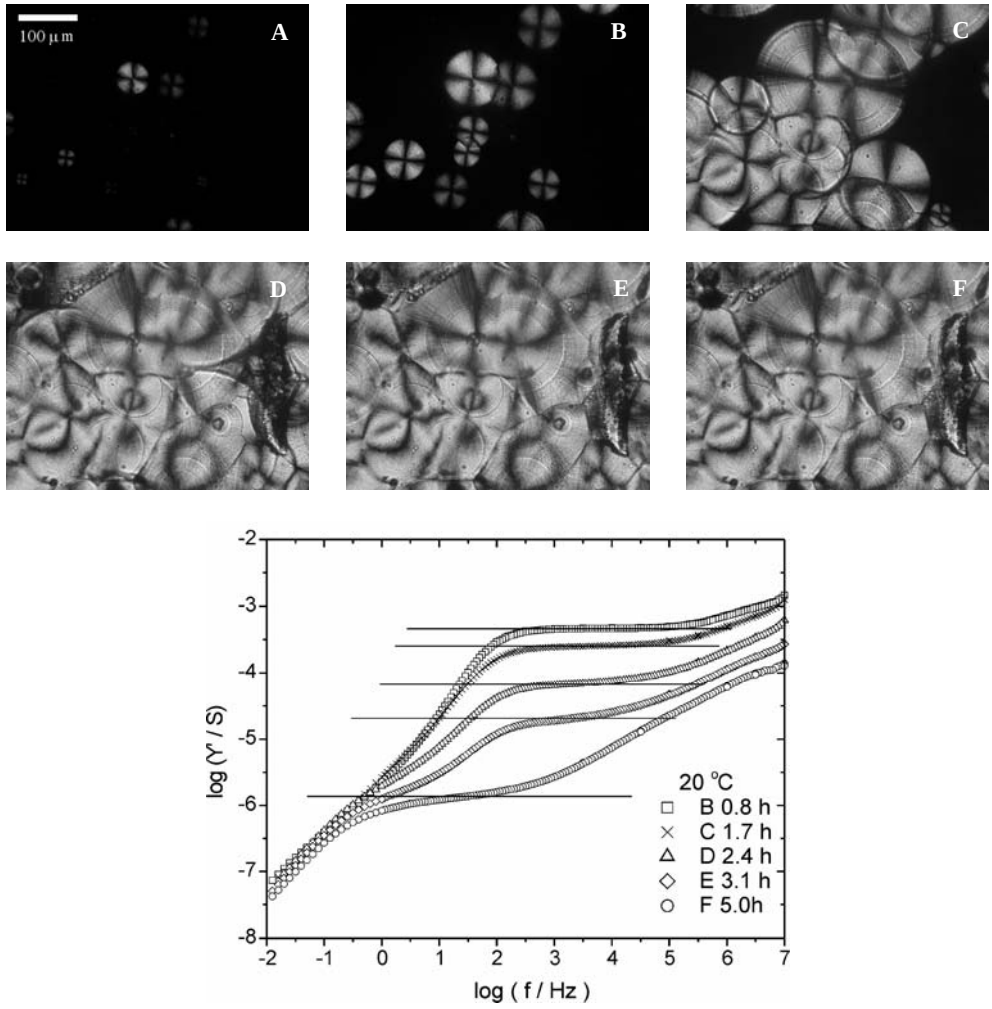

Fig. 4. Polarizing microscope photographs and corresponding spectra of the real part of admittance for PEO_6:$LiN(CF_3SO_2)_2$ during crystallization, after cooling to 20 °C. The time elapsed after cooling to 20 ºC is indicated. Solid lines mark the dc conductivities obtained from a fit

About ten minutes after the temperature of the sample had been stabilized, the first nucleation centres became visible (Fig. 4A). After two hours, the whole observation area was covered with spherulites. The final structure was densely packed, i.e. no black areas corresponding to a free amorphous phase were observed. Large changes were observed in the admittance spectra even after the microscope pictures ceased to exhibit any changes (Fig. 4D–F). The most probable explanation of the continued decrease of conductivity is, like in the case of pure PEO, a densification of the structure (the growth of crystalline structures between existing lamellae) which blocks charge carrier transport through the remaining amorphous phase. In a dense structure, even a small change in the volume fraction of amorphous phase can result in a break in the continuity of the easy conduction path. Another reason for the large drop of conductivity can be an increase in sample stiffness and a loss of contact. This can be related to a transition from spherulites suspended in melt to amorphous regions trapped between dense networks of crystalline lamellae (phase inversion).

4. Conclusions

The results obtained by *in-situ* impedance measurement and optical observations indicate that ionic conductivity of PEO-based electrolytes does not depend directly on the proportions between the amorphous and crystalline phases, but rather on the structure developed during crystallization. Ion transport seems to rely on the existence of amorphous passes between the crystalline structures. In the initial phase of spherulite growth, the changes of impedance were rather small. A significant decrease in conductivity was observed after the borders of spherulites met, and in the subsequent stages of crystallization when changes in the microscope picture were minor. This percolation mechanism of conductivity corresponds well with our earlier results obtained for low-molecular-weight poly(ethylene glycol) [11].

In systems with a developed dense crystalline structure, like pure PEO and the 6:1 PEO:LiTFSI crystalline complex, crystallization strongly affects both bulk and interfacial transport properties. The continuity of the amorphous path through the electrolyte can be broken due to secondary crystallization processes, resulting in a decrease of conductivity. Changes in the electrode part of the impedance spectra may be ascribed to the transition from an amorphous to a solid interface, causing a roughening of the surface and a loss of contact with the electrodes. The cumulative effect of crystallization was a large decrease of conductivity by two orders of magnitude or more.

In dilute systems, like the presented 50:1 EO:Li electrolyte, pure crystalline PEO coexists with an amorphous phase, which seems to have higher salt content than the initial molar ratio. Small areas filled with this phase are seen in the microscope picture, even after long crystallization times. In the grain-like structure, the percolation threshold for ion transport through the remaining amorphous areas can be easily reached. Therefore, the drop in conductivity resulting from crystallization is much smaller.

References

[1] BERTHIER C., GORECKI W., MINIER M., ARMAND M.B., CHABAGNO J.M., RIGAUD P., Solid State Ionics, 11 (1983), 91.
[2] GRAY F.M., *Polymer Electrolytes*, Chapt. 2, Royal Society of Chemistry, Cambridge, UK (1997).
[3] LASCAUD S., PERRIER M., VALLÉE A., BESNER S., PRUD'HOMME J., ARMAND M., Macromolecules, 27 (1994), 7469.
[4] LABRECHE C., LEVESQUE I., PRUD'HOMME J., Macromolecules, 29 (1996), 7795.
[5] EDMAN L., FERRY A., DOEFF M.M., J. Mater. Res., 15 (2000), 1950.
[6] MACGLASHAN G.S., ANDREEV Y.G., BRUCE P.G., Nature, 398 (1999), 792.
[7] GOLODNITSKY D., LIVSHITS E., RESENBERG YU., LAPIDES I., PELED E., Solid State Ionics, 147 (2002), 265.
[8] GOLODNITSKY D., LIVSHITS E., KOVARSKY R., PELED E., Proc. 9th Int. Symp. Polymer Electrolytes, Mrągowo, Poland, August 2004.
[9] DYGAS J.R., MISZTAL-FARAJ B., FLORJAŃCZYK Z., KROK F., MARZANTOWICZ M., ZYGADŁO -MONIKOWSKA E., Solid State Ionics, 157 (2003), 249.
[10] MARZANTOWICZ M., DYGAS J.R., KROK F., MOLENDA A., ZYGADŁO-MONIKOWSKA E., FLORJAŃCZYK Z., Mol. Phys. Rep., 35 (2002), 65.
[11] MARZANTOWICZ M., DYGAS J.R., JENNINGER W., ALIG I., Solid State Ionics 176 (2005), 2115.
[12] MARZANTOWICZ M., DYGAS J.R., KROK F., ŁASIŃSKA A., FLORJAŃCZYK Z., ZYGADŁO-MONIKOWSKA E., Electrochim. Acta, 51 (2006), 1713.
[13] MARZANTOWICZ M., DYGAS J.R., KROK F., ŁASIŃSKA A., FLORJAŃCZYK Z., ZYGADŁO-MONIKOWSKA E., AFFEK A., Electrochim. Acta, 50 (2005), 3969.
[14] DYGAS J.R., KUREK P., BREITER M.W., Electrochim. Acta, 40 (1995), 1545.
[15] DYGAS J.R., BREITER M.W., Electrochim. Acta, 44 (1999), 4163.

Received 23 December 2004
Revised 23 January 2005

Materials Science-Poland, Vol. 24, No. 1, 2006

Novel composite polymer-in-salt electrolytes based on a PVdF matrix obtained with a solvent-free technique

J. PIEKARSKA, M. PTASIŃSKA, G. ŻUKOWSKA, H. WYCIŚLIK, M. SIEKIERSKI*

Warsaw University of Technology, Faculty of Chemistry, Polymer Ionics Research Group, ul. Noakowskiego 3, 00-664 Warsaw, Poland

Polymer-in-salt electrolytes have been widely investigated as potentially interesting materials for applications in both lithium devices and for basic studies of materials being halfway between polymeric electrolytes and conductive inorganic glasses. Novel composite "polymer-in-salt" electrolytes were synthesized based on a poly(vinylidene difluoride) matrix and various lithium salts. The polymer was chosen due to its high chemical, electrochemical, and thermal stability, widely known from the application in gel electrolytes in lithium batteries. On the other hand, it is well known that a solvent, once incorporated into a PVdF structure, is impossible to remove. Thus a novel method, based on thermal sintering of the composite, was developed to avoid contamination of the sample. Electrolytes of different polymer-to-salt molar ratios, varying from 0.5:1 to 2:1, were synthesized. The influence of preparation conditions (sintering time, temperature and the number of sintering cycles) was also examined. Impedance spectroscopy was used to measure electrical conductivity. Infrared spectroscopy was introduced to investigate ion–ion and ion–polymer interactions and the phase structure of the polymer matrix. Additionally, X-ray diffractometry was applied in structural studies.

Key words: *polymer-in-salt electrolyte; electrical conductivity; composite; ion interactions; lithium*

1. Introduction

Polymer-in-salt electrolytes have been extensively studied in recent years [1–4]. The mechanism of conductivity in these systems is intermediate between that of composite polymeric electrolytes and inorganic ionic glasses. On one hand, the highly conductive region is located on the salt grain boundaries; the observed highly defective structure of the particle surface is similar to that observed in inorganic glassy superconductors. On the other hand, the polymeric material included in these compos-

*Corresponding author, e-mail: alex@soliton.ch.pw.edu.pl

ite acts mainly as a binding agent and as a source and stabilizer of the grain surface defects, thus it does not directly take part in charge carrier transport. Percolation between the surface layers of the salt grains must be observed in order to maintain the high mobility paths along the sample, thus a particular minimal volume fraction of the salt in the composite is needed to obtain high conductivity.

The (vinylidene difluoride)-hexafluoropropylene copolymer (Kynar®) matrix has been widely used in gel electrolytes for lithium batteries. The material is known to be chemically, electrochemically, and thermally stable. It is also well known that if a solvent is incorporated into the PVdF structure it is almost impossible to remove it completely [5, 6]. Thus, a typical method of obtaining polymer-in-salt electrolytes based on dissolving the polymer and salt in the solvent, casting the film, and solvent evaporation is unusable when a dry system is taken into consideration.

A thermal method based on the subsequent homogenisation of the polymer and salt mixture, pressing the pellet, and thermal sintering was used to obtain the composites. During the process, temperature was elevated slightly above the melting temperature of PVdF to allow interaction between the salt and matrix. Samples with different sintering times (0.5–12 h) and varying numbers of sintering cycles (1–6) were prepared for various system compositions (salt-to-polymer molar ratios from 0.5:1 to 2:1), for lithium salts including lithium tetrafluoroborate, lithium triflate, LiTFSi, and other lithium salts.

2. Experimental

All the reagents were carefully dried under vacuum (10^{-5} torr, 60 h) prior to use. The drying temperature was in the range 130–160 ºC. The homogenisation process was performed in a nitrogen-filled dry-box with humidity lower than 5 ppm. The pressing process was performed in a steel pan with a working diameter of 13 mm under vacuum (10^{-1}–10^{-2} Torr). The applied load varied with the salt used and was equal to 6000 kg for lithium triflate and 8000 kg for other salts. All the intermittent operations, such as loading of the pan and oven, were also performed in the dry-box. For the sintering process, a vacuum oven made of titanium was used to avoid chemical interaction with the samples. PTFE separators were used on both sides of the sintered pellet. The temperature of the process was equal to 175 ºC and was controlled by a PID regulator. When multi-cycle sintering was performed, the repeated cycle consisted of two hours of sintering in 175 ºC, followed by one hour of cooling to a final temperature of about 120 ºC. For the thermal regime used, not only melting of the crystalline polymer phase was expected (needed for composite formation) but also the phase transition of the PVdF matrix form the α to the β phase.

The sintered pellet used for impedance measurements was covered with a thin gold film by vacuum evaporation to maintain good electrical contact with the test electrodes. The ac impedance was recorded with Atlas 98 HI equipment in the 1 Hz – 100 kHz range for varying temperatures (25–95 ºC). The data obtained were analysed

with Bernard Boukamp's EQ program [7] in order to determine the dc conductivity of the samples. FT-IR measurements of the composites were performed in the Nujol suspension on NaCl plates on a Perkin-Elmer 2000 spectrometer with the resolution of 0.5 cm^{-1}. X-ray diffraction was recorded on a DRON 2 apparatus utilizing CuK_α irradiation with 26 kV and a 16 mA tube current.

3. Results

Impedance spectroscopy measurements show that the dc conductivity of the obtained composites is rather low; at ambient temperature lies in the range 10^{-9} S/cm (Table 1). The differences observed between samples with various compositions and various preparation methods cannot be easily correlated and are not very large. Surprisingly, the expected percolation threshold for samples of higher than 1.25:1 salt-to-polymer ratio, leading to a strong conductivity increase, is also not observed. An exemplary thermal behaviour of conductivity is shown in Figure 1. An Arrhenius-type dependence can be observed for most of the systems studied.

Table 1. Conductivity data for various composite PVdF:salt samples

Sample composition (molar ratio)	Conductivity at 45 °C [S/cm]	Conductivity at 95 °C [S/cm]	Activation energy [kJ/mol]
$LiBF_4$:PVdF, 0.5:1, 2 h	9.19×10^{-10}	5.57×10^{-09}	72.52
$LiBF_4$:PVdF, 0.5:1, 2 h	1.09×10^{-09}	5.35×10^{-09}	79.64
$LiBF_4$:PVdF, 1:1, 0.5 h	3.04×10^{-10}	2.38×10^{-08}	91.52
$LiBF_4$:PVdF, 1:1, 1 h	1.64×10^{-10}	2.28×10^{-08}	102.88
$LiBF_4$:PVdF, 1:1, 1.5 h	1.98×10^{-10}	2.21×10^{-08}	85.95
$LiBF_4$:PVdF, 1:1, 2 h	3.1×10^{-10}	3.3×10^{-08}	99.33
$LiBF_4$:PVdF, 1:1, 6 h	1.01×10^{-09}	1.03×10^{-08}	87.18
$LiBF_4$:PVdF, 1:1, 8 h	1.54×10^{-08}	1.54×10^{-08}	89.21
$LiBF_4$:PVdF, 1:1, 12 h	3.5×10^{-10}	1.56×10^{-08}	94.03
$LiBF_4$:PVdF, 1.5:1, 2 h	3.18×10^{-09}	9.18×10^{-09}	99.85
$LiCF_3SO_3$:PVdF, 1:1, 2 h	2.7×10^{-10}	5.02×10^{-10}	14.32
$LiCF_3SO_3$: PVdF, 1:1, 6 h	2.21×10^{-10}	4.97×10^{-10}	17.67
$LiCF_3SO_3$: PVdF, 0.5:1, 2 h	1.68×10^{-10}	4.68×10^{-10}	19.32
$LiCF_3SO_3$: PVdF, 1.5:1, 2 h	6.06×10^{-11}	4.82×10^{-10}	15.87
$LiAlCl_4$:PVdF, 0.5:1, 2h	2.92×10^{-10}	5.46×10^{-09}	59.98
LiNTFS:PVdF, 0.5:1, 2 h	1.68×10^{-10}	4.68×10^{-10}	34.45
LiNTFS:PVdF, 1:1, 2 h	1.48×10^{-10}	1.14×10^{-08}	82.04
LiNTFS:PVdF, 1.25:1, 2 h	3.50×10^{-09}	1.73×10^{-08}	43.53
$LiAsF_6$:PVdF, 1.5:1, 2h	1.22×10^{-10}	1.67×10^{-09}	52.21
$LiPF_6$:PVdF, 1.5:1, 2 h	1.11×10^{-10}	6.2×10^{-09}	77.05
$LiPF_6$:PVdF, 2:1, 2 h	9.51×10^{-10}	7.14×10^{-07}	93.80

Judging from the FT-IR spectra (Fig. 2), there is no evidence of Li^+ cation coordination by polymer chains in PVdF–$LiCF_3SO_3$ composites for any studied salt-to-

polymer molar ratios (i.e. from 1:2 to 1:0.5). The positions of the characteristic salt peaks in the spectra of composite samples are almost the same as in the spectrum of pure salt. The only observed difference is in the intensity of the higher frequency contribution (with a maximum at ~658 cm^{-1}) of the peak ascribed to δ_s SO_3. In the spectrum of the crystalline salt, the maximum of this peak was found at 652 cm^{-1}, whereas in the spectra of the composite sample with a high (above 1:1) salt-to-polymer molar ratio a splitting of this band was observed.

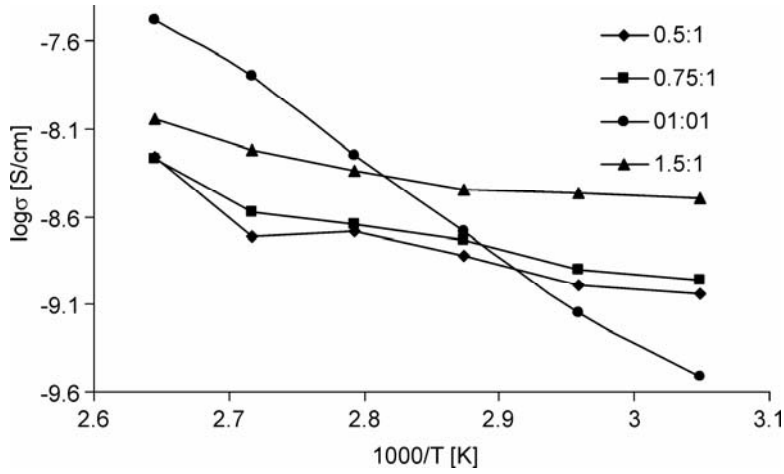

Fig. 1. Thermal dependence of conductivity for PVdF:$LiBF_4$ samples with different compositions

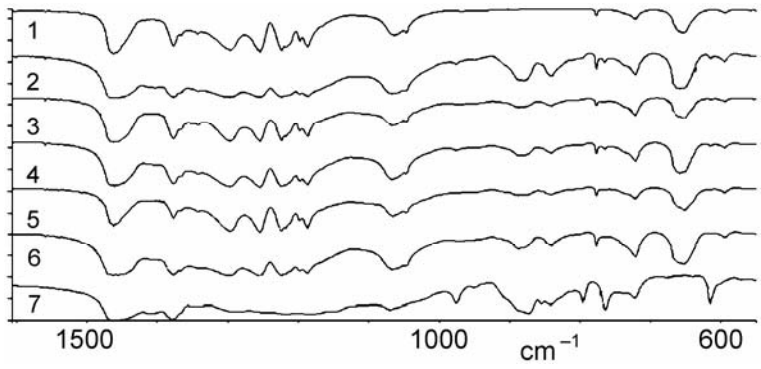

Fig. 2. FT-IR spectra of PVdF–$LiCF_3SO_3$ composites for varying salt-to-polymer molar ratios (2 – 1.5:1, 3 – 1.25:1, 4 – 1.0:1, 5 – 0.75:1, 6 – 0.5:1) compared to pure salt (1) and pure polymer (7)

We found bands ascribed both to the crystalline and amorphous phases in the spectrum of the polymer [8, 9]. It should be noticed that in the spectrum of the pure polymer mostly bands characteristic of the so-called α-phase appear, while in the composite samples we found peaks of the β-phase and of the amorphous phase of the polymer. For example, in the spectrum of PVdF powder we observed strong peaks at

795 and 615 cm^{-1}, due to t_{CH_2} and δ_{CF_2} of the α-phase. On the other hand, two various signals at 873 and 841 cm^{-1} indicate the presence of the β-phase. In the spectra of polymer electrolytes, the bands of the α-phase disappear and new spectral features at 888 cm^{-1} can be observed. All bands become broader, which may indicate a more amorphous structure.

Similar changes in the polymer characteristic pattern can be observed in the spectra of the PVdF–LiTFSI composites (Fig. 3). As in the case of $LiCF_3SO_3$-based electrolytes, the positions of the bands of the salt in the composite samples are close to those of the crystalline salt and not to those of a "free" anion. The interpretation of the spectra of PVdF–$LiBF_4$ electrolytes is more difficult, because of their poor quality. The trend observed was essentially the same, i.e. the transition of PVdF from the α to β phase in the composite samples, a result of their thermal history.

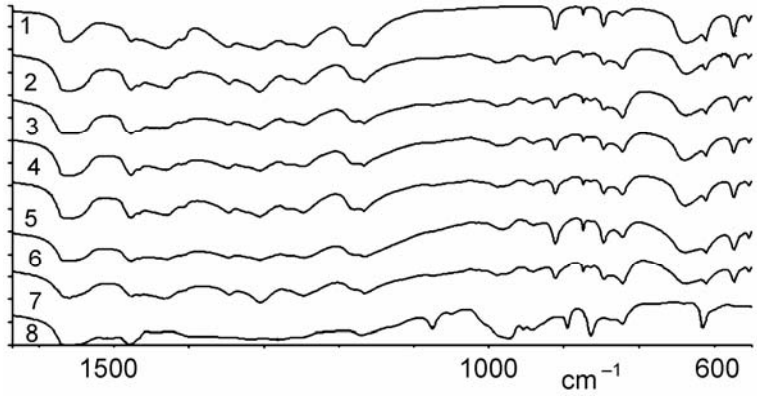

Fig. 3. FT-IR spectra of PVdF-LiTFSi composites for varying salt-to-polymer molar ratios (2 – 0.5:1, 3 – 0.75:1, 4 – 1:1, 5 – 1.25:1, 6 – 1.5:1, 7 – 2.0:1) compared to pure salt (1) and pure polymer (8)

It has to be stressed, however, that the conducting properties of solid electrolytes can be strongly affected by the type and content of the crystalline phases as well as by the distribution of the salt in the polymer matrix. We plan to perform a more detailed study of "polymer-in-salt" electrolyte structure by means of Raman mapping.

XRD experiments were first performed for pellets made of pure salts. All the compounds used were tested. A comparison between the diffraction images recorded for sintered and non-sintered pellets reveals no important differences in either reflex position or their intensity. Thus, it can be claimed that neither phase transition nor material degradation is observed under conditions identical to those used for further composite synthesis. In the second step, a set of pellets made of pure polymer matrix was investigated (Fig. 4). In this case, a recrystallisation process can be observed when comparing data for the pristine pellet (a) to those registered for the one sintered at 160 ºC, i.e. below the melting temperature of the crystalline phase. The intensity of reflex increases and the half-width decreases (Table 2), pointing not only to an in-

crease of the amount of crystalline phase, but also to an increase in crystallite size. For a partially melted sample (c, 170 ºC), a loss of crystallinity is observed. The most

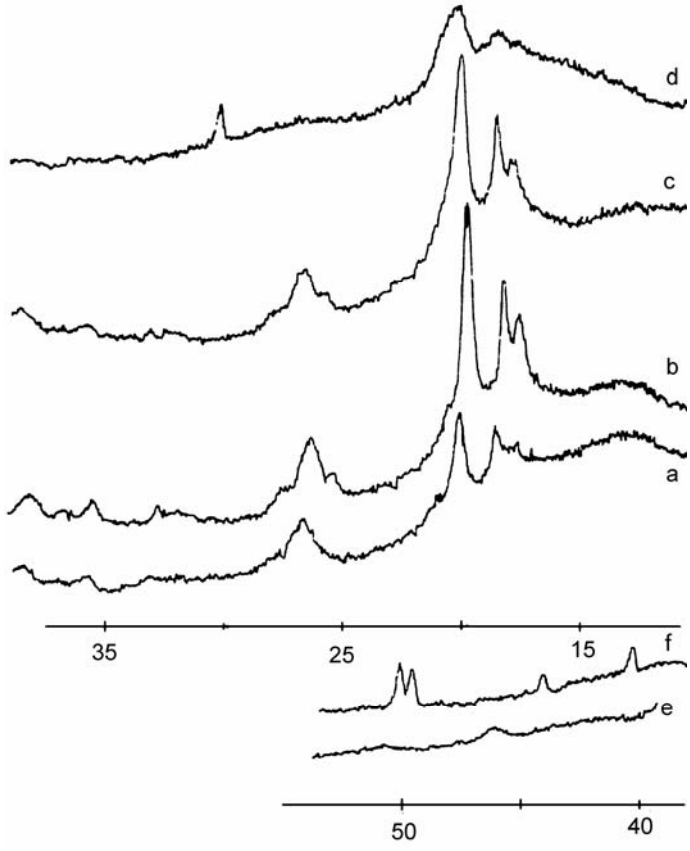

Fig. 4. X-ray diffraction patterns for PVdF pellets; a) pressed, b, e) sintered at 160 ºC, c) partially melted at 170 ºC, d, f) fully melted at 175 ºC

interesting changes are observed for the fully melted sample (d, 175 ºC) – not only does the crystallinity significantly decrease, but also a new phase is observed. The change in the shapes and positions of the peaks around $2\theta = 20^{\circ}$ is in agreement with literature data [9]. Additionally, new reflexes at about 40º and 50º can be observed, proving β phase generation. Finally, composite samples containing $LiBF_4$ were tested. The diffraction image reveals reflexes only from the salt phase. No traces of crystallinity for the polymer matrix were observed, even for the sample with the lowest salt content. These data contradict those obtained from FT-IR experiments. This discrepancy can be easily explained considering the fact that FT-IR collects information from all crystallites independent of their size, while XRD is sensitive only to objects with sizes above a particular threshold. The composite sample can contain a crystalline PVdF phase (mainly β), but in the form of very small regions.

Table 2. X-ray diffraction data collected for pure PVdF samples with different thermal histories

Sample	2Θ	Reflex intensity
PVdF, 160 ºC	17°30′	124
	18°15′	180
	19°45′	390
	26°25′	207
PVdF, 170 ºC	17°45′	116
	18°30′	156
	20°00;	320
	26 °40′	180
PVdF, 175 ºC	20°7′	275
	30°10′	48
	40°20′	40
	44°10′	28
	49°50′	64
	50°20′	78
PVdF, 200 ºC	17°35′	12
	18°30′	72
	20°5′	68
	26°45′	170

Acknowledgements

The authors would like to thank all their co-workers from the research group for help, comments and valuable discussions. The State Committee for Scientific Research is kindly acknowledged for financial support of the presented research under grant No. 134/E-365/S/2004.

References

[1] FERRY A., EDMAN L., FORSYTH M., MACFARLANE D.R., SUN J.Z., Electrochim. Acta, 45 (2000), 1237.
[2] FERRY A., EDMAN L., FORSYTH M., MACFARLANE D.R., SUN J.Z., J. Appl.Phys., 86 (1999), 2346.
[3] FAN J., MARZKE, R.F., SANCHEZ, E., ANGELL, C.A., J. Non-Cryst. Sol., 172–174 (1994), 1178.
[4] FORSYTH M., MEAKIN, P., MACFARLANE, D.R., HILL A.J., J. Phys.: Condens. Matter, 7 (1995), 7601.
[5] LIN D.J., CHANG C.L., HUANG F.M., CHENG L.P., Polymer, 44 (2003), 413.
[6] CHIANG C.Y., SHEN Y.J., REDDY M.J., CHU P.P., J. Power Sources, 123 (2003), 222.
[7] BOUKAMP B.A., Solid State Ionics, 10 (1986), 31.
[8] PENG Y., WU P., Polymer, 45 (2004), 5295.
[9] BOCCACCIO T., BOTTINO A., CAPANNELLI G., PIAGGIO P., J. Membrane Sci., 210 (2002), 315.

Received 10 December 2004
Revised 18 March 2005

Materials Science-Poland, Vol. 24, No. 1, 2006

Application of silicon and titanium alkoxylates as bifunctional additives for composite polymeric electrolytes

A. SITAREK, P. RAJEWSKI, G. ŻUKOWSKA, H. WYCIŚLIK, M. CIOSEK, M. SIEKIERSKI*

Warsaw University of Technology, Faculty of Chemistry, Polymer Ionics Research Group, ul. Noakowskiego 3, 00-664 Warsaw, Poland

Addition of ceramic grains is widely recognized as an important method for polymer matrix modification. As grain size plays an important role (smaller grains interact stronger), a serious problem appears for nano-sized grains due to their easy agglomeration and difficulties with homogenisation. On the other hand, residual water must be carefully removed from the electrolyte. In this work, we propose a method of simultaneous in-site filler generation and water trapping in the hydrolysis of silicon and titanium alkoxylates. $Ti(OEt)_4$ and $Si(OEt)_4$ used are both commercially available. Conductivity studies were correlated with FT-IR investigations to compare the effect of classical (thermo-vacuum) and chemical drying. Lithium perchlorate and lithium trifluoromethanosulfonate were used as doping salts. Low molecular weight polyglycol in the form of mono- and dimethyl ether was used as the polymer matrix. We observed the influence of drying on ion association in the electrolyte, together with respective conductivity changes. The drying process decreases the conductivity of the composite, whereas filler grain formation increases it. The sign of the final conductivity change varies with the matrix and salt type.

Key words: *composite polymeric electrolyte; ceramic filler; hydrolysis*

1. Introduction

The quest for an ideal polymer matrix for electrolytes is as old as the field itself. No existing materials can fulfil all required properties, including stability, high ionic conductivity, and commercial availability. Thus various methods of matrix modification have been introduced to influence its properties. The main disadvantage of the most popular polymeric host – poly(ethylene oxide) – is its low conductivity resulting from a high content of crystalline phase. It has been widely recognized that the addition of a non-conductive filler such as aluminium oxide or silica leads to ion transport

*Corresponding author e-mail: alex@soliton.ch.pw.edu.pl

enhancement, due to the hindrance of formation of highly ordered regions in the system [1–3]. The influence of grain size, surface area, and the surface groups of the filler were also studied. Later, the influence of the additive on fully amorphous liquid systems containing a polyether matrix was also discovered [4–7]. In this case, the observed change cannot be attributed to phase structure effects, as the pristine system is fully amorphous. Conductivity enhancement in the latter case, however, is limited to a narrow salt concentration range [7]. Changes in the ionic conductivity and microstructure of composite polymer electrolytes result from the Lewis acid-base type interactions between a variety of Lewis acids or base type species present in the system. This comprises acid Lewis centres of the filler, alkali metal cations (being hard acids according to the Pearson classification) [8], anions (being weak Lewis bases), and the base centres of polyether oxygen atoms. Preparation and properties of various types of fumed oxides were discussed in the literature [5] as the starting point for their introduction to liquid composite polymeric electrolytes. Fumed oxides comprising fumed silica, alumina, and titania were synthesized by high-temperature hydrolysis of the corresponding gaseous metal chlorides ($SiCl_4$, $AlCl_3$ and $TiCl_4$) in an O_2/H_2 flame [9, 10]. Due to the pyrogenic synthesis method, all fumed oxides possess unique properties: high-chemical purity [9, 10], nanoscale spherical primary particles (5–50 nm) [11], large specific surface area (up to 600 m^2/g) [11], and nonporous structure [9, 10]. The predominant particle structures are branch-like aggregates (100–500 nm, apparent packing density is about 30% of SiO_2, Al_2O_3, or TiO_2), which cannot be disrupted by shear force and consist of partially fused primary particles (ϕ 10 nm) [11–14].

2. Experimental

The reagents used for the preparation of the reference “dry” samples were carefully dried under vacuum (10^{-5} Torr, 60 hours) prior to use. The drying temperature was 90 ºC for the polyglycols and in the range 110–140 ºC for the salts. The “wet” samples were prepared from commercially available compounds (Aldrich) used without any further purification. The titanium and silicon tetraethoxylates were obtained from Sigma-Aldrich and used as shipped. Despite pristine “wet” sample preparation, all operations were performed in a nitrogen filled dry-box with humidity lower than 5 ppm. ac impedance was recorded with Atlas 98 HI equipment in the 1 Hz–100 kHz range for varying temperatures (20–70 ºC). The obtained data were analysed with Bernard Boukamp’s EQ program to determine the dc conductivity of the samples. FT-IR measurements of the electrolytes were performed on the samples placed between NaCl plates with a Perkin-Elmer 2000 spectrometer with a resolution 0.5 cm^{-1}.

3. Results

A set of FT-IR data is collected in Table 1. For monomethyl capped matrix and lithium triflate salt differences in ion associations can be observed between the wet

(with or without $Si(OEt)_4$) and dry samples. The peak located at 638 cm^{-1}, characteristic of the deformation of the SO_3 salt group, can be divided into parts attributed to free ions and ion pairs forming doublets. For dry samples, it is more asymmetric, showing a higher amount of paired species. Parallel to this, the C–O–C stretching vibration for the wet samples is shifted towards lower wave numbers than for the dry ones (to 1103 cm^{-1} and 1106 cm^{-1}, respectively). The 3 cm^{-1} change can be explained by a weaker coordination of the salt to the polymer chain due to a smaller dissociation rate. A similar and even stronger correlation can be observed for the dimethyl-capped matrix. In this case, for the dry samples, the 638 cm^{-1} peak is divided into a clear doublet, with the second maximum at 641 cm^{-1} confirming stronger ion pairing. A shift for the ν_{C-O-C} peak is also observed and even more pronounced (Fig. 1). The stronger effect of drying for the dimethyl-capped matrix can be explained by its lower dielectric constant and weaker coordination properties, limited by the absence of free –OH groups. Samples containing $LiClO_4$ exhibit similar changes. One can also observe a splitting of the $\delta_{sc\ CH2}$ peak for the wet samples, almost disappearing for dried samples. Such behaviour confirms a stronger polymer-cation coordination in the more dissociated wet samples.

Table 1. FT-IR data for samples with and without bifunctional additives*

Samplecode	Sample composition	*v* C-O-C [cm^{-1}]	OH peak intensity	Reference intensity	Relative OH intensity
MTJ	PEO–m–$LiCF_3SO_3$	1103	3.25	4.55	1.40
STJ	PEO–m–$LiCF_3SO_3$	1106	2.70	0.19	0.07
MTJ-S	PEO–m–$LiCF_3SO_3$ + TEOS	1103	1.89	1.29	0.68
MTJ-2T	PEO–m–$LiCF_3SO_3$ + 2% TEOT	1106	11.65	0.21	0.02
MTJ-5T	PEO–m–$LiCF_3SO_3$ + 5% TEOT	1106	1.67	0.2	0.12
STJ-S	PEO–m–$LiCF_3SO_3$ + TEOS	1106	–	–	–
MTD	PEO–dm–$LiCF_3SO_3$	1106	2.72	1.90	0.67
STD	PEO–dm–$LiCF_3SO_3$	1108	5.56	0.35	0.06
MTD-S	PEO–dm–$LiCF_3SO_3$ + TEOS	1106	0.62	0.10	0.17
MTD-2T	PEO–dm–$LiCF_3SO_3$ + 2% TEOT	1108	4.35	0.09	0.02
MTD-5T	PEO–dm–$LiCF_3SO_3$ + 5% TEOT	1108	2.61	0.43	0.16
STD-S	PEO–dm–$LiCF_3SO_3$ + TEOS	1108	–	–	–
MNJ	PEO–m–$LiClO_4$	1090	1.14	5.47	4.80
SNJ	PEO–m–$LiClO_4$	1093	4.41	0.58	0.13
MNJ-S	PEO–m–$LiClO_4$ + TEOS	1093	8.95	1.16	0.13
MNJ-2T	PEO–m–$LiClO_4$ + 2%TEOT	1098	9.92	1.56	0.02
MNJ-5T	PEO–m–$LiClO_4$ + 5%TEOT	1095	3.24	0.464	0.14
SNJ-S	PEO–m–$LiClO_4$ + TEOS	1095	–	–	–
MND	PEO–dm–$LiClO_4$	1088	2.57	4.47	1.74
SND	PEO–dm–$LiClO_4$	1090	6.72	0.45	0.07
MND-S	PEO–dm–$LiClO_4$ + TEOS	1090	12.8	0.79	0.06
MND-2T	PEO–dm–$LiClO_4$ + 2% TEOT	1096	10.13	0.41	0.04
MND-5T	PEO–dm–$LiClO_4$ + 5% TEOT	1094	2.11	0.35	0.17
SND-S	PEO–dm–$LiClO_4$ + TEOS	1092	–	–	–

*S – dry reagents, M – wet reagents, TEOS – $Si(OEt)_4$, TEOT – $Ti(OEt)_4$.

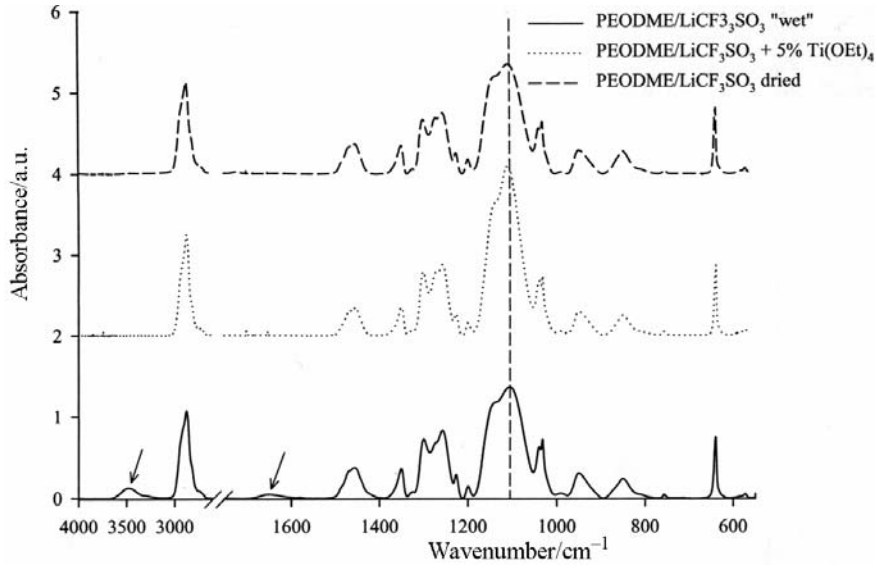

Fig. 1. A comparison of FT-IR spectra for a family of samples with the same polymer matrix and doping salt

In the case of dimethyl-capped polyether, wet samples with the addition of $Si(OEt)_4$ behave identically with the dry ones, thus confirming the efficiency of chemical water removal. The $Ti(OEt)_4$ additive seems to be more effective in water removal when taking into consideration the shift of the peak position. It should be noticed that the position of the ν_{C-O-C} peak is located at lower wave numbers for perchlorate-doped samples than for those containing triflate (respectively 1090–1096 cm^{-1} and 1103–1106 cm^{-1}).

To compare the efficiency of the two drying methods (thermo-vacuum and chemical), a quantitative analysis of the 1650 cm^{-1} peak characteristic of water was performed. The recorded spectra were first baseline corrected. Later, the intensities of the analysed peak were normalized for sample thickness by using a reference peak. For samples containing $LiClO_4$, the band at 1450 cm^{-1} was used as a reference, while the 1350 cm^{-1} peak was used for the ones with $LiCF_3SO_3$. For the $Si(OEt)_4$ additive, the results show that for lithium perchlorate both drying methods are identical in efficiency, leading to about a 30-fold decrease of water content. For lithium triflate, the thermo-vacuum drying leads to water content in the range 5–10% of the start level, while the chemical water removal utilizing $Si(OEt)_4$ is significantly less effective. For a titanium-containing additive, the experiments were performed for samples with two different concentrations of the active compound. Surprisingly, the lower concentration tested is significantly more efficient in the water trapping process. A higher amount of the additive (5 wt./wt. % of the electrolyte) gives worse or comparable results to the thermo-vacuum process, while the lower one produces water contents about five times lower.

Conductivity studies should allow one to easily judge which of the two contrary effects of the process studied is predominant. Introduction of the active compound should decrease conductivity due to water removal. Water traces enhance ionic transport by both decreasing matrix viscosity and by increasing salt dissociation. However, formation of nanosized oxide filler (SiO_2 or TiO_2) grains in the chemical reaction of water with $Si(OEt)_4$ or $Ti(OEt)_4$ is observed, leading to the formation of high conductivity regions. Finally, the overall conductivity of the composite can be either higher, lower, or remain unchanged. In the case of $Si(OEt)_4$ as an additive (see Table 2), the final effect is dependent on the matrix type. For both tested salts and the mono methyl capped matrix, the final conductivity of the composite system is higher than the conductivity of the pristine wet sample. On the contrary, for the dimethyl capped matrix, a decrease of conductivity is observed after adding filler promoter. In any case, the obtained conductivity values were higher in comparison with those of samples obtained by thermo-vacuum drying and not containing any filler. For Ti $(OEt)_4$, a significant increase of conductivity is observed for all studied systems.

Table 2. Conductivity data for samples with and without a bifunctional additives

Sample code	σ [S/cm] at 293 K	E_a [kJ/mol]
MTJ	1.09×10^{-4}	33.5
MTJ –S	1.24×10^{-4}	33.7
MTJ-2T	5.89×10^{-4}	25.6
MTJ-5T	2.64×10^{-4}	25.0
STJ	9.00×10^{-5}	34.0
MTD	1.26×10^{-4}	23.5
MTD-S	9.40×10^{-5}	22.5
MTD-2T	1.76×10^{-4}	22.8
MTD-5T	1.08×10^{-4}	26.0
STD	8.70×10^{-5}	24.0
MNJ	1.11×10^{-4}	39.2
MNJ-S	1.41×10^{-4}	39.4
MNJ-2T	2.73×10^{-4}	30.8
MNJ-5T	2.50×10^{-4}	30.8
SNJ	1.00×10^{-4}	41.0
MND	2.78×10^{-4}	38.1
MND-S	7.65×10^{-5}	40.9
MND-2T	1.55×10^{-4}	25.6
MND-5T	3.35×10^{-4}	26.0
SND	5.32×10^{-5}	44.6

*S – dry reagents, M – wet reagents, TEOS – $Si(OEt)_4$, TEOT – $Ti(OEt)_4$.

The thermal dependence of conductivity exhibits a Vogel-Taman-Fulcher (VTF) shape (see Figure 2). Pseudo activation energies calculated by NLLS fitting to the VTF equation are also collected in Table 2. The values obtained vary in the range

20–40 kJ/mol. The observed differences are significant only for a series of samples with lithium triflate and a dimethyl capped matrix, where the values are around 23 kJ/mol.

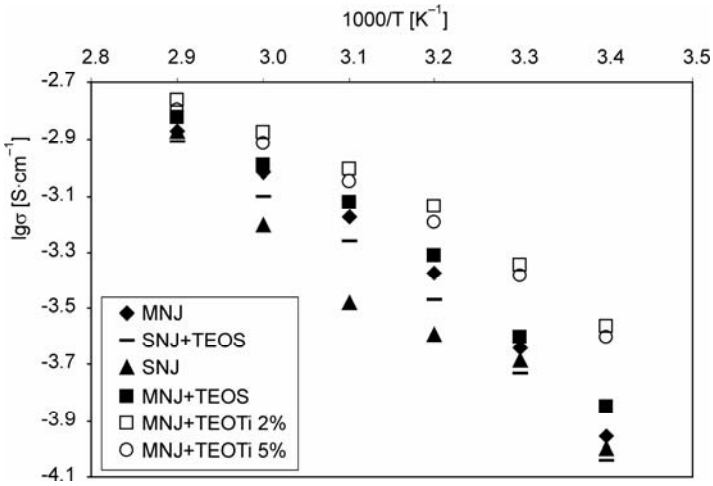

Fig. 2. An exemplary set of thermal dependences of conductivity for a family of samples with the same polymer matrix and doping salt

Within a particular series of samples, neither thermo-vacuum drying nor the addition of $Si(OEt)_4$ cause noticeable changes. The addition of $Ti(OEt)_4$ leads to an observable decrease of activation energy. Only for lithium triflate dissolved in an dimethyl ether matrix do all samples reveal almost identical E_a values.

Acknowledgements

The authors would like to thank all their co-workers from the research group for help, comments, and valuable discussions. The State Committee for Scientific Research is kindly acknowledged for the financial support of the presented research under grant 134/E-365/S/2004.

References

[1] WESTON J., STEELE B.C.H., Solid State Ionics, 7 (1982), 75.
[2] WIECZOREK W., SUCH K., WYCIŚLIK H., PŁOCHARSKI J., Solid State Ionics, 36 (1989), 255.
[3] SKAARUP S., WEST K., ZACHAU-CHRISTIANSEN B., Solid State Ionics, 28–30 (1988), 979.
[4] MARCINEK M., ZALEWSKA A., ŻUKOWSKA G., WIECZOREK W., Solid State Ionics, 136–137 (2000), 1175.
[5] ZHOU J., FEDKIW P.S., Solid State Ionics, 3–4 (2004), 275.
[6] WIECZOREK W., SUCH K., FLORJAŃCZYK Z., STEVENS J.R., J. Phys. Chem., 1994, 98, 6840.
[7] WIECZOREK W., LIPKA P., ŻUKOWSKA G., WYCIŚLIK H., J. Phys. Chem. B 1998, 102, 6968.
[8] FAN J., FEDKIW P.S., J. Electrochem. Soc., 1997, 144, 399.
[9] ETTLINGER M., *Highly Dispersed Metallic Oxides Produced by the AEROSILR Process*, Degussa Technical Bulletin Pigments, No. 56, Akron, OH, 2002.
[10] MICHAEL G., FERCH H., Basic Characteristics of AEROSlLR, Degussa Technical Bulletin Pigment, No. 11, Akron, OH, 1998.

[11] GUN'KO V.M., ZARKO V.I., TUROV V.V., LEBODA R., CHIBOWSKI E., PAKHLOV E.M., GONCHARUK E.V., MARCINIAK M., VORONIN E.F., CHUIKO A.A., J. Colloid Interface Sci., 220 (1999), 302.
[12] KHAVRYUTCHENKO V., KHAVRYUTCHENKO A., BARTHEL H., Macromol. Symp. 169 (2001) 1.
[13] KHAVRYUTCHENKO V., BARTHEL H., NIKITINA E., Macromol. Symp., 169 (2001), 7.
[14] BARTHEL H., ROSCH L., WEIS J., [in:] N. Auner, J. Weis (Eds.), *Organosilicon Chemistry II. From Molecules to Materials*, VCH, Weinheim, 1996, p. 761.

Received 10 December 2004
Revised 18 March 2005

Materials Science-Poland, Vol. 24, No. 1, 2006

Mixed electronic-ionic conductivity in vanadate oxide glasses containing alkaline ions

R.J. BARCZYŃSKI*, L. MURAWSKI

Faculty of Applied Physics and Mathematics, Technical University of Gdańsk,
ul. Narutowicza 11/12, 80-952 Gdańsk, Poland

The conductivity of glasses in $50V_2O_5$–$(50–x)P_2O_5$–xA_2O (A = Li, Na, K, Rb) systems was investigated as a function of composition. In vanadate-phosphate glasses containing various alkali ions, the conductivity decreases with increasing alkali ion content. The decrease in conductivity is larger for heavier alkali ions and reaches more than seven orders of magnitude in the case of glass containing 40 mol % of Rb_2O. Only glasses containing lithium exhibit relatively small conductivity changes – less than one order of magnitude – and an increase for high lithium contents.

Key words: *glass; electronic-ionic conductivity*

1. Introduction

Electrical properties of oxide glasses containing large amounts of transition-metal ions are determined by their presence in two different valence states. The conductivity is described by small polaron hopping between such ions [1, 2]. When an alkali oxide is added during glass preparation, one may also expect mobile alkali ions to contribute to the charge transport and mixed conductivity to be observed. Generally, ionic conductivity depends on alkali concentration and ion mobility. Assuming that the motion of alkali ions and polarons are independent, one may expect electrical conductivity to increase with increasing alkali content. Real transition metal oxide glasses containing alkali, however, exhibit various behaviours – from strong conductivity anomalies to conductivity only slightly dependent on alkali content in the glass [3, 4].

The behaviour of polarons and mobile ions depends on the role of the transition metal ions in the glass structure. One possibility is for them to be a structure modifier, the most popular examples being iron and copper ions. Studies on ac and dc conductivities in oxide glasses containing iron show that their conductivities depend only slightly on alkali contents. It is shown that replacing CaO by Na_2O in modified iron

*Corresponding author, e-mail: jasiu@mif.pg.gda.pl

phosphate glasses causes only a small change in dc and ac conductivities. It seems to be characteristic of glasses containing iron oxides that the alkali ions have a small mobility being bonded to the glass network. ac conductivity studies in copper-containing glass show that a mixed polaron-ionic conductivity mechanism exists even in the absence of alkali ions. Cu(I) ions can play a double role – serve as hopping centres and also contribute to the ionic conductivity [5].

The other family of TMO glasses is based on oxides, which themselves may be glass formers: MoO_3, WO_3, V_2O_5, typical examples being: P_2O_5–V_2O_5–A_2O, P_2O_5–WO_3–A_2O or TeO_2 –V_2O_5–A_2O glasses (where A is an alkali ion). Although their onductivities change significantly with the alkali content, the changes are usually non-monotonic and have anomalies and minima somewhat resembling the mixed alkali effect. Such behaviour has been observed by Bazan et al. [7] in P_2O_5–WO_3–Li_2O glass (minima of four orders of magnitude in conductivity at 10% Li_2O) and by Jayasinghe et al. [8] in TeO_2–$x$$Li_2O$–(1–$x$)$V_2O_5$.

The aim of the present study was to investigate mixed electronic-ionic conductivity in vanadium-phosphate glasses containing various alkali ions. In order to keep transition metal oxide contents at the same level, we prepared glasses containing the same amount of V_2O_5 and changed the ratio of P_2O_5 to Li_2O, Na_2O, K_2O or Rb_2O.

2. Experimental

Glasses of composition $50P_2O_5$–(5O–x)V_2O_5–$x$$A_2O$, where A = Li, Na, K, or Rb, were prepared by the conventional melt quenching technique in air with an alumina crucible. The contents of V^{4+} and V^{5+} ions were determined by chemical analysis.

Great attention has been paid to the electrode preparation process. Golden electrodes with guard rings were evaporated on polished surfaces of the samples, which had been preheated to about 150 °C in high vacuum.

Impedance measurements were carried out with a frequency response analyser Solartron 1250 and a custom trans-impedance amplifier in the frequency range from 10^{-4} to 6.5×10^{4} Hz. The intrinisic Gnuplot program (www.gnuplot.org) and a Marquardt –Levenberg minimisation procedure were used for complex non-linear fitting of the impedance model parameters.

3. Results

Figure 1 shows the dependence of the amount of V^{4+} ions on the total amount of vanadium in all the studied glasses; V^{4+} content decreases on increasing the alkali content. This decrease is more pronounced when more massive alkali ions are added to the mixture, and leads to V^{4+} content being only about 11% in the case of 40% Rb. It has been reported that in binary vanadium-phosphate glass the ratio V^{4+}/ V_{tot} is in the range 0.35–0.5.

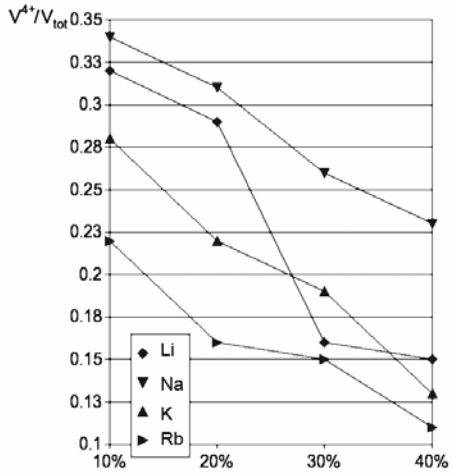

Fig. 1. The ratio of the amount of V^{4+} ions to the total amount of vanadium for various alkali contents

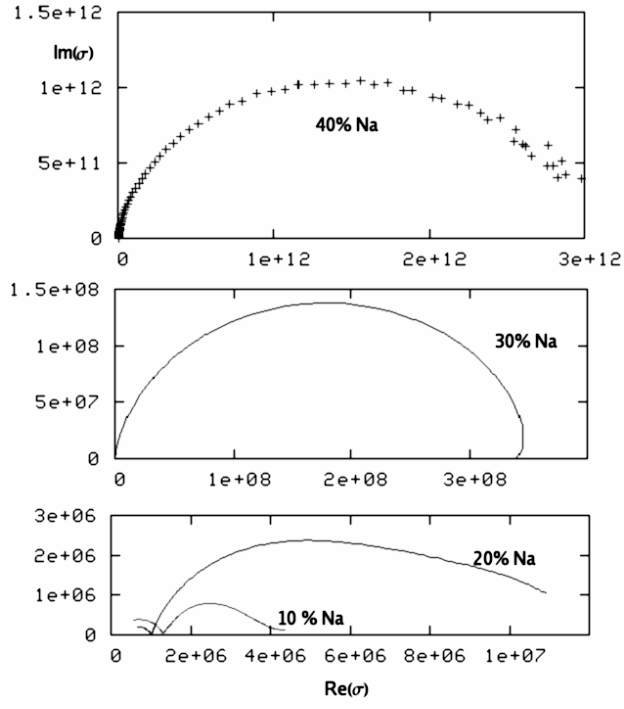

Fig. 2. The resistivity Cole–Cole plots for samples containing from 10 to 40 mol % of Na_2O in the frequency range 10^{-3}–6.5×10^4 Hz

Figure 2 shows complex plots of impedance (Cole–Cole plots) for samples containing from 10 to 40 mol % of Na_2O in the frequency range from 10^{-3} to 6.5×10^4 Hz.

A significant drop in conductivity is visible on increasing alkali content. This trend is characteristic of all families of glasses except those containing lithium, where changes in conductivity are far less pronounced. In order to obtain bulk dc conductivity, the impedance spectra were modelled by two section R-CPE (constant phase element) Maxwell [8] equivalent electrical circuits, and by single R-CPE circuits in the cases of only one semicircle plot. Parameters of the equivalent circuits were obtained directly from the measured impedance data by complex non-linear least squares fitting.

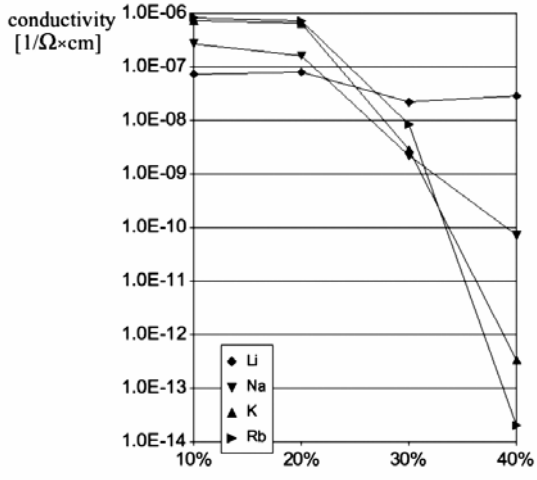

Fig. 3. Bulk dc conductivity of the glasses versus alkali content

Figure 3 presents the bulk dc conductivity versus alkali percentage for all glasses. The decrease in conductivity with increasing alkali content is larger for heavier alkali ions and reaches more than seven orders of magnitude in the case of rubidium. Only glasses containing lithium exhibit relatively small conductivity changes, of less than one order of magnitude, and an increase for large lithium contents.

4. Discussion

Several authors have observed pronounced conductivity minima in TMO glasses in certain alkali admixtures, resembling somewhat the mixed alkali effect. Such behaviour has been observed by Bazan et al. [6] who explained it by ion-polaron interaction. Jayasinghe et al. [7] have also observed this phenomenon and postulated the breaking of percolation paths. Another possibility is a significant change in the concentration ratios of transition metal ions in different valence states, since polaronic conductivity is proportional to the product of the number of ions in both valence states.

Most observations have been based on glasses in which alkali ions were substituted for transition metal ions [7, 9]. Our glasses contain large constant amounts of TMO. V_2O_5 itself is a glass former and we can substitute P_2O_5 with alkali without destroying the glass structure. This changed the variation of conductivity with increas-

ing alkali content, especially in the case of heavy alkali ions. With increasing alkali ion content, polaronic transport is blocked at least in the case of ions heavier than lithium. This cannot be a simple dilution effect, because the concentrations of transition metal atoms remain constant. Such a large drop in conductivity also cannot originate from a change in vanadium valence.

It seems that heavy alkali ions are not mobile in vanadate glass networks and that ionic conductivity cannot develop in the high-alkali region, in contrast to glasses in which the main glass forming component is P_2O_5 and significant ionic conductivity is observed at high alkali concentrations. Recently, Ungureanu et al. [9] have found that $50P_2O_5$–$50[(1–x)V_2O_5$–$xNa_2O]$ glass exhibits a deep minimum for x = 32.5 mol % of V_2O_5. It is interesting that for similar glass compositions, the internal friction reveals a large peak, similar to the "mixed alkali peak" in mixed-alkali glasses [10]. Two relaxation peaks connected with electronic and ionic transport were observed in P_2O_5 –V_2O_5–Na_2O glasses [11].

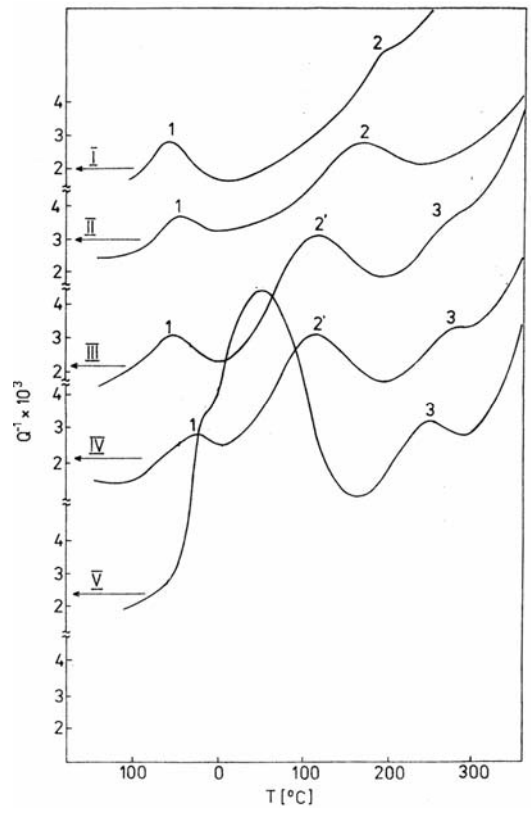

Fig. 4. Internal friction spectra for $50P_2O_5$–$(50–x)V_2O_5$–xNa_2O glasses; x = 0 (I), 7.5 (II), 12.5 (III), 17.5 (IV), 30 mol % (V) [11]

Figure 4 shows the internal friction spectra for several vanadium-phosphate glasses doped by Na_2O. For glasses containing less than 10 mol % of Na_2O (curve I and II), the internal friction spectrum consists of two peaks: a low-temperature peak

(1) and a high-temperature peak (2). Peak 1 is related to the hopping of polarons between V^{4+} and V^{5+} ions, and its activation energy is similar to that of dc conductivity in vanadate-phosphate glasses. The high-temperature peaks 2 and 3 depend on the water content and are caused by the interaction between protons and non-bridging oxygen atoms [12]. For glasses containing more than 10 mol % of Na_2O, another peak (2′) appears above peak 1. This peak can be attributed to the migration of sodium ions. Peaks (1) and (2′) are best separated for glasses containing 12.5 and 17.5 mol % of Na_2O. It is found that the activation energy of peak 2′ is comparable with that of dc conductivity observed in sodium phosphate glasses. For 30 mol % of Na_2O these two peaks overlap and a large mixed electronic-ionic peak appears in the internal friction spectrum. Its high intensity indicates that we still have a high number of mobile ions and polarons in the glass and a deep minimum in conductivity is observed. This effect can be explained based on ion-polaron interaction. By the internal friction method it is possible to observe the relaxation of neutral ion-polaron pairs which can contribute to the broad mechanical loss peak. In the light of the experiments described above, one can suppose that in our glasses polaron-ion interaction is responsible for the strong conductivity decrease with increasing alkali ion content. As shown in Figure 2, however, this effect depends on the size of the alkali ions. We believe that the ion-polaron interaction alone cannot describe the drop in conductivity by seven orders of magnitude in Rb_2O-containing glasses. Breaking of polaron percolation paths and a very low mobility of heavy alkali ions seem to be relevant in such a dramatic change in conductivity.

5. Conclusions

The electrical properties of $50V_2O_5$–$(50–x)P_2O_5$–xA_2O glasses were investigated using impedance spectroscopy. In vanadium-phosphate glasses containing various alkali ions, the conductivity decreases with increasing alkali ion content. The decrease in conductivity is larger for heavier alkali ions and reaches more than seven orders of magnitude in the case of glasses containing 40 mol % of Rb_2O. The alkali ions used are not mobile in the vanadate glass network. Only glasses containing lithium show relatively small conductivity changes – of less than one order of magnitude – and an increase for large lithium contents; these glasses also exhibit the largest mixed electronic-ionic conductivity. Admixtures of alkali ions heavier than Li block polaronic transport in vanadate-phosphate glasses.

References

[1] MURAWSKI L., CHUNG C.H., MACKENZIE J.D., J. Non-Cryst. Solids, 32 (1979), 91.
[2] SAYER M., MANSINGH A., *Non-Crystalline Semiconductors*, Vol. III, M. Pollak (Ed.), CRC Press, Boca Raton, FL, USA, 1987.
[3] BARCZYNSKI R.J., MURAWSKI L., J. Non-Cryst. Solids, 307–310 (2002), 1055.

[4] MURAWSKI L., BARCZYNSKI R.J., SAMATOWICZ D., Solid State Ionics, 157 (2003), 157.
[5] BARCZYNSKI R.J., GAZDA M., MURAWSKI L., Solid State Ionics, 157 (2003), 299.
[6] BAZAN J.C., DUFFY J.A., INGRAM M.D., MALLACE M.R., Solid State Ionics, 86–88 (1996), 497.
[7] JAYASINGHE G.D.L.K., DISSANAYAKE M.A.K.L., BANDARANAYAKE P.W.S.K., SOUQUET J.L., FOSCALLO D., Solid State Ionics, 93 (1997), 291.
[8] MACDONALD J.R., FRANCESCHETTI D.R., *Impedance Spectroscopy Emphasising Solid Materials and Systems*, J.R. Macdonald (Ed.), Wiley, New York, 1987. 98.
[9] UNGUREANU M.C., LEVY M., SOUQUET J.L., Ceramics Silikaty, 44 (2000), 81.
[10] ROLING B., Curr. Opinion Solid State Sci., 5 (2001), 203.
[11] BEDNARCZYK D., Thesis, Technical University of Gdańsk, 1988.
[12] ASS H.M.J.M., STEVELS J., J. Non-Cryst. Solids, 16 (1974), 46.

Received 23 December 2004
Revised 15 July 2005

Materials Science-Poland, Vol. 24, No. 1, 2006

High-temperature phenomena in RbD_2PO_4 and CsH_2PO_4 Polymeric transformations or polymorphic phase transitions?

W. BRONOWSKA*

Institute of Physics, Wroclaw University of Technology, Wybrzeże Wyspiańskiego 27, Wrocław, Poland

X-ray analysis has been performed for RbD_2PO_4 and CsH_2PO_4 over the temperature range from 288 K to 537 K and 507 K, respectively. The refinement of the crystal structure of RbD_2PO_4 at 430 K has revealed that the high-temperature paraelectric phase of this crystal is isomorphic with the monoclinic $P2_1/m$ paraelectric phase of CsH_2PO_4. The X-ray diffraction CCD images obtained for RbD_2PO_4 have proved that the high-temperature paraelectric phase is stable up to approximately 525 K. At this temperature, polycrystallisation of the single-crystal samples and their subsequent decomposition has been observed. CsH_2PO_4 undergoes a structural phase transition at 504 K, from the monoclinic paraelectric phase to a cubic superionic phase ($P2_1/m$ transforms to $Pm\text{-}3m$ symmetry). The reversibility of the superionic phase transition in the crystals is a strong evidence for a polymorphic character of this solid–solid transition.

Key words: *X-ray analysis*; *crystal structure*; *phase transition*; *polymorphic transformation*

1. Introduction

In AH_2PO_4-type crystals (where a = K, Rb, Tl, NH_4 or Cs), two kinds of crystal systems can be stably crystallized at room temperature. The crystals of KH_2PO_4, RbH_2PO_4, and $NH_4H_2PO_4$ belong to the tetragonal system [1–3], whereas the crystals of CsH_2PO_4, TlH_2PO_4, and RbD_2PO_4 belong to the monoclinic system [1, 2, 4–8].

The RbD_2PO_4 crystal exhibits a superlattice structure with the lattice parameters a = 15.352(2) Å, b = 6,184(1) Å, c = 9.566(2) Å, β = 108,8(1)° [9], which are doubled along both the a and c axes compared to the dimensions of the unit cell of ferroelectric CsH_2PO_4 [5]. RbD_2PO_4 undergoes phase transitions at 317 K and 377 K [4]. The low-temperature phase is antiferroelectric or approximately antiferroelectric (fer-

*E-mail: wieslawa.bronowska@pwr.wroc.pl

rielectric with 2*a*, *b*, 2*c*, *Z* = 8, $P2_1$) [4]; the intermediate (non-polar, with *a*, *b*, 2*c*, *Z* = 4, $P2_1/c$, [10]) and high-temperature (*a*, *b*, *c*, *Z* = 2, $P2_1/m$ [9]) phases are paraelectric [11]. The crystal structure of the ferrielectric phase was determined at room temperature [9, 12], the structure of the intermediate phase was determined at 332 K [10]. Suzuki et al. [10] reported that the high-temperature paraelectric phase has the space group $P2_1/m$ with the basic lattice parameters, but the structure of that phase has not yet been determined.

The CsH_2PO_4 crystal exhibits ferroelectric properties below 154 K and has $P2_1$ symmetry [13, 14]. In the paraelectric phase, the crystal has $P2_1/m$ symmetry [5–8, 13, 14]. The ionic conductivity of CsH_2PO_4 undergoes a sharp increase at 504 K [15–17], from 1.2×10^{-5} to 9.0×10^{-3} $ohm^{-1}cm^{-1}$ [18].

Despite extensive studies of high-temperature transitions in MX_2PO_4 (where M = K, Rb, Cs; X = H, D) during the past few years, the microscopic nature of the high-temperature phenomena in these crystals is still not completely understood. Under normal air conditions, their ionic conductivity is related to two competing processes: a polymorphic transition and chemical decomposition with partial polymerisation. Lee [19], Ortiz et al. [16] and recently Park [20], attribute the increase of conductivity of the KDP compounds at high temperatures to the dehydration process starting on the sample surface and partial polymerisation. On the other hand, our previous powder X-ray investigations of CDP under humidified conditions [6, 7] support Baranov's et al. [15] suggestion that the superprotonic phase of CDP is cubic and reversible with hysteresis on cooling. Recently, Boysen et al. [18] and Otomo et al. [21] reconfirmed the reversibility of the superionic phase transition in these crystals.

This paper presents the results of X-ray investigations of RbD_2PO_4 and CsH_2PO_4 over the temperature range from 288 K to 537 K and 507 K, respectively. In order to explain the nature of high-temperature phenomena in these crystals, detailed structure analyses were performed using a KM4-CCD diffractometer.

2. Experimental

Single-crystal measurements of RbD_2PO_4 and CsH_2PO_4 were carried out on a four circle X-ray KM4 diffractometer (Kuma Diffraction Company) equipped with a two -dimensional area CCD detector and a high-temperature attachment. MoKα graphite -monochromated radiation (λ = 0.71073 Å) was used for data collection. The investigated samples were heated in a sealed tube as well as under normal air conditions. Data used for the determination of the crystal structure of the RbD_2PO_4 high -temperature paraelectric phase were collected at *T* = 430 K. An omega scan with $\Delta\Omega$ = 1° for each image was used for data collection. A series of 960 images in six different runs covered 89.5% of the Ewald sphere; 1764 reflections were recorded for RbD_2PO_4, which merged to give a total of 539 unique reflections. The lattice parameters were calculated from all the reflections measured. The structure of RbD_2PO_4 at 430 K was solved by the Patterson method using the SHELXS-97 program. Refine-

ment was carried out using SHELXL-97 [22]. Anisotropic thermal displacement parameters were used for all non-hydrogen atoms. The positions of hydrogen atoms were determined from difference Fourier maps and well refined. A correction for empirical absorption was applied for the observed reflections, and an extinction correction was introduced into the refinement.

3. Results and discussion

The temperature dependences of the lattice parameters for RbD_2PO_4 in the temperature range 288–537 K exhibit anomalies at 317 K and 377 K as well as structural changes at approximately 525 K (Fig. 1).

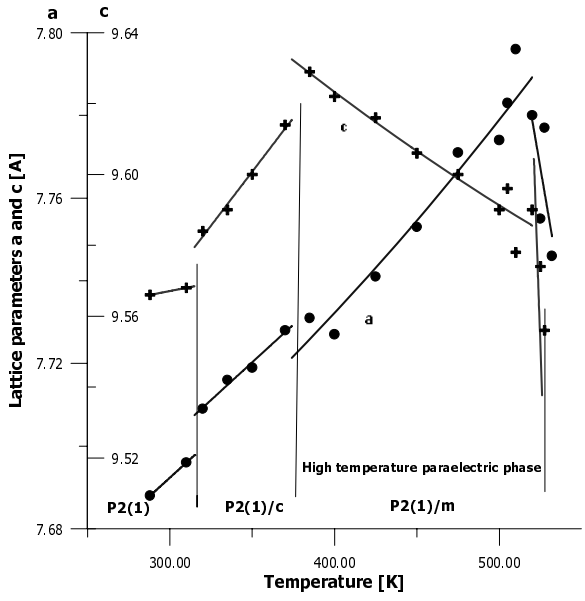

Fig. 1. The temeratpure dependences of the lattice parameters in RbD_2PO_4

The structure analyses of these crystals confirmed that the ferrielectric phase has $P2_1$ symmetry, and that the paraelectric intermediate and high-temperature phases have $P2_1/c$ and $P2_1/m$ symmetry, respectively. X-ray diffraction CCD images obtained for RbD_2PO_4 in a sealed tube above 380 K prove that the high-temperature paraelectric phase of these crystals is stable up to approximately 525 K. Figure 2a presents the X-ray CCD image of a single-crystal sample of RbD_2PO_4 heated in a sealed tube from 380 K to 525 K. The CCD image of this sample taken at 527 K (Fig. 2b) demonstrates the disappearance of the single-crystal paraelectric phase of RbD_2PO_4 and the simultaneous polycrystallisation of the sample. Additionally, X-ray powder high-temperature measurements of RbD_2PO_4, performed in a sealed tube, confirmed that the monoclinic high-temperature paraelectric

phase of the crystals is stable up to approximately 525 K. Investigations under normal air conditions have shown that the paraelectric phase of RbD_2PO_4 is stable only up to about 510 K. Above this temperature, the crystal decomposes by dehydration. The CCD image obtained for RbD_2PO_4 at 515 K has revealed that in normal air the polycrystallisation process is complete at this temperature.

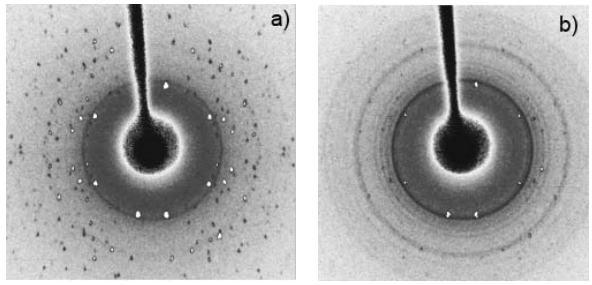

Fig. 2. X-ray diffraction CCD image of RbD_2PO_4 heated in a sealed tube at: a) 515 K, b) 527 K

Table 1. Crystal data and structure refinement for RbD_2PO_4 at 430 K

Identification code	rbd430
Empirical formula	$RbD_2\ PO_4$
Formula weight	184.47
Temperature	430(2) K
Wavelength	0.71073 Å
Crystal system space group	monoclinic $P2(1)/M$
Unit cell dimensions	a = 4.8040(10) Å b = 6.2020(12) Å c = 7.7366(15) Å β = 109.08(3) deg
Volume	217.84(7) Å^3
Z/Calculated density	2/2.812 Mg/m^3
Absorption coefficient	11.606 mm^{-1}
F(000)	172
Crystal size	0.21×0.25×0.29 mm^3
Theta range for data collection	4.31 to 28.41 deg
Index ranges	$-6 \leqslant h \leqslant 6$ $-8 \leqslant k \leqslant 4$ $-9 \leqslant l \leqslant 10$
Reflections collected/unique	1764/539 (R(int) = 0.0669)
Completeness to 2theta	28.41 89.5%
Refinement method	Full-matrix least-squares on F^2
Data/restraints/parameters	539/0/42
Goodness-of-fit on F^2	1.295
Final R indices ($I>\sigma(I)$)	R1 = 0.0334, wR2 = 0.0683
R indices (all data)	R1 = 0.0372, wR2 = 0.0694
Extinction coefficient	0.078(2)
Largest diff. peak and hole	0.519 and –0.566×10^{-3}

The crystal structure of the high-temperature paraelectric phase of RbD_2PO_4 is similar to that of CsH_2PO_4 at room temperature [14] having a monoclinic symmetry with the space group $P2_1/m$ and two chemical units in the unit cell. Nevertheless, the atomic coordinates of RbD_2PO_4 were determined independently. Crystal data and details of data collection and refinement for RbD_2PO_4 at 430 K are shown in Table 1. The final atomic coordinates and equivalent isotropic displacement parameters, with ESDs in parentheses, calculated for this crystal are presented in Table 2 (U(eq) is defined as one third of the trace of the orthogonalised U_{ij} tensor).

Table 2. Atomic coordinates ($\times 10^4$) and equivalent isotropic displacement parameters for RbD_2PO_4 at 430 K

Atom	*x*	*y*	*z*	*U*(eq)
Rb(1)	7081(1)	7500	7622(1)	48(1)
P(1)	2102(1)	2500	7452(1)	32(1)
O(1)	5054(2)	2500	9007(2)	44(1)
O(2)	2102(2)	517(2)	6307(2)	84(1)
O(3)	–197(2)	2500	8341(2)	99(1)
D(1)	6620(4)	2500	8820(3)	70(6)
D(2)	1160(6)	70(6)	5510(5)	98(12)

Figure 3 presents the projection of the atom arrangement in the unit cell of the RbD_2PO_4 crystal along the *b* axis. Some interatomic distances and angles in RbD_2PO_4 are shown in Table 3. Large values of the anisotropic displacement parameters of all oxygen atoms indicate that the structure of RbD_2PO_4 crystals is dynamically disordered. The refinement of the crystal structure revealed the isomorphism of the crystals RbD_2PO_4 at 430 K and CsH_2PO_4 at room temperature.

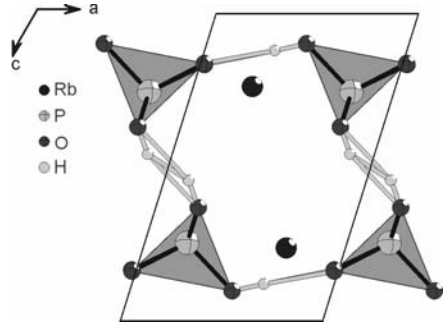

Fig. 3. The projection of the atoms arrangement in RbD_2PO_4 along the *b* axis at 430 K

Our previous powder and single-crystal diffraction investigations of CsH_2PO_4 revealed that the paraelectric phase of these crystals is stable up to approximately 504 K and that at this temperature a structural phase transition from the paraelectric phase to

the superionic phase occurs [5–8]. The superionic phases of these crystals are unstable under normal air due to dehydration.

Table 3. Selected bond lengths [Å]
and angles [deg] for RbD_2PO_4 at 430K

Rb(1)–O(2)#1	2.9437(11)	P(1)–O(3)	1.4798(16)
Rb(1)–O(3)#3	2.9898(17)	P(1)–O(2)	1.5158(11)
Rb(1)–O(1)#3	3.0988(14)	P(1)–O(2)#1	1.5158(11)
Rb(1)–O(3)#5	3.3407(7)	P(1)–O(1)	1.5304(11)
Rb(1)–O(2)#7	3.4188(14)	O(1)–D(1)	0.81(2)
Rb(1)–O(2)#4	3.4582(13)	O(2)–D(2)	0.69(3)
Rb(1)–O(1)	3.5205(8)		

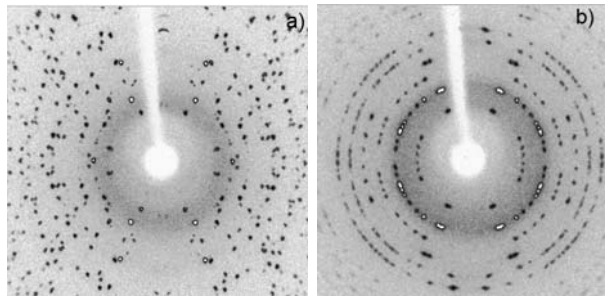

Fig. 4. Rotation CCD image of CsH_2PO_4
heated in a sealed tube at: a) 410 K, b) 509 K

X-ray rotation and oscillation CCD pictures (Fig. 4) of CsH_2PO_4 have reconfirmed that the paraelectric phase of these crystals is stable up to 504 K. At this temperature, a clear structural phase transition from the monoclinic $P2_1/m$ paraelectric phase to the

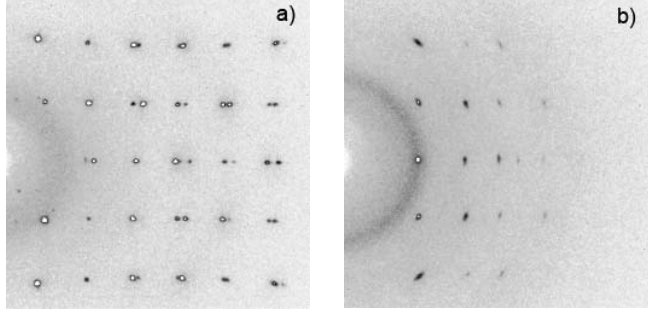

Fig. 5. Oscillation CCD picture of CsH_2PO_4 around *a*-axis
heated in a sealed tube at: a) room temperature, b) 510 K

cubic superionic phase has been observed. Figure 4a shows an X-ray rotation CCD image of a single-crystal sample of CsH_2PO_4 heated in a sealed tube from 288 K to

410 K. The rotation CCD image of this sample taken at 509 K (Fig. 4b) demonstrates an essential structural change accompanied by the superionic phase transition in the crystal.

The oscillation CCD pictures for CsH_2PO_4 around the *a*-axis taken at room temperature and 510 K are shown in Figure 4. These results unequivocally establish a cubic *Pm*-3*m* symmetry (a = 4.952(1) Å) for the superionic phase of CsH_2PO_4. Upon cooling, CsH_2PO_4 remains in the cubic phase down to a temperature of approximately 464 K. The reversible nature of the superionic transformation (with a 40° hysteresis) in CsH_2PO_4 is a strong evidence for the polymorphic character of this solid–solid transition. Detailed data of the crystal structure of the cubic superionic phases of CsH_2PO_4 and CsD_2PO_4 will be published in a following paper.

4. Conclusions

The temperature dependences of the lattice parameters of RbD_2PO_4 have revealed anomalies, which correspond to successive phase transitions at 317 K and 377 K, as well as an anomaly at approximately 525 K. The ferrielectric phase has the $P2_1$ symmetry (with 2a, b, 2c, Z = 8) and the paraelectric intermediate phase has $P2_1$/c symmetry (with a, b, 2c, Z = 4). The high-temperature paraelectric phase of RbD_2PO_4 has the $P2_1/m$ symmetry with the basis lattice parameters and Z = 2. The refinement of the crystal structure of RbD_2PO_4 at 430 K proves that the high-temperature paraelectric phase of the crystal is isomorphous with the paraelectric phase of CsH_2PO_4 at room temperature. The high-temperature paraelectric phase is stable up to approximately 525 K. At this temperature, the polycrystallisation of the single-crystal line samples and polymerisation due to their decomposition was observed.

The paraelectric phase of CsH_2PO_4 is stable up to 504 K. At this temperature, a structural phase transition from the monoclinic $P2_1/m$ paraelectric phase to the superionic phase was observed. These results undoubtedly prove the *Pm*-3*m* cubic symmetry of the superionic phase of the crystals studied. The cubic phase is stable upon cooling over the 40-degree temperature regime. The reversible nature of the superionic transformation (with a 40-degree hysteresis) in CsH_2PO_4 is a strong evidence for a polymorphic character of this solid–solid transition.

References

[1] BLINC R., O'REILLY D.E., PETERSON E.M., WILLIAMS M., J. Chem. Phys., 50 (1969), 5408.
[2] KOMUKAE M., KAWASHIMA K. OSAKA T., J. Phys. Soc. Jpn., 69 (2000), 2076.
[3] MATTAUCH S., PAULUS W., GLINNEMANN J., HEGER G., Physica B, 234–236 (1997), 40.
[4] SUMITA M., OSAKA T., MAKITA Y., J. Phys. Soc. Jpn., 50 (1981), 154.
[5] BRONOWSKA W., PIETRASZKO A., Solid State Commun., 76 (1990), 293.
[6] PRAISINGER A., MEREITER K., BRONOWSKA W., Mat. Sci. Forum, 166–169 (1994), 511.
[7] BRONOWSKA W., Adv. X-Ray Anal., 40 (1998), CD.

[8] BRONOWSKA W., J. Chem. Phys., 114 (2001), 611.
[9] SUZUKI S., ARAI K., SUMITA M., MAKITA Y., J. Phys. Soc. Jpn., 52 (1983), 2394.
[10] HAGIWARA T., ITOH K., NAKAMURA E., KOMUKAE M., MAKITA Y., Acta Cryst.C, 40 (1984), 718.
[11] OSAKA T., SUMITA M., MAKITA Y., J. Phys. Soc. Jpn., 52 (1983), 1124.
[12] MAKITA Y., SUMITA M., OSAKA T., SUZUKI S., Ferroelectrics, 39 (1981), 1017.
[13] LEVSTIK A., BLINC R., KADABA P., CIZIKOV S., LEVSTIK I., FILIPIC C., Solid State Commun., 16 (1975), 1339.
[14] UESU Y., KOBAYASHI J., Phys. Status Solidi (a), 34 (1976), M 475.
[15] BARANOV A.I., KHIZNICHENKO V.P., SHUVALOV L.A., Ferroelectrics, 100 (1989), 135.
[16] ORTIZ E., VARGAS R.A., MELLANDER B.-E., J. Chem. Phys., 110 (1999), 4847.
[17] HAILE S.M., Mater. Res. Soc. Symp. Proc., 547 (1999), 315.
[18] BOYSEN D.A., HAILE S.M., LIU H., SECCO R.A., Chem. Mater., 15 (2003), 727.
[19] LEE K.-S., J. Phys. Chem. Solids, 57 (1996), 333.
[20] PARK J.H., Phys. Rev. B, 69 (2004), 054104.
[21] OTOMO J., Solid State Ionics, 156 (2003), 357.
[22] SHELDRICK G.M., *SHELXL-97, Programs for the Solution and the Refinement of the Crystal Structures from Diffraction Data*, University of Gottingen, 1997.

Received 10 December 2004
Revised 10 September 2005

Materials Science-Poland, Vol. 24, No. 1, 2006

Structural phase transitions and their influence on Cu^+ mobility in superionic ferroelastic Cu_6PS_5I single crystals

A. GĄGOR[1*], A. PIETRASZKO[1], M. DROZD[1], M. POŁOMSKA[2], D. KAYNTS[3]

[1]Institute of Low Temperatures and Structure Research,
Polish Academy of Sciences, ul. Okólna 2, 50-590 Wrocław, Poland

[2]Institute of Molecular Physics, Polish Academy of Sciences,
ul. Smoluchowskiego 17, 60-179 Poznań, Poland

[3]Uzhhorod State University, Uzhhorod, Ukraine

The structural origin of Cu^+ ion conductivity in Cu_6PS_5I single crystals is described in terms of structural phase transitions studied by X-ray diffraction, polarized light microscopy and calorimetric measurements. Below the phase transition temperature at T_c = (144–169) K, Cu_6PS_5I belongs to the monoclinic, ferroelastic phase, with the space group *Cc*. Above T_c, the crystal changes its symmetry to a cubic superstructure, with the space group $\bar{F}43c$ (a' = 19.528); finally, at 274 K, the disordering of Cu^+ ions increases to the symmetry $\bar{F}43m$ (a = 9.794). The phase transition at 274 K coincides well with a strong anomaly in electrical conductivity observed on the Arrhenius plot. Diffusion paths for Cu^+ ions are evidenced by means of atomic displacement factors and a split model. The influence of copper stoichiometry on T_c is also discussed.

Key words: *fast-ion conductor; structural phase transition; X-ray diffraction; argyrodite*

1. Introduction

The investigations presented in this work are a part of the research on ferroelastic, superionic $Cu_6PS_5I_xBr_{1-x}$ crystals which exhibit mixed ionic-electronic conduction. They belong to the argyrodite family of compounds with an icosahedric structure [1, 2]. Among the crystals of this family, Cu_6PS_5Hal (Hal = Cl, Br, I) have been recently extensively studied, because of possible applications in high energy density batteries and sensors, and due to the possibility of phase transitions and order-disorder

*Corresponding author, e-mail: a.gagor@int.pan.wroc.pl

studies [3–7]. Despite numerous papers related to the optical, dielectric, and thermodynamic properties of these compounds, knowledge about the low-temperature crystal structures remains very limited. Furthermore, the temperatures of polymorphic phase transitions reported by different research groups do not correspond to each other. For example, according to Studenyak et al. [8] two phase transitions (PT) are observed at low temperatures, a first-order superionic PT at T_s = (165–175) K and second-order, ferroelastic one at T_c = 269 K. Girnyk et al., on the other hand, report T_s at 210 K and T_c at 180 K [3]. As far as this crystal is concerned, conductivity measurements have been performed only on powder samples. The total conductivity was measured by Khus et al. in the range of 293–300 K [1]. It was established that at room temperature, the conduction is purely ionic ($\sigma_I \approx 4\times10^{-4}$ at RT), with an electronic contribution (hole conductivity σ_h) less than 1%. At higher temperatures, σ_h increases and at 423 K it becomes equal to σ_i. Low-temperature conduction was measured by Beeken et al. [9]; a strong anomaly with a broad and continuous change in activation energy was observed on the Arrhenius plot at 270 K, and much weaker one around 194 K.

In the present work, we analyse the structural changes in Cu_6PS_5I single crystals using X-ray diffraction, domain structure observations, and calorimetric investigations. Our main purpose is to correlate the changes in the structural disordering of Cu^+ mobile ions with the electrical conductivity of this compound.

2. Experimental

Cu_6PS_5I crystals were obtained by the conventional vapour transport method [10] at the Uzhhorod State University. Calorimetric measurements were performed from 130 K to 233 K using a Perkin-Elmer DSC-7 instrument with the scanning rate of 20 K/min. The weight of the sample, consisting of small single crystals obtained under the same growth conditions, was 31.447 mg. Ferroelastic domain studies were carried out using a polarizing microscope equipped with a Linkam temperature controller, for which ΔT = 0.1 K, for thin plate samples oriented in the cubic phase perpendicular to the <100> direction.

Single-crystal X-ray data were collected on a Kuma KM-4 CCD diffractometer with a CCD camera (MoK_α radiation, graphite monochromator) equipped with a nitrogen gas-flow cooling system (Oxford Criosystem Controller), with ΔT = 0.3 K. To minimize the absorption effect, a sphere 0.25 mm in diameter was prepared in a compressed air mill and absorption correction for the sphere was applied. The lattice parameters were determined by the Bond procedure [11] on a Bond diffractometer (CuK_α radiation, graphite monochromator). Data were collected for a spherical sample at 150 K, 235 K, and 293 K. Structure refinement was carried out by direct methods with the SHELXL-97 program package. The positions of Cu^+ ions were taken from the differential Fourier maps.

3. Results and discussion

3.1. DSC and domain structure, and the temperatures and the sequence of structural phase transitions

Differential scanning calorimetry shows that on heating and cooling there are three thermal anomalies connected to the phase transitions, with temperatures on the cooling run as follows: 274 K, 160 K, and 144 K (Fig. 1). A large hysteresis in the low-temperature range and a weaker one in the high temperature range indicate first-order phase transitions.

An investigation of a real ferroelastic domain structure and its temperature behaviour was performed and compared with DSC measurements. On the basis of these studies, the temperature of the ferroelastic phase transition was established and the possibility of an intermediate phase existing between the high- and low-temperature phases was checked.

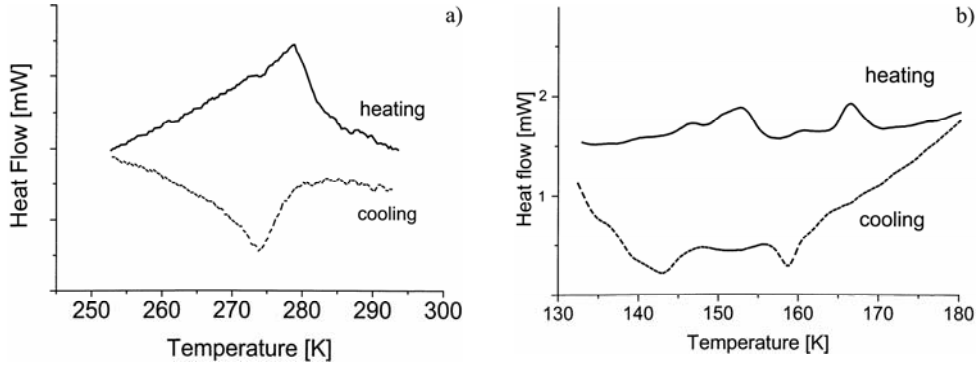

Fig. 1. DSC curves of Cu_6PS_5I: a) high low temperature range, b) low temperature range

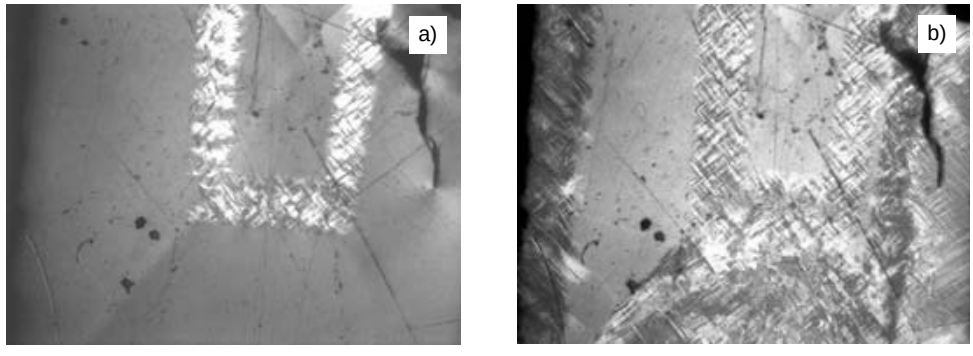

Fig. 2. Domain structure in Cu_6PS_5I in the <100> direction: a) 165 K, b) 144 K

Cu_6PS_5I crystals remain optically isotropic down to 165 K, which corresponds to the second peak on the DSC diagram. Surprisingly, only a part of the sample (rectan-

gular in shape) undergoes the transition (Fig. 2a). Domain structure appears below 144 K in the whole sample (Fig. 2b). This transition corresponds to the third peak on the DSC diagram. It was shown by Studenyak [12] that different technological procedures used in a vapour transport method result in the synthesis of crystals with various copper contents. This leads to different temperatures of the superionic phase transition. In our case, the samples were prepared under the same growth conditions, therefore it seems that seeds with different copper content were obtained.

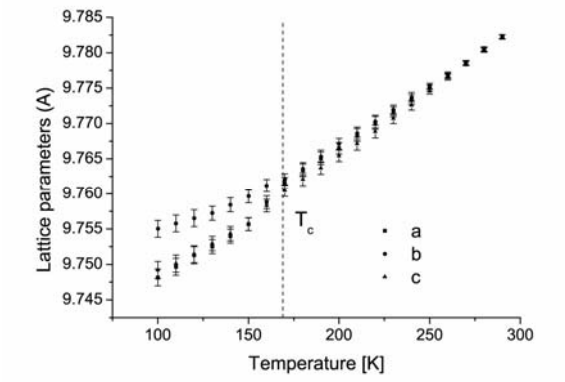

Fig. 3. Temperature dependence of lattice parameters *a*, *b*, and *c* [Å]

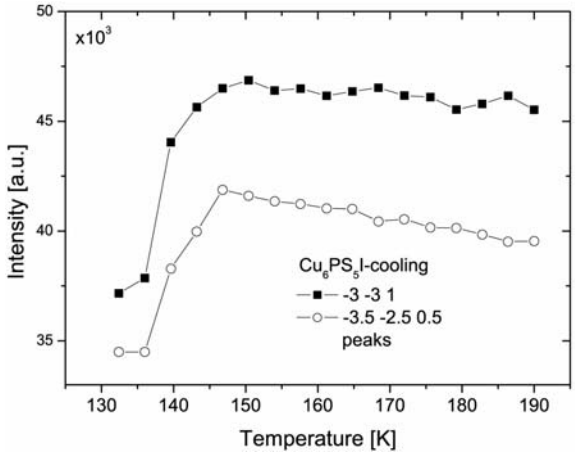

Fig. 4. Temperature dependence of the intensities
of selected reflections indexed in the cubic *F*-43*m* phase

The temperature of the ferroelastic phase transition coincides with the temperature of the superionic phase transition based on the absorption edge energy reported by Studenyak (T_s = 169 K). This means that in Cu_6PS_5I crystals $T_c = T_s$, and two phase transitions occur, a structural one at 274 K, which does not change the crystallo-

graphic system, and the other, ferroelastic transition below 169 K with the transition temperature dependent on Cu content in the sample. To confirm these results, two samples were measured by X-ray diffraction. Precise lattice parameters versus temperature were refined using the Bond method for the first sample, in which the splitting of lattice parameters below 169 K is well pronounced (Fig. 3). In the case of the second sample, changes in the Bragg peak intensities and half widths of the 12 2 2 peak versus temperature were measured (Figs. 4 and 5). Sharp changes in these values occur at 144 K, supporting our interpretation and being in perfect agreement with the results obtained by DSC and domain structure studies. The results are summarized in Fig. 6.

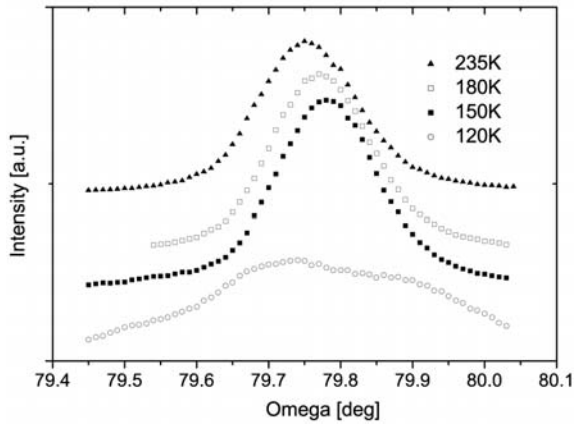

Fig. 5. Temperature dependence of the 12 2 2 Bragg peak profile

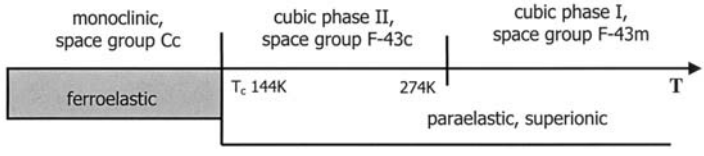

Fig. 6. Phase transitions in Cu_6PS_5I

Above 274 K, Cu_6PS_5I has a cubic structure with the *F*-43*m* symmetry (cubic phase I), common for all Cu_6PS_5Hal. The extinction conditions reflection data set observed below 274 K is in agreement with the *F*-43*c* space group with doubled lattice parameters, a = 19.528 Å (cubic phase II). Below 169 K, the crystal undergoes a ferroelastic and superionic first-order phase transition from a cubic to monoclinic system with the space group *Cc* [13]. The temperature of this phase transition depends on the copper content in the sample. Phase transitions in Cu_6PS_5I are connected with the ordering of the Cu sublattice, leading to the identical arrangement and full occupation of Cu sites in all cells of the monoclinic phase. The basic icosahedral anion sublattice is preserved after the change of symmetry.

Due to the low temperature of the ferroelastic phase transition and existence of cubic phase II between *F*-43*m* and *Cc* symmetries, a detailed study of Cu ordering can be performed in Cu_6PS_5I crystals in the entire range of the superionic phase.

3.2. Cu^+ ionic migration

In cubic phase I, 24 Cu^+ ions partly occupy two systems of equivalent tetrahedral sites within a framework of interpenetrating, centred, distorted anion icosahedra.

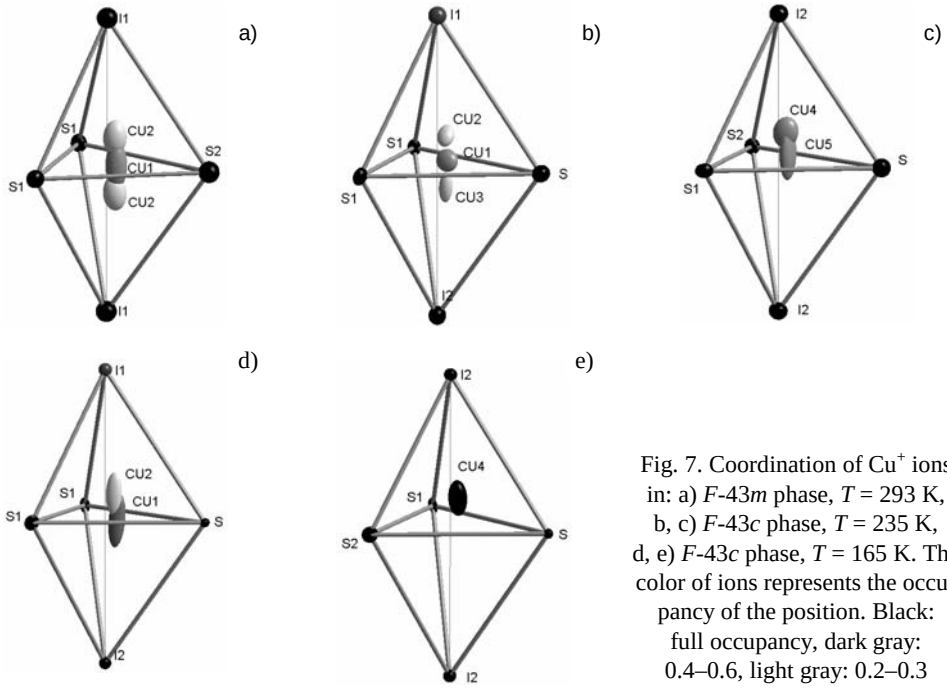

Fig. 7. Coordination of Cu^+ ions in: a) *F*-43*m* phase, T = 293 K, b, c) *F*-43*c* phase, T = 235 K, d, e) *F*-43*c* phase, T = 165 K. The color of ions represents the occupancy of the position. Black: full occupancy, dark gray: 0.4–0.6, light gray: 0.2–0.3

These ions are distributed among 72 positions in unique cells, which provides a favourable means for ionic migration. Cu^+ ions on 48-fold (m) positions are coordinated by distorted S_3I tetrahedra, and ions occupying 24-fold (2mm) sites are coordinated by a planar, triangular S_3 configuration (Fig 7a). The change in symmetry to *F*-43*c* at phase II provides six independent 96-fold Cu positions with point symmetry C_1 in the rigid skeleton of an anion framework and two different tetrahedral coordinations for Cu^+ ions: $I1S_3$ and $I2S_3$. Two tendencies in the ordering process of the Cu sublattice are observed with changing temperature. The $I2S_3$ tetrahedral site is strongly preferred by Cu^+ ions. On decreasing temperature, Cu^+ ions shift from a planar S_3 configuration towards the tetrahedral $I2S_3$ site (Fig. 7b, c). At 165 K, this position is almost fully occupied (Fig. 7d, e). From the other side, ions coordinated by $I1S_3$ tetrahedra prefer the planar triangular S_3 configuration. The occupancy of this site increases with decreasing temperature, but even at 165 K the Cu^+ ions are not

well localized. Temperature displacement factors are elongated along the axis of the tetrahedra. This strong tendency to occupy triangular planar configurations corresponds to the monoclinic *Cc* phase model of Cu arrangement proposed by Haznar et al. for Cu_6PS_5Br compounds [13]. All these structural changes have a great influence on ionic migration. The energy barrier associated with the motion along mobile pathways, from the minima at tetrahedral sites to barrier triangular sites, increases during the ordering of Cu^+ ions in tetrahedral sites. Also, the distances between Cu atoms become longer, thus undoubtedly suppressing the mobility of Cu^+ ions.

4. Conclusions

Structural changes resulting from polymorphic phase transitions have been studied in Cu_6PS_5I single crystals by means of X-ray diffraction, DSC and optical measurements. Below the temperature of the phase transition at T_c = (144–169) K, the crystal belongs to the ferroelastic phase with the space group *Cc*. T_c depends on the copper content in the sample. Above T_c, the crystal changes its symmetry to the cubic superstructure *F*-43*c*, and at 274 K to the *F*-43*m* system in a structural phase transition. In the *F*-43*c* phase, Cu^+ ions have a tendency to locate in tetragonal and planar triangular sites with decreasing temperature, which suppresses ionic mobility.

References

[1] KUHS W.F., NITSCHE R., SCHEUNEMANN K., Mat. Res. Bull., 14 (1979), 241.
[2] KUHS W.F., NITSCHE R., SCHEUNEMANN K., Mat. Res. Bull., 11 (1976), 1115.
[3] GIRNYK I., KAYNTS D., KRUPYCH O., MARTUNYUK-LOTOTSKA I., VLOKH R., Ukr. J. Phys. Opt., 4 (2003), 147.
[4] KRANJCEC M., STUDENYAK I.P., BILANCHUK V.V., DYORDYAY V.S., PANKO V.V., J. Phys. Chem. Solids, 65 (2004), 1015.
[5] STUDENYAK I.P., KRANJCEC M., KOVACS GY.SH., PANKO V.V., MITROVCIJ V.V., MIKAJLO O.A., Mat. Sci. Eng., B97 (2003), 34.
[6] KRANJCEC M., STUDENYAK I.P., KOVACS GY.S., DESNICA-FRANKOVIC I.D., PANKO V.V., GURANICH P.P., SLIVKA V.YU., J. Phys. Chem. Solids, 62 (2001), 665.
[7] STUDENYAK I.P., KRANJCEC M., KOVACS G.S., DESNICA-FRANKOVIC I.D., PANKO V.V., SLIVKA V.YU., Mat. Res. Bull., 36 (2001), 123.
[8] STUDENYAK I.P., KOVAC GY.SH., ORLYUKAS A.S., KOVACS YE.T., Dokl. Akad. Nauk. Ser. Fiz., 56 (1992), 86.
[9] BEEKEN R.B., GARBE J.J., PETERSEN N.R., J. Phys. Chem. Solids, 64 (2003), 1261.
[10] FIECHTER S., ECKSTEIN J., NITSCHE R., J. Cryst. Growth, 61 (1983), 275.
[11] BOND W.L, Acta Cryst., 13 (1960), 814.
[12] STUDENYAK I.P., KRANJCEC M., KOVACS GY.S., PANKO V.V., AZHNIUK YU.M., DESNICA I.D., BORETS O.M., VOROSHILOV YU.V., Mat. Sci. Eng., B52 (1998), 202.
[13] HAZNAR A., PIETRASZKO A., STUDENYAK I.P., Solid State Ionics, 119 (1999), 31.

Received 10 December 2004
Revised 17 January 2005

Materials Science-Poland, Vol. 24, No. 1, 2006

Electrical conductivity in new imidazolium salts of dicarboxylic acids

K. POGORZELEC-GLASER[1], J. GARBARCZYK[1*], CZ. PAWLACZYK[2], E. MARKIEWICZ[2]

[1]Poznan University of Technology, pl. Skłodowskiej-Curie 1, 60-965 Poznań, Poland

[2]Institute of Molecular Physics, Polish Academy of Sciences,
Smoluchowskiego 17, 60-179 Poznań, Poland

Electrical conductivities of powder samples of five new imidazolium salts of aliphatic dicarboxylic acids (imidazolium malonate (**1**), imidazolium glutarate (**2**), imidazolium adipate monohydrate (**3**), diimidazolium suberate (**4**), imidazolium sebacate (**5**) were measured by impedance spectroscopy as a function of temperature. It was found that conductivities increase with temperature. At high temperatures, the lowest conductivity was determined for imidazolium glutarate (10^{-5} S/m) and the highest – for imidazolium sebacate (10^{-1} S/m). The correlation between crystal structures of the investigated salts and their ionic conductivities is discussed.

Key words: *electrical conductivity; imidazolium salt; dicarboxylic acid*

1. Introduction

Imidazole is a nitrogen heterocycle of paramount importance, with special biological properties. The imidazole moiety serves as a proton transfer agent in living systems due to its molecular structure, which allows imidazole to act as a weak acid and as a base. Recently, such properties have been used to design conducting electrolytes for highly efficient fuel cells operating at high temperatures [1].

For the first time, conductivity in pure crystalline imidazole was determined by Kawada et al. [2] and Chojnacki et al. [3]. The ionic conductivities of these materials were explained by the Grotthus model [4]. The imidazole molecule enables the formation of proton defects and provides a fluctuating donor/acceptor function. Furthermore, *ab initio* calculations have showed that hydrogen bonds between imidazole molecules are characterised by a low proton transfer barrier [5].

*Corresponding author, e-mail: garbarc@rose.man.poznan.pl

Kreuer et al. [6] measured electrical conductivity of strong inorganic acids doped with imidazole in the liquid state and analysed the role of this compound in ionic conductivity. It was noticed that the addition of the basic imidazole molecule causes a number of proton defects in HSO_4^- and $H_2PO_4^-$ anions.

In our study, we have obtained and examined new imidazolium salts of aliphatic dicarboxylic acids in the solid crystalline state. The main task of this work was to determine the conductivity and attempt to find a correlation between the ionic conductivities and structures of the obtained crystals.

2. Experimental

Synthesis and crystallisation. Imidazole and dicarboxylic acids were dissolved separately in anhydrous ethyl acetate and then the solutions were mixed together and stirred until a white precipitate appeared. The reaction product was separated and washed with anhydrous ethyl acetate. The starting materials, approximately 99% pure, obtained from Sigma-Aldrich and Fluka, were used without further purification. The crystallisation of all salts was carried out by evaporating the solvent.

Conductivity measurements. The samples of each salt in the form of a powder were pressed at room temperature under p = 50 MPa for t = 20 min. The samples, 1.5–2.5 mm thick and 13 mm in diameter, were covered with silver paste electrodes. The real and imaginary parts of electrical impedance were measured in the frequency range from 100 Hz to 1 MHz by means of a computer-controlled HP-4284A precision LCR meter. The temperature of the samples was stabilized using a CF 1204 Oxford Instruments cryostat, equipped with an ITC4 temperature controller. Data collection for a number of frequencies from the above range was performed after the temperature of the sample was stabilized. The dc resistivity of imidazolium glutarate was directly measured using a Keithley electrometer.

3. Results and discussion

Electrical conductivity measurements were carried out by impedance spectroscopy for tablets made as described above for imidazolium malonate (**1**), imidazolium glutarate (**2**), imidazolium adipate monohydrate (**3**), diimdazolium suberate (**4**), and imidazolium sebacate (**5**). A typical dependence of the imaginary part of impedance Z'' on the real part Z' (Argand diagram) for diimidazolium suberate is shown in Fig. 1.

Such a dependence (one semicircle tending to ($Z' = 0$, $Z'' = 0$) with increasing frequency) is expected when the equivalent circuit of the sample is composed of one resistivity R and one parallel capacity C. The dc resistivity of the sample can be estimated as $Z' = R$ when the frequency $f \rightarrow 0$.

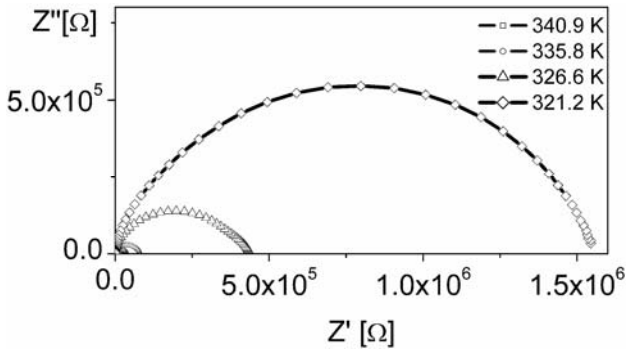

Fig. 1. Argand diagram for diimidazolium suberate

The frequency dependences of ac conductivity (σ_{ac}) for all the compounds are shown in Figs. 2a–e. The dc conductivity σ_{dc} for a given temperature can be read out from the low frequency plateau of each $\sigma_{ac}(f)$ curve.

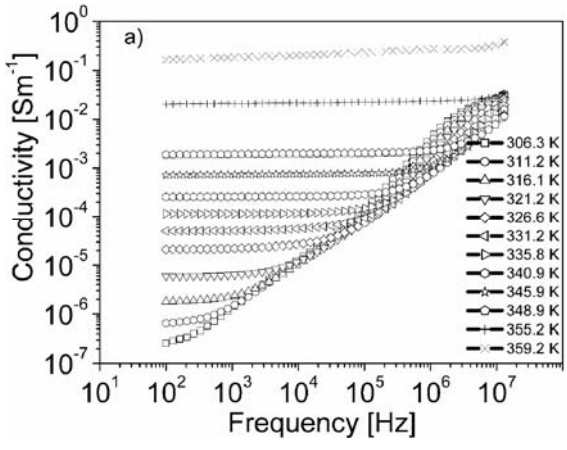

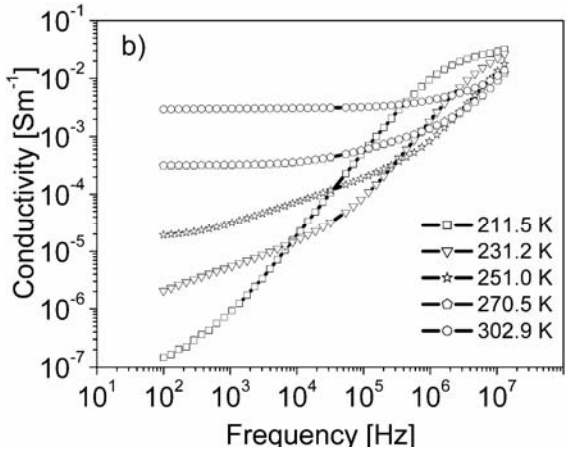

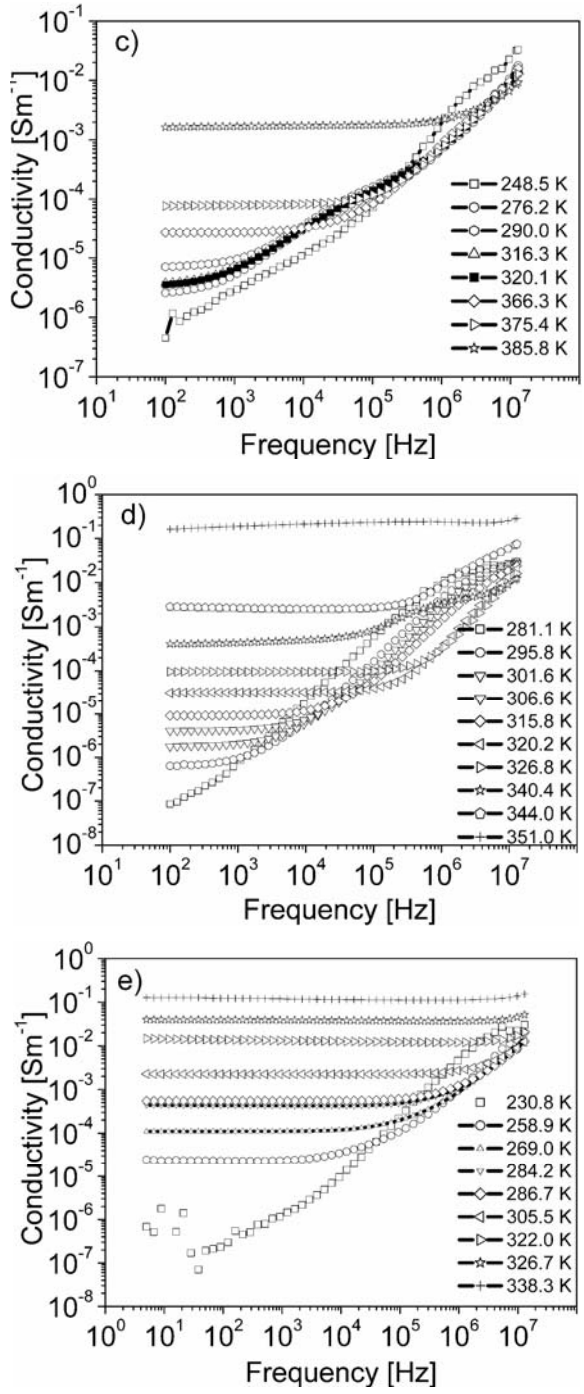

Fig. 2. Frequency dependences of ac conductivity for the investigated salts:
a) diimidazolium suberate, b) imidazolium suberate, c) imidazolium glutarate,
d) imidazolium adipate, e) imidazolium sebacate

The Arrhenius dependence:

$$\sigma = \sigma_0 \exp(-E_a / kT)$$

where E_a denotes the activation energy, σ_0 the pre-exponential factor, and k the Boltzmann constant, is fulfilled in all cases. The Arrhenius plots $\sigma_{dc}(1/T)$ obtained from the ac results for all compounds are displayed in Fig. 3. The activation energies calculated from the Arrhenius formulae are presented in Table 1.

Table 1. The activation energies for imidazolium salts of dicarboxylic acids

Compound	Activation energy [eV]
Imidazolium malonate (**1**)	0.75
Imidazolium glutarate (**2**)	0.70
Imidazolium adipate hydrate (**3**)	1.06
Diimidazolium suberate (**4**)	1.52
Imidazolium sebacate (**5**)	1.68

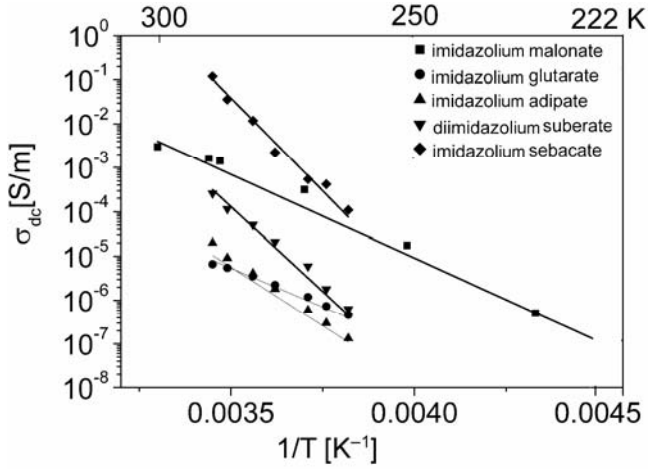

Fig. 3. Arrhenius plot of σ_{dc} for all the investigated compounds

In the case of imidazolium glutarate, the ac conductivity is compared with direct dc measurements (Fig. 4). Both results are in a good agreement.

The activation energies presented in Table 1 may be correlated with the crystal structures of the investigated salts. The crystal data concerning the investigated imidazolium salts are listed in Table 2.

The characteristic feature of the investigated imidazolium salts is that in all (**1–5**) the crystal structures, imidazolium cations and dicarboxylic anions are connected by hydrogen bonds of the N-H···O type, forming in flat ribbons. These ribbons are arranged in two-dimensional layers (see Fig. 5). In these two-dimensional hydrogen

Table 2. Crystal data of imidazolium salts

Property	Compound				
	Imidazolium malonate (**1**) [8]	Imidazolium glutarate (**2**)*	Imidazolium adipate monohydrate (**3**)*	Diimidazolium suberate (**4**)*	Imidazolium sebacate (**5**) [7]
Formula	$C_9H_{12}N_4O_4$	$C_8H_{12}N_2O_4$	$C_{12}H_{18}N_4O_4$	$C_{14}H_{22}N_4O_4$	$C_{18}H_{31}N_2O_6$
Molecular weight	240.23	200.19	282.30	310.36	371.45
X-ray wavelength [Å]	1.54178	0.71073	0.71073	0.71073	1.54178
Crystal system	triclinic				
Space group	*P*-1				
a [Å]	7.2570(6)	8.420(2)	7.484(1)	7.842 (2)	8.825(1)
b [Å]	8.3020(10)	13.685(3)	8.934(2)	8.917 (2)	8.992(1)
c [Å]	9.3410(12)	17.068(3)	10.313	12.388 (2)	12.897(1)
α [°]	62.820(12)	90.62(3)	104.92(3)	88.74 (3)	95.22(1)
β [°]	75.550(9)	103.45(3)	109.01(3)	73.59 (3)	92.91(1)
γ [°]	88.070(8)	91.03(3)	106.55(3)	87.94 (3)	94.62(1)
Volume [Å^3]	482.68(9)	1912.2(7)	576.38(19)	830.4 (3)	1014.1(2)

*Details of the crystal structures are deposited in CCDC(225442–225444) and will be published elsewhere.

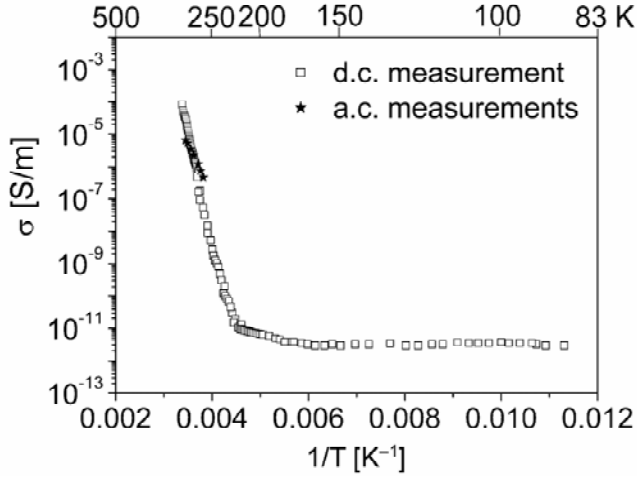

Fig. 4. Comparison of ac and dc conductivity measurements for imidazolium glutarate

bonded systems, the hydrophobic and hydrophilic parts are easily noticeable. The hydrophilic parts, with negative carboxylate anions and positively charged imidazolium cations, may serve as channels for proton transport. The lowest activation energy is noticed for imidazolium glutarate (0.7 eV). Such a low value can be connected to the specific stacking of imidazolium rings among acid molecules. This enables the formation of many possible N–H···O interactions which play a crucial role in the conducting mechanism.

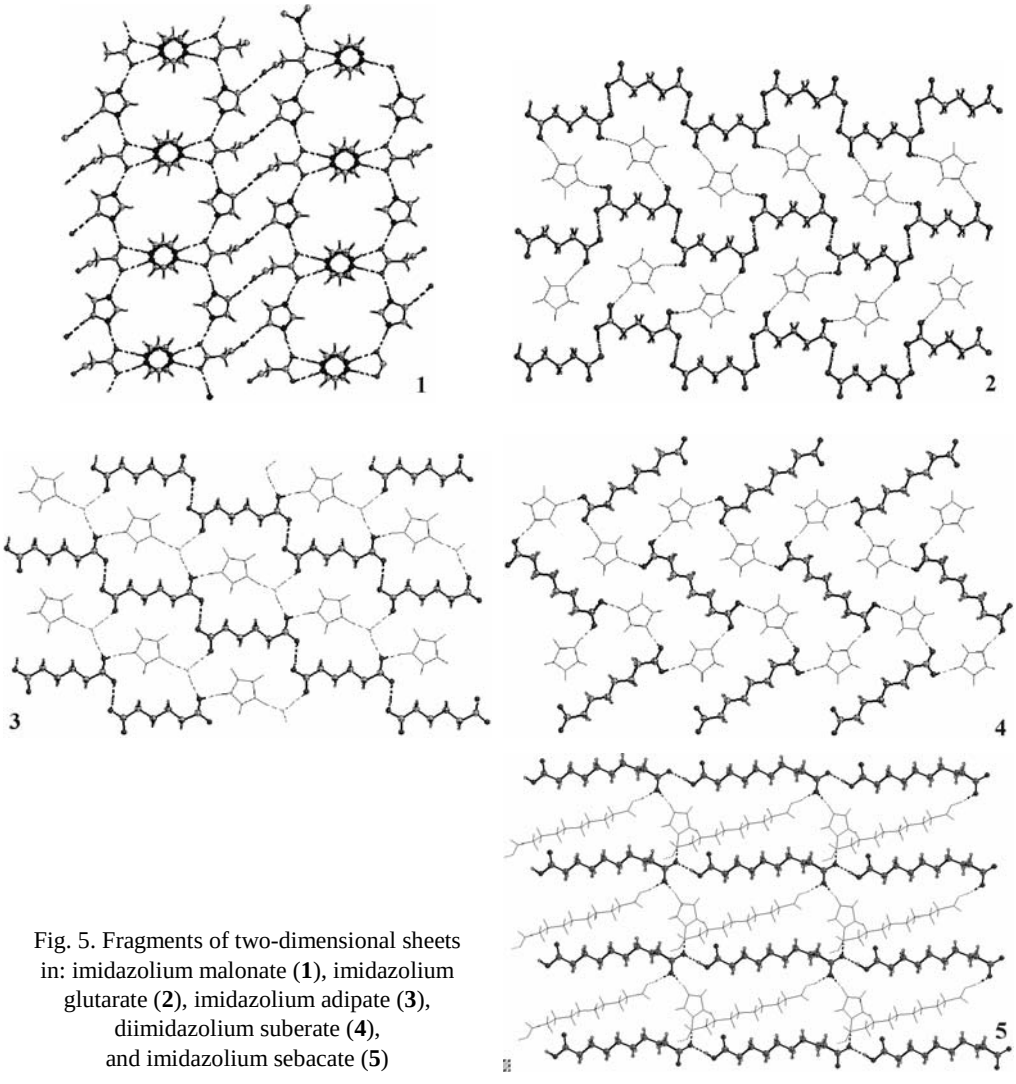

Fig. 5. Fragments of two-dimensional sheets in: imidazolium malonate (**1**), imidazolium glutarate (**2**), imidazolium adipate (**3**), diimidazolium suberate (**4**), and imidazolium sebacate (**5**)

In imidazolium malonate, where a disordering of heterocyclic ring exists (Fig 5, **1**), a similar value of the activation energy (0.75 eV) was noted. For imidazolium adipate, however, in which a water molecule is incorporated into the crystal lattice, the activation energy is higher (1.06 eV). H_2O molecules form additional H-bonds between imidazole and acid moieties. On the other hand, E_a increases with the length of the methylene chain of the acid molecule. The highest activation energies are observed for diimidazolium suberate (**4**) (1.52 eV) and imidazolium sebacate (**5**) (1.68 eV). In the case of diimidazolium suberate, proton transfer is disabled by the unfavourable stacking of imidazolium cations among layers. In salt **5**, the rotation of the imidazolium cation is limited by the presence of acid molecules, which bind adjacent layers.

It is known that the librations and rotations of imidazole molecules can play an important role in the mechanism of conductivity. The vibrations of imidazole molecules create virtual hydrogen bridges, which make the transportation of protons in the crystal easier.

4. Conclusions

The presented results concerning conductivity and its correlation with crystal structures can be summarized as follows:

- At low temperatures all the investigated salts have low conductivities (of about 10^{-12} S/m), typical of crystalline insulators.
- Starting at a certain temperature, the conductivities increase quickly according to the Arrhenius law to values in the range 10^{-5}–10^{-1} S/m just below the respective melting temperatures.
- As conductivity measurements were possible only for tablets (not for single crystals), there is some uncertainty regarding the influence of tablet preparation on the results. Nevertheless, all the investigated salts exhibit high conductivities in some temperature range before melting. The conductivity is comparable to that of superprotonic materials. The transition to the superionic state, which could be characterized e.g., by a low activation energy, is, however, not reached before melting.
- Knowledge of the crystal structures of imidazolium salts allows the conductivity mechanism to be proposed in relation to the arrangement of molecules in the solid state.
- The activation energy of proton conductivity can be discussed pointing the context of librations and rotations of the imidazole group. First, the activation energy strongly depends on the presence (among layers) of polar parts, which may serve as "channels" in the conducting mechanism. Second, the lengthening of acid molecules increases the activation energy.

Acknowledgements

This study was partly supported by grant No. 32-114/04-DS.

References

[1] VIK S.B., ANTONIO B.J., J. Biol. Chem., 269 (1994), 30364.
[2] KAWADA A., MCGHIE A.R., LABES M.M., J. Phys. Chem., 52 (1970), 3121.
[3] CHOJNACKI H., BREDAS J.L., POSKIN M.P., J. Phys. Chem., 88 (1984), 5882.
[4] GROTTHUS C.J.D., Ann. Chim., 58 (1806), 54.
[5] MUNCH W., KREUER K.D., SILVESTRI W., MAIER J., SEIFERT G., Solid State Ionics, 145 (2001), 437.
[6] KREUER K.D., FUCHS A., ISE A., Electrochim. Acta, 43 (1998), 1281.
[7] GARBARCZYK J., POGORZELEC-GLASER K., Zeit. Kristallographie New Crystal Struct., 218 (2003), 567.
[8] POGORZELEC K., GARBARCZYK J., MOL. PHYS. REP., 35 (2002), 132; DEPOSIT CCDC 224836.

Received 10 December 2004
Revised 17 January 2005

Materials Science-Poland, Vol. 24, No. 1, 2006

Calcium zirconate as a solid electrolyte for electrochemical devices applied in metallurgy

M. DUDEK[1*], G. RÓG[1], W. BOGUSZ[2], A. KOZŁOWSKA-RÓG[1], M. BUĆKO[1], Ł. ZYCH[1]

[1]AGH University of Science and Technology, Faculty of Materials Science and Ceramics, al. Mickiewicza 30, 30-059 Cracow, Poland

[2]Faculty of Physics, Warsaw University of Technology, ul. Koszykowa 75, 00-662 Warsaw, Poland

Stoichiometric calcium zirconate and $CaZrO_3$ samples with an excess of calcia or zirconia were obtained from powders prepared by the citrate method. XRD measurements were used to determine the phase compositions of the sintered materials as well as their crystal structures. The compositional dependence of the calcium zirconate cell parameter indicates that an excess of calcia or zirconia form a solid solution. Stoichiometric $CaZrO_3$ appeared to be a rather poor oxygen ion conductor, whereas calcium zirconate samples with an excess of calcia or zirconia exhibit pure oxygen conductivity. The introduction of a respective excess of cations led in both cases to a significant enhancement of conductivity. The fracture toughness, hardness, and flexural strength of the samples were also investigated. The mechanical and electrical properties of $CaZrO_3$-based materials are comparable to those of zirconia solid electrolytes. The lower thermal expansion coefficient and better resistance to thermal shock make $CaZrO_3$ a more suitable solid electrolyte for metallurgical applications.

Key words*: perovskite; oxygen ion conductor; electrolyte; probe; metallic melt*

1. Introduction

Oxygen sensors based on partially or fully (CaO, MgO)-stabilized ZrO_2 have been developed and used for steel making and nickel and copper refining processes. It is known that the electronic conductivity of ZrO_2-based electrolytes should be taken into account when oxygen partial pressure falls below 10^{-7} Pa at temperatures close to 1300 °C [1, 2]. The electronic conductivity introduces time-dependent polarisation effects in the long-time operation of electrochemical oxygen probes. Additionally, at very low oxygen partial pressures, decomposition of zirconia occurs, which may cause serious errors in EMF measurements [3]. Taking the above effects into account,

*Corresponding author, e-mail: potoczek@uci.agh.edu.pl

it is appropriate to search for other solid electrolytes with lower partial electronic conductivities. Good mechanical properties, thermal shock resistance, and thermodynamic stability are also required for electrolytic materials in such applications. The ionic conduction limit for yttria-doped thoria (YDT) is lower than that for stabilized zirconia. Hence, thoria-based electrolytes are superior at low oxygen concentrations. Due to the radioactivity of thorium, however, they have not found application in the steel industry [4]. Several investigators have reported $CaZrO_3$ with excess of zirconia or calcia being also an oxygen-ion conductor which might be applied as a solid electrolyte in electrochemical devices in the temperature range 1200–1600 °C and at partial oxygen pressures down to 10^{-13} Pa. Ceramic electrolytes based on $CaZrO_3$ have been successfully applied as probes in molten steel [5, 6]. One of the main disadvantages of such materials is EMF instability during long-time use. The $CaZrO_3$-based samples with calcia inclusions applied by Janke et al. [6] as solid electrolytes showed significant porosity (15–20%) depending on chemical composition and sintering temperature. Chemical inhomogeneity could be an additional disadvantage for their application. Moreover, at temperatures higher than 1800 °C unfavourable microstructural changes can occur due to the phase transition of orthorhombic $CaZrO_3$ to its cubic form [7].

The present study is focused on the preparation of dense $CaZrO_3$ samples, as well as on investigations of the influence of an excess of zirconia or calcia on the structure and microstructure, and hence on the electrical and mechanical properties of $CaZrO_3$. The practical purpose of this research was to obtain a $CaZrO_3$-based material that could be applied as an electrolyte in electrochemical oxygen sensors with long-term stability.

2. Experimental

Calcium zirconate powders were prepared using the citrate method. Appropriate amounts of calcium carbonate and citric acid powders were dissolved in aqueous solution of zirconyl nitrate. The molar ratio of calcium to zirconium was fixed between 0.43 and 2.33. The solutions were evaporated at 70 ºC to obtain hard gels. The gels were heated to decompose the citric precursor in a sequence of several exo- and endothermic effects. Finally, the powders were calcinated at 900 ºC for 1 hour and then attrition-milled with a zirconia grinding media in dry ethanol. The pellets were isostatically pressed under 300 MPa and sintered at 1500 ºC for 2 hours in air. The phase composition of the powders and sintered samples was evaluated by X-ray diffraction analysis. Scanning electron microscopy was used to observe the microstructure of the samples. The fracture toughness was determined using the Vickers indentation method. The specimens for three-point bending tests were cut from plates and their flat surfaces were polished. Thermal expansion coefficients were measured in the temperature range 20–1200 °C. The electrical conductivity was measured by ac impedance spectroscopy in the temperature range of 200–900 ºC. For each sample,

impedance measurements were performed over two heating and cooling cycles. The transference oxygen number in all prepared samples was estimated from EMF measurements of a typical oxygen galvanic cell

$$\text{Pt} \mid \text{Fe, FeO} \mid \text{CaZrO}_3 \mid \text{Ni, NiO} \mid \text{Pt} \tag{1}$$

in the temperature range of 550–1100 ºC. The two-phase mixtures (Fe, Fe_xO) and (Ni, NiO) with known equilibrium oxygen partial pressures were used as the half-cells. The procedure was practically the same as that presented in Ref. [8]. If an electrolyte separating the half cells in cell (1) had a pure ionic conduction, and only O^{2-} ions were transported, the EMF, E_t would be given by the Nernst equation:

$$E_t = \frac{RT}{4F} \ln \frac{p_{O_2(\text{Ni, NiO})}}{p_{O_2(\text{Fe, Fe}_x\text{O})}} \tag{2}$$

where p_{O_2} is the equilibrium oxygen partial pressure. In the case of an electrolyte which contains another mobile charged species, the EMF of cell (1) can be expressed as

$$E = t_{\text{ion}} E_t \tag{3}$$

if only t_{ion} does not depend on the oxygen partial pressure in the galvanic cell. In such a case the term t_{ion} can be regarded as corresponding to the oxygen transference number in the $CaZrO_3$-based samples.

3. Results

Orthorhombic $CaZrO_3$ was the only phase detected by XRD in the samples containing from 0.50 to 0.515 mol fraction of calcia. Changes in the phase content of the samples strongly depended on the oxide, being in excess. Even in the sample with the smallest ZrO_2 excess, a significant amount of cubic zirconia solid solution was observed. In the case of samples with an excess of calcia, only very weak lines attributed to the CaO phase were detected for the material with the molar ratio $CaO:ZrO_2$ equal to 0.52:0.48. Figure 1 illustrates $CaZrO_3$ weight fraction changes, determined as a function of the initially assumed calcia to zirconia molar ratio. On the basis of X-ray investigations, the cell parameters and cell volume of $CaZrO_3$ with excess of calcia were calculated.

Figure 2 presents the compositional dependence of the $CaZrO_3$ cell volume. In both cases (excess of calcia and zirconia), an increase of volume cell was observed. In samples with excess of CaO, this increase is rather small and reaches a maximum for the material with 6 mol % of excess of calcia. The changes in cell parameters suggest that both excess of zirconia and calcia are in a solid solution form.

Figures 3a–c show typical microstructures of the samples. Generally, all samples achieved relative densities higher than 98%. Only the presence of CaO as a second

phase led to poorer densification and to the appearance of open porosity in samples. As shown in Figure 3, $CaZrO_3$ grain size decreases with the increasing excess of calcia or zirconia. The samples with an excess of zirconia exhibited an average grain size from 0.8 to 1.1 μm, whereas in those with excess of calcia the grain size ranged from 0.5 to 0.9 μm.

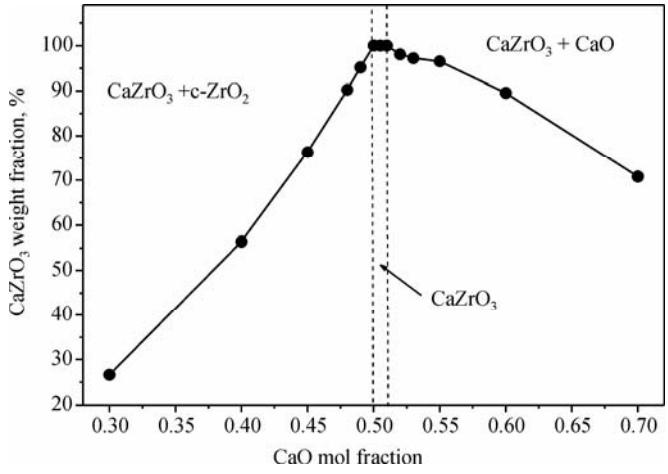

Fig. 1. Calcium zirconate weight fraction
as a function of initially assumed calcia to zirconia molar ratio

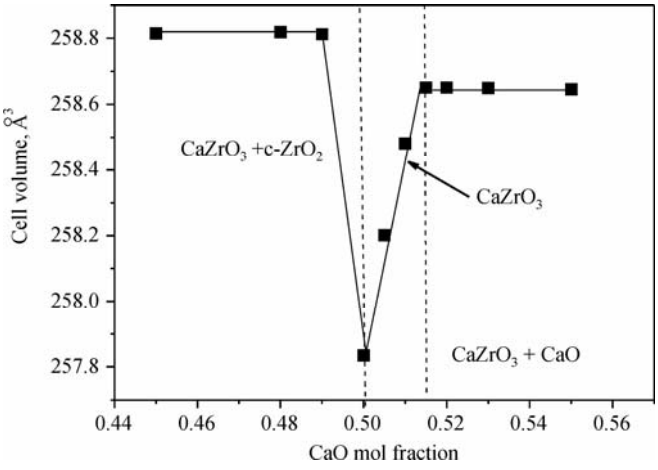

Fig. 2. Dependence of cell volume on molar fraction
of calcia in all samples investigated

The K_{IC} measurements (Fig. 4) indicated relatively small increases in fracture toughness with increasing calcia concentration. On the other hand, in the case of samples with an excess of ZrO_2 K_{IC} remains unchanged within an experimental error.

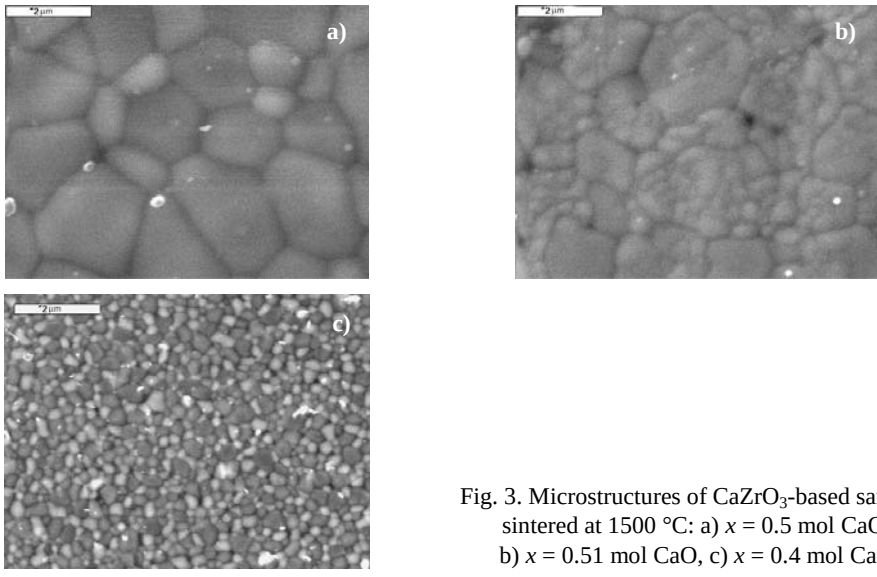

Fig. 3. Microstructures of $CaZrO_3$-based samples sintered at 1500 °C: a) x = 0.5 mol CaO, b) x = 0.51 mol CaO, c) x = 0.4 mol CaO

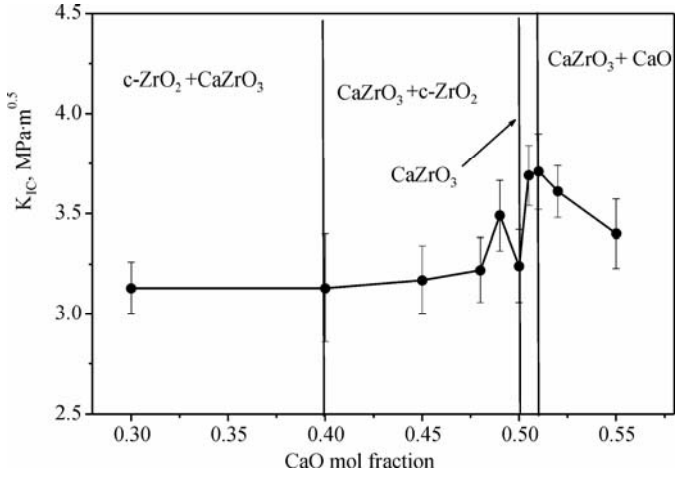

Fig. 4. Dependence of fracture toughness K_{IC} of calcium zirconate samples on calcia or zirconia excess

Mechanical properties of selected $CaZrO_3$-based materials as well as of solid ZrO_2-based electrolytes being potential electrolytes for oxygen-sensing applications are given in Table 1. These data clearly indicate that the mechanical properties of $CaZrO_3$-based materials are comparable to those of zirconia-based solid solutions. Considering $CaZrO_3$-based materials as potential solid electrolytes for applications in electrochemical oxygen probes used to determine oxygen activity in molten metals, it is required to have control over the expansion coefficient. Table 1 also compiles the determined values of the thermal expansion coefficient for selected $CaZrO_3$ samples

and for fully stabilized zirconia. The $CaZrO_3$-based samples exhibited lower thermal expansion coefficients than that of zirconia solid electrolytes. This might indicate a better resistance to thermal shock in operating conditions involving temperature fluctuations.

Table 1. Selected properties of $CaZrO_3$ and calcia-, magnesia- or yttria- fully stabilised zirconia materials

Material	HV [GPa]	K_{IC} [MPa×m$^{0.5}$]	σ_f [MPa]	α [K^{-1}]
$CaZrO_3$ 0.51 CaO 0.49 ZrO_2	9.20± 0.17	3.43± 0.12	208 ± 11	8.4×10^{-6}
$CaZrO_3$ 0.45 CaO 0.55 ZrO_2	10.61± 0.11	3.11± 0.15	198 ± 16	8.9×10^{-6}
15 mol % CaO in ZrO_2	12.20 ± 0.13	2.30± 0.15	220 ±13	2.1×10^{-5}
9 mol % MgO wZrO_2	11.80±0.16	2.22± 0.11	212 ± 21	1.9×10^{-5}
8 mol % Y_2O_3 in ZrO_2	12.86 ± 0.21	2.65 ± 0.15	222 ± 11	1.7×10^{-5}

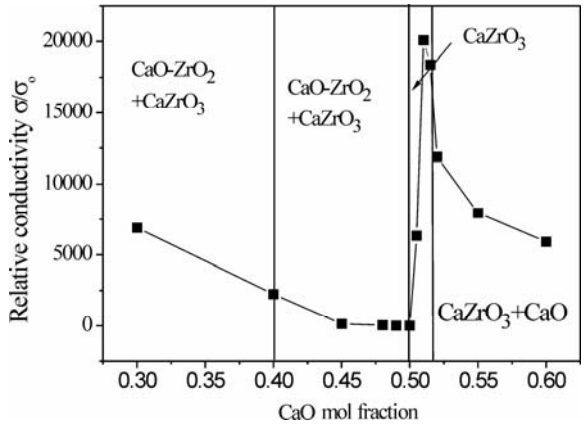

Fig. 5. Dependence of relative conductivity σ/σ_0 of calcium zirconate on calcia or zirconia excess

Impedance spectroscopy enabled determination of the bulk and grain boundary ionic conductivities of the sintered samples. Figure 5 illustrates the influence of the excess of zirconia or calcia on calcium zirconate electrical properties. In this figure, the relative total conductivity σ/σ_0 measured at 800 °C is plotted versus calcia mol fraction; σ_0 denotes the conductivity of stoichiometric calcium zirconate. An excess

of zirconia from 4 to 20 mol % leads to electrical conductivity enhancement by a factor from 3 to 48, respectively. A considerable increase in conductivity for samples

Table 2. Electrical properties of $CaZrO_3$ and calcia or magnesia fully-stabilised zirconia solid electrolytes in the temperature range of 200–1000 ºC

Material	σ_c [S/cm] (at 1000 °C)	E_a [eV]
$CaZrO_3$	1.3×10^{-6}	2.20
$CaZrO_3$ (0.51 CaO, 0.49 ZrO_2)	1.4×10^{-2}	0.90
$CaZrO_3$ + c.s.s CaO–ZrO_2 (0.6 CaO; 0.4 ZrO_2)	2.6×10^{-3}	1.32
$CaZrO_3$ + c.s.s CaO–ZrO_2 (0.7 CaO, 0.3 ZrO_2)	6.2×10^{-3}	1.31
15 % mol CaO in ZrO_2	5.2×10^{-2}	1.15
9 % mol MgO inZrO_2	4.5×10^{-2}	1.30

c.s.s – cubic solid solution CaO in ZrO_2.

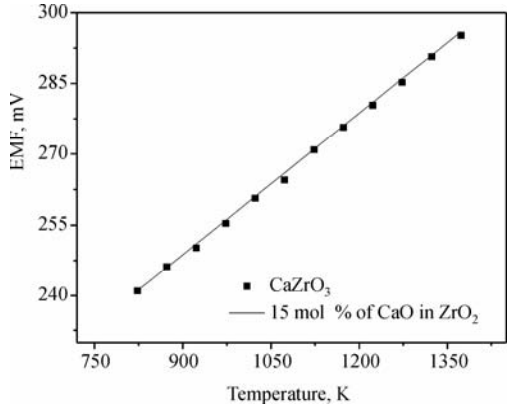

Fig. 6. The EMF of cell (1) as a function of temperature

with a larger excess of zirconia corresponds to the formation of cubic zirconia as a continuous phase, due to its better conduction properties as compared to $CaZrO_3$ electrolytes. On the other hand, introducing 4 mol % of calcia into calcium zirconate significantly increases conductivity by a factor of 2×10^4. An increase of the excess of calcia by more than 6 mol % results in the formation of a larger CaO heterophase and leads to a decrease in electrical conductivity. The analysis of electrical conductivities of all samples investigated reveals that the bulk conductivity reaches a maximum value for the CaO:ZrO_2 ratio being 0.51:0.49. The calculated values of ionic conductivity at 1000 °C for the selected samples are shown in Table 2. For comparison, the values of electrical conductivity (σ_c) and activation energy (E_a) are also presented for calcia-, magnesia-, and yttria-stabilized zirconia. The data regarding electrical proper-

ties clearly indicate that the samples based on $CaZrO_3$ exhibit electrical conductivities and activation energies close to those of calcia and magnesia-stabilized zirconia.

The EMF value of cell (1) measured at temperatures from 823 to 1273 K (Fig. 6) was compared to the respective EMFs measured with the same cell containing fully calcia-stabilised zirconia as a reference solid electrolyte (E_t). The calculated $CaZrO_3$ oxygen transference numbers (t_{ion}) were found to vary from 0.99 to 1, which indicates practically pure oxygen ion conduction. The chemical stability of $CaZrO_3$-based electrolytes in liquid metals such as nickel was also investigated.

Microstructural observations carried out with scanning microscopy and EDS analysis did not indicate any products of the reaction between $CaZrO_3$-based samples and nickel or copper melts.

4. Conclusions

The introduction of excess of CaO or ZrO_2 into calcium zirconate leads to a significant enhancement of electrical conductivity and to the improvement of the fracture toughness (K_{IC}) of $CaZrO_3$-based samples. The highest values of total electrical conductivity and fracture toughness were found in the calcium zirconate solid electrolyte containing 0.51 mol of CaO and 0.49 mol of ZrO_2. Its electrical and mechanical properties are comparable to ZrO_2-based solid electrolytes used commonly for oxygen probes in molten melts. The highest thermal shock resistance in cyclic temperature conditions and good corrosion resistance in molten metals make the prepared material a promising electrolyte for metallurgical applications.

Acknowledgement

This work was financially supported by the University of Science and Technology in Cracow under the contract No. 11.11. 160.110. One of authors, M. Dudek, acknowledges the financial support grant of the Foundation for Polish Science, awarded for young scientists in 2004.

References

[1] JANKE D., [in:] *Science and Technology of Zirconia*, A. Heuer, W. Hobbs (Eds.), The American Ceramic Society, Inc., Columbus, OH, 1980, p. 419.
[2] PLUSCHKELL W., Archiv für Eisenhuttenwesen, 46 (1975), 11.
[3] JANKE D., Metallurgical Trans., 13B (1982), 227.
[4] JACOB K.T., MATHEWS T., [in:] *High Conductivity Solid Ionic Conductors – Recent Trends and Applications*, Takahashi T. (Ed.), World Scientific, Singapore, 1989.
[5] FISCHER W., JANKE D., Archiv für Eisenhuttenwesen, 47 (1976), 51.
[6] FISCHER W., JANKE D., Archiv für Eisenhuttenwesen, 47 (1976), 525.
[7] KOOPMANS H.J., VAN DE VELDE G.M , GELLINGS M.P., Acta Cryst. C, 39 (1983), 1323.
[8] CHARETTE G., FLENGAS S., J. Electrochem. Sci., 115 (1968), 796.

Received 28 December 2004
Revised 17 January 2005

Materials Science-Poland, Vol. 24, No. 1, 2006

Electrocatalytic gas sensors based on Nasicon and Lisicon

G. JASINSKI[1*], P. JASINSKI[1], B. CHACHULSKI[2], A. NOWAKOWSKI[1]

[1]Faculty of Electronics, Telecommunications and Informatics,
Gdansk University of Technology, ul. Narutowicza 11/12, 80-952 Gdańsk, Poland

[2]Chemical Faculty, Gdansk University of Technology, ul. Narutowicza 11/12, 80-952 Gdańsk, Poland

The principle of operation, construction, and properties of gas sensors based on Nasicon and Lisicon are presented. These types of materials are known to exhibit high ionic conductivities and relatively high chemical stabilities at elevated temperatures. Electrocatalytic sensors have been prepared using ceramic technology. Their working principle is based on electric current acquisition, when a voltage ramp is applied to the sensor. The current–voltage plot has a unique shape, depending on the surrounding gas and its concentration. Measurements conducted in mixtures of nitrogen dioxide, sulphur dioxide, and synthetic air are presented.

Key words: *solid-state electrolyte; gas sensor; Nasicon; Lisicon*

1. Introduction

In recent years, solid-state ion conducting materials, also known as superionic or fast ion conductors, have been intensively developed. These materials exhibit relatively high ionic conductivities at elevated temperatures, resulting from high concentration and mobility of ion charge carriers. Such conductors are characterized by the crystallographic structure, in which mobile ions can be delocalised over a number of free interstices in an immobile sublattice. Solid-state electrolytes exhibit potential for applications in a variety of solid-state electrochemical devices such as sensors, fuel cells, membranes, and pumps [1].

With increasing environmental protection awareness and due to many advantages, such as low cost, small size and the ability of operating on-line or under continuous deleterious conditions, special attention has been paid to solid-state gas sensors [2–4].

[*]Corresponding author, e-mail: gregor@biomed.eti.pg.gda.pl

There are several types of solid-state gas sensors, based on a variety of principles and materials [5–7]. Solid state electrochemical sensors have become very popular, in which chemical species reacting at an electronic conductor–ionic conductor interface exchange electric charges, resulting in an electric signal. The output of the electrochemical sensors is directly related to the concentration or partial pressure of gaseous species. Depending on whether the output is an electromotive force or an electrical current, the electrochemical gas sensors can be classified as potentiometric or amperometric. Lack of selectivity, however, is sometimes a shortcoming of such sensors. It seems that an improvement in selectivity can be obtained using electrocatalytic sensors.

Electrocatalytic sensors belong to a new and particularly interesting group of electrochemical gas sensors which employ cyclic voltammetry techniques to solid electrolytes [8–10]. Cyclic voltammetry is a method widely used in liquid electrochemistry for determining concentrations of chemical species. The method is based on the oxidation and reduction of chemical species on electrodes polarised using a linearly varying voltage. Gas concentrations can be determined using information from electrokinetic reactions occurring in a sensor. In the presence of the applied voltage, gases react on the surface of the electrodes, influencing the current flowing through the sensor. This results in a unique voltammetric plot for different types and concentrations of gases. Apart from other features, the current-voltage response of the sensor potentially allows a couple of gases to be detected simultaneously [10].

The most widely used solid-state electrolyte is yttria-stabilized zirconia (YSZ), an oxygen ion conductor. A potentiometric oxygen sensor based on YSZ is used for combustion control in all modern automotive engines. Other very popular solid electrolytes used in sensors are Nasicon and Lisicon, which have mobile sodium and lithium cations, respectively. They are used mostly in potentiometric sensors [11, 12]. In this work, a study of electrocatalytic gas sensors employing Nasicon and Lisicon is presented. The properties of the developed sensors, exposed to mixtures of nitrogen dioxide, sulphur dioxide, and synthetic air are investigated.

2. Experimental

Nasicon powder (with the chemical formula of $Na_{2,8}Zr_2Si_{1,8}P_{1,2}O_{12}$) was prepared by the conventional solid-state ball milling method [13]. A mixture of chemically pure $NaHCO_3$, ZrO_2, SiO_2, and $NH_4PO_4{\cdot}3H_2O$ was milled several times, and then calcinated at 900 °C and fired at 1200 °C to finalize synthesis. Lisicon (with a chemical formula of $Li_{14}Zn(GeO_4)_4$) powders were prepared by the conventional solid-state reaction [14]. Stoichiometric quantities of Li_2CO_3, GeO_2, and ZnO were thoroughly milled and then calcinated for 2 hours at 700 °C in platinum boats. The products were reground and fired again for 1 hour at 1100 °C to complete the reaction. White, fine-grained powders were obtained in both cases.

The structure of the sensor made in this way is shown in Fig. 1. Pellets in the form of discs 12 mm in diameter and 1 mm thick were prepared by isostatic pressing and sintering. Electrodes were made by coating opposite pellet faces with gold paste (ESL 8880) for the Lisicon-based sensor and with platinum paste (ESL 5542) for the Nasicon-based sensor.

Fig. 1. Structure of the sensor

Measurements were conducted in mixtures of high-purity gases: nitrogen dioxide, sulphur dioxide and synthetic air with controlled concentrations. A precision mass flow controller (Tylan) was used to obtain gas mixture compositions. A constant gas flow of 100 sccm was maintained. The measuring stand consisted of a tube furnace, impedance analyser SI 1260, electrochemical interface SI 1287, and a PC computer with suitable software for system control and data acquisition. The measurements were performed in the temperature range 200–500 °C. While a linearly changing voltage of symmetrical triangular shape (ranging from 5 V to –5 V) was applied to the sensor, its current response was recorded. The voltage sweep rate was adjusted from 20 to 50 mV/s. Impedance measurements were conducted in the frequency range 100 mHz–1 MHz, with an excitation amplitude of 20 mV.

3. Results and discussion

The electrical conductivity of the prepared sensors was determined by means of ac admittance spectroscopy. In the measured frequency range, a well-resolved semicircular arc appears in the Nyquist plot. This arc is attributed to the bulk properties of the electrolyte. On the basis of this plot, the resistive component of total impedance was established and used to derive conductivity as a function of temperature. Typical Arrhenius plots for both electrolytes are shown in Figure 2. The conductivity of Nasicon is higher than that reported for Lisicon, which makes Nasicon-based sensors very promising for operation at lower temperatures. Activation energies of 0.19 eV for Nasicon and 0.4 eV for Lisicon were determined.

The performance of Nasicon and Lisicon electrocatalytic sensors exposed to mixtures of nitrogen dioxide of various concentrations and synthetic air was investigated at 300 °C. In the case of the Nasicon sensor, current-voltage plots (Fig. 3) show two relatively steep peaks near ±2.3 V. In the case of Lisicon (Fig. 4), two sets of rather broad peaks are observed near ±0.8 V and ±1.9 V. As shown in Figure 5, for both kinds of sensors an almost linear dependence of the peak current on NO_2 concentration is observed with the slopes about 24 μA/ppm and 35 μA/ppm for the Nasicon and

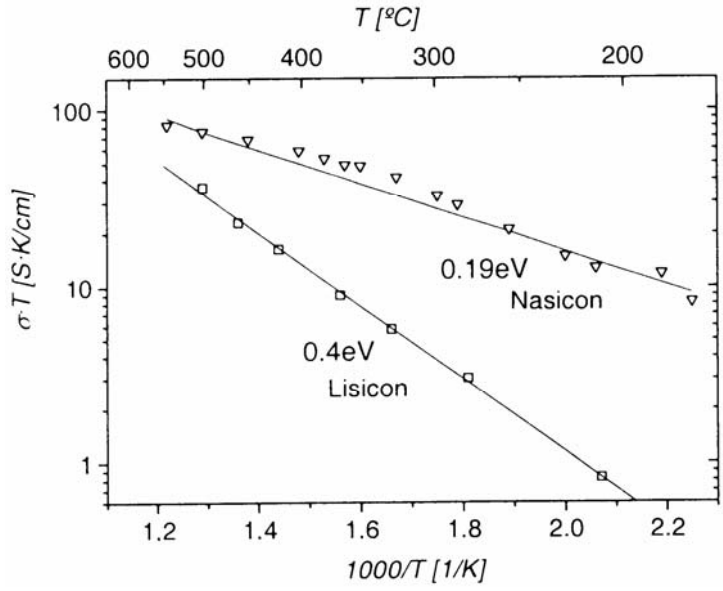

Fig. 2. Arrhenius plots of the sample's electrical conductivity

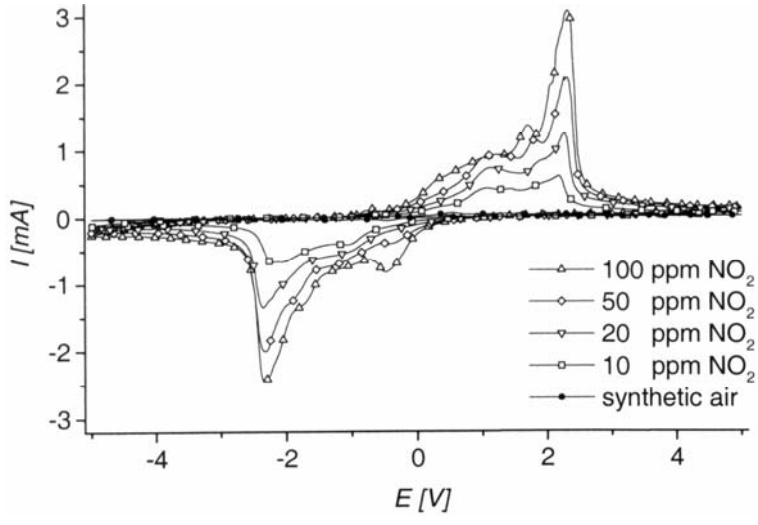

Fig. 3. Nasicon sensor response to different NO_2 concentrations (300 °C, 20 mV/s)

Lisicon sensors, respectively. At higher temperatures, the positions and shapes of both current–voltage plots remain almost the same (Fig. 6). The Nasicon sensor at those temperatures has a much higher nitrogen dioxide sensitivity due to low values of current measured in synthetic air. Lisicon and Nasicon sensors do not respond to NO_2 at temperatures higher than 500 °C and 600 °C, respectively. Therefore, they can be

used for multi-gas detection when their temperature of operation is altered during detection. Both sensors respond similarly to sulphur dioxide (Fig. 7). In this case, however, a higher sensitivity is observed for the Lisicon electrolyte.

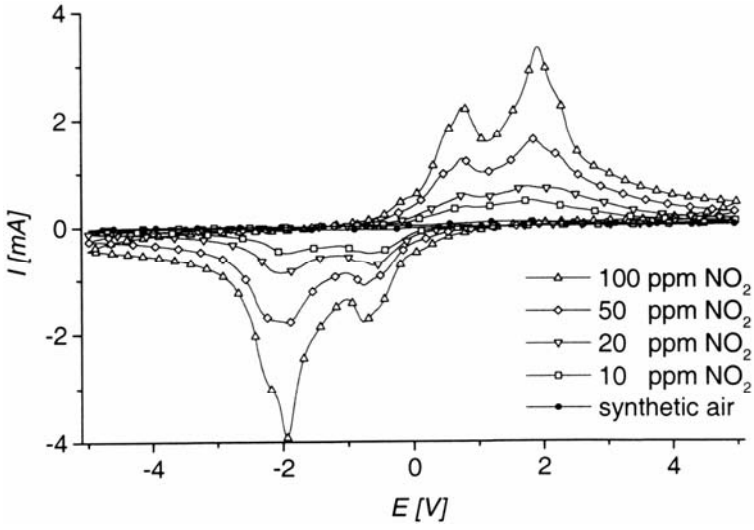

Fig. 4. Lisicon sensor response to different NO_2 concentrations (300 °C, 20 mV/s)

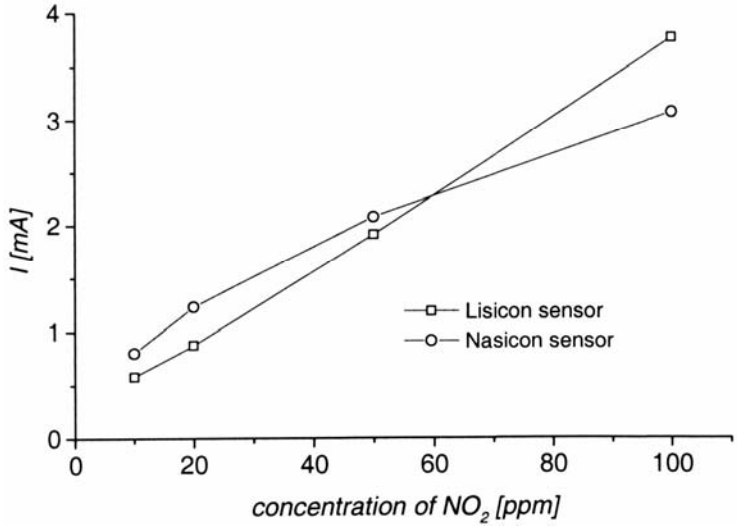

Fig. 5. Maximum current value of the NO_2 peak (300 °C, 20 mV/s)

In the case of a solid electrolyte with mobile Li^+ ions and gases used in the experiment, the following chemical reactions can be responsible for the peaks occurring on the current–voltage plots [15]:

$$Li^+ + e^- + NO_2(g) + 1/2O_2(g) \longleftrightarrow LiNO_3(s) \quad (1)$$

$$Li^+ + e^- + NO_2(g) \longleftrightarrow LiNO_2(s) \quad (2)$$

$$2Li^+ + 2e^- + SO_2(g) + 1/2O_2(g) \longleftrightarrow Li_2SO_3(s) \quad (3)$$

$$2Li^+ + 2e^- + SO_2(g) + O_2(g) \longleftrightarrow Li_2SO_4(s) \quad (4)$$

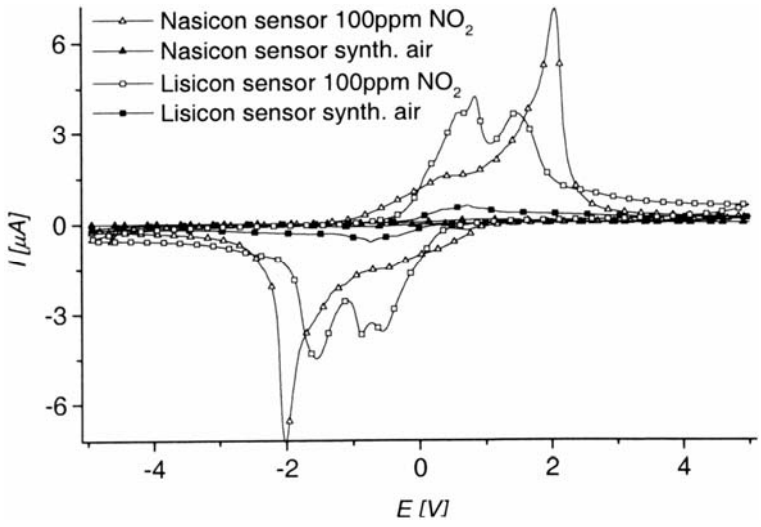

Fig. 6. Sensor response to NO_2 at 400 °C (50 mV/s)

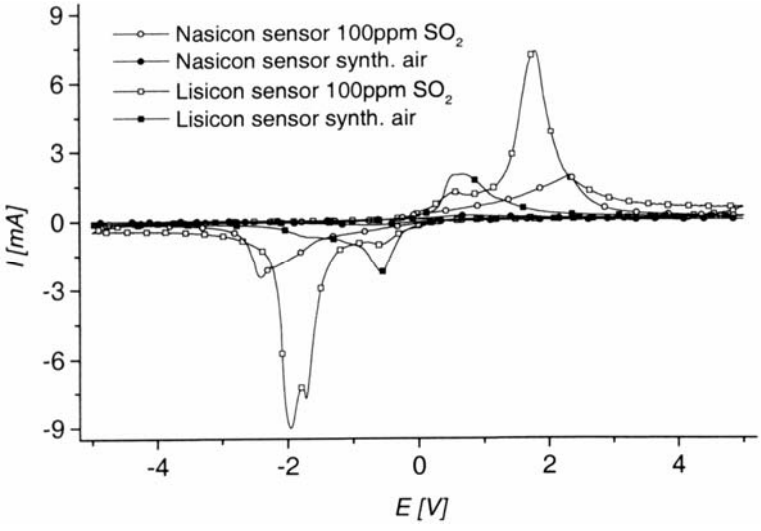

Fig. 7. Sensor response to SO_2 at 500 °C (50 mV/s)

and the following ones in the case of a solid electrolyte with mobile Na^+ ions [16]:

$$Na^+ + e^- + NO_2(g) + 1/2O_2(g) \longleftrightarrow NaNO_3(s) \tag{5}$$

$$Na^+ + e^- + NO_2(g) \longleftrightarrow NaNO_2(s) \tag{6}$$

$$2Na^+ + 2e^- + SO_2(g) + 1/2O_2(g) \longleftrightarrow Na_2SO_3(s) \tag{7}$$

$$2Na^+ + 2e^- + SO_2(g) + O_2(g) \longleftrightarrow Na_2SO_4(s) \tag{8}$$

These reactions are very similar but their kinetics might be different. Therefore, the peaks in the current–voltage plots are different for Nasicon and Lisicon.

It is interesting to note that the peak current of the Lisicon sensor is larger than that for the Nasicon-based sensor, even though the conductivity of Lisicon is lower than that of Nasicon. Moreover, gold was used as an electrode material in the case of the Lisicon-based sensor, which is known to have a lower catalytic activity than platinum (used in the Nasicon-based sensor). Therefore, it can be inferred that the larger peak current in the case of the Lisicon sensor is related to lithium ion reactivity.

4. Conclusions

In this paper, the results of cyclic voltammetry for electrocatalytic gas sensors employing solid electrolytes that conduct lithium or sodium ions are presented. It was shown that both investigated sensors could be used for detecting NO_2 and SO_2. The current-voltage response depends in a unique way on the type of gas and its concentration exposed to the sensor. Nasicon and Lisicon respond in a similar way, confirming that they have a similar working principle. The number, positions, and heights of the peaks, however, are different due to the occurrence of different chemical reactions at the sensor electrodes. Sensors can be used for multi-gas detection if their temperature of operation is altered.

Acknowledgements

This work was partially supported by the Polish State Committee for Scientific Research (KBN), grant No. 8T10C 01221.

References

[1] JAKUBOWSKI W., *Przewodniki superjonowe – właściwości fizyczne i zastosowania*, WNT, Warszawa, 1988.
[2] YAMAZOE N., MIURA N., Sensors and Actuators B, 20 (1994), 95.
[3] LEE D.-D., LEE D.-S., IEEE Sensor J., 1 (2001), 214.
[4] JASINSKI P., NOWAKOWSKI A., Biocybernetics Biomed. Eng., 19 (1999), 49.

[5] MADOU M.J., MORRISON S.R., *Chemical Sensing with Solid State Devices*, Academic Press, New York, 1989.
[6] WEPPNER W., Solid State Ionics, 53–56 (1992), 29.
[7] MOSELEY P. T., Measurement Sci. Technol., 8 (1997), 223.
[8] SHOEMAKER E.L., VOGT M.C., DUDEK F.J., Solid State Ionics, 92 (1996), 285.
[9] JASINSKI P., NOWAKOWSKI A., WEPPNER W., Sensor Mater., 12 (2000), 89.
[10] JASINSKI P., NOWAKOWSKI A., Ionics, 6 (2000), 230.
[11] KIDA T., MIYACHI Y., SHIMANOE K., YAMAZOE N., Sensors and Actuators B, 80 (2001), 28.
[12] MIN B.-K., CHOI S.-D., Sensors and Actuators B, 93 (2003), 209.
[13] QUON D.H.H., WHEAT T.A., NESBITT W., Mater. Res. Bull., 15 (1980), 1533.
[14] HONG H.Y.-P., Mater. Res. Bull., 13 (1978), 117.
[15] JASINSKI G., JASINSKI P., CHACHULSKI B., NOWAKOWSKI A., J. Europ. Ceramic Soc., 25 (2005), 2969.
[16] JASINSKI P., JASINSKI G., CHACHULSKI B., NOWAKOWSKI A., Proc. SPIE, 5124 (2003), 338.

Received 10 December 2004
Revised 25 January 2005

Materials Science-Poland, Vol. 24, No. 1, 2006

Solid-state electrochemical gas sensors

P. JASIŃSKI*

Department of Biomedical Engineering, Gdańsk University of Technology,
ul. Narutowicza 11/12, 80-952 Gdańsk, Poland

Various types of solid-state electrochemical gas sensors are presented. The sensing mechanism and examples of potentiometric, amperometric and electrocatalytic sensors are described. The possibility of multi-gas detection in the case of amperometric and electrocatalytic sensors is characterized. The principle of operation of the wide-band oxygen sensor, combining the potentiometric and amperometric modes, is presented.

Key words: *electrochemical gas sensor; solid electrolyte; air monitoring*

1. Introduction

A lot of recent work focuses on the development of solid-state gas sensors [1]. Especially interesting are electrochemical sensors, because they can be compact, robust, and cost effective in large-scale production. Solid electrolytes are key components of electrochemical gas sensors. They usually operate at elevated temperatures because most solid electrolytes have low conductivity at room temperature. A higher temperature of operation is an advantage, because electrode reactions proceed much faster and the sensor can work in demanding environments (e.g. exhaust gases). Depending on the mode of operation, electrochemical sensors are divided into potentiometric, amperometric and electrocatalytic ones. In the potentiometric mode, the measured signal is an electromotive force, while in the amperometric mode an electric current is recorded. In the case of electrocatalytic sensors, the current–voltage plot should be analysed.

2. Potentiometric sensors

Galvanic cells consisting of a solid electrolyte and two electronically conducting electrodes, reversible against mobile or immobile ions of the electrolyte, are used for potentiometric measurements. The electrodes are often called the reference electrode

*E-mail: pijas@eti.pg.gda.pl

(R) and working (sensing) electrode (W). Chemical potentials are formed at the electrode–electrolyte interfaces due to equilibria of electrochemical reactions. Namely, chemical potentials are created at the electrolyte-reference electrode interface and at the electrolyte-sensing electrode interface, where an equilibrium with the ambient gas is established. The gradient of chemical potential across the electrolyte results in an electrical potential drop, which can be measured as an electromotive force (EMF) of the galvanic cell. The EMF is related to the gas partial pressure through the Nernst equation:

$$\mathrm{EMF} = E_0 + \frac{RT}{nF} \ln \frac{p_w}{p^\circ} \tag{1}$$

where, E_0 is the EMF at a standard pressure of 1 bar, R – the gas constant, F – the Faraday constant, n – the number of electrons involved in the electrochemical reaction of the gas molecule, T – the absolute temperature, p_w is the gas partial pressure at the working electrode and p° is the standard pressure (1 bar).

The essential requirement for a reference electrode is its independence of the investigated gas. Usually, the chemical potential at the reference electrode–electrolyte interface is fixed by an electrochemically reversible reference gas or a solid solution. In the former case, the sensor consists of two gas chambers separated by an electrolyte. One chamber is filled or exposed to a reference gas, while the other is exposed to the gas whose concentration is to be determined [2]. In the latter case, the solid solution which can electrochemically equilibrate with the electrolyte, is in contact with the electrolyte. Any reaction with the surrounding gas is not acceptable, because the reaction products might influence the chemical potential. Therefore, the reference electrode is often sealed [3]. Sealing is usually a difficult technological process, because of different temperature expansion coefficients of the sealant, electrolyte and reference electrodes, different sintering temperatures of sensor components, and possible high reactivity of the reference electrode.

The best-known potentiometric sensor is the Lambda sensor, used in stoichiometric-burn engines to control the air-fuel ratio. The classical construction of the Lambda sensor is presented in Figure 1 [4]. It consists of platinum electrodes and a thimble-shaped oxygen-ion electrolyte which is typically made of doped zirconium oxide. The interior of the thimble is exposed to atmospheric air, while the outside to the exhaust gas. Oxygen molecules equilibrate at the interface of the electrolyte and platinum electrode, in accordance with the following electrochemical reaction:

$$\mathrm{O_2(gas)} + 4\mathrm{e^-(electrode)} \rightarrow 2\mathrm{O^{2-}(electrolyte)} \tag{2}$$

When the air-to-fuel mixture is rich, the EMF of the sensor is about 0.9 V, while in the lean mixture about 0.1 V is observed (Fig. 2). At the stoichiometric point, when an air-to-fuel mass ratio of 14.7:1 is reached, the EMF is 0.45 V. The Lambda sensor is suitable for controlling the air-fuel mixture at the stoichiometric point, while it is

unsuitable for determining the air-to-fuel ratio in lean or rich regimes. Therefore, other types of sensors (e.g., wide-band oxygen sensor) are used to control lean-burn or rich-burn engines.

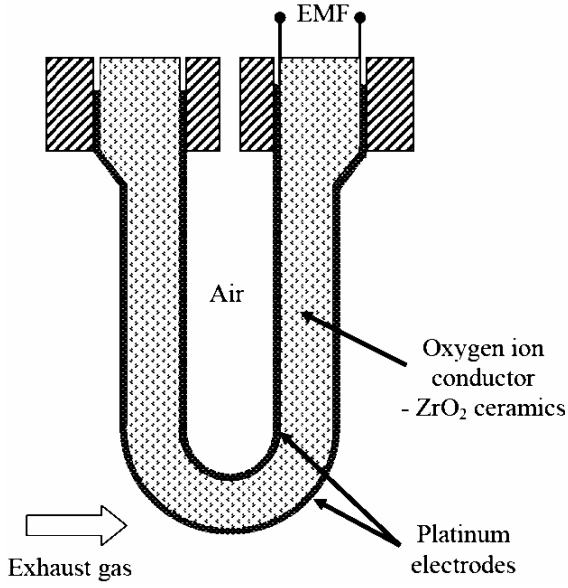

Fig. 1. Simplified schematic diagram of an unheated thimble-type oxygen sensor (reprinted from [4] with the permission from Elsevier)

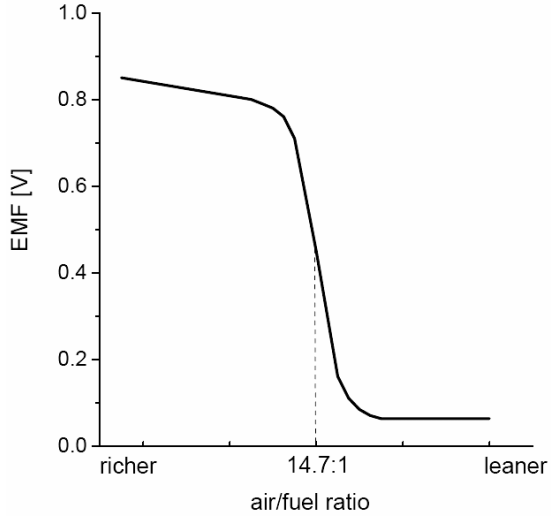

Fig. 2. Dependence of an air-to-fuel mixture on EMF of the sensor

An example of a carbon dioxide sensor with a sealed solid reference electrode is a cell with its reference electrode constructed of Na_xCoO_2, Na-β alumina electrolyte,

and Na_2CO_3 sensing electrode [5]. In this case, however, EMF of the sensor depends on both CO_2 and O_2 partial pressures. This is characteristic of a sensor with a sealed reference electrode and is caused by the fact that both carbon dioxide and oxygen influence the chemical potential of the sensing electrode. In contrast to sensors with sealed reference electrodes, this sensor can be insensitive to oxygen partial pressure when a proper material is used for the unsealed reference electrode. Such a sensor is often called a sensor with an open reference electrode. An example of a carbon dioxide sensor with an open reference electrode is a cell with a reference electrode constructed from a mixture of $Na_2Ti_6O_{13}$ and $Na_2Ti_3O_7$, an Na-β'' alumina electrolyte, and Na_2CO_3 sensing electrode [6]. Such a sensor is only sensitive to carbon dioxide because changes in oxygen partial pressure affect the chemical potential of the sensing and reference electrodes in the same way. Therefore, variations in oxygen concentration do not influence the EMF of the sensor. In contrast, variations in carbon dioxide concentration affect only the chemical potential of the sensing electrode, because of the high chemical stability of the reference electrode material towards carbon dioxide [7].

3. Amperometric sensors

Amperometric sensors, in contrast to potentiometric ones, feature a linear dependence of the electric signal on gas concentration, small temperature sensitivity, and lack of any reference electrode. The later significantly simplifies sensor construction. Due to their detection range, sensitivity and high temperature operation, amperometric sensors are widely used in controlling the operation of lean-burn engines [8]. A typical structure of an amperometric oxygen sensor with a hole as the diffusion barrier is presented in Figure 3. When external voltage is applied across the galvanic cell, the following electrochemical reaction occurs at the cathode (negative terminal):

$$O_2(\text{gas}) + 4e^-(\text{electrode}) \longrightarrow 2O^{2-}(\text{electrolyte}) \tag{3}$$

Generated oxygen ions move across the electrolyte to the anode (positive terminal), where they recombine to give oxygen molecules in an ambient gas:

$$2O^{2-}(\text{electrolyte}) \longrightarrow O_2(\text{gas}) + 4e^-(\text{electrode}) \tag{4}$$

In other words, oxygen molecules reduce to oxygen ions at the cathode, and then are transported across the electrolyte to the anode, where their re-oxidation to oxygen molecule occurs. The limiting current is related to geometrical parameters of the diffusion barrier and oxygen concentration, as defined by Fick's first law of diffusion, the ideal gas equation, and Faraday's law [9]:

$$I_{\text{lim}} = -\frac{nFD_{O_2}AP}{RTL}\ln(1 - x_{O_2}) \tag{5}$$

where I_{lim} is the limiting current, n is the number of electrons involved in the reaction, F is the Faraday constant, D_{O_2} is the diffusion coefficient of gaseous O_2, A is the area of the diffusion hole, P is barometric pressure, R is the gas constant, T is the operating temperature, L – the length of the diffusion hole, and x_{O_2} – the oxygen mole fraction. For small values of oxygen mole fraction (below 10% [10]), the logarithm becomes linear and I_{lim} can be approximated by:

$$I_{\text{lim}} = -\frac{nFD_{O_2}Ac_{O_2}}{L} \tag{6}$$

where c_{O_2} is the oxygen concentration.

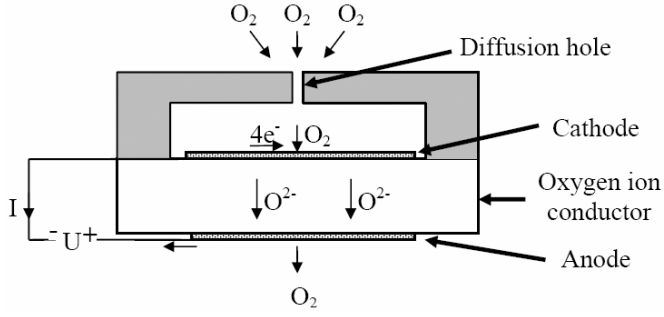

Fig. 3. Design and sensing mechanism of an amperometric oxygen sensor with a hole as the diffusion barrier

In general, the principle of operation of the solid-state amperometric gas sensor is very similar to the polarographic method known from liquid electrochemistry. In this case, however, the diffusion barrier is not applied, because diffusion in liquids proceeds much slower than in gases. For example, the diffusion coefficient of oxygen in water at 25 °C is 2.4×10^{-5} cm^2/s, while in nitrogen at 20 °C it is 0.16 cm^2/s. At 700 °C, the diffusion coefficient of oxygen in nitrogen reaches 1.5 cm^2/s. Therefore, in order to obtain similar limiting currents, the electrode area of a solid state amperometric sensor should be several orders of magnitude smaller than that used in liquid polarography. This demand cannot be fulfilled, and the diffusion barrier must be introduced in order to obtain limiting currents [11].

The determination of oxygen requires the application of an oxygen ion conducting electrolyte, since it is necessary to transport reduced oxygen across the electrolyte. The same mechanism may be used for determining other gases. The number of electrolytes conducting different kinds of ions is limited, however, which restricts the number of determined gases. Nevertheless, some other gases can be detected using an

indirect amperometric mechanism, based on electrodissociation or chemical oxidation/reduction reactions.

The electrodissociation of a gas molecule (e.g. CO_2 or H_2O) at the cathode electrode may occur when a sufficiently high voltage is applied to the sensor. The electrodissociation voltage for each reaction at a given temperature can be determined from Gibbs' free energy of reaction:

$$E_D = \frac{\Delta G}{nF} \tag{7}$$

It is known that water vapour electrodissociates at voltages higher than 1.2 V at 800 °C [9, 12]:

$$H_2O(\text{gas}) + 2e^-(\text{electrode}) \longrightarrow H_2(\text{gas}) + O^{2-}(\text{electrolyte}) \tag{8}$$

while carbon dioxide at the voltages higher than 1.6 V [9, 12]:

$$CO_2(\text{gas}) + 2e^-(\text{electrode}) \longrightarrow CO(\text{gas}) + O^{2-}(\text{electrolyte}) \tag{9}$$

This opens a possibility for sequential detection of few gases using the same sensor structure, by periodically varying the applied voltage.

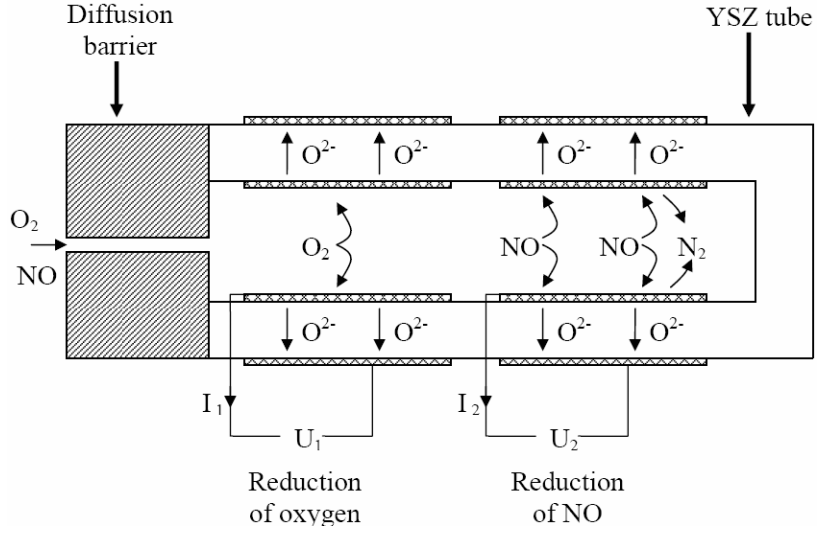

Fig. 4. Design and sensing mechanism of an amperometric sensor for simultaneous determination of nitrogen oxide and oxygen (reprinted from [13] with the permission from Elsevier)

When the sensor structure is modified, the amperometric sensing mechanism can be employed not only for sequential, but also for simultaneous measurements of multi-gas mixtures. In this case, the sensor structure is supplemented with an additional pair of electrodes. Various gases after diffusion through the barrier are conse-

quently electrodissociated at the electrodes polarized with selected voltages. This principle of operation was used in a sensor design for the simultaneous determination of nitrogen oxide and oxygen (Fig. 4) [10, 13, 14]. The voltage of 300 mV was used for the reduction and measurement of oxygen at the first pair of electrodes, while 550 mV for the reduction and measurement of nitrogen monoxide at the second pair of electrodes. A similar sensor configuration was used for the simultaneous determination of hydrocarbons and oxygen [15, 16].

4. Advanced sensor design

Recently, oxygen sensors combining potentiometric and amperometric modes have been developed for automotive applications. The so-called wide-band oxygen sensor and universal air-to-fuel ratio exhaust gas oxygen (UEGO) sensors are used in engines operating in the lean regime (air-to-fuel ratio (20–25):1)) or in special conditions (e.g., to obtain the maximum power of a gasoline engine, an air-to-fuel ratio of 12.6:1 is necessary) [17]. A schematic diagram of the Bosch LSU 4 version of the UEGO sensor is presented in Figure 5 [8]. The sensor structure, which is based on doped zirconium oxide ceramics, consists of a Lambda sensor and oxygen pump. One side of

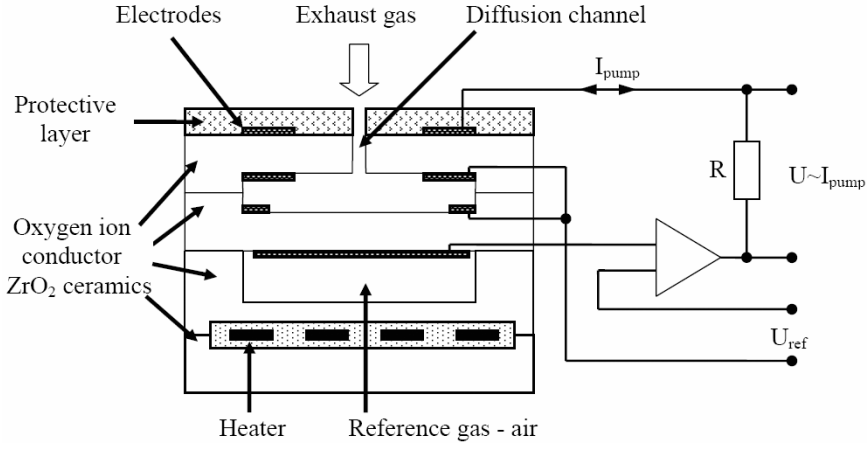

Fig. 5. Schematic diagram of Bosch LSU 4 wide-band oxygen sensor (reprinted from [8] with permission from Elsevier)

the oxygen pump is exposed to the exhaust gas, while one side of the Lambda sensor is exposed to atmospheric air. The other electrode of the oxygen pump and Lambda sensor are buried in the diffusion gap, exposed to exhaust gas through the diffusion barrier. The electrodes of both structures are wired in such a way that the oxygen level in the diffusion gap is balanced by the current flowing through the oxygen pump. The measurement of this current allows a precise determination of the air-to-fuel ratio from 10:1 to pure

air. A built-in heater maintains a constant sensor temperature of about 750 °C, which can be obtained from a cold start within 15 s.

5. Electrocatalytic sensors

A deviation of kinetic processes from thermodynamic equilibrium due to voltage or current excitation is used in electrocatalytic gas sensors. This type of sensor may potentially provide more information than conventional potentiometric or amperometric electrochemical sensors. Its principle of operation is based on the excitation of a galvanic cell with a periodic signal, whose amplitude is so large that the sensor responds non-linearly. Usually, a triangular voltage is used as the excitation signal, while an electric current is recorded. The positions and heights of peaks in the current–voltage plot obtained in this way depend on the gas type and concentration. The working principle is similar to cyclic voltammetry, which is used in liquid electrochemistry for, e.g., detecting traces of heavy metals in water [18].

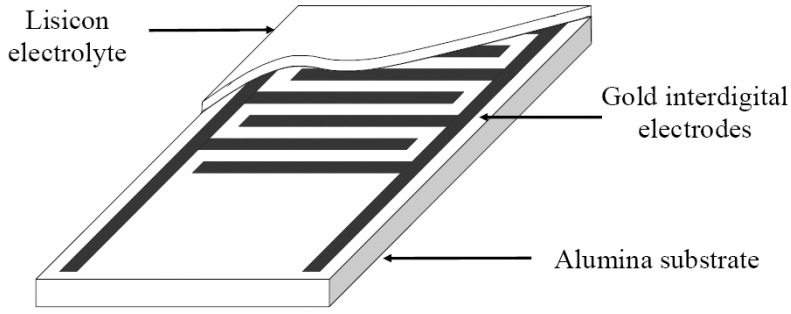

Fig. 6. Structure of the electrocatalytic gas sensor
based on Lisicon solid electrolyte [25]

The concept of the electrocatalytic sensor has been investigated using various solid electrolytes [19–24] and is based on the growth and decomposition of the gas-sensitive layer and the reactivity of this layer with the surrounding gas. Figure 6 presents the structure of an electrocatalytic sensor based on Lisicon solid electrolyte [25]. When a voltage ramp is applied to the sensor, Li^+ ions in the electrolyte migrate away from the positively polarized electrode towards the negative electrode. This activates the formation of the gas-sensitive layer at the negatively polarized electrode, while at the positively polarized electrode the decomposition of the existing gas sensitive layer proceeds correspondingly. When the voltage is reversed, the formation and decomposition occur at the opposite electrodes.

Figure 7 shows the current–voltage plot of the sensor exposed to synthetic air, 100 ppm of NO_2 and 100 ppm of SO_2 at 450 °C [25]. The existence of nitrogen dioxide in air is manifested by “positive” and “negative” peaks at about ±2.2 V, while sulphur

dioxide at about ±4 V. The heights of these peaks depend on the toxic gas concentrations. It might be expected that there is an opportunity for the simultaneous determination of various gases. The current–voltage plot of the sensor, however, when is exposed to a mixture of NO_2 and SO_2 in air, shows only one pair of peaks. It is still possible to detect NO_2 and SO_2 in air when the temperature of the sensor is altered. It can be shown that above 500 °C the Lisicon sensor is insensitive to NO_2, while below 300 °C it is over two order of magnitude more sensitive to SO_2 than to NO_2.

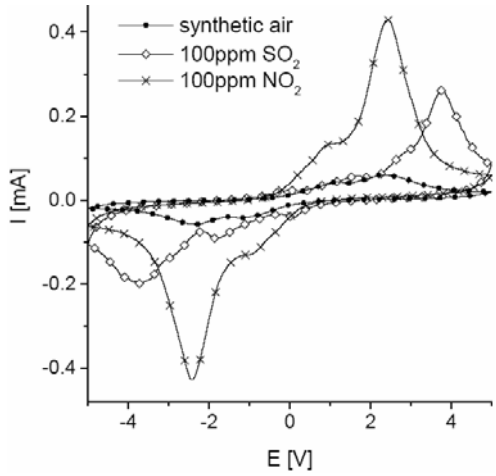

Fig. 7. Response of the Lisicon electrocatalytic gas sensor at 450 ºC [25]

6. Summary

An overview of electrochemical solid-state sensors was presented. Sensors were categorized and described based on their principle of operation. The overview covered potentiometric, amperometric and electrocatalytic sensors. A special attention was drawn to multi-gas detection and the design of the amperometric sensor for sequential and simultaneous multi-gas detection. The response of Lisicon electrocatalytic gas sensors was analysed. It was concluded that, at the current stage of the electrocatalytic sensor development, the current–voltage response must be analysed and the temperature of operation of the sensor must be altered in order to measure multi-gas mixtures.

References

[1] LEE D.-D., LEE D.-S., IEEE Sensors, 1 (2001), 214.
[2] YAMAZOE N., MIURA N., IEEE Trans. Compon. Pack. A, 18 (1995), 252.
[3] PARK C.O., AKBAR S.A., WEPPNER W., J. Mater. Sci., 38 (2003), 4639.
[4] GIBSON R.W., KUMAR R.V., FRAY D.J., Solid State Ionics, 121 (1999), 43.

[5] SCHETTLER H., LIU J., WEPPNER W., HUGGINS R.A., Appl. Phys., A57 (1993), 31.
[6] HOLZINGER M., MAIER J., SITTE W., Solid State Ionics, 86–88 (1996), 1055.
[7] HOLZINGER M., MAIER J., SITTE W., Solid State Ionics, 94 (1997), 217.
[8] IVERS-TIFFEE E., HARDTL K.H., MENESKLOU W., RIEGEL J., Electrochim. Acta, 47 (2001), 807.
[9] MASKELL W.C., PAGE J.A., Sens. Actuators, B 57 (1999), 99.
[10] SOMOV S. I., REINHARDT G., GUTH U., GOPEL W., Sens. Actuators, B 35–36 (1996), 409.
[11] DIETZ H., Solid State Ionics, 6 (1982), 175.
[12] LOGOTHETIS E.M., VISSER J.H., SOLTIS R.E., RIMAI L., Sens. Actuators, B 9 (1992), 183.
[13] SOMOV S.I., REINHARDT G., GUTH U., GOPEL W., Sens. Actuators, B 65 (2000), 68.
[14] SCHMIDT-ZHANG P., SANDOW K.-P., ADOLF F., GOPEL W., GUTH U., Sens. Actuators, B 70 (2000), 25.
[15] MAGORI E., REINHARDT G., FLEISCHER M., MAYER R., MEIXNER H., Sens. Actuators, B 95 (2003), 162.
[16] SOMOV S. I., GUTH U., Sens. Actuators, B 47 (1998), 131.
[17] RIEGEL J., NEUMANN H., WIEDENMANN H.-M., Solid State Ionics, 152–153 (2002), 783.
[18] BARD A.J., FAULKNER L.R., *Electrochemical Methods. Fundamentals and Applications*, Wiley, New York, 2001.
[19] LIU J., WEPPNER W., Appl. Phys., A 55 (1992), 250.
[20] SHOEMAKER E.L., VOGT M.C., DUDEK F.J., Solid State Ionics, (1996), 92, 285.
[21] SHOEMAKER E.L., VOGT M.C., DUDEK F.J., TURNER T., Sens. Actuators, B 42 (1997), 1.
[22] VOGT M.C., SHOEMAKE E.L., TURNER T., Sens. Actuators, B 36 (1996), 370.
[23] JASINSKI P., NOWAKOWSKI A., Ionics, 6 (2000), 230.
[24] JASINSKI P., NOWAKOWSKI A., WEPPNER W., Sensor Mater., 12 (2000), 89.
[25] JASIŃSKI G., JASIŃSKI P., NOWAKOWSKI A., CHACHULSKI B., Proc. 28th Internat. Conf. IMAPS -Poland Chapter 2004, Wrocław, 2004, p. 269.

Received 10 December 2004
Revised 11 April 2005

Materials Science-Poland, Vol. 24, No. 1, 2006

Application of Nasicon and YSZ for the construction of CO_2 and SO_x potentiometric gas sensors

P. PASIERB*

AGH University of Science and Technology, Faculty of Materials Science and Ceramics,
al. Mickiewicza 30, 30-059 Cracow, Poland

Solid-state potentiometric CO_2 and SO_x sensors were fabricated using Nasicon ($Na_3Zr_2Si_2PO_{12}$) or YSZ (ZrO_2 + 8 mole % of Y_2O_3) solid electrolytes, with fused carbonates or sulphates as sensing electrodes and $Na_2Ti_6O_{13}$–$Na_2Ti_3O_7$ two-phase systems or porous platinum as reference electrodes. A comparison of the performance and long-term stability of the prepared sensors was made. More stable behaviour of CO_2 sensors was observed for cells prepared from Nasicon while SO_x sensors with YSZ used as the solid electrolyte displayed a better performance. The sensing mechanism and long-term stability of the investigated cells was discussed in terms of the possible reactivity of solid electrolytes with the electrode materials and the formation and modification of "ionic-bridges" at the solid electrolyte–electrode interface.

Key words: *potentiometric gas sensor; CO_2; SO_x; Nasicon; YSZ; carbonate; sulphate*

1. Introduction

A typical potentiometric gas sensor consists of a solid electrolyte (YSZ, Nasicon, Na^+ β-alumina) as well as sensing and reference electrodes attached to both sides of the solid electrolyte. The simplicity of construction, low cost in large-scale production, compatibility with classical electronic devices, short response time, good selectivity, and known dependence of the measured signal on gas content (Nernstian behaviour) are the main advantages of such devices. The main difficulty in applying such sensors is signal instability during long-term use. Numerous efforts have been undertaken to develop systems exhibiting the most stable behaviour. Also, many papers have concerned theoretical aspects of the working mechanism of investigated cells. Various solid electrolytes and sensing and reference electrodes have been proposed and tested to a large extent [1–5].

*E-mail: ppasierb@uci.agh.edu.pl

The aim of this work was to compare the performance and working mechanisms of potentiometric gas sensors prepared using either a Na^+ ion conductor (Nasicon) or O^{2-} ion conductor (ZrO_2:Y_2O_3) as the solid electrolyte. A comparison was made for sensors designed for detecting CO_2 and SO_x.

2. Materials and measurements

Powders of YSZ (ZrO_2 + 8 mole % of Y_2O_3, Tosoh Corp., Japan) and $Na_3Zr_2Si_2PO_{12}$ (Nasicon) prepared by the co-precipitation method [6] were used. Powders were formed in a pellet die (75 MPa), isostatically pressed (250 MPa), and sintered at 1673 K (5 h) in the case of ZrO_2 and at 1500 K (24 h) in case of Nasicon.

Li_2CO_3–$BaCO_3$ and Li_2SO_4–$CaSO_4$ (2:3 molar ratio) were used to form electrodes sensitive to CO_2 and SO_x, respectively. Porous platinum or $Na_2Ti_6O_{13}$–$Na_2Ti_3O_7$ mixtures were used in the construction of reference electrodes. $Na_2Ti_6O_{13}$–$Na_2Ti_3O_7$ materials were prepared by the solid-state reaction of TiO_2 (anatase, Cookson technology) with sodium carbonate (Sigma-Aldrich). Details are given elsewhere [7, 8].

The electromotive force (EMF) of the prepared cells was measured as a function of temperature (300–650 °C), CO_2 (10–1500 Pa) or SO_2 (0.1–10 Pa) partial pressures, and time. Details concerning the experimental setup are given elsewhere [7, 8].

Additionally, XRD (X-ray diffraction), DTA & TG (differential thermal analysis and thermogravimetry), SEM (scanning electron microscopy), EIS (electrochemical impedance spectroscopy), and MS (mass spectrometry) were used to assist the interpretation of the results.

3. Results and discussion

3.1. Sensing characteristics

The CO_2 sensor has the following electrochemical cell structure:

$$CO_2, O_2^{(1)}, Me \mid Li_2CO_3\text{-}BaCO_3 \mid SE \mid B(Na), Pt, O_2^{(2)}$$

where SE is a solid electrolyte ($Na_3Zr_2Si_2PO_{12}$ or YSZ), B(Na) denotes a $Na_2Ti_6O_{13}$ –$Na_2Ti_3O_7$ mixture (applied when Nasicon was used as SE), Me = Ag, Au, or Pt, and superscripts (1) and (2) denote sensing and reference electrodes, respectively.

SO_x sensors were prepared similarly as the CO_2 sensors. The following electrochemical cells were prepared:

$$SO_x, O_2^{(1)}, Me \mid Li_2SO_4\text{-}CaSO_4 \mid SE \mid B(Na), Pt, O_2^{(2)}$$

Figure 1 shows example dynamics at 748 K for a CO_2 sensor with Nasicon used as the solid electrolyte. Abrupt changes in carbon dioxide partial pressure (solid line,

right axis) cause changes in the electromotive force (EMF). In the case of SO_x sensors with a silver electrode (Me = Ag), no acceptable sensor characteristics were obtained. The observed EMF changes with changes in SO_x partial pressure were not reversible, probably due to silver corrosion by SO_x. The replacement of Ag by Au was also unsuccessful, and typical sensor characteristic were still not observed. Only the use of Pt at the sensing electrode led to stable sensor characteristics.

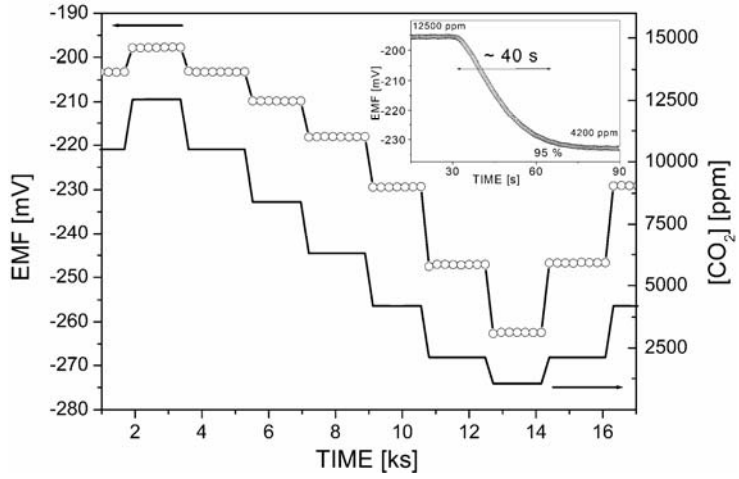

Fig. 1. Response of the carbon dioxide sensor with Nasicon as a solid electrolyte at T = 748 K. Stepwise changes in CO_2 partial pressure are shown as solid lines (right axis). The determination of the response time is shown in the inset

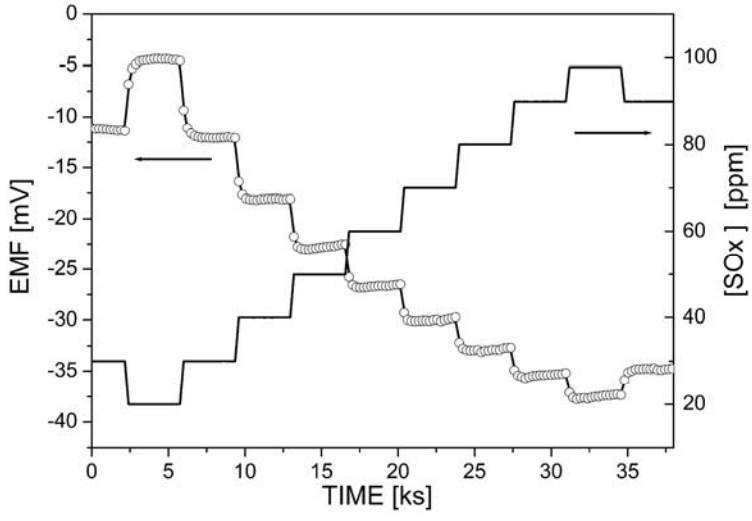

Fig. 2. Response of the sulphur oxide sensor with YSZ as the solid electrolyte at T = 873 K. Stepwise changes in SO_2 partial pressure are shown as solid lines (right axis)

Figure 2 shows the SO_x sensor dynamics measured at T = 873 K for the sensor prepared using YSZ as the solid electrolyte. As can be seen, the measured electromotive force follows the changes in SO_x partial pressure (solid line, right axis). The constructed prototype sensor exhibited a reversible signal in short time experiments. The response and recovery times of the CO_2 sensors ranged from 30 s to 60 s, depending on the gas flow rate (20–100 cm^3/min.), as shown in the inset of Figure 1. The response time of SO_x sensors was several minutes.

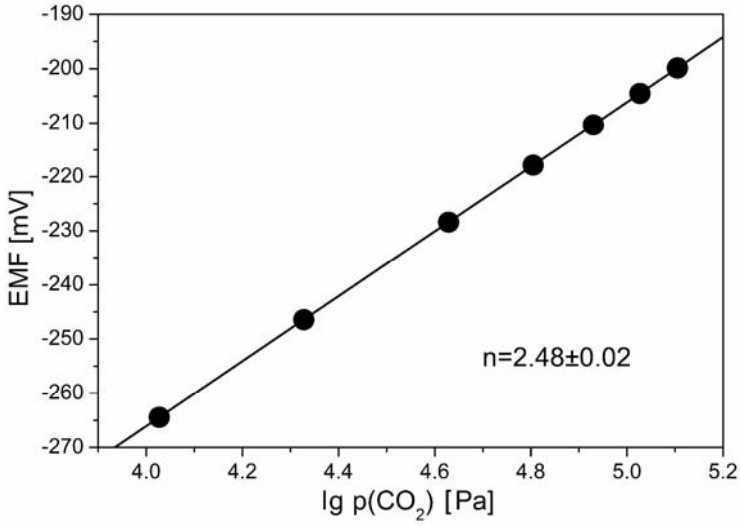

Fig. 3. Measured electromotive force EMF as a function of the logarithm of carbon dioxide partial pressure shown for the data from Fig. 1

The obtained results were fitted using the Nernst equation, as shown in Figure 3. The determined parameter n (corresponding to the number of electrons in the electrode reaction) was found to be between 2.2 and 2.8. The observed discrepancy of the parameter n from the theoretical value (n = 2) may be explained by the mixed conductivity of either sensing carbonates or electrolyte phases [7, 9]. In the case of SO_x sensors, the explanation of the observed non-integer n values must include the SO_2/SO_3 gas equilibrium [3]. Mass spectroscopy measurements confirmed that the Pt connection acts as a catalyst in the oxidation of SO_2 to SO_3 at the temperatures above 673 K. Above T = 723 K, a partial reduction of SO_3 to SO_2 may occur, thus affecting the measured EMF signal. The obtained results agreed well with thermodynamic predictions for a system of $SO_2 + O_2$.

3.2. Sensor long-term stability

CO_2 sensors with Nasicon as the solid electrolyte exhibited a stable behaviour over long time (above 6 months). Excellent long-term stability in this case may be

attributed to the formation of a liquid phase at the sensing electrode/solid electrolyte interface and well-defined ion transport [8]. On the other hand, a long-term drift of the sensing signal was observed for CO_2 sensors with stabilised zirconia as the solid electrolyte. Thermodynamic considerations as well as DTA, XRD, and SEM [8] analyses indicate that the observed instability may result from an irreversible chemical reaction between carbonate and stabilised ZrO_2 phases. EIS measurements showed that the uncontrolled reaction above $T = 723$ K between carbonate and YSZ leads to a continuous, substantial decrease of the electrical conductivity of the cell, as shown in Figure 4.

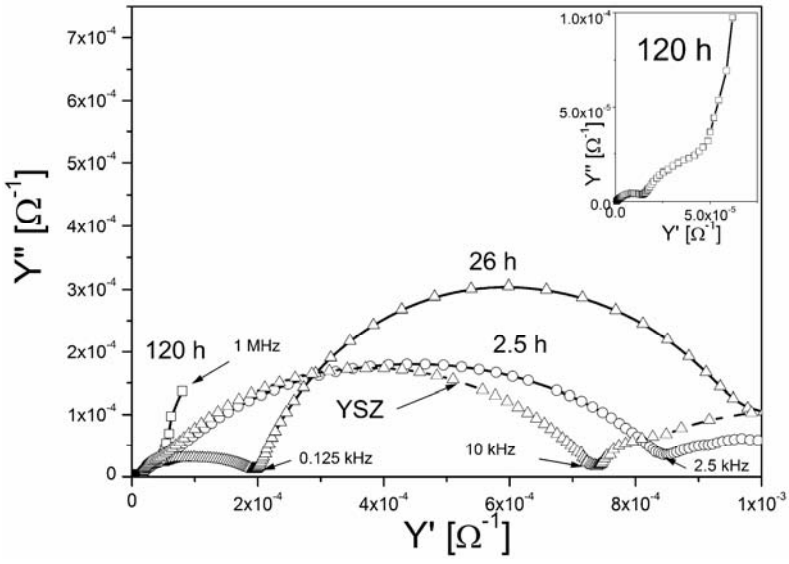

Fig. 4. Admittance diagrams for the $Li_2CO_3 + BaCO_3$|Au|YSZ|Pt cell after heating at 773 K for 2.5 h, 26 h and 120 h. The admittance diagram for a Pt|YSZ|Pt cell is shown for comparison

A drift of the electromotive force was also observed in the case of both SO_x sensors (Nasicon and YSZ based) during long-term experiments (carried out for several weeks). The observed drift cannot be explained by uncontrolled chemical reactions in the solid state alone, as is the case of YSZ-based CO_2 sensors. The thermodynamic analysis excluded the possibility of a reaction between the sulphate phase and the solid electrolyte. The lack of local equilibrium at the electrode/solid electrolyte interface may be the reason for the unstable behaviour of SO_x sensors.

4. Conclusions

Experimental results concerning potentiometric CO_2 and SO_x sensors have been described in this work. Most of the sensors exhibited a reproducible signal during

short-time experiments (below 24 h). The measured electromotive force (EMF) of the cells was found to be linear with the logarithms of CO_2 and SO_x concentration in the measured ranges of concentration (100–15000 ppm of CO_2 and 1–100 ppm of SO_x). These sensors exhibited quasi-Nernstian behaviour, with the n parameter having a non-integral value higher than the theoretical one ($n = 2$). The operating temperature range was 300–500 ºC and 500–650 ºC for CO_2 and SO_x sensors, respectively. The response time was found to be below 60 s and several minutes for CO_2 and SO_x, respectively. The most stable behaviour was observed in the case of the Nasicon-based CO_2 sensor working in the presence of a liquid phase at the electrode–solid electrolyte interface. In case of SO_x sensors, the lack of local equilibrium at the electrode/solid electrolyte interface may be responsible for unstable behaviour.

Acknowledgements

The financial support of Polish State Committee for Scientific Research (KBN), Project No. 7 T08A 030 21, is acknowledged.

References

[1] GAUTHIER M., CHAMBERLAND A., J. Electrochem. Soc., 124 (1977), 1579.
[2] MARUYAMA T., SAITO Y., MATSUMOTO Y., YANO Y. , Solid State Ionics, 17 (1985), 281.
[3] RÓG G., KOZŁOWSKA-RÓG A., ZAKUŁA K., BOGUSZ W., PYCIOR W., J. Appl. Electrochem., 21 (1991), 308.
[4] MIURA N., YAO S., SHIMIZU Y., YAMAZOE N., J. Electrochem. Soc., 139 (1992), 1384.
[5] HOLZINGER M., MAIER J., SITTE W., Solid State Ionics, 86–88 (1996), 1055.
[6] BOILOT J.P., SALANIE J.P., DESPLANCHES G., LE POTIER D., Mat. Res. Bull., 14 (1979), 1469.
[7] PASIERB P., KOMORNICKI S., GAJERSKI R., KOZIŃSKI S.AND RĘKAS M., Solid State Ionics, 157 (2003), 357.
[8] PASIERB P., KOMORNICKI S., KOZIŃSKI S., GAJERSKI R., RĘKAS M., Sensors Acuators, B101 (2004), 47.
[9] NÄFE H., Sensors Actuators, B21 (1994), 79.

Received 10 December 2004
Revised 31 January 2005

Materials Science-Poland, Vol. 24, No. 1, 2006

TiO_2:Au thin film electrodes for electrochemical solar cells

M. RADECKA*

Faculty of Material Science and Ceramics, AGH University of Science and Technology,
al. Mickiewicza 30, 30-059 Cracow, Poland

TiO_2 nanocermets are obtained by RF reactive co-sputtering from mosaic targets of Au:Ti or by sequential deposition from metallic Ti and Au targets. The influence of noble metal content on the microstructure of thin film nanocermets has been studied by means of optical, structural, and electrochemical measurements. Increased photocurrent responses have been observed over the visible range of the light spectrum. TiO_2 samples with a discontinuous Au film give significantly better photoresponses than those with Au in the bulk.

Key words: *photoelectrolysis; titanium dioxide; nanocermet*

1. Introduction

The photoelectrolysis of water, i.e water decomposition into hydrogen and oxygen as a result of the absorption of sunlight is considered to be the most important unconventional future energy source. This process is conducted in a photoelectrochemical cell (PEC) composed of an aqueous electrolyte and two electrodes [1]. At least one electrode, typically the anode, should be formed from a semiconducting material. Titanium dioxide, TiO_2, is one of the most suitable candidates for the photoanode material in the photoelectrochemical solar cell (PEC) due to its high resistance to corrosion, stability and a negative flat band potential. The band gap of TiO_2 is of the order of 3 eV, too high for the efficient absorption of the sunlight. Several methods providing higher sunlight conversion efficiency and improving the photo-response of TiO_2 have been proposed. These methods include: a) doping with aliovalent ions in order to produce an additional band within the band gap of TiO_2 [2], b) band gap self-regulation in solid solutions and photoelectrode sensitisation [3], c) incorporation of

*E-mail: radecka@uci.agh.edu.pl

noble metals [4–7], and d) coating with organic dyes [8]. All these methods rely on modifying the spectral dependence of the absorption coefficient of TiO_2 with the goal of matching the solar spectrum.

One of the most promising methods is the incorporation of noble metal nanoparticles (Au) into the TiO_2 dielectric matrix. Thus obtained nanocermets show an additional absorption feature due to the surface plasmon resonance (SPR) occurring over the visible range of the light spectrum. This phenomenon results from the excitation of collective oscillations of conduction electrons in the noble metal inclusions under the influence of electromagnetic radiation.

The purpose of this work was to study the performance of thin films of TiO_2:Au in photoelectrochemical systems.

2. Experimental

Sample preparation and characterization. Thin films of TiO_2:Au were deposited by RF reactive co-sputtering from Ti:Au mosaic targets and by the sputtering of Au onto the surface of TiO_2 (sequential deposition). NaCl, carbon foil, titanium foil and amorphous silica were used as the substrates. The film thickness varied from 20 to 200 nm. The sputtering conditions have been described in detail elsewhere [4–6].

The microstructure of the thin-film nanocermets was characterized by transmission electron microscopy (TEM), atomic force microscopy (AFM), and X-ray diffraction at grazing incidence (GID). X-ray photoelectron spectroscopy (XPS) was used with a multi-technique system of VSW Science Instruments. The binding energy shifts due to surface charging were corrected assuming the C 1s XPS peak is located at 285.0 eV.

Optical studies were carried out with the Perkin Elmer double beam spectrophotometer Lambda 19 over a wavelength range of 220–2500 nm.

Electrochemical measurements. Electrochemical measurements were performed in an experimental cell consisting of a photoanode, a working electrode, and a reference electrode (SCE) with a TRIAX 180 Jobin Yvon monochromator and a 450W Xe lamp as the light source. The electrodes were immersed in a buffer solution with pH = 8. The photocurrent was recorded with a Keithley 6517A electrometer. Bias voltages were supplied by a Hewlett-Packard 34401A power supply.

3. Results and discussion

According to the experimental evidence provided by GID and TEM, TiO_2 dielectric matrix is amorphous when nanocermets are obtained by co-sputtering. Crystallized gold nanoparticles are distributed within the bulk of TiO_2 [6, 7]. On the contrary, thin-film nanocermets prepared by sequential deposition consist of 200–300 nm thick TiO_2 covered by a thin overlayer of noble metal (Au, or Ti with Au) with the thick-

ness depending on the deposition time. AFM micrographs for TiO_2 covered with Au reveal that the overlayer is discontinuous. The morphology of a titanium dioxide film 200–300 nm thick depends on the substrate temperature [5, 9]. Films crystallized at an elevated temperature of 350 ºC give a significantly better photoresponse than those deposited at room temperature [5].

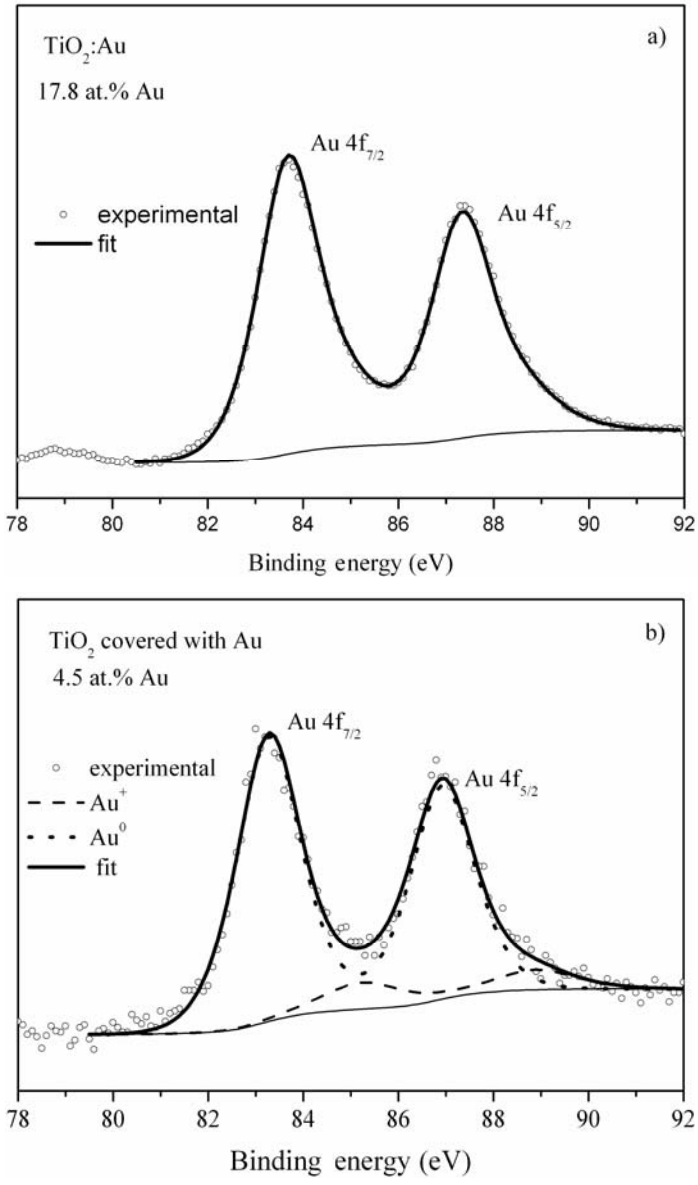

Fig. 1. XPS spectra of TiO_2 thin films with Au:
a) TiO_2:Au nanocermet; b) TiO_2 covered with a thin, discontinuous Au layer

X-ray photoelectron spectroscopy (XPS) has been used to study the oxidation states of Ti and Au. This is very important, especially in view of the fact that TiO_2:Au thin films are grown in the presence of oxygen. Figure 1 illustrates the XPS spectra for thin films of TiO_2 with Au. The incorporation of Au into TiO_2 (Fg. 1a) gives one double peak, attributed to Au $4f_{7/2}$ (83.5 eV) and Au $4f_{5/2}$ (87.4) at binding energies corresponding to Au^o [10]. This indicates that metallic gold is present as an inclusion. Figure 1b shows a Au 4f doublet measured in thin films of TiO_2 covered with gold. The Au 4f XPS peak could be resolved into two contributions. The highest energy components (85.2 eV) have been assigned to Au^+ [10].

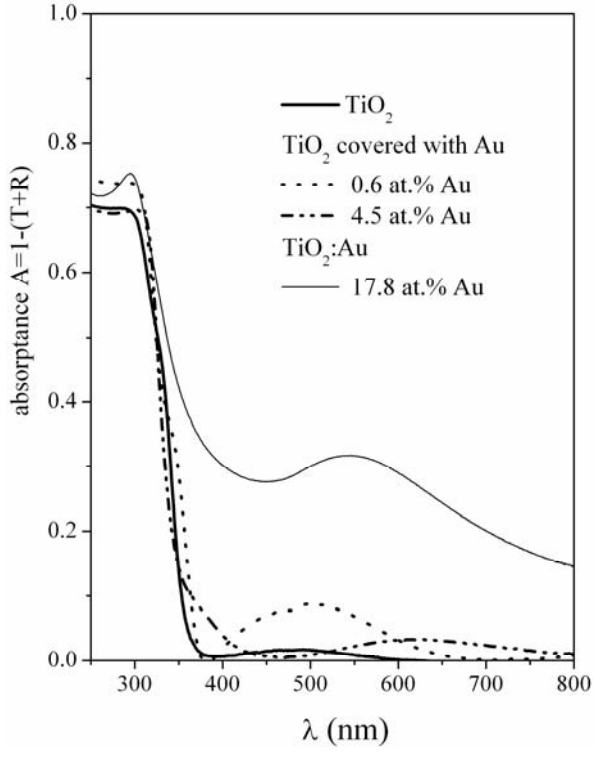

Fig. 2. Optical absorptance spectra for TiO_2:Au nanocermets and TiO_2 thin film covered with a discontinuous gold film

Absorption spectra, calculated from the measured transmittance $T(\lambda)$ and reflectance $R(\lambda)$ coefficients, are presented in Fig. 2. TiO_2 thin film nanocermets show, besides the fundamental absorption edge below 350 nm due to the band-to-band transition, an additional peak located in the visible range of the spectrum. This additional absorption feature results from surface plasmon resonance (SPR) and has been found to be correlated with the type, size, and distribution of noble metal inclusions [6, 7]. The SPR is located at λ = 500–600 nm for TiO_2:Au thin films obtained by co-sputtering. As shown in Figure 2, the SPR is shifted to a shorter wavelength λ = 500 nm when the

noble metal is deposited at the TiO_2 film surface, i.e. by the sequential sputtering of TiO_2 and Au (1 sec). A longer deposition time of TiO_2:Au (8 sec) results in some red shift of the absorption peak. This behaviour is similar to that observed for nanocermets with a bulk distribution of noble metal [5].

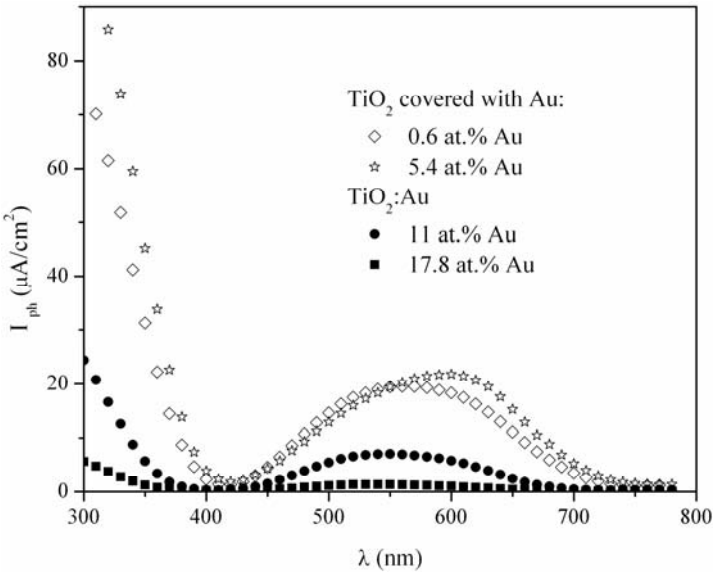

Fig. 3. Photocurrent densities for TiO_2:Au thin film nanocermets and TiO_2 covered with a discontinuous Au film

The effect of gold nanoparticles in the bulk of TiO_2 thin films and that of a discontinuous gold film covering the TiO_2 film surface on the spectral dependence of the photocurrent density in the PEC is presented in Figure 3. The photoresponse is high over the UV region due to the fundamental absorption edge of TiO_2. An additional, local maximum in the photocurrent appears over the visible range of the light spectrum, between 500 nm and 600 nm in the case of discontinuous thin films of gold on TiO_2. For nanocermets, a local maximum in the photocurrent appears at about 540 nm. This effect is related to the spectral dependence of optical absorption (Fig. 2). Samples covered with a discontinuous Au film, however, give a significantly better photoresponse than those with Au in the bulk. A correlation exists between the microstructure, optical properties, and photoresponse of the photoanodes based on TiO_2. As expected, gold distributed in the bulk of TiO_2 nanocermets modifies the spectral dependence of absorption in the vicinity of the fundamental absorption edge and at longer wavelengths. This means that the incorporation of gold into the TiO_2 lattice affects the electronic structure of TiO_2 and extends the fundamental absorption edge to longer wavelengths. As demonstrated in our previous work [2, 11], an enhanced recombination process of photoelectrons and holes may be correlated with the formation of this absorption "tail" in the band gap of TiO_2.

On the contrary, for TiO_2 covered with a thin layer of Au, the absorption spectra are strongly modified only over the spectral range 500–600 nm. The electronic structure of TiO_2 is apparently not affected by the deposition of a thin layer of gold on top of TiO_2.

4. Conclusions

The effects of gold nanoparticles in the bulk of TiO_2 thin films and of a discontinuous gold overlayer on the optical and photoelectrochemical properties of TiO_2 thin film photoanodes have been investigated. Thin film nanocermets based on TiO_2 with noble metal inclusions seem to be promising candidates for photoanodes in photoelectrochemical systems. The presence of Au in TiO_2 increases optical absorption over the visible range of the light spectrum, thus improving the photoresponse of the system under illumination. Increased optical absorption in nanocermets results from Surface Plasmon Resonance (SPR) and affects the spectral dependence of the photocurrent density. Photoanodes of TiO_2 with a discontinuous Au film give a significantly better photoresponse than those with Au in the bulk. A careful characterization of the material microstructure is necessary for the successful application of such systems in photoelectrochemical applications.

Acknowledgements

This project is supported by the Polish State Committee for Scientific Research under grant No. 4T08A02524. The author would like to thank dr hab. inż. K. Zakrzewska for inspiring discussions, and to acknowledge dr inż. K. Kowalski for the XPS.

References

[1] FUJISHIMA A.K., HONDA H., Nature, 238 (1972), 37.
[2] RADECKA M., ZAKRZEWSKA K., WIERZBICKA M., GORZKOWSKA A., KOMORNICKI S., Solid State Ionics, 157 (2003), 379.
[3] GORZKOWSKA A., RADECKA M., Mol. Phys. Rep., 35 (2002), 126.
[4] MAY M., DEBRUS S., PINÇON N., PROT D., PALPANT B., CHARRON E., RADECKA M., OSUCH W., ZAKRZEWSKA K., Suppl. Le Vide: Science, Technique et Application, 295 (2000), Société Française du Vide, Paris, France, pp. 318–320.
[5] RADECKA M., GORZOWSKA-SOBAS A., ZAKRZEWSKA K., SOBAS P., Opto-Electron. Rev., 12, (2004), 53.
[6] ZAKRZEWSKA K., RADECKA M., KRUK A., OSUCH W., Solid State Ionics, 157 (2003), 349.
[7] ZAKRZEWSKA K., Thin Solid Films, 451–452 (2004), 93.
[8] GRATZEL M., Nature, 414 (2001), 338.
[9] RADECKA M., Thin Solid Films, 451–452 (2004), 98.
[10] NIST Standard Reference Database 20, version 3.2 (Web Version) (http://srdata.nist.gov/xps).
[11] RADECKA M., WIERZBICKA M., KOMORNICKI S., REKAS M., Physica B 348 (2004) 160.

Received 10 December 2004
Revised 27 January 2005

Materials Science-Poland, Vol. 24, No. 1, 2006

Electrooxidation of methanol in alkaline solution on composite electrodes

J. M. SKOWROŃSKI[1, 2*], A. WAŻNY[2]

[1]Poznań University of Technology, Institute of Chemistry and Technical Electrochemistry, ul. Piotrowo 3, 60-965 Poznań, Poland

[2]Central Laboratory of Batteries and Cells, ul. Forteczna 12, 61-362 Poznań, Poland

The electrooxidation of methanol in an alkaline electrolyte has been studied on nickel foam-based composite electrodes. The aim of this work was to establish the electrochemical usefulness of electrodes in alkaline fuel cells. Nickel foam, exhibiting electrocatalytic activity, was modified by covering it with a polyaniline (PANI) film, followed by the electrodeposition of platinum particles on the PANI matrix (Ni | PANI | Pt). For comparison, platinum was also deposited directly on the surface of the nickel substrate. The results show that Ni | PANI | Pt electrodes exhibit the highest electrocatalytic activity for methanol oxidation in the reaction occurring in the potential range of NiOOH formation.

Key words: *methanol oxidation; nickel, platinum; polyaniline; electrocatalysis*

1. Introduction

Large energy consumption and a global increase in ecological awareness have created a strong demand for new, efficient and ecological sources of energy. An attractive alternative to the combustion of fossil fuels is the fuel cell [1, 2]. At present, extensive works are being carried out in many laboratories on new types of electrode materials involving electronically conducting polymers (ECP) [3–6] which offer wide possibilities for practical application as electrodes in alkaline fuel cells. Platinum and other noble metal microparticles dispersed on materials with high surface area are of considerable interest in catalysis [4–10]. It has been proved that such electrodes exhibit electrocatalytic behaviour toward the electrooxidation of various organic substances which may be used as fuels, e.g., methanol [11]. Although the process of anodic methanol oxidation has been intensively studied over many years, the mechanism of the reaction is still under discussion [12–18]. The process, occurring with a platinum catalyst, is described by the overall reaction [13]:

*Corresponding author, e-mail: jan.skowronski@put.poznan.pl

$$CH_3OH + H_2O = CO_2 + 6H^+_{aq} + 6e^- \quad (1)$$

The fact that the overall process involves six electrons per methanol molecule to produce carbon dioxide makes methanol a promising fuel for direct fuel cells. The reaction in Eq. (1) is favoured in alkaline solution due to generation of hydrogen ions. There are many mechanisms proposed for methanol oxidation in an alkaline medium. One path is the following process [14]:

$$Pt + OH^- \longleftrightarrow Pt\text{–}(OH)_{ads} + e^- \quad (2)$$

$$2Pt + CH_3OH \longleftrightarrow PtH + Pt\text{–}(CH_3O)_{ads} \quad (3)$$

$$Pt\text{–}(CH_3O)_{ads} + Pt\text{–}(OH)_{ads} \longrightarrow Pt_2\text{–}(CH_2O)_{ads} + H_2O \quad (4)$$

$$Pt_2\text{–}(CH_2O)_{ads} + Pt\text{–}(OH)_{ads} \longrightarrow Pt_3\text{–}(CHO)_{ads} + H_2O \quad (5)$$

$$Pt_3\text{–}(CHO)_{ad} + Pt\text{–}(OH)_{ads} \longrightarrow Pt_2\text{–}(CO)_{ads} + 2Pt + H_2O \quad (6)$$

$$Pt_2\text{–}(CO)_{ads} + Pt\text{–}(OH)_{ads} \longrightarrow Pt\text{–}(COOH)_{ads} + 2Pt \quad (7)$$

$$Pt\text{–}(COOH)_{ads} + Pt\text{–}(OH)_{ads} \longrightarrow 2Pt + CO_2\uparrow + H_2O \quad (8)$$

Various intermediates formed during the main reaction [15] result in poisoning the electrode surface [15, 16]. It is generally accepted that the most poisoning species are adsorbed CO molecules [17]. The most important reasons for using microcrystalline platinum dispersed onto a polymer matrix are: (a) a catalyst exhibits higher tolerance toward poisoning by intermediate species occurring in the oxidation process (mainly by absorbed CO), (b) electrodes containing fine platinum particles are cheaper than bare platinum [19]. Numerous publications have been devoted to examining the electrocatalytic properties of platinum particles deposited onto ECP films (mainly on polyaniline, polypyrrole, and polythiophene), and it has been reported that such electrodes exhibit even higher catalytic activity for methanol oxidation than bare platinum [5, 6]. El-Shafei [20] examined methanol oxidation on a nickel | glassy carbon composite electrode, whereas Rahim et al. [21] have studied this reaction on a nickel | graphite composite electrode. The results reported in both publications led to the conclusion that methanol is oxidized with the participation of trivalent nickel, after nickel anodically oxidizes to NiOOH. Skowroński and Ważny [22] have shown that methanol is oxidized on a nickel foam electrode in 6 M KOH via a NiOOH layer formed on the electrode surface in the potential range 0.4–0.5 V vs. the Hg | HgO electrode.

The aim of this work was to make an attempt to prepare new composite electrodes for methanol oxidation in an alkaline electrolyte based on nickel foam, which is both lightweight and highly porous (above 95%), and to estimate the electrochemical activity of these electrodes.

2. Experimental

Electrochemical measurements were performed using a potentiostat-galvanostat PGSTAT 30 Autolab (Eco Chemie B.V.). All experiments were carried out in a three-electrode system. The working electrodes were: (a) a nickel | polyaniline electrode (Ni | PANI), (b) a nickel | polyaniline | platinum electrode (Ni | PANI | Pt), and (c) a nickel | platinum electrode (Ni | Pt). Nickel foam with a thickness of 1.6 mm, density 500 g/m^2, and porosity higher than 95% (produced by Nitech) was modified to prepare these electrodes. The geometrical area of all the electrodes was 1 cm^2. The counter electrode was the nickel-sintered electrode filled with cadmium hydroxide. The Hg | HgO | 6 M KOH system was employed as the reference electrode (E = 0.098 V vs. NEW). The electrolyte was a 6 M KOH solution, either with or without CH_3OH (0.1 M). The catalytic activity of all the composite electrodes in methanol oxidation was measured by cyclic voltammetry (CV) in the potential range 0.1–0.7 V at a scan rate of 50 mV/s.

Using the CV technique, the nickel foam electrode (density 500 g/m^2, thickness 1.6 mm, geometric surface 1 cm^2) was coated with polyaniline film in a freshly prepared solution of 0.1 M H_2SO_4 + 0.1 M aniline, purged with argon to remove oxygen. For each electrode, 50 oxidation/reduction cycles were made in the potential range –0.66–0.37 V vs. Hg | Hg_2SO_4 | 1 M H_2SO_4 (E = +0.674 V vs. NEW) at a scan rate of 10 mV/s. A lead sheet (containing 0.6% of Ca and 1% of Sn) was used as a counter electrode. Platinum microparticles were dispersed on the PANI film by the galvanostatic reduction of chloroplatinic acid (0.03%) in 0.1 M H_2SO_4 for 2 h using a cathodic current of 1 mA/cm^2. All measurements were performed at a temperature of 20 ºC.

3. Results and discussion

Nickel | PANI electrode. The nickel | polyaniline (Ni | PANI) electrode was prepared by electrodepositing a polyaniline film on the porous surface of nickel foam. As can be seen in Fig. 1a, the nickel foam corroded in the acid solution admixed with aniline during a few cycles until a PANI film of sufficient thickness covering the electrode protected it effectively. After about the first ten cycles, the PANI film thickened systematically along with an increase in anodic peaks (Fig. 1b). The electrochemical activity of the Ni | PANI electrode for methanol oxidation was estimated in a 6 M KOH solution containing 0.1 M CH_3OH. As can be seen from Fig. 2 (solid line), the Ni | PANI electrode exhibits a total lack of electrochemical activity. Instead of an anodic peak, a steep and linear rise of current, a typical resistor-like characteristic, is observed. On the contrary, this electrode is active in a KOH solution free of CH_3OH, for which a distinct anodic peak noted at a potential of about 450 mV corresponds to the oxidation reaction β-$Ni(OH)_2 \rightarrow (\beta,\gamma)$-NiOOH [21, 22] (Fig. 3, solid line).

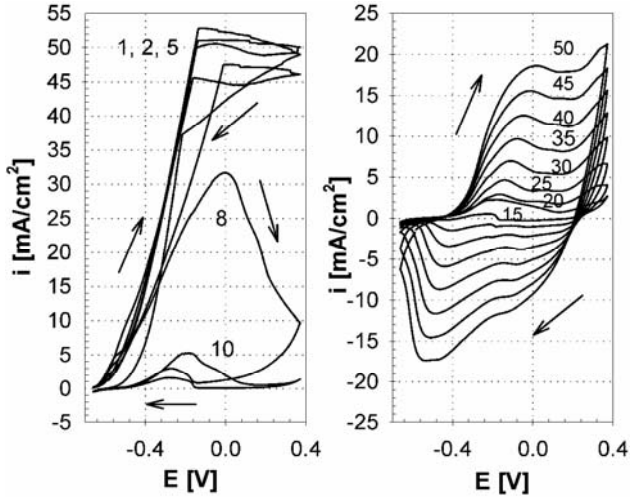

Fig. 1. Cyclic voltammograms illustrating the formation of polyaniline on the nickel foam electrode in a 0.1 M aniline | 0.1 M H_2SO_4 solution: a) cycles 1–10, b) cycles 15–50. Scan rate: 10 mV/s. Potential range: –0.66–0.37 V vs. Hg | Hg_2SO_4 | 1 M H_2SO_4

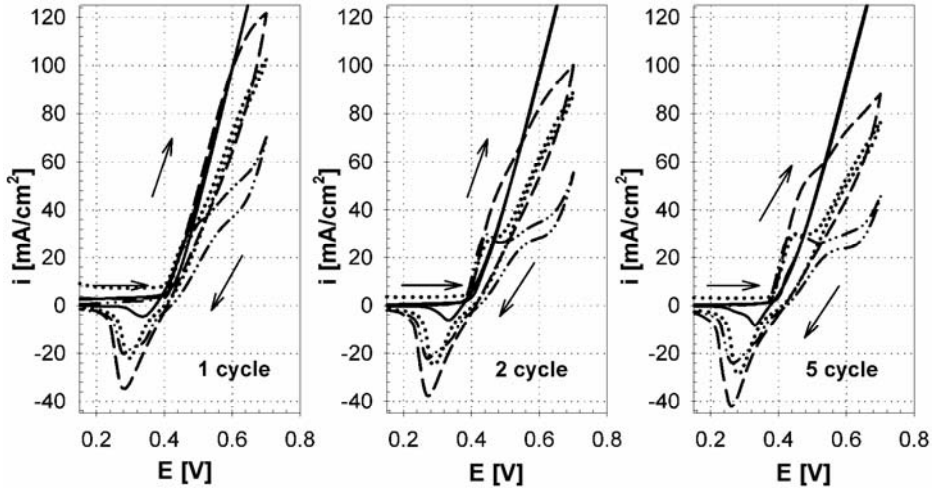

Fig. 2. Cyclic voltammograms of methanol oxidation in a 0.1 M CH_3OH | 6 M KOH solution on a nickel foam electrode (- ·· -), Ni | PANI electrode (——), Ni | PANI | Pt electrode (----), and Ni | Pt electrode (····); potential range: 0–0.70 V, scan rate: 50 mV/s

From this comparison, one can assume that the Ni | PANI electrode surface is blocked by passive products of methanol oxidation in the CH_3OH/KOH solution. The different behaviour of the electrode, depending on whether or not methanol is present in the KOH solution suggests that the PANI film is partially permeable to hydroxyl ions and that it is too dense to allow the penetra-

tion of methanol or/and the product of methanol oxidation to the nickel foam surface. From these results, one can infer that the Ni | PANI electrode can be used as a catalyst carrier, but not as a self-contained catalyst in the reaction of methanol oxidation. Taking this into account, in the following experiments the PANI film was used as an organic substrate for the platinum catalyst.

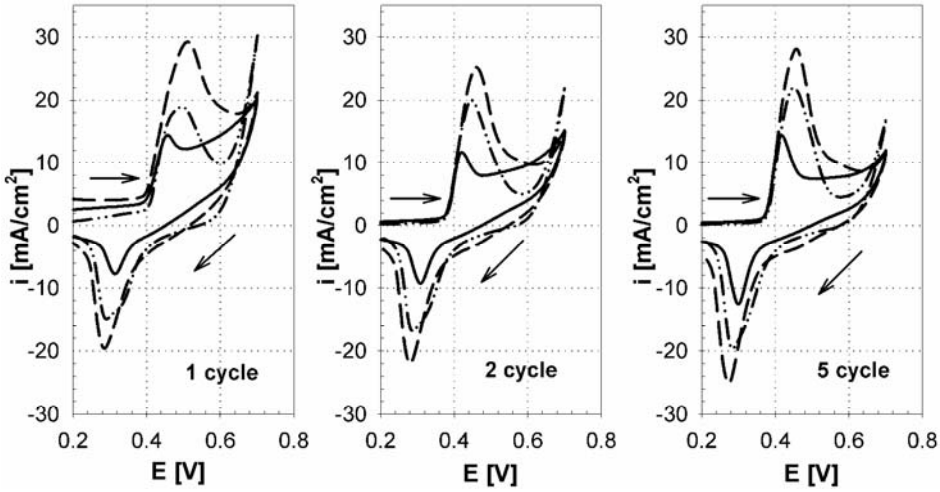

Fig. 3. Cyclic voltammograms recorded in 6 M KOH for
a nickel foam electrode (- ·· -), Ni | PANI electrode (——), Ni | PANI | Pt electrode (----),
and Ni | Pt electrode (····); potential range: 0–0.70 V, scan rate: 50 mV/s

Nickel | PANI | platinum electrode. The deposition of platinum particles on a freshly prepared polyaniline film was carried out using the CV technique. The obtained three-component electrode (Ni | PANI | Pt) was examined in a CH_3OH/KOH solution (Fig. 2, dashed line) and the recorded CV curves were compared to those obtained in a pure KOH solution (Fig. 3, dashed line). From comparing these figures, it is clear that after the Pt particles are dispersed on the PANI film, the catalytic activity of the Ni | PANI | Pt electrode, expressed by an anodic peak positioned in the potential range of the Ni(II) → Ni(III) transformation, is considerably higher in a methanol-containing electrolyte than in a pure KOH solution. The increase in anodic charge can simply be related to methanol oxidation. The reactivation of the Ni | PANI electrode towards methanol oxidation due to incorporating Pt particles into the PANI matrix may be accounted for by changes in the morphology of the polymeric layer covering the Ni substrate, and by the formation of some connections between the Ni surface and PANI layer. In this way, the Pt catalyst dispersed in the polymer lattice acts as both a catalyst for methanol oxidation and a promotor of the Ni(II) → Ni(III) oxidation reaction. Such an explanation is consistent with CV curves for different types of electrodes (Fig. 2). The contribution of the polyaniline matrix to increasing the elec-

trochemical activity is substantiated by the fact that methanol oxidizes less effectively on the Ni | Pt electrode (Figs. 2 and 4).

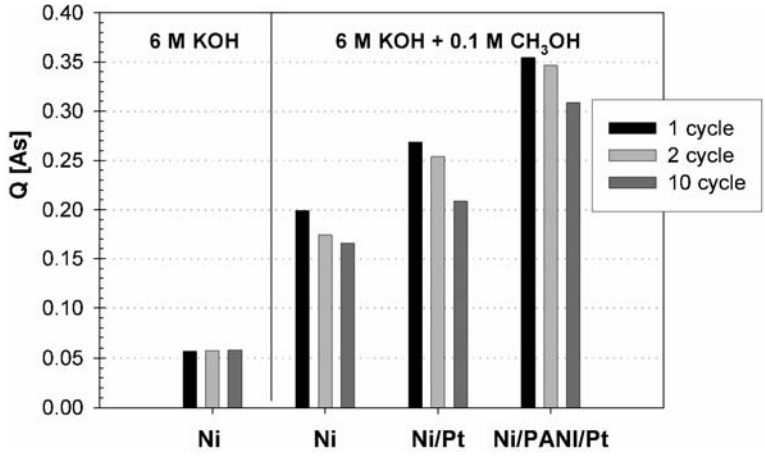

Fig. 4. Effectiveness of various electrodes in methanol oxidation estimated by comparing anodic charges calculated from CV curves recorded in a solution of 0.1 M CH_3OH | 6 M KOH (Fig. 2) and 6 M KOH (Fig. 3). Potential range: 0.38–0.60 V

Nickel | platinum electrode. The influence of platinum on the activity of nickel foam electrodes towards methanol oxidation is illustrated on the CV curves in Figure 2 (dotted line). It is clearly seen from this figure that after platinum is deposited the anodic peak attributed to methanol oxidation increases in intensity and is shifted by about 100 mV, compared to that of uncovered nickel foam. This result shows that the presence of platinum particles modifies the mechanism of the reaction β-$Ni(OH)_2 \rightarrow (\beta,\gamma)$-NiOOH in such a way that the formation of Ni(III) ions becomes easier. This phenomenon remains to be examined in the future.

4. Conclusions

Nickel foam can be successfully modified to prepare a new type of electrode material for methanol electrooxidation in alkaline solution. Based on the differences in the anodic charge of the current peaks recorded in a CH_3OH/KOH solution (Fig. 2), the catalytic activities of the examined electrodes can be concluded to decrease in the order: Ni | PANI | Pt > Ni | Pt > nickel foam (Fig. 4). As can be seen from Fig. 4, the activity of the Ni | PANI | Pt electrode is about 30% higher compared to the Ni | Pt electrode, and about 75% higher compared to the unmodified nickel foam electrode. It was clearly shown that the activity of the unmodified electrode can be improved after coating the nickel surface with platinum. It is likely that the presence of Pt particles makes the $Ni(OH)_2 \rightarrow$ NiOOH reaction more effective and, as a consequence, more

active NiOOH species can take part direct methanol oxidation. The best results were obtained for a sandwich-like electrode consisting of three layers - Ni | PANI | Pt. It is assumed that the polyaniline interlayer enhances the dispersion of platinum and brings about the formation of Ni-Pt sites, which facilitate charge transfer for oxidizing methanol. The Ni | PANI | Pt electrode seems to be a promising catalyst for methanol oxidation, for which high current densities can be reached in practical fuel cells (it exceeds 100 mA/cm^2 in Fig. 2). Figure 4 shows that the anodic charge associated with methanol oxidation decreases on cycling. In the future, three possibilities should be taken into account to elucidate this phenomenon: (a) an exhaustion of methanol at the electrode/electrolyte interface, (b) changes in the chemical composition and structure of nickel oxide, (c) the role of organic poisoning intermediates formed during methanol oxidation.

Acknowledgements

This work was supported by the State Committee for Scientific Research (KBN) of Poland, Grant No. 3 T09B 127 26.

References

[1] DELL R.M., RAND D.A.J., J. Power Sources, 100 (2001), 2.
[2] CONTE M., IACOBAZZI A., RONCHETTI, M., Vellone R., J. Power Sources, 100 (2001), 171.
[3] PRASAD K.R., MUNICHANDRAIAH N., Synth. Met., 130 (2002), 17.
[4] KULESZA P.J., MATCZAK M., WOLKIEWICZ A., GRZYBOWSKA B., GALKOWSKI M., MALIK M.A., WIECKOWSKI A., Electrochim. Acta, 44 (1999), 2131.
[5] CASTRO LUNA A.M., J. Appl. Electrochem., 30 (2000), 1137.
[6] PRASAD K.R., MUNICHANDRAIAH N., J. Power Sources, 103 (2002), 300.
[7] CROISSANT M.J., NAPPORN T., LEGER J.-M., LAMY C., Electrochim. Acta, 43 (1998), 2447.
[8] KISHIDA M., ICHIKI K., HANAOKA T., NAGATA H., WAKABAYASHI K., Catal. Today, 45 (1998), 203.
[9] KISHIDA M., UMAAKOSHI K., ISHIYAMA J., NAGATA H., WAKABAYASHI K., Catal. Today, 29 (1996), 355.
[10] HEPEL M., J. Electrochem. Soc., 145 (1998), 124.
[11] MIKHAYLOVA A.A., MOLODKINA E.B., KHAZOWA O.A., BAGOTZKY V.S., J. Electroanal. Chem., 509 (2001), 219.
[12] BORKOWSKA Z., TYMOSIAK-ZIELIŃSKA A., SHUL G., Electrochim. Acta, 49 (2004), 1209.
[13] LOVE J.G., BROOKSBY P.A., MCQUILLAN A.J., J. Electroanal. Chem., 464 (1999), 93.
[14] BEDEN B., KADIRGAN F., LANY C., LEGER J.M., J. Electroanal. Chem., 142 (1982), 171.
[15] MANOHARAN R., PRABHURAM J., J. Power Sources, 96 (2001), 60.
[16] ACRESS G.J.K., J. Power Sources, 100 (2001), 60.
[17] SPENDELOW J.S., LU G.Q., KENIS P.J.A., WIECKOWSKI A., J. Electroanal. Chem., 568 (2004), 215.
[18] TRIPKOVIĆ A.V., POPOVIĆ K.DJ., LOVIĆ J.D., JOVANOVIĆ V.M., KOWAL A., J. Electroanal. Chem., 572 (2004), 119.
[19] ZHANG X., TSANG K.Y., CHAN K.Y., J. Electroanal. Chem., 573 (2004), 1.
[20] EL-SHAFEI A.A., J. Electroanal. Chem., 471 (1999), 89.
[21] RAHIM ABEL M.A., HAMEED ABEL R.M., KHALIL M.W., J. Power Sources, 134 (2004), 160.
[22] SKOWROŃSKI J.M., WAŻNY A., Mol. Phys. Rep., 35 (2002), 49.

Received 10 December 2004
Revised 10 January 2005